Design Automation Towards Sustainable Self-Compacting Concrete via Machine Learning Models

Tianyi Cui

B.Sc., M.Sc.

This thesis is being submitted in partial fulfilment of the requirements for the degree of Doctor of Philosophy

School of Engineering

Cardiff University

December 2024

ACKNOWLEDGEMENT

In 2018, I came to Cardiff University to pursue my second master's degree, transitioning from engineering management and economics to civil engineering. This shift meant I had to dedicate extra effort to bridge the gaps in my professional knowledge. Fortunately, I encountered many exceptional lecturers at the School of Engineering who inspired confidence in my studies and motivated me to continue into doctoral research.

I am deeply grateful to the joint scholarship program offered by the China Scholarship Council and Cardiff University School of Engineering, which provided me with the opportunity to live abroad and explore academic research more profoundly. Time has flown, and my four-year PhD journey is coming to an end. I would like to express my heartfelt gratitude to all of those who have supported and cared for me along the way.

I extend my deepest thanks to my supervisor, Dr. Siva Kulasegaram, for his invaluable guidance during both my master's and PhD studies. His extensive expertise and dedication to research have been a source of inspiration, teaching me invaluable lessons that I will carry forward. His encouragement and recognition gave me the confidence to approach every step of this journey with determination.

I also wish to thank my co-supervisor, Prof. Haijiang Li, for his guidance and insights during the writing of my journal articles. His organization of workshops fostered valuable interactions among students from different research groups, allowing me to make many academic connections.

A special thanks goes to Dr. Riccardo Maddalena, who provided me with opportunities to gain teaching experience and participate in the WASC project during my PhD. These experiences significantly improved my English proficiency, enhanced my professional skills, and expanded my social network, enriching my doctoral journey. His enthusiasm for both work and life has been inspiring and has had a lasting impact on my future career path.

I would also like to thank every technician in the School of Engineering lab, especially Carl, for always offering his encouragement and assistance during SCC mix design and testing. Your support and care have meant so much to me.

To my friends in the office and research group, particularly Tianchi Wu and Zhenghui Gao, thank you for your help, even though our research focuses differ. Your willingness to assist with experimental challenges and reviewer feedback has been invaluable. I also cherish the companionship and conversations that added vibrancy to my life.

Additionally, I am grateful to the friends I made in Cardiff, Honghong Song and Xiang Li, for the delicious meals, shared joys, and heartfelt moments. I hope we will always stay true to ourselves and pursue our dreams with passion.

Lastly, I want to express my deepest gratitude to my husband, parents, brother, and friends from afar. Thank you for your unconditional love and support, even I am not perfect. Your care has been my anchor throughout this whole journey.

SYNOPSIS

This thesis investigates the design, optimisation, and performance prediction of self-compacting concrete (SCC), with a focus on high strength SCC (HSSCC) and steel fibre reinforced SCC (SFRSCC). The research addresses critical challenges in SCC mix design and performance evaluation, aiming to improve efficiency, sustainability in modern construction.

A pragmatic mix design methodology for HSSCC was developed, incorporating supplementary cementitious materials (SCMs) to achieve target compressive strengths of 70-100 MPa. This methodology reduces cement consumption and carbon emissions, contributing to sustainable construction practices. Design charts were created to provide practical guidance for selecting optimal mix proportions. Experimental validation confirmed that the proposed HSSCC mixes met performance requirements, with significant reductions in CO_2 emissions and improvements in fresh and hardened properties.

Machine learning models, including support vector machines (SVM), artificial neural networks (ANN), decision trees (DT), and random forests (RF) were employed to predict the properties of SCC mixes containing fly ash. The results highlight the potential of machine learning to replace traditional methods by efficiently capturing the complex interactions between SCC components and their performance. Feature importance analysis provided a detailed understanding of the contributions of specific mix components, offering valuable guidance for optimising SCC formulations.

For SFRSCC, advanced ensemble learning models, including RF, gradient boosting decision trees (GBDT), XGBoost, and LightGBM, were applied alongside traditional machine learning approaches. Ensemble methods consistently outperformed traditional models in predicting compressive, tensile, and flexural strengths. Feature analysis was also employed for the best-performing models to assess the impact of the components on SFRSCC properties.

This research makes significant contributions by introducing a pragmatic mix design methodology, integrating machine learning for efficient performance prediction, and providing advanced ensemble models for analysing SFRSCC properties. Overall, this research advances the understanding of SCC and its derivatives, contributing to the development of sustainable concrete technologies.

CONTENTS

LIST OF FIGURES

LIST OF TABLES

LIST OF PUBLICATIONS

1. **Cui, T.,** Kulasegaram, S. and Li, H. 2022. Predicting fresh and hardened properties of self-compacting concrete containing fly ash by artificial neural network model. In: *MATEC Web of Conferences: Concrete Solutions 2022 – 8th International Conference on Concrete Repair, Durability & Technology*. Leeds, UK: EDP Sciences, p. 05005. doi: 10.1051/matecconf/2022361050 05.
2. Alshahrani, A., **Cui, T.** and Kulasegaram, S. 2022. Influence of sand to aggregate ratio on the fresh and mechanical properties of Self-compacting high-performance concrete. In: *Proceedings of the 7th World Congress on Civil, Structural, and Environmental Engineering (CSEE'22)*. ICSECT. doi: 10.11159/icsect22.171.
3. Alshahrani, A., **Cui, T.** and Kulasegaram, S. 2022. Effect of Sand to Aggregate Ratio on the Properties of Self-Compacting High-Performance Concrete. *International Journal of Civil Infrastructure* 5, pp. 37–42. doi: 10.11159/ijci.2022.006.
4. **Cui, T.,** Kulasegaram, S. and Li, H. 2023. Prediction of Mechanical Properties of Steel Fibre-Reinforced Self-compacting Concrete by Machine Learning Algorithms. In: *RILEM Bookseries*. Cham, Switzerland: Springer., pp. 703–711. doi: 10.1007/978-3-031-33187-9_65.
5. **Cui, T.,** Alshahrani, A. and Kulasegaram, S. 2024. Effects of mineral additions on the rheological properties of self-compacting concrete: a review. *Proceedings of Institution of Civil Engineers: Construction Materials*. doi: 10.1680/jcoma.22.00105.
6. **Cui, T.**, Kulasegaram, S. and Li, H. 2024. Design automation of sustainable self-compacting concrete containing fly ash via data driven performance prediction. *Journal of Building Engineering* 87, p. 108960. doi: 10.1016/J.JO BE.2024.108960.

7. Alshahrani, A., **Cui, T.**, Almutlaqah, A. and Kulasegaram, S. 2024. Designing sustainable high-strength self-compacting concrete with high content of supplementary cementitious materials. *European Journal of Environmental and Civil Engineering* 28(8), pp. 1830–1849. doi: 10.1080/19648189.2023.2279563.

NOTATIONS

NVC	Normal vibrated concrete
SCC	Self-compacting concrete
HSSCC	High strength self-compacting concrete
SFRSCC	Steel fibre reinforced self-compacting concrete
SCMs	Supplementary cementitious materials
SVM	Support vector machine
SVR	Support vector regression
ANN	Artificial neural network
DT	Decision tree
RF	Random forest
GBDT	Gradient boosting decision tree
AdaBoost	Adaptive boosting
CatBoost	Categprocal boosting
GBoost	Gradient boosting
XGBoost	Extreme gradient boosting
LightGBM	Light gradient boosting machine
HistGBM	Histogram-based gradient boosting
BPNN	Backpropagation neural network
BBP	Biogeographical-based programming
ABCP	Artificial bee colony programming
MARS	Multivariate Adaptive Regression spline
MPMR	Minimax Probability Machine Regression
GEP	Gene expression programming
MEP	Multi-gene expression programming

RBFNN	Radial basis function neural network
FOA	Firefly optimization algorithm
MLR	Multiple Linear Regression
MRM	Multivariable regression model
GAM	Generalized additive model
HRWR	High-range water reducers
VEA	Viscosity-enhancing admixture
SR	Segregated ratio
ITZ	Interfacial transition zone
w/cm	Water to cementitious material ratio
w/p	Water to powder ratio
S/A	Sand to aggregate ratio
P/S	Paste to solid ratio
OPC	Ordinary Portland cement
F	Fly ash
GGBS	Ground granulated blast furnace slag
CA	Coarse aggregate
maxCA	Maximum size of coarse aggregate
FA	Fine aggregate
SP	Superplasticizer
LP	Limestone powder
LD	Limestone dust
CS	Copper slag
RSF	Recycled steel fibre
MSF	Manufactured steel fibre
VF	Volume fraction of steel fibre

AR	Aspect ratio of steel fibre
RMDA	Rational mix design approach
PF	Packing factor
PDF	Probability density function
KNN	K-nearest neighbours
CHAID	Chi-squared automatic interaction detection
CART	Classification and regression trees
RBF	Radial basis function
REC	Regression error characteristic
SHAP	Shapley additive explanation
D_{slump}	Final slump flow diameter, mm
T_{500}	The time taken for the mix to spread 500 mm in slump test, s
D_{J-ring}	Final J-ring flow diameter, mm
T_{500j}	The time taken for the mix to spread 500 mm in J-ring test, s
T_{200}	The time taken for the mix to reach the 200 mm line in L-box test, s
T_{400}	The time taken for the mix to reach the 400 mm line in L-box test, s
d_1	Maximum diameter of the concrete spread, mm
d_2	The diameter perpendicular to d_1, mm
H_1	The height of the mix in the vertical section in L-box test, mm
H_2	The height of the mix in the horizontal section in L-box test, mm
W_c	Initial mass of concrete placed on the sieve, g
W_p	Mass of the sieve receiver, g
W_{pc}	Mass of both receiver and collected concrete, g

τ	Shear stress, Pa
τ_0	Yield stress, Pa
$\tau_{1/2}$	Shear stress at which viscosity is twice the zero-shear, Pa
$\dot{\gamma}$	Rate of shear strain, s^{-1}
λ	Time constant, s
η	Apparent viscosity, Pa s
η_p	Plastic viscosity, Pa s
$[\eta]$	Intrinsic viscosity, Pa s
η_∞	Limit shear viscosity, Pa s
η_0	Initial shear viscosity, Pa s
K	Consistency coefficient
α	Flow behaviour index for the Ellis model
n	Liquidity index
c	Decay constant
σ	Standard deviation of the sample data
μ	Mean value of sample data
R	Correlation coefficient
R^2	Coefficient of determination
MSE	Mean squared error
$RMSE$	Root mean squared error
MAE	Mean absolute error
$MAPE$	Mean absolute percentage error
P	Predicted result
P_A	Average values of predicted result
E	Actual result
E_A	Average values of actual result

N	Total number of samples
$K(\boldsymbol{x}_i, \boldsymbol{x}_j)$	Kernel function of SVM
f_{cu}, Fcu	Compressive strength, MPa
Fts	Tensile strength, MPa
Ff	Flexural strength, MPa
ϕ_m	Maximum particle volume fraction
SD	Slump flow diameter in modelling, mm
VF	V-funnel flow time in modelling, s

Chapter 1 Introduction

1.1 Background

With the rapid development of the construction industry, the applications of concrete have expanded significantly, and its usage environments have become increasingly complex. Large-scale infrastructure and high-rise buildings often require dense reinforcement to ensure structural integrity. However, such complex designs pose challenges for normal vibrated concrete (NVC), including difficulties in compaction, uneven density, and potential safety risks. As a result, there is a pressing need for innovative concrete materials with enhanced workability and performance.

Self-compacting concrete (SCC) was first introduced in the 1980s by Ozawa at the University of Tokyo (Ozawa 1989). Unlike NVC, SCC exhibits superior flowability without segregation, along with excellent passing and filling capabilities. SCC achieves compaction under its own weight without the need for mechanical vibration, resulting in a homogeneous and dense concrete structure (EFNARC 2005). Over time, SCC has become an important branch of construction materials research and is widely applied in modern construction projects (Ouchi et al. 2003; Wu et al. 2021).

The application of SCC offers several advantages, such as reducing the need for manual labour, lowering construction costs, minimizing noise pollution during placement, and improving the working environment for labourers. Furthermore, many supplementary cementitious materials (SCMs) can partially replace cement and fine aggregates in SCC, contributing to reduced CO_2 emissions during cement production and enabling the recycling of industrial by-products (Corinaldesi and Moriconi 2011; Gupta et al. 2021). Consequently, the development of sustainable SCC supports energy conservation, environmental protection, and the transition of the construction industry toward green and sustainable practices.

In high-rise construction, SCC demonstrates unique advantages due to its exceptional flowability, allowing it to be easily pumped to heights of several hundred meters. However, the base structures of high-rise buildings bear significant loads from upper levels, necessitating the use of high strength SCC (HSSCC). Employing HSSCC reduces the overall volume of concrete required, thereby enhancing energy efficiency and economic feasibility. Despite its many advantages, concrete inherently has a low tensile strength, which leads to limited fatigue resistance (Miarka et al. 2022). To address this limitation, steel fibre-reinforced self-compacting concrete (SFRSCC) has been developed, combining the advantages of SCC with the enhanced tensile and dynamic properties of fibre-reinforced concrete.

The performance of SCC is highly sensitive to its constituent materials and their proportions. The mix design largely determines both its fresh-state workability and hardened-state performance. Poor workability can result in issues such as pump blockages and uneven placement, affecting construction quality and progress. On the other hand, inconsistencies in hardened properties may lead to structural deficiencies, failing to meet engineering requirements. Therefore, both fresh and hardened properties must be carefully considered during SCC mix design. Currently, SCC mix design methods lack standardization and primarily rely on iterative experimental procedures. While effective, this approach is time-consuming and labour-intensive. There is a pressing need for more efficient, sustainable, and cost-effective design methodologies to enhance the performance and reliability of SCC.

Improving the current mix design practices for SCC can mitigate undesirable performance outcomes. Accurate performance prediction and effective quality control of SCC are essential for enhancing industry efficiency and promoting its broader adoption. Numerical simulations have proven to be valuable tools for understanding the flow behaviour of SCC and ensuring compliance with self-consolidating standards (Bao et al. 2020; Zhang et al. 2021). However, due to the complexity of SCC—particularly the interactions between cementitious materials and chemical admixtures—numerical simulations often lack flexibility.

With advancements in computational power and artificial intelligence, machine learning has demonstrated exceptional capabilities in solving complex problems such as classification, regression, clustering, and pattern recognition (Sharifani and Amini 2023). Machine learning excels in addressing problems with opaque mechanisms and multiple influencing factors, making it a promising tool for civil engineering applications. For SCC, machine learning offers a faster and more adaptable approach to performance prediction, providing the way for more precise and efficient mix designs. By leveraging machine learning techniques, a comprehensive framework can be established to map SCC performance, facilitating its application in modern construction.

1.2 Aims and objectives

The overarching motivation for this thesis is driven by the need to optimise the methods and efficiency involved in SCC mix design and performance prediction. To achieve this goal, this research aims to establish a comprehensive framework encompassing experimental mix design and machine learning-based performance prediction of SCC, with a specific focus on the incorporation of SCMs and steel fibres. The specific objectives of this research are as follows:

- Formulate an HSSCC mix design incorporating SCMs to achieve target viscosity and compressive strength, optimising both performance and environmental sustainability by reducing cement consumption. A series of HSSCC design charts will be generated to facilitate the selection of mix proportions that meet the desired performance requirements.
- Conduct experimental validation of the proposed HSSCC mix designs to ensure they meet the specified performance criteria. Perform a

sustainability assessment of the developed mixes to evaluate their environmental benefits.

- Develop and refine machine learning algorithms for predicting the properties of SCC mixes containing fly ash, one of the most commonly used SCMs. Investigate the influence of mix components on SCC performance, focusing on their contribution to fresh properties and mechanical properties.
- Build and optimise advanced ensemble machine learning models to analyse and predict the mechanical properties of SFRSCC. Examine the contribution of steel fibres and other mix constituents to critical performance metrics, thereby providing insights into their interaction mechanisms and their influence on mechanical performance.

1.3 Outline and structure of the thesis

This research is organised into seven chapters, with the contents of the following chapters are summarised below. The technical route of this research is shown in Figure 1.1, providing a comprehensive overview of the methodology and key steps undertaken throughout the thesis.

Chapter 2 presents a comprehensive review of SCC, covering its key properties and testing methods. It also examines the effects of incorporating SCMs and steel fibres and summarises the current mix design methodologies, highlighting their limitations and opportunities for improvement.

Chapter 3 provides an overview of machine learning models, detailing the working principles of key algorithms. It also summarises the state-of-the-art applications of machine learning in SCC research, identifying gaps and challenges addressed in this thesis.

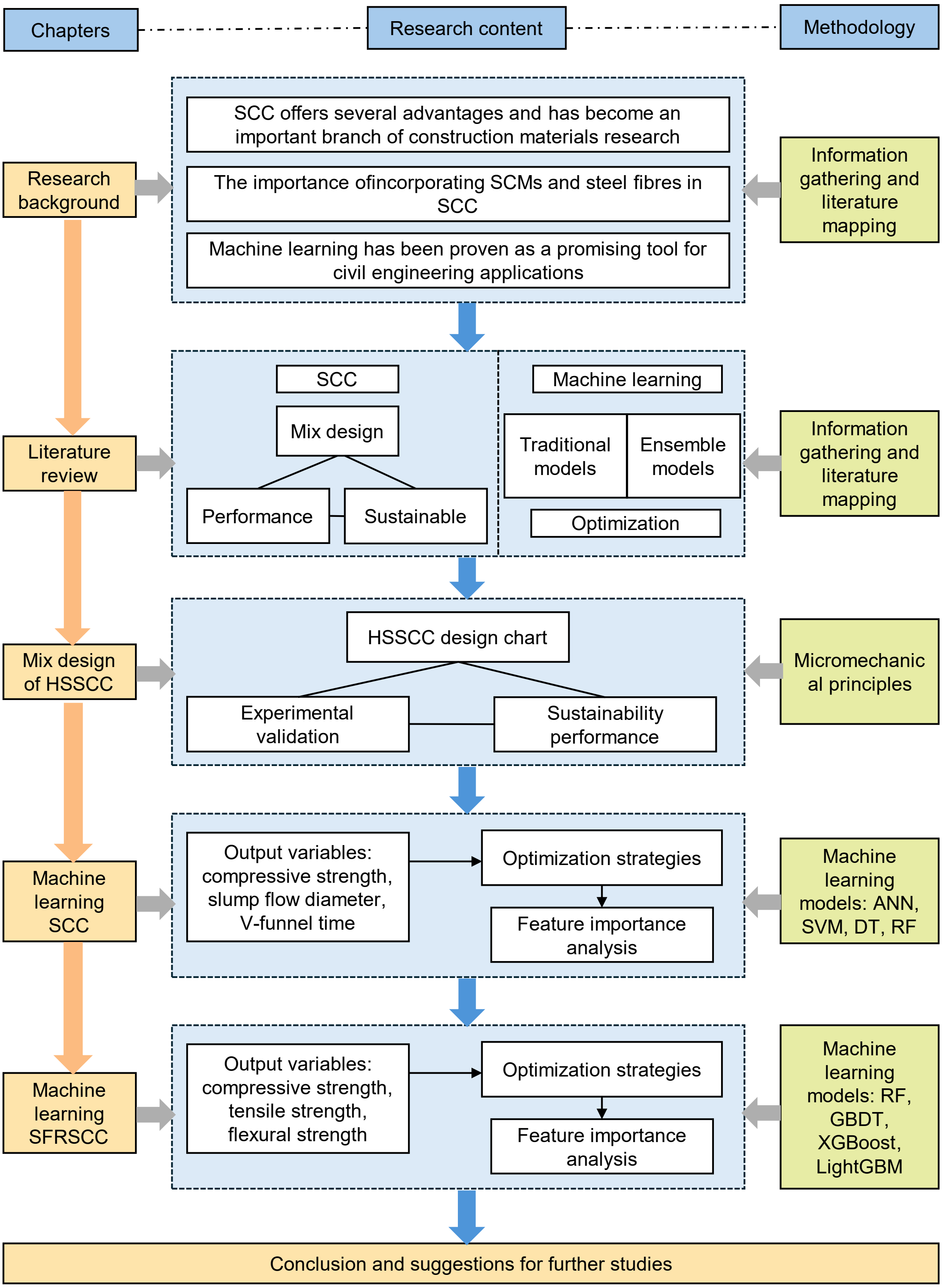

Figure 1.1 Technical route of this research

Chapter 4 introduces a pragmatic method for designing HSSCC mixes. It begins with an in-depth analysis of target compressive strength and plastic viscosity, followed by a detailed explanation of the proposed mix design methodology. Experimental validation of the method is conducted using selected materials and design procedures, and a practical example demonstrates the application of the developed design charts.

Chapter 5 presents the development of machine learning models, including support vector machines, decision trees, random forests, and artificial neural networks to predict both the fresh and hardened properties of SCC mixes containing fly ash. A structured data-driven framework is proposed, showcasing the potential for practical application in mix design optimisation.

Chapter 6 focuses on predicting the mechanical properties of SFRSCC using traditional supervised learning models and advanced ensemble learning models. These models are refined using optimisation techniques. Feature importance analysis is conducted to provide insights into the influence of various mix components on SFRSCC properties.

Chapter 7 summarises the key findings of the research, discusses its contributions, and provides recommendations for future studies.

1.4 Research contribution

This thesis makes several original contributions to the field of SCC and its performance prediction using machine learning techniques. The novelty of the research lies in the development of innovative methods and frameworks that advance both the theoretical understanding and practical application of SCC. The key contributions are summarised as follows:

- A pragmatic mix design approach is proposed for HSSCC (70-100 MPa), focusing on optimising both fresh properties and hardened properties. The methodology incorporates SCMs to achieve superior mechanical performance while reducing cement content, promoting environmental sustainability. The creation of HSSCC design charts provides a practical tool to efficiently select mix proportions for target performance requirements.

- The study evaluates the environmental performance of the developed HSSCC mixes, demonstrating their potential to reduce CO_2 emissions and utilise industrial by-products to minimise waste. This contribution aligns with global efforts to transition the construction industry towards greener and more sustainable practices.
- A comprehensive machine learning framework is developed to predict both fresh and hardened properties of SCC mixes containing SCMs. The research leverages multiple ML algorithms, offering a data-driven approach to enhance SCC design and quality control.
- Advanced ensemble learning models are applied to predict the mechanical properties of SFRSCC. The proposed models outperform traditional prediction methods, offering higher accuracy and reliability.
- The research includes a detailed feature importance analysis, identifying key mix components and their influence on fresh and hardened properties of SCC and SFRSCC. This analysis provides valuable insights for both researchers and engineers, facilitating the optimization of mix designs.
- The thesis introduces a unified framework combining experimental design, sustainability assessment, and machine learning prediction. This framework not only streamlines SCC mix design but also bridges the gap between research and practical applications in the construction industry.

Chapter 2 Self-Compacting Concrete

2.1 Introduction

Self-compacting concrete (SCC) is defined as a high-performance concrete that can achieve full compaction and form without the need for mechanical vibration, relying solely on its own weight. It maintains stability during flow without segregation and passes through obstacles without blockage. The self-compacting ability of SCC typically encompasses key characteristics: filling ability (flowability), passing ability, segregation resistance (stability) (Elyamany et al. 2014; Rasekh et al. 2020). Therefore, in contrast to normal vibrated concrete (NVC), which requires external vibration for compaction, SCC offers both high fluidity and excellent passing and anti-segregation properties. These qualities ensure the uniformity and stability of the concrete mix during transportation, placement, and formwork filling processes.

This chapter delves into the key properties of SCC, focusing on its fresh state behaviour, alongside the methods used for evaluating these characteristics. It also explores the effects of cementitious materials like fly ash, ground granulated blast furnace slag (GGBS), and limestone powder on the rheological properties of SCC, providing insights into their contributions to enhancing mix performance. Furthermore, the incorporation of steel fibres is discussed, highlighting their impact on improving mechanical properties and durability. Various mix design methodologies are reviewed, showcasing the evolution of SCC design approaches.

2.2 Overview of SCC development

In the mid-to-late 1980s, Japanese researchers introduced the concept of SCC in response to a declining number of skilled labourers. SCC was initially developed by Ozawa and his team at the University of Tokyo in 1986, with the first publication appearing in 1989 (Ozawa 1989). A conference paper on the subject was presented at the Fourth CANMET and ACI International

Conference in 1992 (Ozawa 1992). Global attention was attracted to the potential of SCC applications (Miura et al. 1993; Tanaka et al. 1993; Hayakawa et al. 1995). Following this, intensive research began and led by large construction companies in Asia. The primary motivation behind developing SCC was to enhance construction quality by improving both the safety and durability of the projects, while also reducing labour and construction costs associated with concrete placement (Okamura et al. 2000; Okamura and Ouchi 2003). Although SCC production costs are higher than NVC, these costs were offset by the reduction in concrete placement expenses, especially given the high labour costs in Japan. The benefits offered by SCC led to a growing global demand for this technology.

In the early years, SCC was predominantly used in Asia, then gradually spreading to Europe, North and South America. Numerous commercial projects have been developed, and the details have been reported in papers (Sonebi and Bartos 1999; Brameshuber and Stephan Uebachs 2001; Centing et al. 2002; Collepardi et al. 2003; Lessard et al. 2003; Paris M et al. 2003). SCC has found diverse applications, ranging from large-scale projects such as suspension bridge anchor blocks to smaller scale uses like concrete repairs.

The practical application of SCC in engineering relies on thorough research and analysis of its diverse properties. Present studies are primarily focused on preparation techniques, performance enhancement, and sustainable development (Long et al. 2015; Busari et al. 2018; Ashish and Verma 2019; Ferdosian and Camões 2021). Since its introduction in the 1980s, extensive research has been conducted by scholars and research institutions in these crucial areas, resulting in significant advancements. These achievements have laid a solid foundation for the widespread adoption of SCC in engineering practice.

2.3 Fresh properties of SCC

Distinguished from NVC, high-quality SCC must possess three key attributes: filling ability, passing ability, and segregation resistance. When evaluating the performance of SCC, these workability characteristics should be assessed individually. Moreover, these properties may vary depending on the intended application and design requirements of SCC. Typically, enhancing all three of these characteristics simultaneously leads to increased costs. For instance, improving filling ability often heightens sensitivity to segregation, posing greater challenges in material selection and design (Dey et al. 2021). To achieve satisfactory self-compacting performance while meeting fresh concrete requirements, SCC must also satisfy the demands for strength and durability in its hardened state. Consequently, striking a balance between these critical properties remains a key focus of SCC research.

2.3.1 Filling ability

The filling ability refers to its capacity to fill the mould under its own weight, even in the presence of obstacles that may hinder its flow. This characteristic is closely related to the filling ability of the cement paste. The filling ability of the paste can be enhanced by using high-range water reducers (HRWR) and adjusting the water to powder ratio (w/p). The inclusion of HRWR increases the filling ability of the cement paste by lowering its yield stress, and the reduction in viscosity is typically limited. As a result, the concrete achieves higher fluidity without significantly compromising cohesiveness. Additionally, an increased w/p ratio contributes to better filling ability. The powder component includes cementitious materials and other fine particles, such as recycled powders or waste materials. However, as water content rises, the cohesion of the paste decreases, which can lead to segregation between the aggregates and the paste, thus affecting the uniformity of the SCC flow. Therefore, maintaining a good filling ability in SCC requires balancing the use of HRWR and the w/p.

Another key factor influencing the filling ability is the friction between SCC solid particles, including aggregates and powders. As concrete spreads in confined spaces, the increased interaction between particles leads to higher friction levels, which in turn raises the viscosity and restricts the flow and filling ability of the fresh SCC. The reduction of friction can be fixed by using HRWR and finer fillers (Khaleel et al. 2011).

2.3.2 Passing ability

The passing ability of SCC refers to its capacity to flow through narrow spaces, such as the gaps between reinforcing bars, under its own weight. If the passing ability is insufficient, coarse aggregates may become trapped between the bars, leading to an uneven structure. Increasing the viscosity of the mix ensures that solid particles remain well-suspended during flow, reducing the risk of blockage. This can be achieved by reducing the w/p or adding an appropriate amount of viscosity enhancing admixture (VEA). Additionally, increasing the volume of the paste and reducing the proportion of coarse aggregate can further improve the passing ability of the concrete. By lowering the ratio of coarse to fine aggregates, individual coarse aggregate particles are fully surrounded by a layer of mortar. This helps to minimise the risk of interlocking or bridging between aggregates when the mix passes through narrow openings or gaps between reinforcement, thereby enhancing the passing ability of SCC (Dey et al. 2021).

2.3.3 Segregation resistance

Segregation resistance, or stability, refers to the ability of concrete to maintain its homogeneity both during flow and when at rest. Good segregation resistance ensures that the aggregate particles are distributed uniformly throughout the mix, with no separation occurring in either the vertical or horizontal directions (Bui et al. 2002). Concrete with low cohesion is more prone to segregation, as it cannot effectively suspend the aggregates, particularly when passing through confined sections of the formwork. In such cases, some of the coarse aggregates may separate, increasing the local density and leading to blockages caused by aggregate clumping and arching. Therefore, it is essential to enhance the bond between the mortar and coarse aggregates to provide sufficient cohesion, ensuring the uniform distribution of both the solid and liquid phases (Khayat 1999). Typically, limiting the volume and proportion of coarse aggregates can improve segregation resistance. Additionally, reducing the water content or using an appropriate dosage of VEA can further minimise bleeding and maintain the stability of the mix.

2.4 Tests for fresh SCC

Due to the unique properties of SCC, the testing methods and standards for the fresh properties of NVC are no longer suitable. This section reviews main testing methods used to evaluate the filling ability, passing ability, and segregation resistance of SCC.

2.4.1 Filling ability tests

2.4.1.1 Slump flow and T_{500} time

The slump flow and T_{500} time method is primarily used to assess the flowability of SCC mixtures due to its simplicity in terms of equipment and procedure, making it the most common on-site testing method. The slump flow value not only provides a straightforward measure of the fluidity of mix but also allows for the evaluation of its workability and resistance to segregation during the spreading process. The extended flow value quantifies the flow of concrete under its own weight, overcoming yield stress, viscosity, and friction. Therefore, the slump flow test often serves as an initial control measure for concrete mix design.

As shown in Figure 2.1, The left subfigure shows the vertical release of concrete from an Abrams cone (diameter: top 100 mm, bottom 200 mm, height 300 mm) placed on a smooth baseplate. The right subfigure shows the horizontal spread measurement, where the average of two perpendicular diameters (d_1 and d_2) is recorded to determine the slump flow diameter using the following equation:

$$Slump\ flow = \frac{d_1 + d_2}{2} \tag{2.1}$$

where d_1 is the maximum diameter of the concrete spread, and d_2 is the diameter perpendicular to d_1.

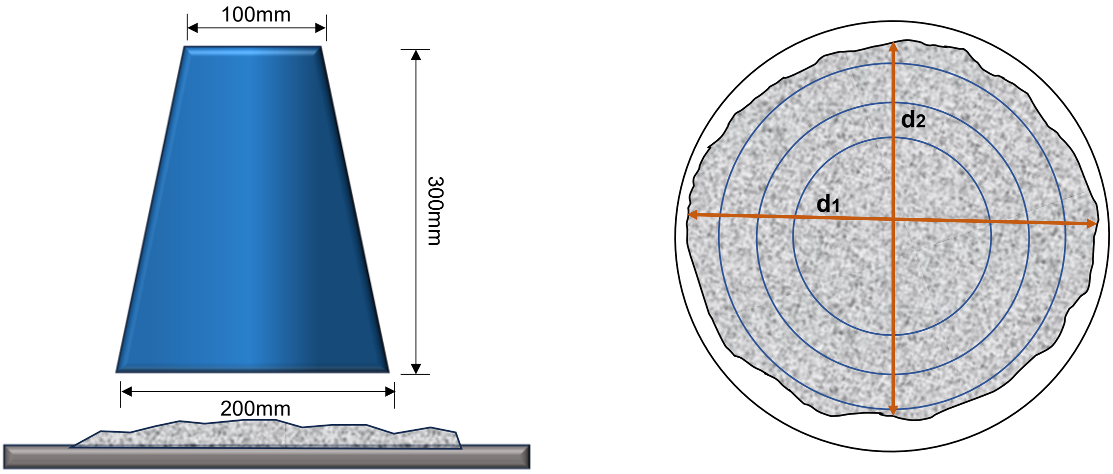

Figure 2.1 Slump test apparatus

The more circular the spread of the concrete, the more homogeneous the mixture. A concrete mix that displays no aggregate accumulation at the centre of the spread and has a uniform distribution of aggregates indicates better segregation resistance and stability. According to BS EN 206-9 (2010), the slump flow of SCC is classified into three consistence categories based on consistency. Class SF1 corresponds to slump flow values between 550 and 650 mm； class SF2 defines slump flow values ranging from 660 to 750 mm; class SF3 represents slump flow values between 760 and 850 mm.

The time taken for the concrete mix to spread to a diameter of 500 mm after the slump cone is lifted, known as T_{500}, is recorded to assess the viscosity of the mixture. Two viscosity classes are defined based on the T_{500} time: viscosity Class 1 (VS1) for $T_{500} \leqslant 2s$, and viscosity Class 2 (VS2) for $T_{500} > 2s$.

2.4.1.2 V-funnel test

Another method for evaluating the viscosity and filling ability of SCC is the V-funnel test, as shown in Figure 2.2. The V-funnel has a top opening of approximately 500 mm × 75 mm and a bottom outlet of 65 mm × 75 mm. The height of the funnel is approximately 600 mm. In this test, fresh concrete is poured into a V-shaped funnel, and the time it takes for the concrete to completely flow out of the funnel is measured, with the result recorded as the V-funnel flow time, accurate to the nearest 0.1 seconds (BS EN 12350-9 2010). Any potential blockage of aggregates in the narrower section of the funnel can influence the flow time. According to BS EN 206-9 (2010), two viscosity classes are defined: viscosity Class 1 (VF1), where the flow time is less than 8.0 seconds, and viscosity Class 2 (VF2), where the flow time falls between 8.0 and 25.0 seconds.

The V-funnel test can also be used to evaluate the segregation resistance of SCC. If the flow time increases significantly after the concrete has rested for five minutes, this suggests a higher susceptibility to segregation (Dey et al. 2021). Furthermore, an uneven flow from the funnel may indicate poor segregation resistance.

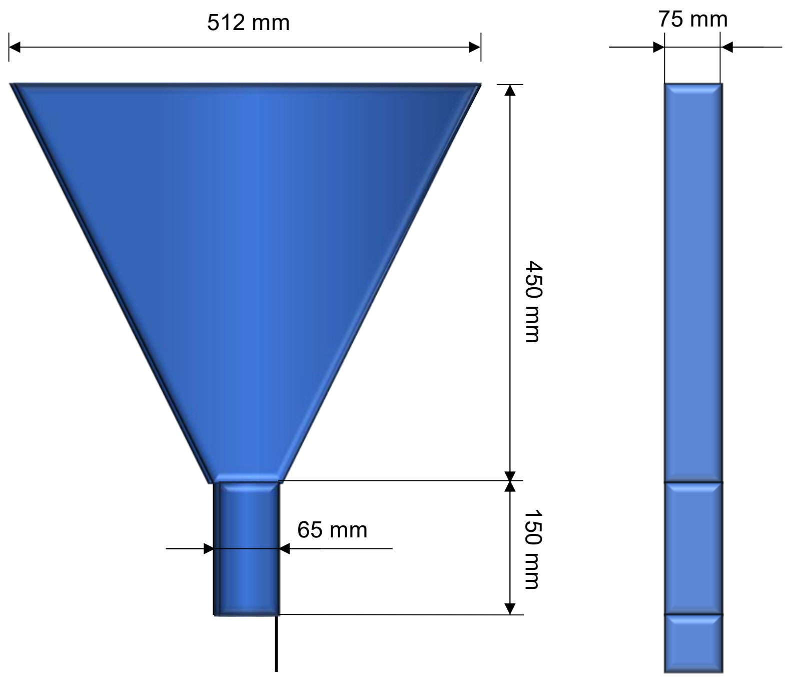

Figure 2.2 V-funnel test apparatus

2.4.2 Passing ability tests

2.4.2.1 J-ring test

The J-ring test follows a similar setup and procedure to the slump flow test, with the main difference being the inclusion of J-ring bars, as shown in Figure 2.3. This test is primarily used to evaluate the passing ability of SCC by measuring the time it takes for the concrete to flow through the bars. The J-ring consists of 16 vertical steel bars, each with a diameter of 16 mm, spaced 41 mm apart, and arranged in a circular ring with a diameter of 300 mm. As shown, the slump cone is placed within the ring, and spread measurements (d_1 and d_2) are taken similar to the slump flow test. The spacing between the bars can be adjusted based on specific requirements. During the test, the time taken for the spread diameter to reach 500 mm is recorded as T_{500j}, accurate to the nearest 0.5 seconds (BS EN 12350-12 2010). The final diameter is measured by Eq. (2.2).

$$SF_J = \frac{d_1 + d_2}{2} \tag{2.2}$$

Additionally, the height difference between the concrete inside and outside the J-ring is measured, which serves as an indicator of the passing ability of the mix. The entire slump flow and J-ring test process should be completed within 6 minutes. Potential blockage issues, which may be related to the size of the aggregates and the spacing between the rebars, are assessed by comparing the final spread diameters from the tests (Yahia and Aïtcin 2016).

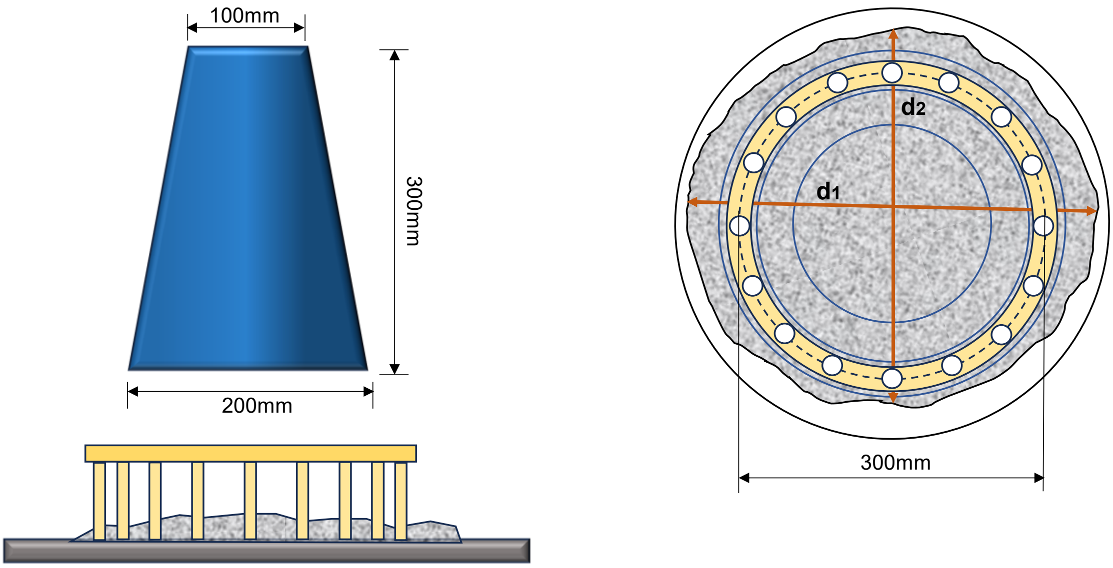

Figure 2.3 J-ring test apparatus

2.4.2.2 L-box test

The L-Box test is another method for evaluating the passing ability of SCC. As illustrated in Figure 2.4, the test uses an L-shaped container divided into vertical and horizontal sections, separated by a sliding gate (BS EN 12350-10 2010). In the horizontal section, three reinforcing bars act as obstacles, allowing the SCC to flow from the vertical section into the horizontal section. The test measures the time it takes for SCC to travel 200 mm (T_{200}) and 400 mm (T_{400}) along the horizontal part. The passing ability is further assessed by the ratio of the height of the SCC in the horizontal section (H_2) and that in the vertical section (H_1). Furthermore, EFNARC (2005) classifies the passing ability of SCC into two classes. PA1 classifies mixes that achieve a passing ability of ≥0.80

with 2 rebars, while PA2 applies to mixes with ≥0.80 passing ability using 3 rebars.

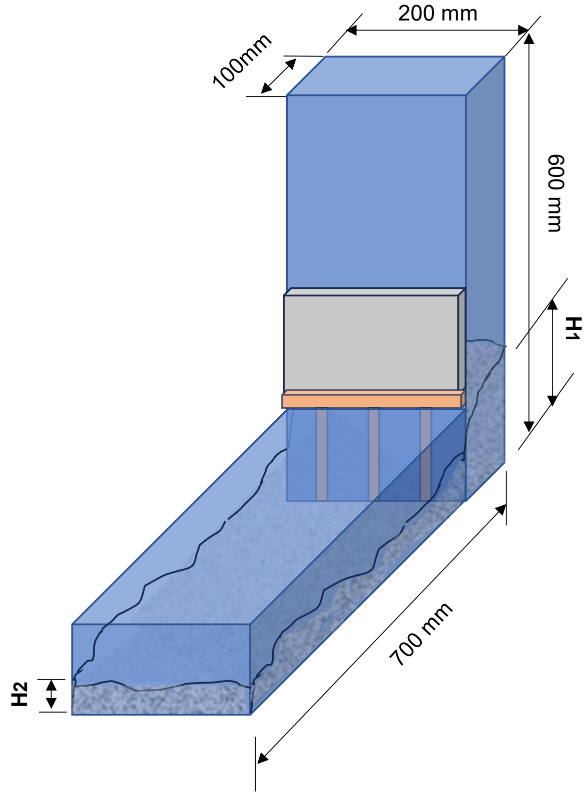

Figure 2.4 L-box test apparatus

2.4.3 Segregation resistance tests

The segregation resistance of SCC can be determined by the separation between coarse aggregates and mortar. Following BS EN 12350-11 (2010), fresh concrete is poured into a cylindrical container and allowed to rest undisturbed for approximately 15 minutes, during which time the occurrence of any bleed water is observed and noted. After this resting period, the concrete (including any bleed water) is gently poured onto the centre of a 5 mm mesh sieve placed over a receiving container. The total initial mass of concrete poured is recorded as W_c. After lifting the sieve, the final mass of both receiver and concrete that has passed through the sieve is written as W_{pc}. The segregated ratio SR can be expressed as:

$$SR = \frac{W_{pc} - W_p}{W_c} \times 100\% \quad (2.3)$$

where W_p is the mass of the receiver. The segregation resistance of SCC is classified into two levels: SR1 allows a maximum segregation of 20%, while SR2 requires a stricter limit of 15%, indicating higher stability of the mix (EFNARC 2005).

Overall, the classification of self-compacting concrete (SCC) is typically based on its fresh properties, including filling ability, passing ability, and segregation resistance. Table 2.1 summarises the standard classification criteria according to BS EN 206-9 (2010) and EFNARC (2005).

Table 2.1 Classification criteria of SCC based on workability parameters

Property	Class	Criteria
Slump Flow (mm)	SF1	550 - 650
	SF2	660 - 750
	SF3	760 - 850
V-funnel time (s)	VF1	< 8.0
	VF2	8.0 - 25.0
L-box passing ability	PA1	≥ 0.80 with 2 rebars
	PA2	≥ 0.80 with 3 rebars
Segregation Resistance	SR1	≤ 20% segregation
	SR2	≤ 15% segregation

2.5 Hardened properties of SCC

Hardened SCC exhibits diverse material properties depending on factors such as the water to cementitious material ratio (w/cm), sand content, and the characteristics of its components. However, certain differences in performance between SCC and NVC may arise due to the distinct mix designs tailored to meet workability requirements of SCC, such as the need for a lower w/cm ratio and higher paste content. This section reviews the mechanical properties and durability of SCC, drawing comparisons with NVC based on existing research.

The data presented in Figure 2.5, which shows the distribution of 28 days compressive strength for SCC applications, aligns with the analysis of SCC usage from 2008 to 2022 across different countries (Khatib 2008; Sukumar et al. 2008; Sonebi and Cevik 2009; Güneyisi 2010; Liu 2010; Şahmaran et al. 2011; Siddique 2011; Jalal and Mansouri 2012; Uysal et al. 2012; Cuenca et al. 2013; Ramanathan et al. 2013; Siad et al. 2013; Nepomuceno et al. 2014; Ponikiewski and Gołaszewski 2014; Güneyisi et al. 2015; Zhao et al. 2015; Bani Ardalan et al. 2017; Dadsetan and Bai 2017; Esquinas et al. 2018; Matos et al. 2019; Anjos et al. 2020; Choudhary et al. 2020; Guo et al. 2020a; Ting et al. 2020; Sambangi and Arunakanthi 2021; Kumar et al. 2022; Zhao et al. 2022). A wide range of compressive strength values are used in SCC applications, from 10 MPa to 100 MPa. The most commonly used strength range is between 30 MPa and 40 MPa, which indicates the balance between the performance and cost-effectiveness of C30-C40 SCC. Higher and lower strength classes are used less frequently, suggesting their application in more specialized construction needs.

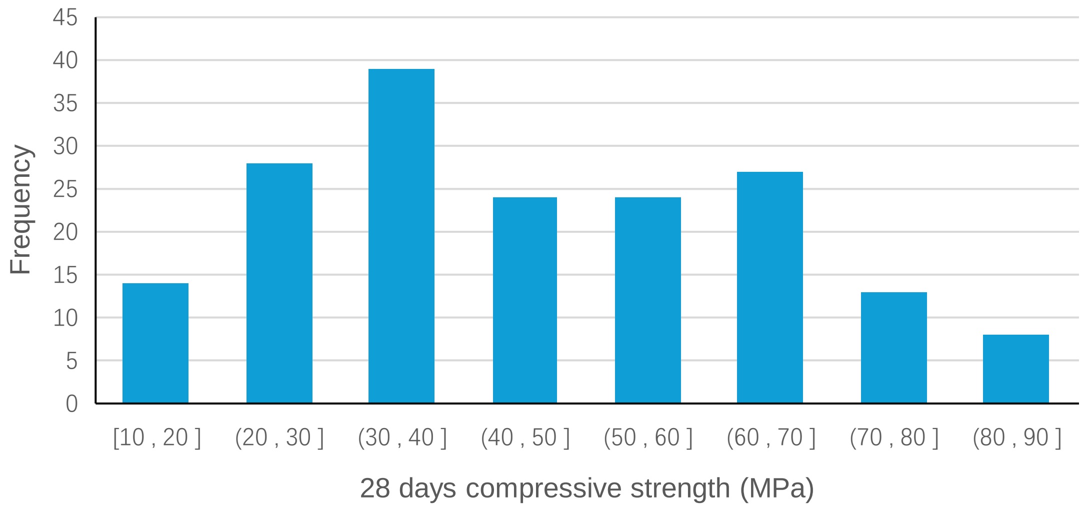

Figure 2.5 Distribution of SCC 28 days compressive strength

Numerous studies (Persson 2001; Revilla-Cuesta et al. 2020; Sai Neeraja and Sharma 2023) indicate that the progression of key mechanical properties in SCC, including compressive strength, tensile strength, flexural strength, and elastic modulus, follows patterns similar to those observed in NVC. In contrast to NVC, the increase in porosity in the interfacial transition zone (ITZ) of SCC is less pronounced (Leemann et al. 2006). This results in a denser and more uniformly distributed ITZ around the coarse aggregates, enhancing the bonding between the paste and reinforcement (Kanellopoulos et al. 2020). Consequently, SCC exhibits improved bonding strength compared to NVC, which contributes to its superior mechanical properties. This characteristic not only improves the overall durability of SCC but also highlights its advantages in structural applications.

Concrete durability is an integrated result of various properties. It is commonly evaluated through indicators such as resistance to permeability, freeze-thaw cycles, and chloride ion penetration. Studies by Kanellopoulos et al. (2012) have shown that SCC exhibits better durability potential than NVC, even though SCC generally contains more water. This increased durability is mainly due to the higher fine particle content in SCC, which refines its microstructure and enhances the pore network. Moreover, the incorporation of supplementary cementitious materials can further enhance durability by significantly improving particle packing in the microstructure, thus reducing pore connectivity and permeability (Chandru et al. 2018).

2.6 Effects of cementitious materials on SCC rheology

SCC mixes are typically proportioned with increased amounts of fine powder materials and chemical admixtures to achieve the desired rheological and deformability properties. While this may not always entail a higher cement content, the overall powder content is generally elevated, often incorporating mineral additives to enhance performance and sustainability. Given the environmental impact and performance requirements, there is a pressing need to understand how mineral additives impact the fresh and rheological performance of SCC. The content of this section is a part of the published work in the Proceedings of Institution of Civil Engineers: Construction Materials (Cui et al. 2024a); details are provided in the List of Publications.

2.6.1 Rheological Dynamics of SCC

The main research focus in understanding rheology is to establish the constitutive relationship between matter and material based on experimental or theoretical methods and to use this constitutive relationship and conservation laws to analyse the rheological properties of the given system. However, it is challenging to numerically describe and predict the flow and deformation of complex fluids such as SCC (Yahia and Khayat 2001). The most widely used theological models are summarized in Table 2.2. Due to the inherent complexity of the interactions among various components in the flow process of SCC, to obtain the overall characteristics of SCC flow, the numerical model needs to be appropriately simplified. Among many SCC rheological models described based on the relationships between shear stress and shear rate, the Bingham model and Herschel-Bulkley model have gained widespread recognition (Wallevik and Wallevik 2011a).

The Bingham model assumes that, once a specific yield stress is exceeded, shear stress is linearly proportional to the shear rate (Heirman et al. 2008). This proportionality is referred to as plastic viscosity, which measures a material's resistance to flow. The flow of SCC ceases when the shear stress reaches the yield stress (Sonebi and Yahia 2020). Although the Bingham model is widely applicable, it does not always fully capture the behaviour of fresh SCC. Recent research has demonstrated that SCC containing high levels of superplasticizers may exhibit non-linear flow behaviour, sometimes even showing a negative yield stress (Feys et al. 2008). As a result, the Herschel-Bulkley model, which is less susceptible to negative yield stress (Wallevik and Wallevik 2011a), often provides a more accurate representation of non-linear rheological properties of SCC and is thus preferred for modelling such behaviour.

Table 2.2 Commonly used rheology models

Model	Formula	Main application
Ellis model	$\frac{\eta}{\eta_0} = 1 + (\frac{\tau}{\tau_{1/2}})^{\alpha-1}$	Shear stress dependent viscosity
Carreau model	$\frac{\eta_0 - \eta_\infty}{\eta - \eta_\infty} = [1 + (\lambda\dot{\gamma})^2]^{(n-1)/2}$	Non-Newtonian fluids at low shear rates
Bingham model	$\tau = \tau_0 + \eta_p\dot{\gamma}$	Bingham plastic fluids
Herchel-Bulkley model	$\tau = \tau_0 + K\dot{\gamma}^n$	Non-linear Bingham fluids
Modified Bingham model	$\tau = \tau_0 + \eta_p\dot{\gamma} + c\dot{\gamma}^2$	Non-linear Bingham fluids
Casson model	$\sqrt{\tau} = \sqrt{\tau_0} + \sqrt{\eta_p}\sqrt{\dot{\gamma}}$	Biomedical fluids
Sisko model	$\eta = \eta_\infty + \eta_p\dot{\gamma}^{n-1}$	Calculate ultimate shear viscosity
Williamson model	$\eta = \frac{\eta_0}{1 + (K\dot{\gamma})^n}$	Viscosity generated at low shear rates

2.6.2 Fly ash

Fly ash is a solid fine-grained material produced by the combustion of pulverized coal in the furnace of a power station. The chemical and mineral composition of fly ash depends on the characteristics and composition of coal burned in the power plants. Due to rapid cooling during combustion, fly ash primarily (50–90%) consists of glassy spherical particles, rather than wellcrystallised minerals. Fly ash is particularly rich in SiO_2, Al_2O_3 and Fe_2O_3, and also contains other oxides, such as CaO, MgO, MnO, TiO_2, Na_2O, K_2O, SO_3, etc. Particularly, fly ash with high CaO content (15% to 40%) may be considered hydraulically latent and can cause the weakening of mortar and concrete. Physically, the specific surface or fineness of fly ash measured by the Blaine method varies from 250 to 550 m^2/kg (Wesche 1991). Figure 2.6 and Table A.7.1 (please see Appendix A) summarise the effects of fly ash on SCC rheological properties as reported in the literature.

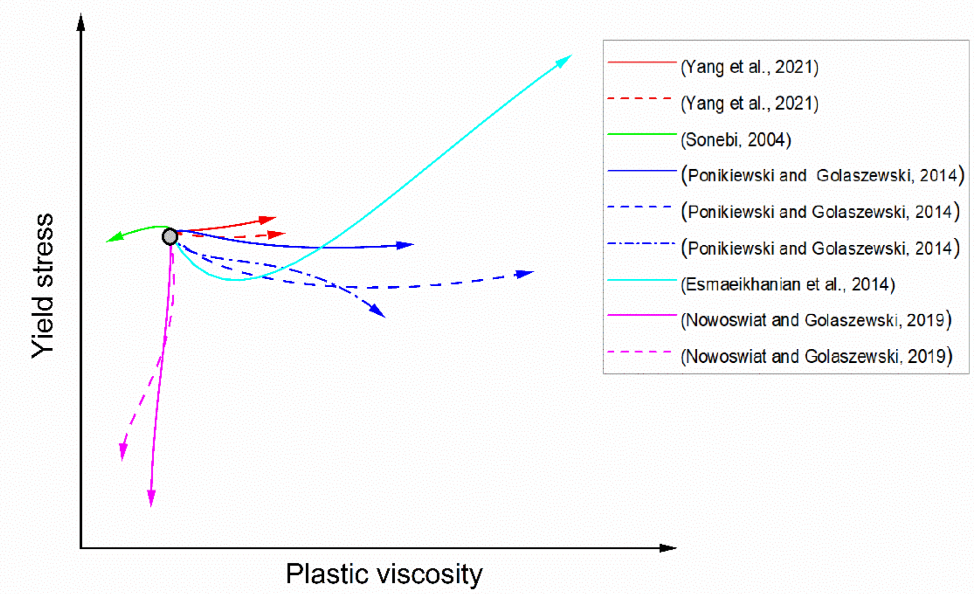

Figure 2.6 Effects of fly ash on rheological properties of SCC

The arrows in Figure 2.6 represent trends reported in the literature, where the base circle indicates the control mix without fly ash, and the arrows show the change in rheological properties as the change of fly ash. For example, spherical particles of fly ash tend to reduce the yield stress due to improved dispersion and packing, while higher volumes or fineness can increase plastic viscosity. These directional effects are supported by experimental findings from the studies referenced in the legend.

Studies on high volumes of fly ash in concrete have been carried out since the 1990s (Berry et al. 1990; Feldman et al. 1990; Atiş 2002). It was demonstrated that better mechanical properties of concrete could be achieved by replacing cement with fly ash with a proportion of more than 40% (Habert and Roussel 2009; Wang and Park 2015; Kurad et al. 2017). Nevertheless, the use of high levels of fly ash can significantly impact the rheological properties of concrete (Bentz et al. 2013; Khodair and Bommareddy 2017), especially for SCC (Van Der Vurst et al. 2017). Thus, the properties of fly ash play a vital role in the performance of fresh SCC.

2.6.3 Ground granulated blast furnace slag

Ground granulated blast furnace slag (GGBS) is the waste slag that leaves the blast furnace during pig iron making. It is a fusible mixture and can be processed into recycled materials with multiple uses by various processes. After blast furnace slag is quenched with a large amount of water, it can be made into fine-grained slag mainly containing glass body, which can show hydraulic cementing performance under the action of activators such as cement clinker, lime, gypsum, etc. Generally, the specific gravity of GGBS is about 2.90 with the bulk density varies in the range of 1200-1300 kg/m^3. The reactivity of GGBS is determined by its surface area. But surface area of GGBS varies region to region due to the influence of processing factors used in practice. The surface area of GGBS in the United Kingdom is 375-425 m^2/kg, while the surface area of some slags in the United States is 450-550 m^2/kg; this value is 450 m^2/kg and 350 to 450 m^2/kg in Canada and India, respectively (Pal et al. 2003). Apart from physical characteristics, properties that affect the reactivity of GGBS are usually glass content, chemical composition, mineral composition, grinding fineness and others (Hooton and Emery 1983). The effects of GGBS on SCC rheological properties, reported in the literature, are summarised in Figure 2.7 and Table A.7.2 (please see Appendix A).

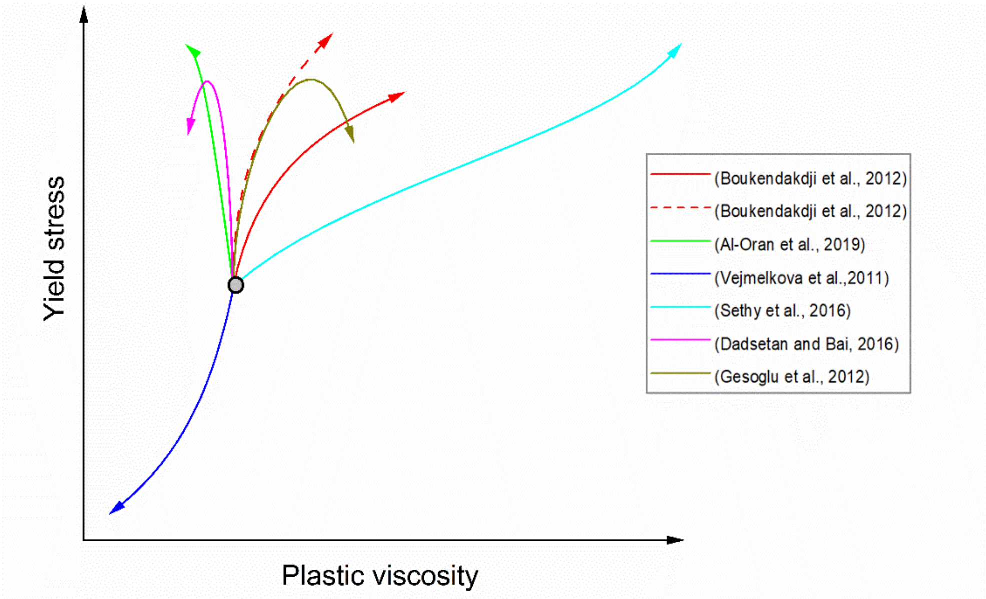

Figure 2.7 Effects of GGBS on rheological properties of SCC

In Figure 2.7, each curve reflects the response of SCC to increasing GGBS dosage based on the referenced literature. The origin point indicates the mix without GGBS, and the arrows show either an increase or decrease in yield stress and plastic viscosity. These changes are attributed to GGBS properties such as fineness, glass content, and replacement levels. Typically, GGBS reduces yield stress due to better packing, while the effect on viscosity depends on particle characteristics and dosage.

2.6.4 Limestone powder

Limestone powder (LP) is the powdery material with a certain purity of limestone as a raw material, which is ground to a specified fineness. LP is an economical mineral additive compared to cement due to its wide-spread availability and simple processing technology (Wang et al. 2018). The role of LP in cement-based materials can be attributed to physical filling effect and chemical activity effect. Due to the low activity of LP, it is often used as an inert filler in consideration of physical effects. However, LP can act as nucleation agent in the cement hydration reaction, thereby accelerating and participating in the cement hydration reaction. Limestone particles can provide nucleation points for hydration products by absorbing Ca^{2+} released during hydration process of C_3S and reducing the concentration and orientation of $Ca(OH)_2$ crystals at the interface, thereby increasing the content of C-S-H at the interface (Péra et al. 1999). Figure 2.8 and Table A.7.3 (please see Appendix A) show the effects of LP on SCC rheological properties based on observations presented in existing literature.

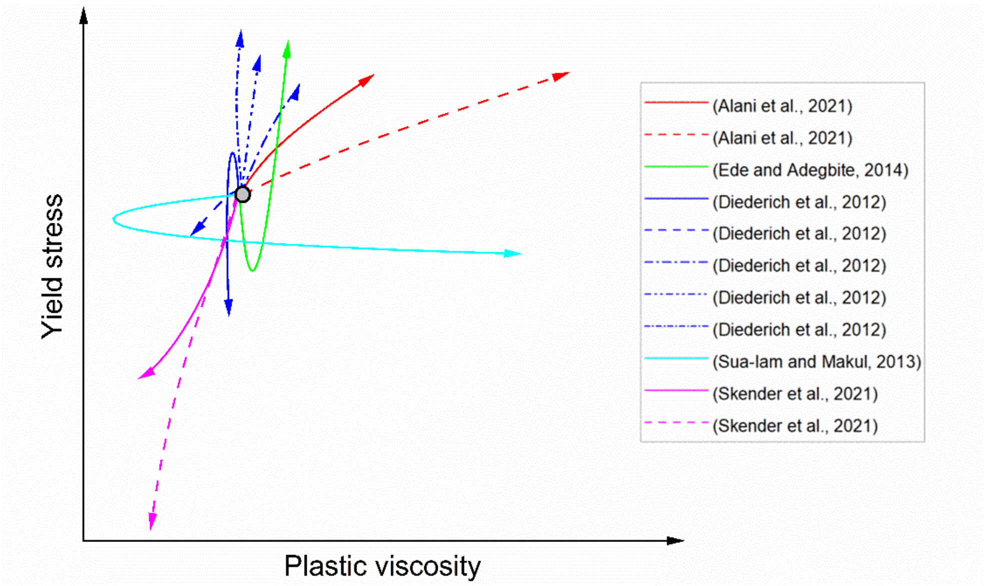

Figure 2.8 Effects of limestone powder on rheological properties of SCC

The trend arrows in Figure 2.8 are derived from experimental studies, showing the influence of increasing limestone powder content. The base point corresponds to the control mix, and arrows illustrate changes in plastic viscosity and yield stress. LP generally increases yield stress due to its filler effect and surface interactions, while plastic viscosity may also rise depending on dosage and fineness. These directional changes help visualise how LP affects the rheology of SCC, based on the cited sources.

2.7 Steel fibre reinforced SCC

Concrete technology has advanced significantly, and the improvement of concrete properties has become a key direction for further development. One of the effective methods to enhance these properties is by adding steel fibres to the mix. Steel fibre reinforced self-compacting concrete (SFRSCC) represents an advancement over conventional SCC. It maintains the advantages of SCC, such as high fluidity and the elimination of the need for mechanical vibration during placement. Additionally, as a fibre-reinforced material, SFRSCC exhibits superior tensile strength and impact resistance compared to standard SCC. Moreover, SFRSCC offers better resistance to shrinkage (Ahari et al. 2015). Fibres are also utilized to control the crack width, which positively impacts the durability of the concrete (Frazão et al. 2015). The higher cementitious content in SFRSCC enhances its performance by strengthening the bond between the steel fibres and the concrete matrix.

Some researchers have focused on evaluating the performance of SCC incorporating steel fibres. Khaloo et al. (2014) investigated the impact of different steel fibre volume fractions on the rheological and mechanical properties of medium and high-strength SCC, revealing that while increased fibre content reduces workability and rheological performance, it enhanced tensile strength, flexural strength, and toughness, though compressive strength decreased. Ferrara et al. (2012) examined the evaluation of static and dynamic segregation resistance in SFRSCC and correlates fibre dispersion in the fresh state with fracture toughness in the hardened state. Various testing methods were analysed, providing insights into the relationship between fresh state performance and mechanical properties, with a focus on enhancing material acceptance tests for quality control. Turk et al. (2021) examined the impact of different combinations of macro and micro steel fibres on the performance of SHFRSCC. The results showed that hybrid fibre mixes, particularly with 1.20% macro and 0.30% micro fibres, demonstrated superior compressive strength, flexural toughness, and ductility compared to single fibre mixes.

Other studies have examined the influence of various replacement materials and fibre combinations on the performance of SCC. Guecioueri et al. (2022)

developed a SFRSCC using marble powder as a partial cement substitute, analysing the effects of fibre dosage, paste volume, and gravel/sand ratio on rheological and mechanical properties. The results showed that while increasing fibre dosage reduces flow capacity, higher paste volume and gravel/sand ratio improved flow, with significant improvements in flexural strength and ductility as these parameters increase. Afshoon et al. (2023) explored the use of copper slag (CS) as a partial replacement for coarse aggregates in steel fibre SFRSCC, evaluating the effects on concrete properties. The results showed that while increasing CS improved fresh concrete characteristics, and the compressive and tensile strengths varied based on CS and fibre content. Liu et al. (2023) experimentally investigated the fracture behaviours of SFRSCC with varying steel fibre volumes and high fly ash content (40-70%). The results showed that adding steel fibres improved fracture properties, with increases in peak load, fracture toughness, and fracture energy. Zhuang et al. (2022) investigated the dynamic behaviour of SFRSCC containing rubber content. The results showed that while increasing rubber content decreased dynamic compressive strength and improved toughness, steel fibres enhanced both dynamic compressive strength and toughness, with minimal impact on stress and strain impact factors.

Additionally, various researchers have investigated the effects of different fibre types and compositions on the mechanical and durability properties of SCC. The study of Ponikiewski and Katzer (2014) determined the maximum fibre dosage for achieving the self-compacting effect in SCC modified with steel and polymer fibres. Through an orthogonal experimental design, the research identified the optimal fibre compositions, with slump flow and L-box tests providing insights into the filling, passing ability, and segregation resistance of the fibre-modified SCC. Simalti and Singh (2021) investigated the use of recycled steel fibre (RSF) from shredded tires in SCC, comparing it with manufactured steel fibre (MSF) in terms of concrete properties. The results indicated that SCC with 1.5% RSF showed the best overall performance, offering a sustainable and economically viable alternative to SCC with MSF, with the added benefit of reducing carbon emissions. Khan and Ayub (2022) developed a hybrid SFRSCC using polyvinyl alcohol (PVA) and polypropylene (PP) fibres to address issues associated with steel fibres. The results demonstrated that the hybrid mix significantly enhanced strength, ductility, and crack control, outperforming the SCC control mix and fibre-only mixes in both fresh and hardened properties. Ganta et al. (2020) evaluated the effect of fibre type (steel, glass and hybrid) and aggregate content on the hardened and durability properties of SCC. The results indicated that optimal fibre dosages were 1.0% for steel and 0.05% for glass, and the packing factor significantly influenced mechanical properties, with hybrid-reinforced SCC showing superior performance in both mechanical and durability aspects.

2.8 Mix design methods of SCC

Compared with the mature design method of NVC, the general proportioning principle of SCC is to reduce the yield stress of concrete mixture to the appropriate range by selecting high-efficiency admixture (i.e. superplasticizer), mineral admixture, coarse and fine aggregate and careful design of mix ratio. In addition to having excellent fluidity, the mixture must have sufficient plastic viscosity to suspend the aggregate in the cement slurry without segregation and bleeding. During the casting process, the cement slurry can drive the aggregate to flow together and fill the space inside the template. It is known that SCC has a large amount of cementitious material, high sand ratio and the larger amount of high-efficiency water reducing agent than NVC. Therefore, the NVC mix design method is no longer applicable to SCC.

The factors to be considered in the design of SCC mix ratio are more complex than NVC, which includes the structural conditions, construction conditions, environmental conditions and economic efficiency of the building. In general, the work performance, strength and durability are the fundamental requirements for SCC mix design. A considerable amount of research has been done on the design and calculation method of SCC mix ratio, while no unified design calculation method has been formed so far. This section reviews five mixture design methods.

2.8.1 Rational mix design approach

The rational mix design approach (RMDA) for SCC, distinct from traditional vibrated concrete mix design methods, was first formally introduced by the professors from University of Tokyo (Okamura and Masahiro 2003). The method outlines that self-compacting properties in concrete can be achieved by reducing the content and maximum size of coarse aggregates and selecting appropriate mortar characteristics, such as using a lower w/p and a higher dosage of superplasticizers. In this method, the coarse aggregate content should constitute 50% of the total concrete volume; fine aggregate should account for 40% of the mortar volume; and the w/p (where particles smaller than 0.09 mm are considered powder) should be within the range of 0.9 to 1.0, depending on desired flowability. Finally, the amount of superplasticizer is adjusted based on specific project requirements. The flow chart of the mix design is shown in Figure 2.9.

The RMDA mix design process begins with the paste containing particles smaller than 0.09 mm, and then gradually adjusts the w/p to meet both mortar fluidity and SCC workability. Though the process is relatively complex and tends to result in higher cementitious material content, this method serves as a key reference for improvements and optimizations in subsequent mix design methodologies.

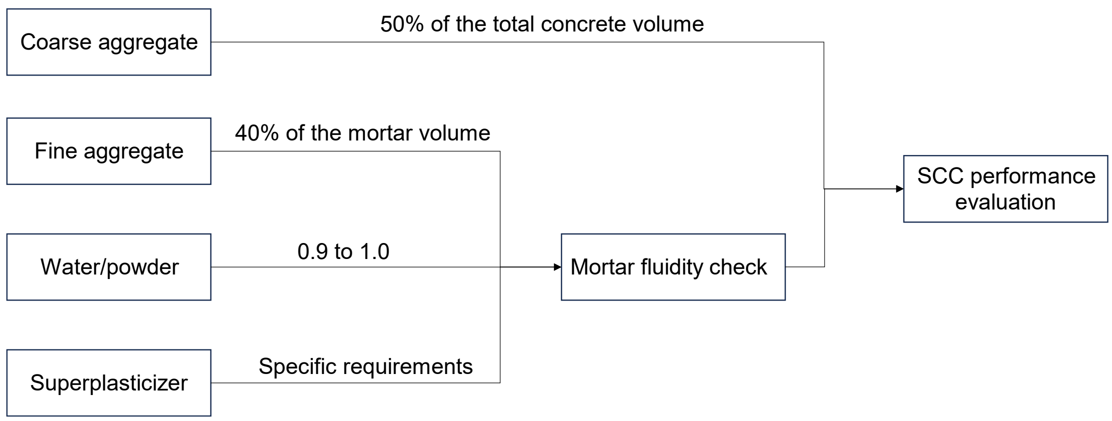

Figure 2.9 Flow chart of the rational mix design approach

2.8.2 Particle packing approach

Several scholars emphasize the importance of aggregate particle packing and particle size distribution in influencing the workability of fresh SCC (Wang et al. 2014; Zuo et al. 2018). A widely recognized SCC mix design method, introduced by Su et al. (2001), incorporates the concept of the packing factor (PF). The PF represents the ratio of the aggregate mass in a compacted state to that in a loose state within SCC. When the PF value is high, the content of aggregates increases, while binder content decreases, resulting in lower workability and strength. On the other hand, a low PF leads to a higher binder content, improving workability but increasing costs and potentially causing greater shrinkage in the hardened concrete, which can negatively affect durability and service life. This approach is straightforward, reduces binder usage, and lowers costs. However, one limitation is that the method does not account for the impact of mineral admixtures on concrete strength. More hybrid-mix design methods are proposed based on this approach (Campos et al. 2020a; Kurda et al. 2022).

2.8.3 Strength based approach

This method bases the selection of cement, admixtures, water, and aggregates on the target compressive strength of the concrete. Ghazi and Al Jadiri (2010) developed a proportioning approach where the quantity of coarse aggregate depends on its maximum particle size and the fineness modulus of the fine aggregate, while the w/p by volume is determined according to the compressive strength requirements of the SCC. Dinakar et al. (2013) also designed an SCC mix using ground granulated blast furnace slag, guided by the target compressive strength. This compressive strength-based method is effective for accurately determining the required quantities of ingredients, thereby reducing the need for extensive trial mixtures. However, one notable limitation is that it requires frequent adjustments of all the components, in order to achieve an optimal mix proportion (Shi et al. 2015).

2.8.4 Statistical factorial approach

This method is based on the use of SCC composition parameters as independent variables and performance metrics as the dependent variables, employing statistical techniques and software to define the relationship between the two for SCC. Contributions from researchers highlight the use of statistical factors in designing SCC mix proportions and predicting performance outcomes (Khayat et al. 1999; Khayat et al. 2000; Sonebi 2001; Sonebi 2004). Given the complex interactions between the numerous components in SCC, the correlation between these composition parameters and performance is more intricate compared to NVC. This statistical approach offers a more intuitive understanding of how each material parameter influences the overall workability of SCC. Additionally, it enables the design of SCC mixes with significantly reduced cementitious content, optimizing both performance and material efficiency (Mukharjee and Patra 2022).

2.8.5 Rheology of paste approach

Aaron et al. (2001) introduced a rheology-based approach to SCC mix design, indicating that the segregation of aggregates is primarily influenced by the yield stress, viscosity, and density of the cement paste. Building on this, researchers established recommended rheological ranges for various types of SCC and developed a mix design method from a rheological standpoint (Wallevik 2003; Wallevik and Wallevik 2011b). This approach involves testing concrete mixtures to meet specific strength and durability criteria, and deriving rheological parameters such as yield stress and plastic viscosity. The fresh properties of SCC, such as slump flow, are verified through experimental testing, and the mix design is subsequently refined based on the results.

2.9 Summary and main gaps declared

This chapter provided an extensive review of SCC, emphasizing its fresh and hardened properties while exploring the various methods used to assess key characteristics such as workability, passing ability, and segregation resistance. Notable testing methods, including the slump flow, T_{500}, J-ring, and L-box tests, were discussed to evaluate the performance of SCC in fresh states. Additionally, the incorporation of steel fibres to enhance mechanical properties, including flexural strength, toughness, and impact resistance, was examined in depth.

The chapter also outlined multiple mix design approaches that have been proposed in the literature. Each of these methods plays a significant role in influencing final performance of SCC; however, their efficiency in optimizing both fresh and hardened properties remains inconsistent. The effect of supplementary cementitious materials, on rheological properties was highlighted. The review further revealed that combining steel fibres with SCC not only improves the mechanical performance but also alters the rheological dynamics, creating additional challenges in mix design optimization.

Despite the valuable insights presented, several critical gaps in the existing research were identified:

- While various mix design methods have been introduced for SCC and

SFRSCC, a unified and comprehensive approach that can simultaneously optimize both fresh and hardened properties is still not fully formulated. The existing methods often yield different outcomes regarding workability, strength, and durability, underscoring the need for a more consistent framework. Notably, the rheological properties, which significantly affect workability and segregation resistance, are frequently overlooked in mix design, resulting in an incomplete understanding of how these properties interact with mechanical performance.

- The majority of research on SCC and SFRSCC relies on large-scale experimental approaches, which can be time-consuming and resource intensive. There is a growing need for more efficient methods to analyse and optimize the mix design, potentially through a combination of experimental work and predictive analytics. Machine learning models offer a promising solution to streamline this process by predicting how various mix parameters will influence the final concrete properties, thereby reducing the reliance on extensive trial-and-error experimentation.
- Although machine learning has been employed to predict concrete properties, its application to the complex behaviour of SCC, especially in fibre-reinforced variants, is still in its infancy. The intricate relationship between fibre properties, cementitious materials, and rheological behaviour is not fully captured by current predictive models. This gap presents an opportunity to leverage advanced computational methods to enhance the accuracy of mix designs and predict performance with greater reliability.

In the following chapters, a new mix design method will be proposed to address these gaps, emphasizing a balanced approach to optimizing both fresh and hardened properties. Additionally, machine learning techniques will be introduced to predict the mechanical performance of SFRSCC, providing a more efficient and accurate approach to mix design and evaluation.

Chapter 3 Machine learning models

3.1 Introduction

Machine learning allows computers to emulate human learning by analysing and mining data to uncover valuable insights and guidance. It combines elements from multiple disciplines, such as probability theory, statistics, information theory, and computer science. Through decades of development, it has established a comprehensive theoretical framework and methodology. In recent years, machine learning has been effectively utilized in areas such as computer vision, natural language processing, and information retrieval and analysis, emerging as a central force in these fields (Sharifani and Amini 2023). It has notably enhanced our ability to solve problems and revolutionized conventional methods and techniques.

This chapter reviews machine learning theories and models, focusing on their application in predicting SCC properties. It covers key theories such as dataset construction, model selection, and model evaluation. Traditional supervised learning models and ensemble models are summarized in detail. The chapter concludes by addressing the current applications of machine learning in SCC research and identifying gaps for further exploration.

3.2 Development of machine learning

The experience that machine learning models rely on is typically represented and stored in computers as data. Consequently, the primary focus of machine learning research is to develop algorithms that generate learning models from the data stored in computers. Once trained, these models can analyse new data, provide insights, and support effective decision-making. The ability of a learning model to accurately predict and make judgments on unseen data is referred to as its generalization capability. The ultimate goal of machine learning research is to ensure that these models possess strong generalization abilities.

Machine learning is an ever-evolving science and technology, with research in the field dating back to the 1940s. The development of machine learning can be summarized in Table 3.1, from early neural networks to the rise of deep learning.

Table 3.1 Evaluation of machine learning models

Stage	Key Developments
Foundations of Neural Networks	Perceptron was introduced by Rosenblatt (1958), laying the foundation for neural networks. Hubel-Wiesel vision model inspired convolutional networks (Hubel and Wiesel 1962). Backpropagation was introduced by Rumelhart et al. (1986), enabling training of multi-layer networks.
Statistical Learning Theory	Started in the 1960s with key concepts like support vectors and structural risk minimization (Vapnik 1999). Support Vector Machine (SVM) was popularized due to its strong classification abilities and kernel methods (Han et al. 2017). Solves complex optimization problems, improving regression and classification accuracy.
Rise of Deep Learning	Emerged in the 21st century, driven by big data and advances in GPU computing (Lecun et al. 2015). Incorporates multiple hidden layers, excelling in modelling complex nonlinear relationships. Expanded applicability in artificial intelligence and other domains (Kamilaris and Prenafeta-Boldú 2018; Zhao et al. 2019).

3.3 Fundamental theories of machine learning

Mathematically, the process of machine learning can be described as follows: Let (x, y) be a sample from the problem space W, i.e., $(x, y) \in W(x, y)$. In practical scenarios, we can only obtain information from a proper subset Q of W, denoted as $Q \subset W$, which is referred to as the dataset. The objective is to construct a model M based on Q such that the model's prediction accuracy for all samples in W exceeds a specified constant θ. Consequently, the machine learning process involves the following three critical components:

- Dataset construction

  In constructing the dataset Q, sample data are typically characterized by distinct features. This process often necessitates data preprocessing and feature extraction to ensure the data are in a suitable form for analysis.
- Development of model M

  The model M represents a generalization over the problem space W. The development of M involves critical stages such as training, validation, and testing to optimize the algorithm's performance and generalize well to unseen data.
- Constant θ

  The constant θ acts as a performance metric for the model M, commonly evaluating aspects such as accuracy, and ensuring that the model meets the predefined performance thresholds.

The general construction process of machine learning models is shown in Figure 3.1.

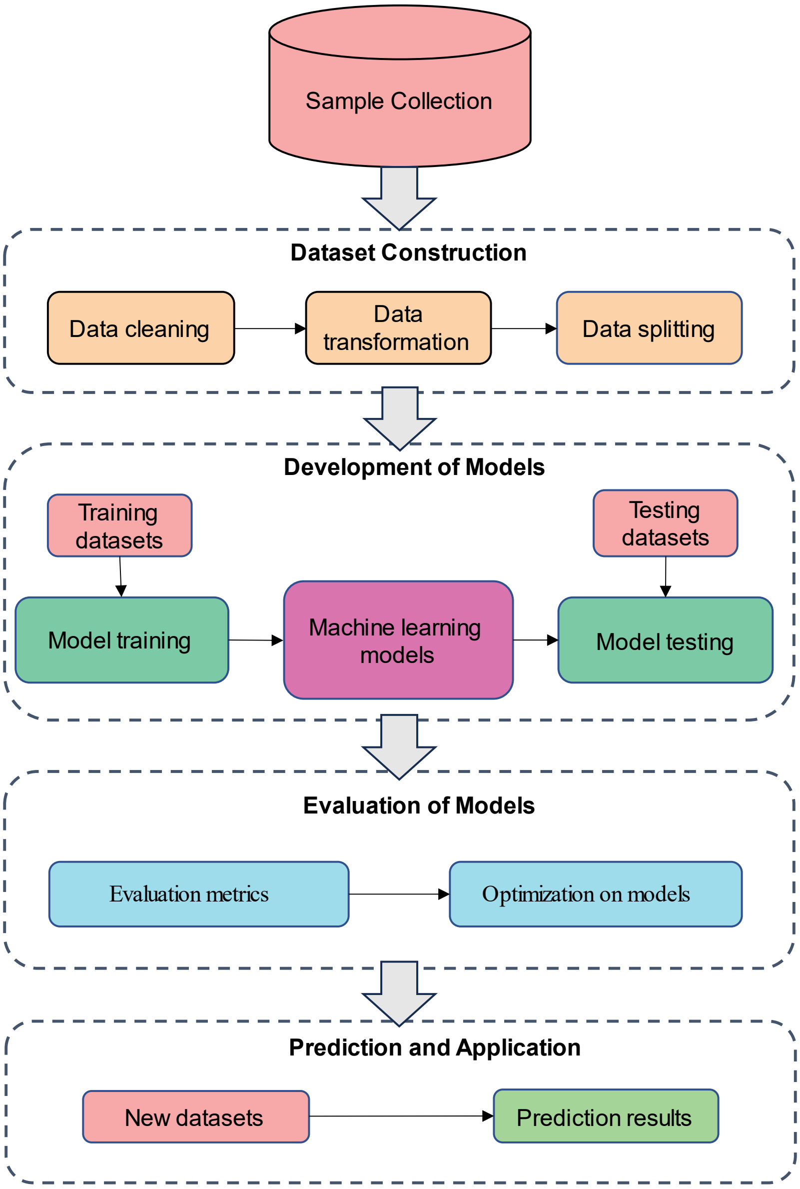

Figure 3.1 The construction process of machine learning models

3.3.1 Dataset Construction

Among the many tasks that machine learning must address, data collection is emerging as a critical component. It is well recognized that end-to-end machine learning is fundamentally data-driven, with the majority of the time being used to data preparation. This process encompasses various stages, including data collection, cleaning, analysis, visualization, and feature engineering (Roh et al. 2021).

After data collection, raw data can be processed to prepare it for machine learning tasks. This processing typically involves tasks such as removing duplicate data, imputing missing values, and detecting outliers. The primary goal of these steps is to resolve inconsistencies in the data and ensure high data quality, thereby improving model accuracy (Gudivada et al. 2017).

During the collection of SCC experimental data, there can be instances of data duplication, particularly when different publications by the same author may share overlapping experimental data due to differing research objectives. Although this is a rare occurrence, it can be addressed manually without significantly impacting the model's results. Missing data is another common issue in data analysis. When only a small portion of the data is missing, imputation methods such as mean imputation, binary imputation, regression, or sampling methods can be employed. Alternatively, some studies prefer to use model-based approaches for imputing missing data, utilizing algorithms like Naive Bayes, decision trees, or K-means clustering (Pigott 2001; Ngueilbaye et al. 2021). Missing values, erroneous data, sparsity, and outliers can introduce noise into machine learning processes. Generally, outliers can be effectively detected using statistical methods, such as calculating the mean and standard deviation of the data. The probability density function (PDF) can be employed to describe the rate of change in probability within a specified neighbourhood for continuous random variables, and its graphical representation can be useful for identifying anomalies in the dataset.

Once the relevant attributes of the sample data have been statistically analysed, further steps are required to prepare the data for machine learning models. This includes performing correlation analysis and data formatting, which aim to eliminate data correlation and enhance model performance.

To optimize the performance of machine learning models, it is often essential to format raw data through techniques such as logarithmic transformation or normalization. These processes adjust data with differing scales or units to a common range, preventing larger values from overshadowing smaller ones (Sun and Xia 2024). This adjustment is crucial for avoiding issues like poor convergence and low precision during model training. Classification algorithms, such as artificial neural networks, K-nearest neighbours (KNN), and support vector machines (SVM), particularly benefit from data scaling. These algorithms perform regression or classification by calculating the distances and similarities between samples, and well-formatted data can significantly enhance convergence speed and computational efficiency. Conversely, for algorithms that rely on inequality rules or the distribution of features, such as decision trees and random forests, data scaling offers limited advantages. In these cases, the influence of scaling on overall model performance is generally negligible.

Widely used scaling techniques include min-max normalization and Z-score standardization. Min-max normalization involves a linear transformation of the original data, mapping the resulting values to the [0, 1] range. The transformation function is defined as:

$$x_{scaled} = \frac{x - x_{min}}{x_{max} - x_{min}} \tag{3.1}$$

where x_{min} and x_{max} represent the minimum and maximum values of the sample data, respectively. This approach preserves the relationships within the original data; however, when new data is introduced, changes in the dataset's minimum and maximum values may necessitate re-normalization.

Z-score standardization normalizes the original data using its mean and standard deviation. The resulting data conforms to a standard normal distribution, with a mean of 0 and a standard deviation of 1. The transformation function is given by:

$$x_{scaled} = \frac{x - \mu}{\sigma} \tag{3.2}$$

where μ and σ represent the mean and standard deviation of the sample data, respectively. This method is particularly useful when the maximum and minimum values of the sample are unknown or when outliers are present.

3.3.2 Selection of models

When selecting a machine learning model, it is essential to consider both the training and test set errors. Focusing solely on reducing error during model training can lead to overfitting, which increases the model's complexity. Conversely, prioritizing the minimization of test set error may result in underfitting, thereby significantly reducing the model's generalization capability. The discrepancy between the predicted and actual values, known as error, can be quantified using a loss function, given by:

$$L1(y, \hat{y}) = \frac{1}{N}\sum_{i=1}^{N} |y(i) - \hat{y}(i)| \tag{3.3}$$

where N is the sample size, y represents the actual values, and $\hat{y}$ denotes the predicted values.

Thus, selecting an appropriate model involves balancing the loss function for both the training and test sets, effectively managing the trade-off between overfitting and generalization. Techniques such as regularization and cross-validation are commonly used for model selection to achieve this balance.

3.3.2.1 Regularization

Regularization adds a penalty term to the empirical risk (average loss), which is expressed as follows:

$$min \frac{1}{N}\sum_{i=1}^{N} L(y_i, f(x_i)) + \lambda J(f) \tag{3.4}$$

Here, the penalty term is typically a monotonically increasing function of the model's complexity, and $\lambda \geq 0$ indicates that the complexity of the model is directly proportional to the penalty term. The purpose of regularization is to select a model that achieves a balance between low empirical risk and manageable model complexity.

3.3.2.2 Cross validation

Cross-validation is a commonly used method in machine learning for building models and verifying model parameters (Bro et al. 2008). It aims to improve the generalization ability of the model by dividing the sample datasets and combining them into different training and testing sets. In addition, the limited amount of available data can be reused to improve the modelling efficiency (Kohavi 1995). An example of 5-fold cross-validation is illustrated as follows.

Step 1. Randomly divide all datasets into 5 subsets by sampling without repetition.

Step 2. Train the model by using 4 of the 5 subsets and the remaining 1 subset is used for testing.

Step 3. Repeat the previous step five time to ensure each subset is used once as the test set.

Step 4. Save the evaluation index of all five models.

Step 5. Calculate the mean error of the test results of 5 models as the cross-validation error.

All steps of the model training process, including model selection and feature selection, are performed independently within a single ‘fold’. The schematic description of five-fold cross-validation is presented in Figure 3.2.

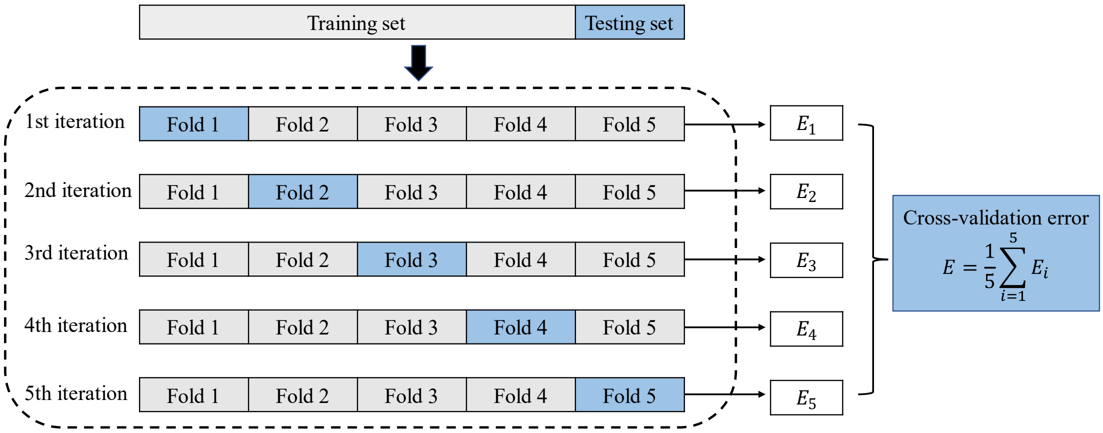

Figure 3.2 The schematic structure of five-fold cross-validation

3.3.3 Evaluation criteria of models

Model evaluation is an essential component of the model development process, as it helps assess the performance and generalization capability of a model. Depending on the target values in the dataset, model evaluation in machine learning can be categorized into classification and regression evaluation. The machine learning task addressed in this study is a regression task, which is a typical example of supervised learning.

The performance of the developed regression models was evaluated using both traditional statistical measures and graphical methods. The accuracy indicators employed in this study are correlation coefficient (R), coefficient of determination (R^2), mean squared error (MSE), root mean squared error ($RMSE$), mean absolute error (MAE), and mean absolute percentage error ($MAPE$). The mathematical expressions are given in Eqs. (3.5) - (3.10).

$$R = \frac{\sum_{i=1}^{N}(P_i - P_A)(E_i - E_A)}{\sqrt{\sum_{i=1}^{N}(P_i - P_A)^2 \sum_{i=1}^{N}(E_i - E_A)^2}} \tag{3.5}$$

$$R^2 = 1 - \frac{\sum_{i=1}^{N}(P_i - E_i)^2}{\sum_{i=1}^{N}(E_i - E_A)^2} \tag{3.6}$$

$$MSE = \frac{1}{N}\sum_{i=1}^{N}(P_i - E_i)^2 \tag{3.7}$$

$$RMSE = \sqrt{\frac{1}{N}\sum_{i=1}^{N}(P_i - E_i)^2} \tag{3.8}$$

$$MAE = \frac{1}{N}\sum_{i=1}^{N}|P_i - E_i| \tag{3.9}$$

$$MAPE = \frac{1}{N}\sum_{i=1}^{N}\frac{|P_i - E_i|}{P_i} \times 100\% \tag{3.10}$$

Where P is the predicted result, E is the actual result, and N is the total number of samples. P_A and E_A are the average values of predicted and actual results, respectively. To demonstrate higher accuracy, R and R^2 values should be closer to 1, indicating a strong correlation between the predicted and experimental values and signifying that they tend to vary in a similar manner. An R value close to 0 suggests a lack of linear correlation, though nonlinear relationships might still exist between the variables (Adler and Parmryd 2010).The values of MSE, $RMSE$, MAE and $MAPE$ are the measurements of the difference, near to zero means greater accurate, as they indicate smaller deviations between the predictions and the actual data.

In addition to these numerical metrics, graphical evaluation tools were used to provide a more intuitive assessment of model performance and interpretability. The regression error characteristic (REC) curve illustrates the cumulative distribution of errors by plotting the error tolerance on the x-axis and the percentage of predictions within that tolerance on the y-axis (Asteris et al. 2021). A model with perfect predictions would align with the y-axis. The area over the REC curve serves as a performance indicator, where a smaller area corresponds to higher prediction accuracy. The Taylor diagram graphically summarises various statistical indicators in a single plot (Taylor 2001). This allows for a simultaneous assessment of model performance relative to observed data, providing a concise visual comparison across different models. Shapley additive explanations (SHAP) values quantify the contribution of each feature to the prediction of models. This approach is proposed based on cooperative game theory principles and was first introduced by Lundberg and Lee (2017). SHAP values are widely used for interpreting machine learning models, as they provide insights into feature importance. These values offer two levels of interpretation: global explanations, which reflect the average contribution of each input feature across all predictions, and local explanations, which describe the influence of individual features on specific predictions.

By integrating these quantitative and graphical evaluation methods, a comprehensive assessment of model accuracy, robustness, and interpretability can be achieved. This approach complements the traditional statistical metrics and enhances the reliability of the developed machine learning models .

3.4 Traditional supervised learning models

Machine learning models can be categorized into supervised and unsupervised learning models, depending on whether the training dataset contains labels. Since the SCC mix proportions and related properties reported in the literature are labelled data, this study primarily focuses on the application of supervised learning algorithms in predicting SCC properties.

Supervised learning is a method that utilizes labelled data to train a model. The core idea is to learn the mapping between input variables (features) and output variables (labels) using the labelled training data. During the training process, the model's parameters are iteratively adjusted to ensure that the predicted values closely approximate the true values (Caruana and Niculescu-Mizil 2006).

A key characteristic of supervised learning is the use of labelled input-output data for training. If the goal is to predict a continuous target variable, the task is referred to as regression; conversely, if the goal is to predict a discrete target variable, the task is classification. The workflow of supervised learning is illustrated in Figure 3.3.

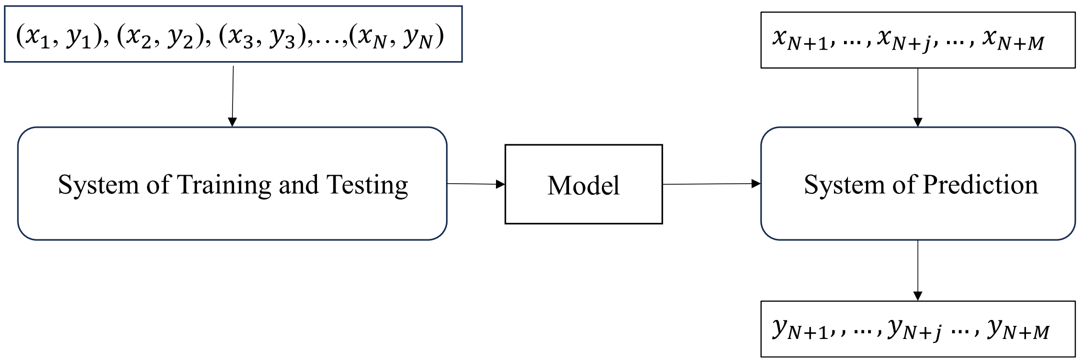

Figure 3.3 The workflow of supervised learning

In this context, $(x_1,\ y_1)$, $(x_2,\ y_2)$, $(x_3,\ y_3)$,…,$(x_N,\ y_N)$ represent the training and testing datasets, where $(x_i,\ y_i)$ denotes a sample point, with $i = 1,2,3, \ldots, N$. Here, x_i is the input sample, and y_i is the corresponding output sample. Given the dataset, the machine learning training process develops a model. If the model demonstrates strong predictive capability, then y_{N+j} will closely approximate the actual value.

3.4.1 Support vector machine

Support vector machines (SVMs), originally developed by Vapnik and his colleagues (Cortes et al. 1995; Drucker· et al. 1996; Vapnik 1999) in the 1900s, have undergone significant expansion and are widely applied in the domains of computer vision and data mining. In the context of binary classification, a SVM is defined as a linear classifier that aims to achieve the maximum margin between two classes in the characteristic space. The learning strategy of SVM focuses on maximizing this margin, which ultimately translates into the solving of a convex quadratic programming problem (Sánchez 2003). The optimization process facilitates optimal class separation, resulting in enhanced generalization capabilities and superior performance when encountering previously unseen data. However, the data is not linearly separable in most cases. To address the challenge of separating the nonlinear data that are not effectively separated within the 2D plane, the linear inseparable data is mapped into a higher dimensional space through the kernel function (Hsu et al. 2003). This transformation is illustrated in Figure 3.4, where the kernel function enables a more effective separation of the data points.

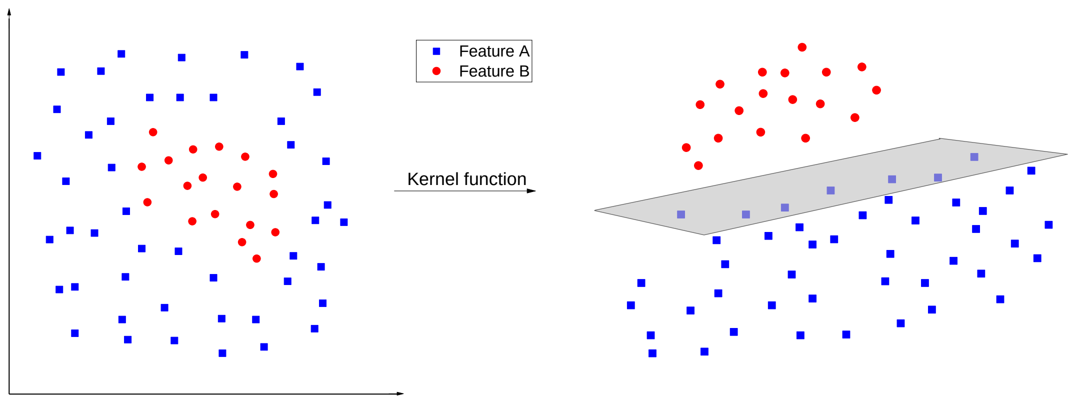

Figure 3.4 Mapping data to 3D space using kernel function

Corresponding to the classification function of SVM, support vector regression (SVR) is characterized by the utilization of kernels and loss functions to regulate the margin width and the number of support vectors for the hyperplane (Figure 3.5). For a given training dataset $x_i, y_i,\ i = 1, \dots, n$, the ε-loss function $L(y, f(\boldsymbol{x}, \boldsymbol{w}))$ is defined as Eq. (3.11) (Vapnik 1999).

$$L(y, f(\boldsymbol{x}, \boldsymbol{w})) = \begin{cases} 0, & |y - f(\boldsymbol{x}, \boldsymbol{w})| < \varepsilon \\ |y - f(\boldsymbol{x}, \boldsymbol{w})| - \varepsilon, & otherwise. \end{cases} \quad (3.11)$$

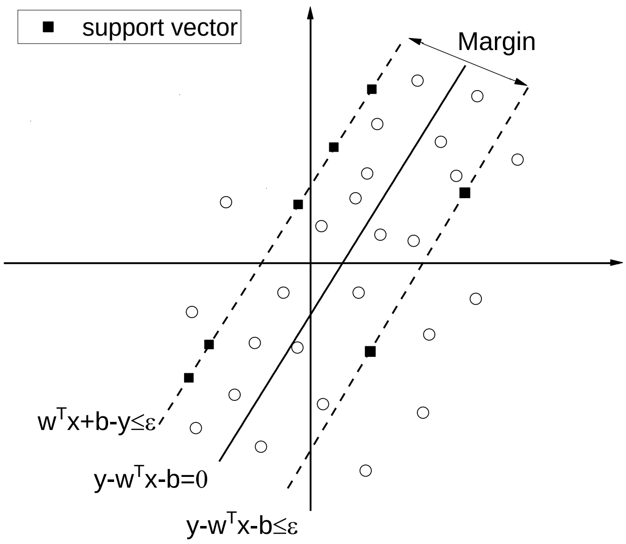

Figure 3.5 Margins and support vectors of the hyperplane in SVM

The loss function determines an ε-tube with a width of 2ε centred on $f(\boldsymbol{x})$ as shown in Figure 3.6.

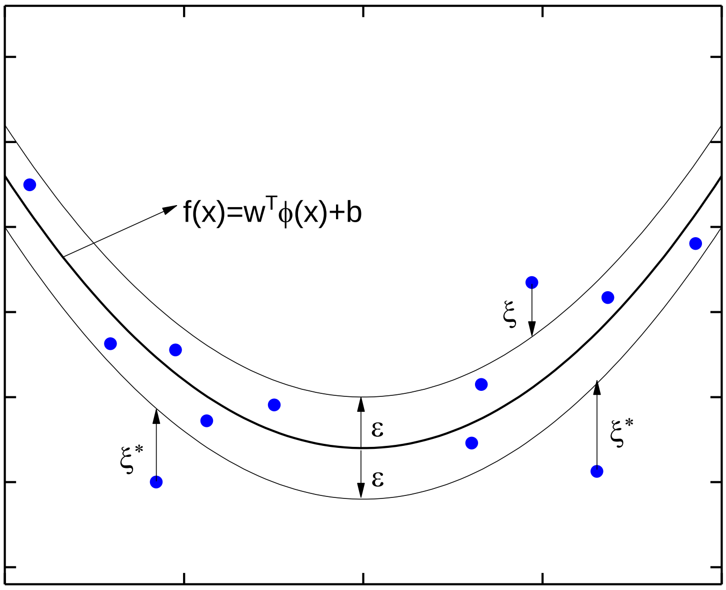

Figure 3.6 The quadratic ε-loss function of SVM

When $f(\boldsymbol{x})$ is a nonlinear function.

$$f(\boldsymbol{x}) = \boldsymbol{w}^{\boldsymbol{T}}\phi(\boldsymbol{x}) + b \tag{3.12}$$

where $\phi(\boldsymbol{x})$ is unknown and the kernel function $K(\boldsymbol{x}_i, \boldsymbol{x}_j)$ is used to obtain the inner product of samples in high-dimensional space.

$$K(\boldsymbol{x}_i, \boldsymbol{x}_j) = \langle \phi(\boldsymbol{x}_i), \phi(\boldsymbol{x}_j) \rangle, \qquad i, j = 1, \dots, n \tag{3.13}$$

Minimizing the ε-insensitive loss is equivalent to solving the optimization problem with respect to $\boldsymbol{w}$ and b.

$$\min_{\boldsymbol{w},b} \frac{1}{2} \|\boldsymbol{w}\|_2^2 + C \sum_{i=1}^{n} (\xi_i + \xi_i^*) \tag{3.14}$$

$$\text{Subjected to} \quad \begin{cases} y_i - \boldsymbol{w}^{\boldsymbol{T}} \phi(\boldsymbol{x_i}) - b \leq \varepsilon + \xi_i{}^* \\ \boldsymbol{w}^{\boldsymbol{T}} \phi(\boldsymbol{x_i}) + b - y_i \leq \varepsilon + \xi_i \\ \xi_i, \xi_i{}^* \geq 0, \end{cases} \quad i = 1, \dots, n$$

where C, the penalty parameter, is employed to balance the generalization ability of the test dataset, $\xi_i, \xi_i{}^*$ present the slack variables corresponding to $\boldsymbol{x}_i$.

The solution of Eq. (3.14) can be obtained by transforming it to the dual form.

$$\begin{aligned} \min_{\alpha,\alpha^*} \frac{1}{2} \sum_{i,j=1}^{n} (\alpha_i - \alpha_i^*) K(\boldsymbol{x}_i, \boldsymbol{x}_j)(\alpha_i - \alpha_i^*) \\ + \varepsilon \sum_{i=1}^{n} (\alpha_i + \alpha_i^*) - \sum_{i=1}^{n} y_i(\alpha_i - \alpha_i^*) \end{aligned} \tag{3.15}$$

$$\text{Subjected to} \quad \begin{cases} \sum_{i=1}^{n} (\alpha_i - \alpha_i^*) = 0 \\ 0 \leq \alpha_i, \qquad \alpha_i^* \leq C \end{cases} \quad i = 1, \dots, n$$

$\alpha_{i,}\alpha_i{}^*$are the Lagrange multipliers corresponding to $\boldsymbol{x}_i$. $\boldsymbol{w}$ and $f(\boldsymbol{x})$ can be presented by Eqs. (3.16) and (3.17).

$$\boldsymbol{w} = \sum_{i=1}^{n} (\alpha_i - \alpha_i^*) \phi((x)_i) \tag{3.16}$$

$$f(\boldsymbol{x}) = \sum_{i=1}^{n} (\alpha_i - \alpha_i^*) K(\boldsymbol{x}_i, (x)) + b \tag{3.17}$$

To improve the estimation accuracy and generalization ability of SVR models, the setting of parameters C, ε and kernel function-related parameters is required to be considered. The larger the C, the smaller the margin, and the higher the probability of the model overfitting. The flowchart of SVR modelling is shown in Figure 3.7.

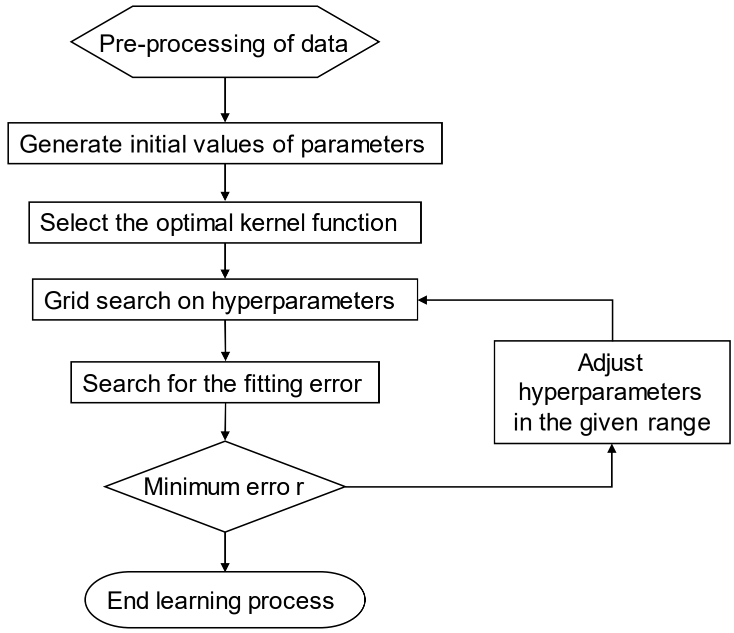

Figure 3.7 The flowchart of SVM modelling in this study

3.4.2 Decision tree

The decision tree (DT) is a commonly used machine learning algorithm to solve classification and regression problems. Its distinctive tree-like structure facilitates rapid data processing and efficiently represents the relationships among data, making it a powerful tool for various applications (DeRousseau et al. 2018). The decision tree employs a top-down recursive learning approach. The fundamental concept is to construct a tree that exhibits the fastest entropy reduction, ultimately reaching a leaf node with zero entropy. To enhance the accuracy of the prediction ability of the decision tree, it is crucial to determine an appropriate impurity splitting criterion, which guides the selection of features and partitions at each internal node. The prediction of numerical outcomes based on input variables predominantly utilizes four decision tree algorithms, which include CHAID (Chi-squared automatic interaction detection), CART (classification and regression trees), C4.5, and C5.0 (Tso and Yau 2007). In CART, each non-leaf node in the tree branches into two child nodes. Figure 3.8 illustrates an exemplary structure of a CART decision tree, as employed in this study. This visual representation highlights the binary branching nature of the algorithm and the decision-making process at each internal node.

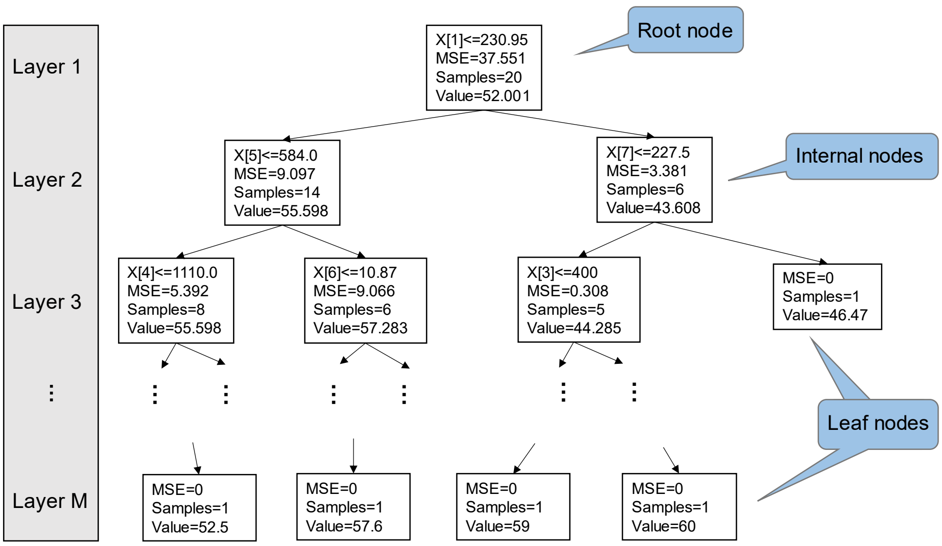

Figure 3.8 The representative structure of a CART decision tree

Decision trees offer several advantages of estimating the discrete datasets. For example, the tree structure shows the importance of attributes in the regression process, and the resulting diagram is easily comprehensible. Accordingly, decision trees possess the ability in handling multi-output problems and accommodate missing values of dependent and independent variables, making them a versatile and robust choice for different machine learning tasks (Ayaz et al. 2015). However, a common limitation of decision tree regression is its susceptibility to overfitting. To address this issue, the tree-based ensemble learning algorithm, random forest (RF), has been introduced.

3.4.3 Artificial neural networks

The artificial neural network (ANN) is designed to replicate specific functions by emulating the biological neural structures of the human brain. Fundamentally, it is a mathematical model used to reason about complex logical relationships and to process information efficiently. The core processing unit of an ANN is the artificial neuron. Each neuron receives signals from connected neurons, with varying weights that indicate the strength of the influence between them.

A typical ANN comprises three main components: structure, activation functions, and learning rules. The architecture defines the variables and their topological relationships within the network. An ANN generally includes an input layer, one or more hidden layers, and an output layer, which together facilitate the transformation of input data into meaningful predictions or classifications. The activation function, typically nonlinear, determines how neuron activation values are modified based on the activity of other neurons within the network. This nonlinearity allows the ANN to model complex relationships in the data, thereby improving its predictive accuracy (Beale et al. 2010). Learning rules govern the adjustments of weights between neurons over time, enabling the network to enhance its performance as more data is processed. This study utilizes a backpropagation neural network (BPNN), a type of multi-layer feedforward network. The configuration, including the number of hidden layers and nodes within these layers, is determined by the characteristics and features of the dataset (Oreta and Kawashima 2003).

Figure 3.9 describes a representative BP network structure consisting of three layers. The steps involved in setting up and training the BP network are exhibited in Figure 3.10. The network is well trained until the error is minimized and lies within an acceptable range.

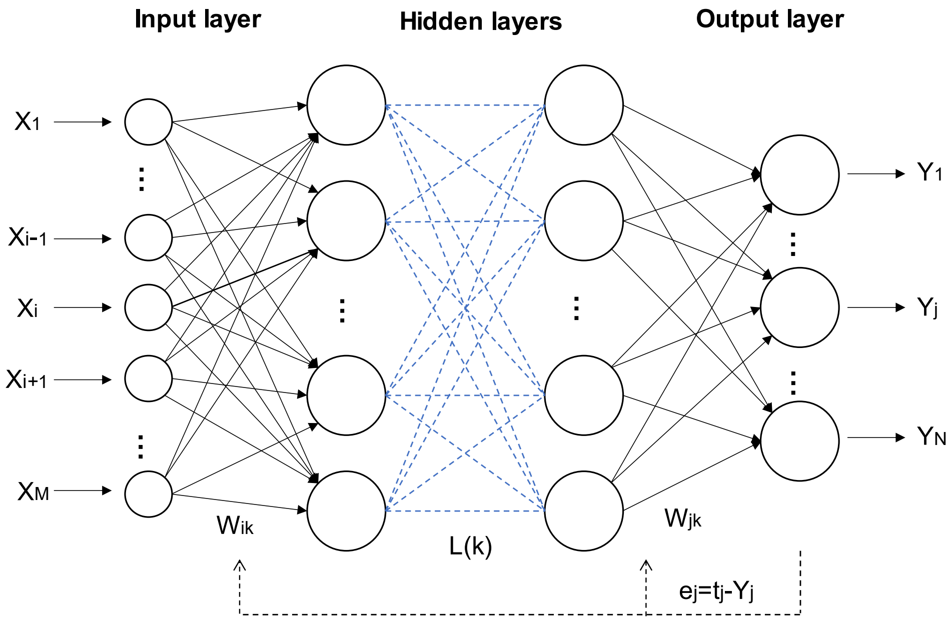

Figure 3.9 The architecture of an ANN model

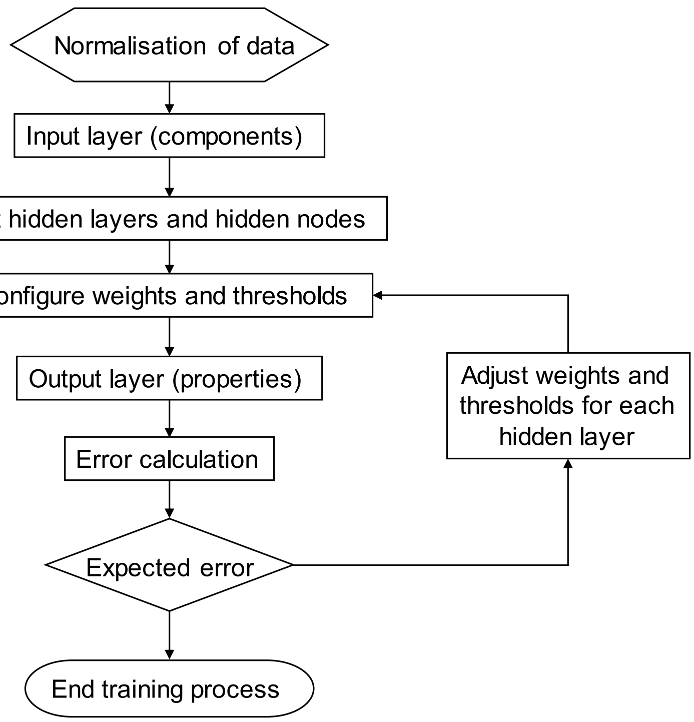

Figure 3.10 The flowchart of ANN modelling in this study

3.5 Ensemble models

Ensemble learning achieves the learning task through aggregation of multiple weak learners using a specific strategy. This approach leverages the advantages of individual models to create a strong learner, resulting in improved performance. Based on the relationships among weak learners, ensemble learning is categorized into bagging (Breiman 1996a), boosting (Freund and Schapire 1997), and stacking (Breiman 1996b).

3.5.1 Random forest

Random forest (RF), as a bagging algorithm, combine the results predicted by multiple decision tree models, where each decision tree is generated from an independently drawn random sample (Breiman 2001). In contrast to traditional decision trees, which select the optimal attribute from the entire set of attributes at each node, the random forest algorithm introduces an element of randomness during base decision tree construction.

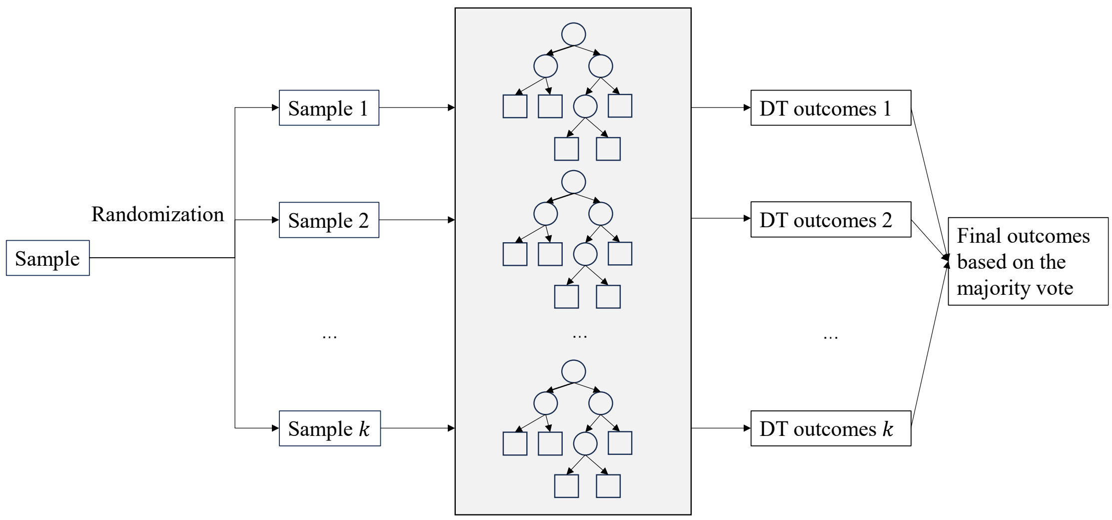

Figure 3.11 Diagram of random forest algorithm

The basic idea behind random forest classification is as follows: First, k samples are drawn from the original training set using bootstrap sampling, with each sample having the same size as the original dataset. Then, a decision tree model is built for each of the k samples, resulting in k classification outcomes.

Finally, the final classification for each record is determined through a majority vote based on these k classification results. A schematic diagram of this process is shown in Figure 3.11. This process adds diversity to the ensemble, enhancing its robustness and reducing overfitting.

3.5.2 Gradient Boosting Decision Tree

Gradient Boosting Decision Tree (GBDT) is a boosting-based ensemble learning algorithm that iteratively trains DTs to improve the overall accuracy. In each iteration, GBDT focuses on the residuals produced in the current round, using them as inputs for the next model to reduce these residuals progressively (as shown in Figure 3.12). Thus, each weak learner in GBDT is trained in a way that aligns with the direction of the gradient that reduces the loss function (Friedman 2001). GBDT is highly accurate and adept at handling high-dimensional and non-linear data, with a straightforward implementation. However, conventional GBDT methods face limitations with large datasets due to the need for multiple full-data passes at each iteration, which leads to high memory consumption and prolonged data processing times.

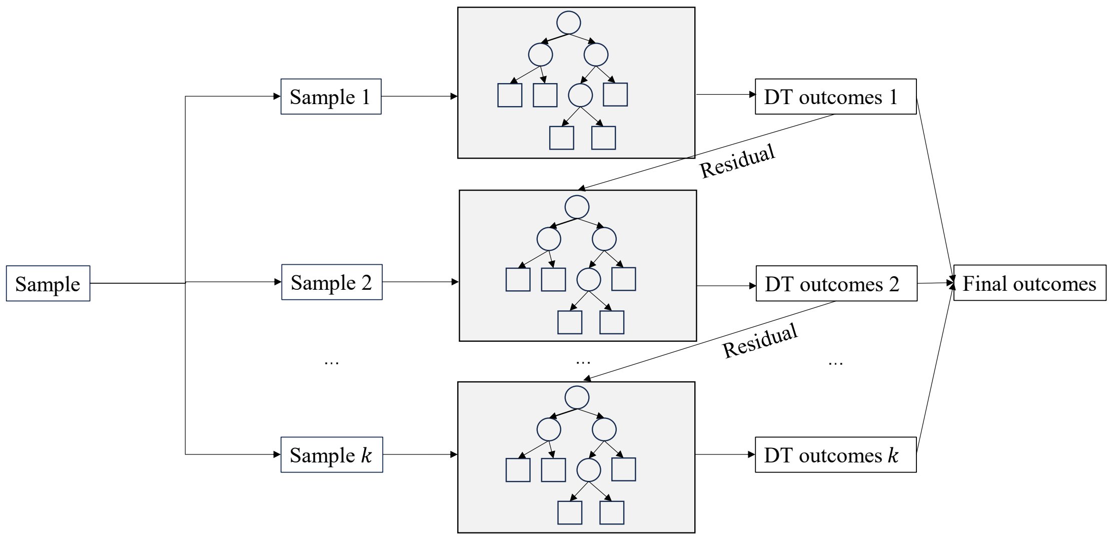

Figure 3.12 Diagram of GBDT algorithm

3.5.3 Extreme gradient boosting

Extreme gradient boosting (XGBoost) is an advanced algorithm built upon GBDT, with enhancements aimed at improving both accuracy and efficiency. Unlike traditional GBDT, which relies solely on first-order gradients, XGBoost approximates the loss function using a Taylor expansion up to the second order, thereby incorporating both first order and second order gradient information to guide the optimization more accurately (Chen and Guestrin 2016). This results in a more precise fitting direction and faster convergence. Additionally, XGBoost introduces regularization terms (including L1 and L2 regularization) into its tree-building process, effectively controlling model complexity and reducing the risk of overfitting, which is a limitation often observed in standard GBDT.

In terms of computational efficiency, XGBoost leverages multiple optimization techniques, such as parallel processing and cache optimization, significantly reducing training time and offering faster processing on large datasets compared to traditional GBDT (Chen and He 2015). The main advantages of XGBoost include high accuracy, faster training speed, and flexible hyperparameter tuning. However, its drawbacks lie in the higher memory demands, especially when handling large datasets. Furthermore, due to the numerous trees of varying depth that it generates, the predictive results of XGBoost lack transparency, making it challenging to clearly interpret the impact of individual features on final predictions.

3.5.4 Light gradient boosting machine

Light gradient boosting machine (LightGBM) is an algorithm built upon the GBDT model, which was designed by Microsoft in 2017 to optimize traditional GBDT algorithms (Ke et al. 2017). LightGBM overcomes the limitation of GBDT by introducing a histogram-based method and a leaf-wise growth strategy with depth constraints. The histogram-based approach involves discretizing continuous feature values into a predefined number of bins. LightGBM then constructs histograms where gradients and sample counts are accumulated within each bin. By aggregating this information during a single pass through the data, LightGBM efficiently identifies the optimal split points for each feature, effectively minimizing both data storage and computational costs. Figure 3.13 demonstrates this histogram-based approach for decision tree construction.

Compared to other gradient boosting tools, LightGBM is recognized for its faster training, achieving speeds up to ten times that of XGBoost (Ke et al. 2017). This performance boost stems from the histogram method's efficiency in reducing the volume of data to be processed, as well as from its exclusive feature bundling technique, which further compacts memory use. These advancements make LightGBM particularly suited for large-scale datasets, providing an efficient solution for high-dimensional data with reduced computational demands.

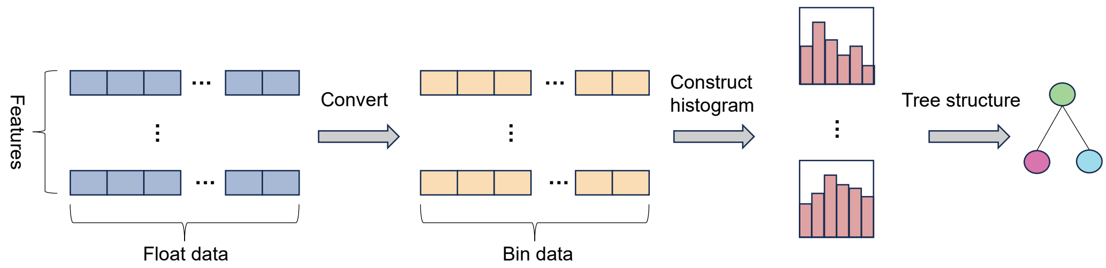

Figure 3.13 Histogram technique in LightGBM

3.6 Applications of machine learning models in SCC

With the development of big data processing techniques and the continuous improvement of computer performance, machine learning technology has been widely used in various fields such as data mining, natural language processing, etc. However, the technology is in its early stages of implementation in the construction industry. With regards to the prediction of concrete properties, smart computing algorithms are utilized in the aim of achieving greater accuracy by minimizing the error between predicted results and data obtained from experiments or literature (Cheng et al. 2012). Young et al. (2019) presented statistical and machine learning models to estimate the compressive strength based on concrete proportions in which a large dataset was taken into account. Subsequently, predictive models were utilized to design concrete mixtures that are optimal in terms of both cost and environmental impact. Sun et al. (2019) utilized a laboratory-prepared specimen to propose an evolved support vector regression tuned by antennae search, which predicted the permeability and unconfined compressive strength of pervious concrete. In the neural network model proposed by Behnood et al. (2015), the tensile strength of steel fibre-reinforced concrete was predicted using compressive strength as an input variable. Recently, ensemble methods have also been developed and employed to predict concrete properties using various algorithms. Asteris et al. (2021) proposed a hybrid ensemble model that utilizes four conventional machine learning algorithms to predict the compressive strength of concrete. The proposed model was demonstrated to achieve higher predictive accuracy compared to the individual models. Nafees et al. (2022) predicted the compressive strength of silica fume-based concrete based on six main input factors. In their study, the ensemble models showed a great improvement on the prediction efficiency.

The popularity of SCC has grown significantly due to its excellent performance in terms of workability and mechanical properties. As a result, several studies have been conducted to predict the properties of SCC in recent years. Table 3.2 outlines some recent studies that adopted various machine learning algorithms for accessing SCC properties, detailing the datasets and variables employed in each study. It is evident that the majority of the research has focused on developing prediction models based on the content of the primary SCC ingredients and the substitution level of SCMs, emphasizing their importance in SCC performance.

ANN models are among the most commonly used for compressive strength prediction due to their ability to capture nonlinear relationships. For example, Asteris et al. (2016) demonstrated that computational environment, initial weights, and model architecture significantly influence the performance of ANN models in predicting SCC properties. These models outperformed existing literature models, achieving higher accuracy and efficiency in predicting 28 days compressive strength.

Compressive strength remains the most frequently studied output variable in SCC research due to its critical role in structural applications. Recent studies, such as those by Huang et al. (2023a) and Jagadesh et al. (2023), have applied advanced ensemble techniques, including XGBoost, CatBoost, and LightGBM, to enhance the predictive accuracy of compressive strength models. These ensemble approaches consistently outperformed traditional machine learning methods.

While compressive strength dominates as the primary focus, some studies have incorporated both fresh and hardened properties as output variables to provide a more holistic view of SCC performance. For example, Belalia Douma et al. (2017) employed an ANN to predict both compressive strength and rheological properties, conducting parametric analysis to evaluate the influence of input variables. Similarly, Azimi-Pour et al. (2020) and Saha et al. (2020) developed SVM models to predict the fresh and hardened properties of SCC. These models, using various kernel functions such as radial basis function and exponential radial basis function, achieved reasonable accuracy when validated against experimental datasets. However, these multi-property prediction studies typically relied on relatively simple model architectures and limited dataset sizes, which may restrict their ability to capture complex interactions between SCC mix parameters and performance outcomes. This highlights the need for more robust models and larger, more diverse datasets to improve predictive reliability.

Fewer studies have focused on durability-related properties, which are critical for long-term performance. Golafshani and Ashour (2016) proposed a novel biogeographical-based programming (BBP) model for predicting the elastic modulus of SCC, using compressive strength as the primary input variable. Sensitivity analysis revealed that increasing habitat size, colony size, and maximum tree depth improved BBP performance effectively. Kumar et al. (2020) developed predictive models using multivariate adaptive regression splines (MARS) and minimax probability machine regression (MPMR) to estimate chloride penetration in SCC, incorporating the effects of fly ash, silica fume, and elevated temperature curing. Both models demonstrated strong potential for predicting rapid chloride penetration test results, with a comparative analysis highlighting their effectiveness.

The popularity of artificial neural network-based methods used in SCC highlights its adaptability, while the adoption of ensemble models showcases advancements in predictive accuracy. Notably, a growing trend is observed in modelling sustainable materials like recycled aggregates and SCMs, aligning research with green construction goals.

Table 3.2 Summary of research on the prediction of SCC properties based on machine learning models

Ref.	Model	Data	Input variables	Output variables
Aggarwal and Aggarwal (2011)	ANN-I	80	Cement, water/powder, FA, CA, SP, fly ash	Compressive strength
	ANN-II	31	Cement, water, water/powder, SP, FA,	Compressive strength

			CA, bottom ash, fly ash	
Asteris et al. (2016)	ANN	169	Cement, water, FA, CA, RHA, SP, VMA, limestone powder, fly ash, GGBS, silica fume	Compressive strength
Golafshani and Ashour (2016)	BBP ABCP	413	Compressive strength	Elastic modulus
Belalia Douma et al. (2017)	ANN	114	Binder, water/binder, FA, CA, SP, fly ash percentage	Compressive strength, slump diameter, V-funnel time, L-box ratio
Kaveh et al. (2018)	DT	114	Binder, water/binder, FA, CA, SP, fly ash	Compressive strength, slump diameter, V-funnel time, L-box ratio
Asteris and Kolovos (2019)	ANN	205	Cement, water, FA, CA, RHA, SP, VMA, limestone powder, fly ash, GGBS, silica fume	Compressive strength
Saha et al. (2020)	SVM	115	Binder, water/powder, FA, CA, SP, fly ash	Compressive strength slump diameter V-funnel time

				L-box ratio
Azimi-Pour et al. (2020)	SVM	340	Cement, water/cement, water/powder, water/binder, FA/powder, CA/powder, HWR/powder, VMA/powder, fly ash/binder, microsilica/binder	Compressive strength slump diameter V-funnel time Orimet U-box L-box ratio
Kumar et al. (2020)	MARS MPMR	360	Fly ash/binder, silica fume/binder, temperature	Rapid chloride permeability
Farooq et al. (2021)	ANN SVM GEP	300	Cement, water/binder, FA, CA, SP, fly ash	Compressive strength
Serraye et al. (2021)	ANN	366	Binder, water/binder, FA, CA, SP, age, silica fume	Compressive strength
Pazouki et al. (2021)	ANN RBFNN FOA	327	Cement, water, FA, CA, SP, age, fly ash	Compressive strength
Yousef et al. (2022)	MLR RF DT	100	Water absorption, void ratio, sonic velocity at 1 day and 7 days,	Compressive strength

	SVM		compressive strength at 1 day and 7 days	
Ben aicha et al. (2022)	MRM ANN	59	Slump flow diameter, V-funnel time, L-box ratio	Yield stress, viscosity
de-Prado-Gil et al. (2022)	Nine ensemble models GAM	515	Cement, water, FA, CA, SP, Mineral admixture	Compressive strength
Abunassar et al. (2022)	ANN SVM	85	Cement, water/binder, FA, CA, SP, fly ash, silica fume	Compressive strength
Faraj et al. (2022)	ANN	400	Cement, water/binder, FA, CA, recycled plastic aggregate, SP, age, fly ash, silica fume, limestone powder, GGBS	Compressive strength
Huang et al. (2023a)	SVM KNN DT RF ANN GBoost XGBoost AdaBoost CatBoost LightGBM	337	Cement, SCMs, w/cm, FA, CA, recycled CA replacement ratio, SP, Cubic size, Curing age,	Compressive strength

	HistGBM GEP			
Mahmood et al. (2023)	KNN SVM DT RF Gboost XGBoost AdaBoost BPNN	133	Cement, rice husk ash, marble powder, SP, CA, FA, water	Compressive strength
Long et al. (2023)	SVM RF	255 349	Cement grade, cement, fly ash, limestone powder, sand, CA, the maximum size, water/binder, SP/binder, metakaolin, GGBS, silica fume, water, SP.	Compressive strength Slump flow
Chen et al. (2023)	GEP MEP	169	FA, cement, SP, rice husk ash, limestone powder, fly ash, CA, GGBS, silica fume, water	Compressive strength
Jagadesh et al. (2023)	Gboost XGBoost AdaBoost LightGBM	515	Natural /recycled aggregate, cement, admixture, natural FA, natural CA, recycled	Compressive strength

	CatBoost	FA, recycled CA
	KNN	
	DT	
	RF	
	SVM	

3.7 Summary and main gaps declared

This chapter provided a comprehensive review of various machine learning models, including traditional supervised learning models and ensemble models. The discussion covered the fundamental principles of each algorithm, the processes of model training and evaluation, and the practical applications of these models in predicting SCC properties. The core concepts of supervised learning were also addressed, particularly focusing on how labelled datasets are used for training models to predict outcomes effectively. Specific techniques such as cross-validation, regularization, and scaling methods were explored as strategies to enhance the generalization capability of models and prevent issues like overfitting and underfitting. Section 3.6 delves into the practical applications of various machine learning models for predicting the properties of SCC. These models leverage the relationships between SCC ingredients and their mechanical properties to improve accuracy and efficiency.

Throughout the chapter, the aim is to demonstrate how machine learning can offer significant improvements in the accuracy and efficiency of SCC property prediction, while also highlighting the challenges and limitations associated with these models. Despite the significant advancements outlined in the chapter, several gaps in the application of machine learning to SCC research remain:

- Many existing studies have focused solely on predicting individual mechanical properties of SCC, such as compressive strength. However, there is a gap in research that simultaneously considers both fresh and hardened properties within a unified framework. Fresh properties are crucial for ensuring workability and ease of placement, particularly in complex structural applications.

- Although some studies have investigated both fresh and hardened properties, the models applied were often of single types, and the datasets used were limited in size and diversity. This limitation restricts their ability to capture complex interactions within SCC mixtures and hinders the generalisation of their findings, especially for HSSCC formulations.
- The addition of steel fibres to SCC can significantly enhance its mechanical properties, particularly its tensile strength, toughness, and resistance to cracking. However, current machine learning studies rarely account for their influence on hardened properties such as compressive, tensile, and flexural strength.
- The performance of machine learning models is highly dependent on the selection of optimal hyperparameters. Hyperparameter tuning techniques, such as cross validation and grid search could help improve model performance.
- Hybrid and ensemble models have shown great potential in improving predictive accuracy and robustness by combining the strengths of multiple machine learning algorithms. However, the application of hybrid and ensemble models in SCC prediction is still in development.

In summary, addressing these gaps is critical to advancing the application of machine learning in the field of SCC. By overcoming these challenges, machine learning can play a pivotal role in designing and optimizing SCC mixtures that meet both performance and workability criteria, while also considering the contributions of steel fibre reinforcement to improve mechanical strength of SCC.

Chapter 4 A pragmatic mix design method for sustainable high strength self-compacting concrete

4.1 Introduction

The workability of the concrete mix is a critical prerequisite for successfully producing self-compacting concrete (SCC). In normal vibrated concrete (NVC), mechanical vibration induces a local reduction in yield stress due to thixotropic behaviour, enabling the mix to become sufficiently flowable for compaction and placement within the vibration-affected zone (Bocciarelli et al. 2018). In contrast, SCC achieves workability by selecting appropriate admixtures, cementitious materials, and aggregates to lower the yield stress to an optimal range while maintaining sufficient plastic viscosity to suspend the aggregates in the cement paste without segregation. Thus, the key to a successful SCC formulation lies in balancing flowability with cohesiveness. It is well-established that SCC generally has a much lower yield stress compared to NVC (Dransfield 2003), which places higher demands on achieving the right mix design to ensure the success of SCC production.

Compared to NVC, SCC generally requires a higher cement content to achieve its superior workability and self-compacting properties. The increased cement consumption in SCC contributes to a higher carbon footprint, primarily due to the CO_2 emissions associated with cement production (Liu et al. 2020). To mitigate these environmental concerns, researchers have explored the use of supplementary cementitious materials as partial replacements for cement in SCC mixes (Alipour et al. 2019). These materials not only reduce the amount of cement required but also improve the mechanical and durability properties of SCC, including reduced permeability and enhanced long-term strength (Pang et al. 2022). However, balancing the reduction of cement content with maintaining high performance of SCC remains challenging, as lower cement content can affect both workability and mechanical strength (Robalo et al. 2021).

This chapter introduces a pragmatic high-strength self-compacting concrete

(HSSCC) mix design method aimed at optimizing both mechanical performance and environmental sustainability by reducing cement content. It begins with a detailed analysis of target compressive strength and plastic viscosity, followed by outlining the steps of the proposed proportioning method. An example is provided to demonstrate the application of the method, culminating in the conclusions on its effectiveness. The experimental validation of the method is carried out using selected materials and specific mix design procedures. The results of the fresh and hardened properties tests, alongside an assessment of sustainability performance, are discussed.

The contents of this chapter have been published in European Journal of Environmental and Civil Engineering (Alshahrani et al. 2024); details are provided in the List of Publications.

4.2 Mix design methods of sustainable HSSCC

With advancements in equipment and production efficiency, the production techniques for self-compacting concrete (SCC) have matured. However, there remains significant room for improvement in SCC mix design methods, as outlined in section 2.8 of chapter 2. Deeb and Karihaloo (2013) proposed a scientific approach to designing high-performance SCC based on plastic viscosity. This method builds upon the principles established by Ghanbari and Karihaloo (2009), utilizing a micromechanical model to estimate the plastic viscosity of SCC from the known viscosity of the cement paste. The expression derived indicates that the solid phase, including fillers and aggregates, increases the viscosity of the paste. The volume fraction and shape of each component in the solid phase significantly influence the overall viscosity. As a result, the equation for plastic viscosity is the product of the known paste viscosity and a factor accounting for the solid phase. This approach offers an alternative to time-consuming experimental trials. Subsequently, Abo Dhaheer et al. (2016) introduced compressive strength as a design parameter for SCC, developing a mix design method capable of achieving compressive strengths of up to 80 MPa.

Building on these methods, the approach proposed in this chapter focuses on the design of HSSCC mixes based on target compressive strength and plastic viscosity. In particular, the method is aimed at producing SCC with compressive strengths in the range of 70-100 MPa. To address environmental concerns associated with higher cement content, this method also incorporates fly ash and GGBS as partial replacements for cement. By reducing cement consumption, this method not only enhances the mechanical performance of SCC but also minimizes its carbon footprint, contributing to a more sustainable construction process.

4.2.1 Target compressive strength and plastic viscosity

Numerous experimental studies have demonstrated that the w/cm plays a crucial role in determining concrete strength (Felekoğlu et al. 2007; Aïtcin 2016). Variations in the w/cm directly impact the quality of the concrete. Researchers have proposed various models to explore this relationship, including statistical models and machine learning prediction models (Moro et al. 2021; Li and Song 2022; Mostofinejad et al. 2023). According to Abram's law, for a given type of cement, test method, and curing time, the compressive strength of concrete is primarily governed by the w/cm. In this context, cementitious materials refer to reactive binders that contribute to the hydration process and strength development, including Portland cement (CEM I), GGBS and fly ash. Building on this principle, Abo Dhaheer et al. (2016) developed a model to determine the 28 days compressive strength (f_{cu}) of SCC mixtures using the following equation (with an R^2 = 0.9366).

$$f_{cu} = \frac{195}{12.65^{w/cm}} \tag{4.1}$$

The proposed formula has been applied to predict the compressive strength of SCC in the range of 30-80 MPa, while in this chapter, it will be extended to target strengths up to 100 MPa. However, it should be noted that for lower strength mixes, particularly those with higher powder content, this formula may tend to overestimate the compressive strength. To adjust for overcome this issue, it is recommended that for a 30 MPa mix, the w/cm predicted by Eq. (4.1) be reduced by approximately 14%, while for a 40 MPa mix, it should be reduced by about 8%.

It should be noted that Eq. (4.1) assumes a consistent relationship between the w/cm and compressive strength. However, this assumption may not always hold true, particularly in high-performance SCC, where the interaction between water demand, binder type, and particle packing becomes increasingly complex. Moreover, the formula does not account for the influence of SCMs, the efficiency of chemical admixtures, or variations in aggregate properties. Therefore, while this formula serves as a useful initial design tool within a reasonably defined range, its extrapolation requires careful interpretation. For greater reliability, complementary validation through experimental testing or data-driven modelling approaches (as presented in Chapter 5) is recommended to confirm the predicted performance.

4.2.2 Target plastic viscosity

In the last decade, numerous methods to measure concrete flow have been developed, primarily to assess concrete quality on job sites or to determine the optimal mix for specific uses. Despite their prevalence, these methods largely rely on empirical approaches rather than directly measuring rheological properties. Key resources such as the RILEM report (Bartos et al. 2002) and the ACI 238 (ACI Committee 238 2008) report provide comprehensive overviews of these tests.

Recently, the industry has shifted towards more objective measures using rheometers to assess concrete rheology. These instruments, which evaluate critical rheological parameters such as plastic viscosity and yield stress, promise a deeper understanding of fresh state of concrete. However, variability among rheometer models can lead to differing results for the same mixture, though they reliably offer qualitative distinctions between mixes. Challenges in capturing precise rheological parameters in fundamental units highlight the complexity of concrete behaviour and the limitations of current testing apparatus (Feys 2006; Vasilić 2015; Feys et al. 2017).

Ghanbari and Karihaloo (2009) introduced a micromechanical approach to estimate the plastic viscosity of SCC mixtures, based on the known plastic viscosity of the paste. In this model, SCC is considered a two-phase suspension, where solid particles are suspended within a viscous liquid phase. Using a two-phase suspension model, the increase in plastic viscosity is progressively calculated as more solid materials are added, starting from fine particles and continuing to coarser ones. By following this process, all materials are gradually incorporated into the mixture, leading to the development of the final SCC mix. This process is visually summarized in Figure 4.1, which illustrates the step-by-step addition of materials and the corresponding increase in plastic viscosity. Air content is also treated as a secondary phase (solid phase) within the suspensions.

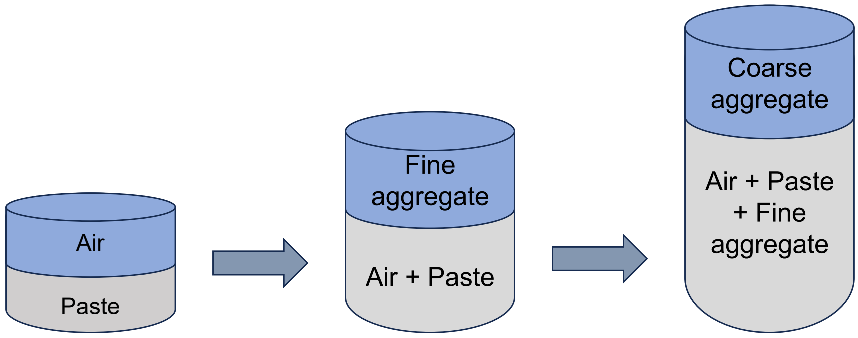

$\eta_1 = \eta_{paste} \times f_1(\phi_1)$ $\quad$ $\eta_2 = \eta_1 \times f_2(\phi_2)$ $\quad$ $\eta_3 = \eta_2 \times f_3(\phi_3)$

Figure 4.1 A hierarchical structure of two-phase suspensions in SCC mix

As a result, the plastic viscosity of the i^{th} liquid-solid suspension can be expressed as a function of the plastic viscosity of the $(i-1)^{th}$ suspension phase, indicating by Eq. (4.2).

$$\eta_i = \eta_{i-1} \times f_i(\phi_i) \tag{4.2}$$

where η_i is the plastic viscosity of the i^{th} suspension; η_{i-1} is the plastic viscosity of the $(i-1)^{th}$ suspension; $f_i(\phi_i)$ is the relative viscosity, which used to account for the increase in plastic viscosity due to the addition of the i^{th} solid phase with a volume fraction ϕ_i. When i=1, η_0 represent the plastic viscosity of paste.

Hence, the plastic viscosity of the mix can be expressed by:

$$\eta_{mix} = \eta_{paste} \times f_1(\phi_1) \times f_2(\phi_2) \times \cdots \times f_n(\phi_n) \tag{4.3}$$

where n is the total number of solid phases in the mix.

More than a century ago, Einstein conducted pioneering work on the viscosity of dilute suspensions containing solid spheres, leading to the formulation of the well-known Einstein's viscosity equation (Einstein 1956; Liu et al. 2019). This formula highlights a fundamental concept: the macroscopic rheological properties of multiphase flows are intricately linked to microscale physical interactions, especially when hydrodynamic forces dominate. Based on

Einstein's equation, the relative viscosity of a suspension $f_i(\phi_i)$ can be determined using Eq. (4.4).

$$f_i(\phi_i) = 1 + [\eta]\phi_i \tag{4.4}$$

$[\eta]$ represents the intrinsic viscosity, which is a measure of the effect of individual particles on viscosity. The value of $[\eta]$ is equal to 2.5 in three-dimensional cases (Brady 1983), applying specifically to rigid spherical particles. Studies have also shown that for rigid ellipsoidal particles with an aspect ratio smaller than 3, the same value of 2.5 is applicable (Struble and Sun 1995; Koehler and Fowler 2007). In contrast, for randomly packed hexagonal arrays of spherical air bubbles, the intrinsic viscosity equals 1.

At higher concentrations of the solid phase, where the volume fraction exceeds 10% and approaches the maximum particle volume fraction (ϕ_m), the hydrodynamic interactions between particles, along with Brownian motion, become significant and cannot be ignored. Under these conditions, the Krieger–Dougherty formula (Krieger and Dougherty 1959) is considered more suitable for modelling the behaviour of the liquid-solid suspensions, as shown in Eq. (4.5).

$$f_i(\phi_i) = (1 - \frac{\phi_i}{\phi_m})^{-[\eta]\phi_m} \tag{4.5}$$

The value of ϕ_m for paste is largely governed by the void fraction, or the porosity, of the packing particles. Therefore, the particle size distribution and size of SCC materials play a significant role in determining ϕ_m (Xing et al. 2020). Moreover, similar to $[\eta]$, ϕ_m is also influenced by the applied shear rate in the system: as rate increases, ϕ_m tends to rise, while $[\eta]$ shows the opposite behaviour (Ghanbari and Karihaloo 2009). The combined behaviour of these two parameters under shear conditions suggests that their product (the exponent in Eq. (4.5)) remains nearly constant across various conditions, averaging around 1.9 (De Kruif et al. 1985; Abo Dhaheer et al. 2016).

In terms of HSSCC mixes, the total volume fraction of fine and coarse aggregates exceeds 10%. Consequently, the Krieger–Dougherty formula is applied to calculate the relative viscosity of the suspension. It is assumed that the air content in concrete is approximately 2% of the total volume. By incorporating this assumption into Eq. (4.3), the plastic viscosity of the mixture is derived, as shown in Eq. (4.6). In this calculation, the 2% increase in viscosity due to trapped air is included in the viscosity of the paste.

$$\eta_{mix} = \eta_{paste} \times (1 - \frac{\phi_{FineAgg.}}{\phi_m})^{-1.9} \times (1 - \frac{\phi_{CoarseAgg.}}{\phi_m})^{-1.9} \tag{4.6}$$

where $\phi_{FineAgg.}$ and $\phi_{CoarseAgg.}$ are the volume fraction of the fine and coarse aggregates, respectively.

The packing density (maximum packing fraction, ϕ_m) increases progressively as more solid phases are introduced. As noted by Abo Dhaheer et al. (2016), when fine aggregate is incorporated into the paste, the packing arrangement can be approximated as cubic packing, with ϕ_m set at 0.63. Once the final solid phase, typically coarse aggregate, is added to the suspension, the packing becomes denser and transitions into close hexagonal packing, with ϕ_m increasing to 0.74.

4.2.3 Steps of the proposed method

The proposed methodology for the mix design of HSSCC is based on achieving a target plastic viscosity while satisfying both mechanical and rheological requirements. The design process consists of a systematic set of calculations to determine the optimal proportions of constituent materials, ensuring that the final mix conforms to EFNARC (2005) guidelines and volumetric constraints.

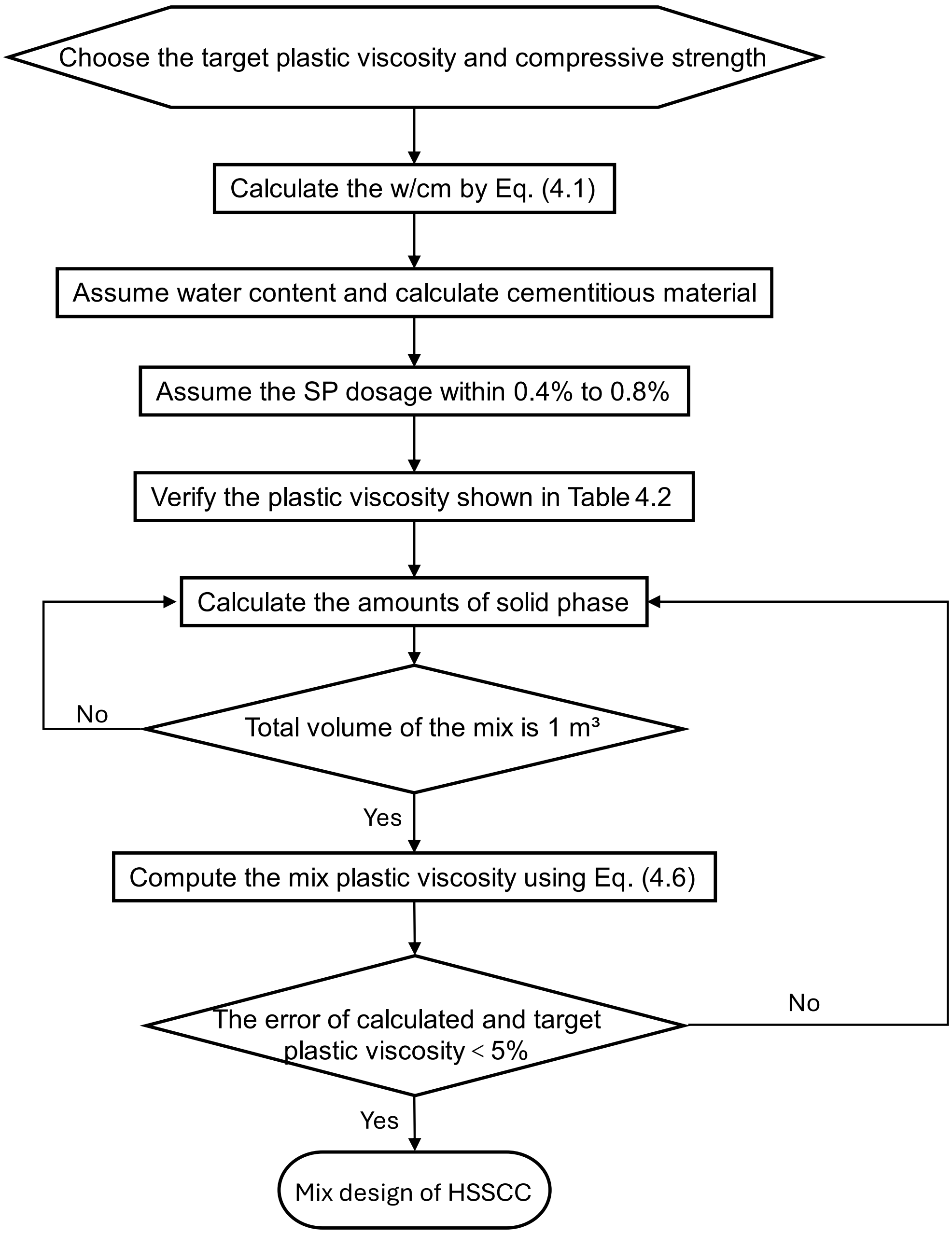

Figure 4.2 The procedure of the proposed methodology of HSSCC mix proportions

The step-by-step procedure is outlined as follows (Figure 4.2):

1. Set the target plastic viscosity of the HSSCC mix within the range of 3-15 Pa·s, following the EFNARC (2005) for appropriate viscosity selection.

2. Calculate w/cm based on the target compressive strength using Eq. (4.1).

3. Assume the water content to be within the range of 150-210 kg/m³, in line

with the EFNARC (2005) (see Table 4.1). From this, the total cementitious materials content is calculated. The binder consists of 60% cement (CEM I 52.5N), 20% GGBS, and 20% fly ash by mass.

4. Assume a SP dosage between 0.4–0.8% of the binder mass. The SP dosage refers to the commercial aqueous solution (not the pure polymer content).
5. Apply the plastic viscosity of HSSCC cement paste obtained from the viscometer tests as shown in Table 4.2 (Alshahrani et al. 2024).
6. Calculate the amounts of solid phase components based on the volume fractions.
7. Adjust the total volume of the mix to ensure it equals 1 m³, including 2% air content.
8. Compute the overall mix plastic viscosity using Eq. (4.6) and compare it with the target value. If the difference is within $\pm$5%, the design is acceptable; otherwise, the volume fractions are adjusted, and the process is repeated.

Table 4.1 Typical range of SCC mix compositions according to EFNARC (2005)

Constituent	Typical range by mass (kg/m^3)	Typical range by volume $(liters/m^3)$
Powder*	380-600	–
Paste	–	300-380
Water	150-210	150-210
Coarse aggregate	750-1000	270-360
Fine aggregate	Typically, 48-55% of total aggregate weight	
Water/Powder radio by Vol	0.85-1.10	

*Material of particle size smaller than 0.125 mm

Table 4.2 Plastic viscosity of HSSCC cement paste (60% CEM I 52.5N, 20% GGBS, 20% fly ash, SP, and water)

Mix code	w/cm	η_{paste} (Pa·s)	$\eta_{paste+airvoids}$ (Pa·s)
C70	0.40	0.053	0.054
C80	0.35	0.073	0.075
C90	0.30	0.177	0.180
C100	0.26	0.381	0.390

To better interpret the values presented in Table 2, the plastic viscosity of the paste was experimentally determined using a rotational viscometer (Brookfield DV2T). The test was performed on fresh cementitious paste without aggregates, incorporating cement, fly ash, GGBS, water, and superplasticiser according to the designed proportions. After mixing, the paste was allowed to rest for approximately 2 minutes to eliminate entrapped air bubbles. The test was performed at a controlled room temperature of 20 ± 1 °C using a standard RV-series spindle (model RV-03). The paste sample was placed in a container, and the spindle was fully immersed. A controlled shear rate sweep was applied ranging from 0 to 100 s^{-1} and then back to 0 in discrete steps. The displayed torque and shear rate were recorded continuously, and the average plastic viscosity was calculated once a steady-state value was observed. Each test was repeated at least twice, and the mean value of plastic viscosity was used as the reference for the target viscosity in the mix design framework.

To streamline this procedure and enable rapid identification of feasible mix proportions, the design methodology was implemented using MATLAB (see Appendix B). The program automates the process of iterating volume fractions, validating each constituent against practical limits, and outputting acceptable mix compositions. The corresponding design charts, generated from the MATLAB model, are provided in Figure 4.3, which illustrate mix design options for target compressive strengths of 70, 80, 90, and 100 MPa.

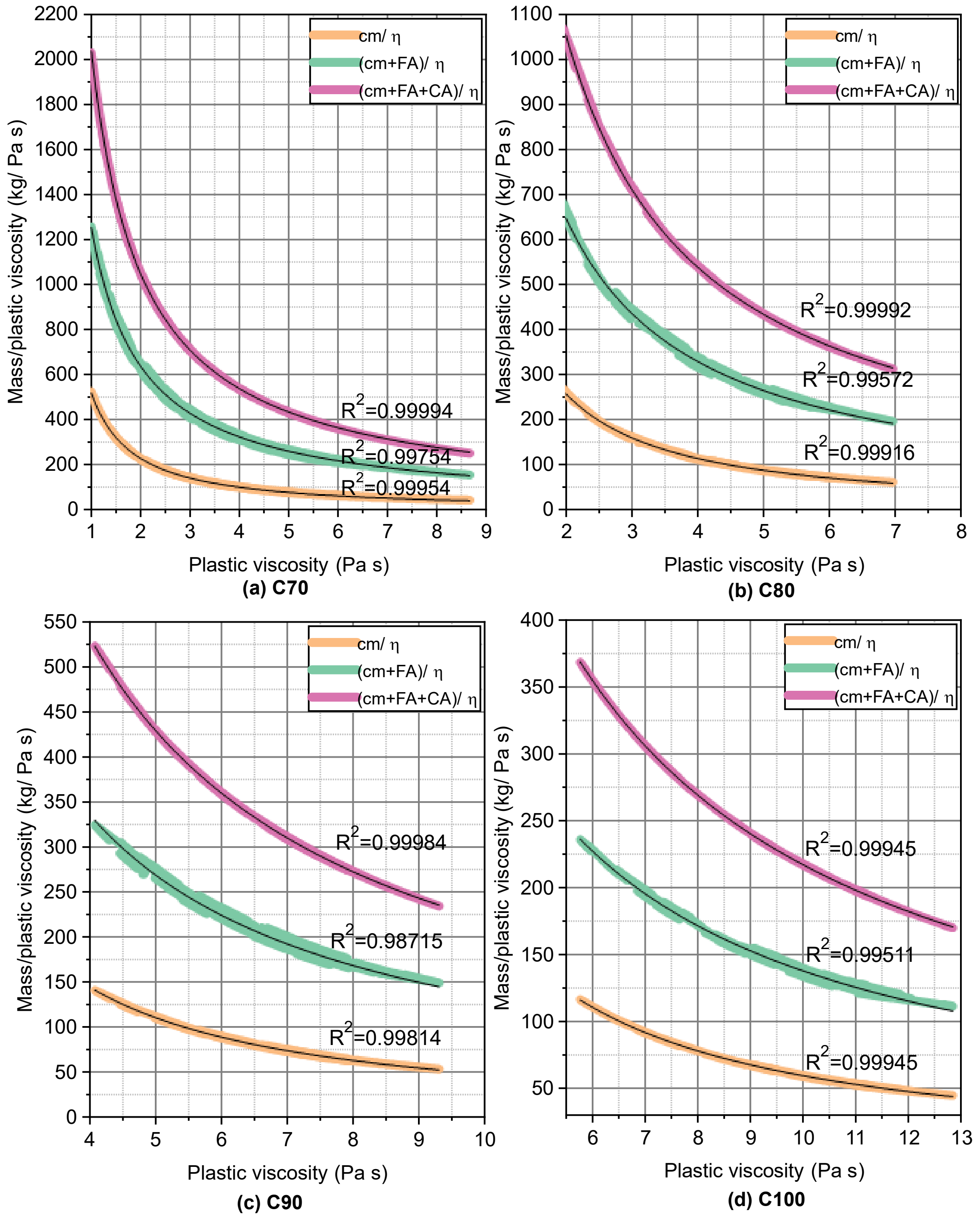

Figure 4.3 Design charts of HSSCC based on plastic viscosity

(a) C70, (b) C80, (c) C90 and (d) C100

4.2.4 Example of applying the proposed design method

This section demonstrates the application of the design charts presented in Figure 4.3. These steps are simplified for practical use, allowing mix designers to directly retrieve optimal proportions based on target strength and plastic viscosity without running the full computational process. Following the steps outlined earlier, the process of calculating w/cm, solid phase components, and plastic viscosity are explained in detail. This example will offer a practical illustration of how to achieve an optimal mix design, ensuring both mechanical performance and workability for HSSCC. The resulting mix design will aim to meet specific strength and rheological criteria while adhering to the environmental considerations discussed in previous sections.

An example of the mix proportioning procedure is given below for a mix with a target compressive strength of 90 MPa and plastic viscosity of 6 Pas. The applicable design chart is given in Figure 4.4.

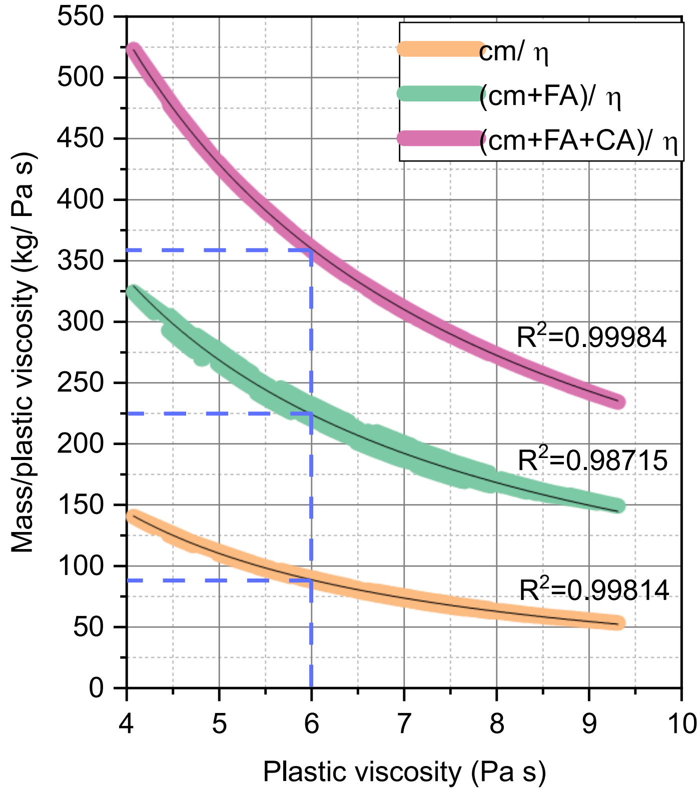

Figure 4.4 Mix design chart of 90 MPa HSSCC

1. Set the target plastic viscosity $\eta_{mix} = 6\ Pa\ s$.
2. Calculate water to cementitious material ratio from Eq. (4.1).

   For a compressive strength $f_{cu} = 90MPa,\ w/cm = 0.30$.

3. Determine the cementitious materials content based on the orange curve in Figure 4.4.

   $cm/\eta = 89\ kg/Pa\ s$, then $cm = 534\ kg/m^3$

   As per the mix design, 20% of the cement is replaced with fly ash and another 20% with GGBS. Hence, $cement = 320\ kg/m^3$, $GGBS = 106.8\ kg/m^3$, and $fly\ ash = 106.8\ kg/m^3$.

4. Calculate water content.

   As $w/cm = 0.30$, then $w = 0.3 \times 534 = 160.2\ \ \mathrm{kg/m^3}$.

5. Assume SP content to be 0.7% of total cementitious materials.

   $m_{sp}/m_{\mathrm{cm}} = 0.7\%$, $cm = 534\ \ kg/m^3$, then $\mathrm{SP} = 3.74\ \mathrm{kg/m^3}$.

6. Calculate the solid phase component.

   Using the green curve in Figure 4.4 for fine aggregate,

   $(cm + FA)/\eta = 224.15\ kg/m^3$.

   As $\eta_{mix} = 6\ Pa\ s$, $\quad cm = 534\ kg/m^3$, then $FA = 810.9\ \ kg/m^3$.

   Similarly, from the pink curve for coarse aggregate content,

   $(cm + FA + CA)/\eta = 358.22\ kg/m^3$, then $CA = 804.42\ \ kg/m^3$.

7. Check the total volume.

   Ensure the designed concrete mix has a total volume of 1 m³. Given the densities of the components (cement, fly ash, GGBS, sand, and coarse aggregate are 3150, 2400, 2400, 2550, and 2650 kg/m³ respectively), the total volume is calculated as:

$$T_V = \frac{320}{3150} + \frac{106.8}{2400} + \frac{106.8}{2400} + \frac{160.2}{1000} + \frac{3.74}{1070} + \frac{810.9}{2550} + \frac{804.42}{2650} + 0.02 = 1m^3$$

8. Determining the plastic viscosity of the mix by using Eq. (4.6).

$$\phi_{\ fine\ agg} = \frac{\frac{FA}{\rho_{FA}}}{\frac{c}{\rho_c} + \frac{GGBS}{\rho_{GGBS}} + \frac{fly\ ash}{\rho_{fly\ ash}} + \frac{w}{\rho_w} + \frac{SP}{\rho_{SP}} + \frac{FA}{\rho_{FA}} + 0.02} = 0.456$$

$$\phi_{coarse\ agg} = \frac{\frac{CA}{\rho_{CA}}}{\frac{c}{\rho_c} + \frac{GGBS}{\rho_{GGBS}} + \frac{fly\ ash}{\rho_{fly\ ash}} + \frac{w}{\rho_w} + \frac{SP}{\rho_{SP}} + \frac{FA}{\rho_{FA}} + \frac{CA}{\rho_{CA}} + 0.02} = 0.304$$

$$\eta_{mix} = \eta_{paste} * \left(1 - \frac{\phi_{\ fine\ agg}}{\phi_{\ m}}\right)^{-1.9} * \left(1 - \frac{\phi_{coarse\ agg}}{\phi_{\ m}}\right)^{-1.9}$$

$$= 0.18 * \left(1 - \frac{0.456}{0.63}\right)^{-1.9} * \left(1 - \frac{0.304}{0.74}\right)^{-1.9} = 5.76\ Pa\ s$$

where, η_{paste} obtained by viscometer $= 0.18$.

9. The difference between the desired viscosity and the calculated viscosity is:

   $Diff. = (5.76 - 6)/6 = 4\% < 5\%$,

   which is in the acceptable range. Thus, the final proportions are presented in Table 4.3.

Table 4.3 Mix design of C90 HSSCC mix with plastic viscosity of 6 Pa s

Materials	Water	Cement	GGBS	Fly ash	SP	FA	CA
Mass ($\mathrm{kg/m^3}$)	160.2	320	106.8	106.8	3.74	810.9	804.42

4.3 Experimental validation on the proposed method

In order to validate the accuracy and practicality of the proposed HSSCC mix design method, experimental tests were conducted. This section outlines the experimental procedure, including the preparation of materials, mixing techniques, and testing methods for both fresh and hardened properties of the concrete. The objective is to assess whether the calculated values from the mix design align with the actual performance of the concrete in terms of workability and compressive strength. Thus, the effectiveness of the proposed mix design methodology can be evaluated.

4.3.1 Materials

The materials utilized in the experimental HSSCC mixes included ordinary Portland cement (OPC), ground granulated blast furnace slag (GGBS), fly ash, and SP. The OPC was of grade 52.5 MPa, with a specific gravity of 3.15 and a fineness of 384 m²/kg. GGBS and fly ash were employed as supplementary cementitious materials, both possessing a specific gravity of 2.4. The superplasticizer used was MasterGlenium ACE 499, a polycarboxylate ether-based polymer, with a specific gravity of 1.07. The chemical composition of cementitious materials is detailed in Table 4.4. These data were obtained from the technical datasheets of manufacturers provided for each material batch used in the study.

Table 4.4 Chemical compositions of the cementitious materials in HSSCC mixes

Material	SiO_2	Al_2O_3	Fe_2O_3	CaO	K_2O	Na_2O	MgO	SO_3	TiO_2
OPC	19.69	4.32	2.85	63.04	0.74	0.16	2.17	3.12	0.33
GGBS	34.34	12.25	0.32	39.90	0.45	0.41	7.70	0.23	0.65
Fly Ash	53.10	20.64	8.93	6.12	2.17	1.68	1.79	1.93	0.90

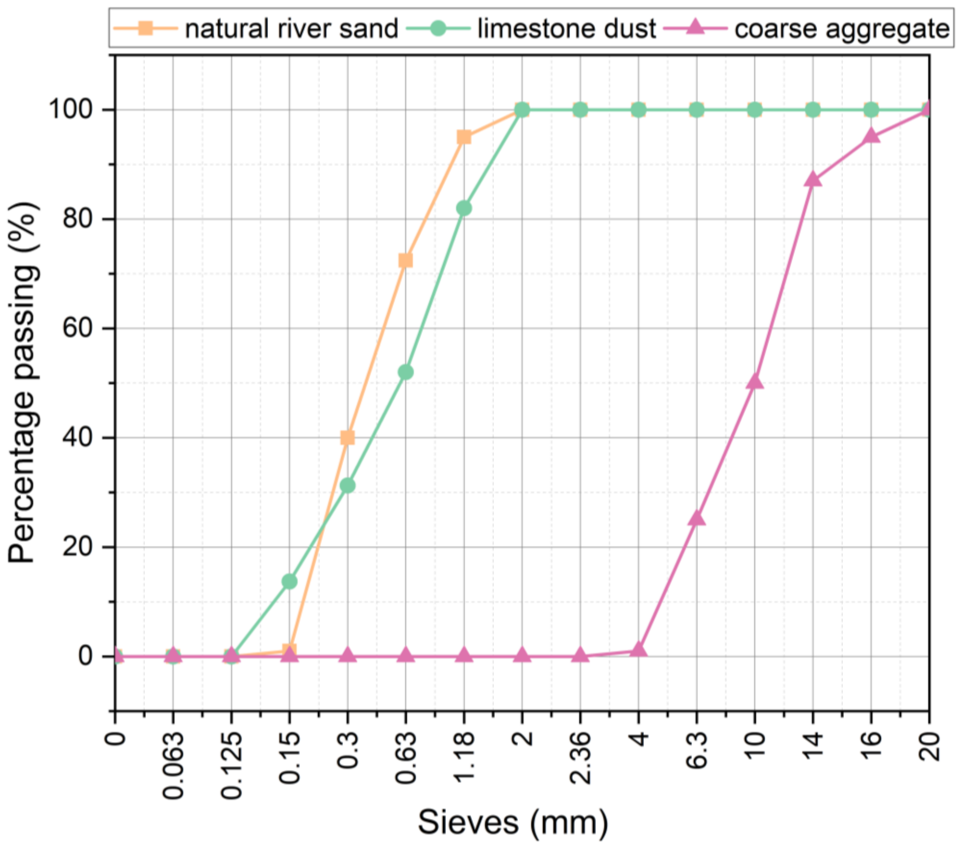

Figure 4.5 Particle size distribution of aggregates

The aggregates consisted of crushed limestone as coarse aggregate (CA), which had a specific gravity of 2.65 and a maximum particle size of 20 mm, and natural river sand as fine aggregate (FA), with a specific gravity of 2.55 and a maximum particle size of 2 mm. Additionally, 30% of the fine aggregate was substituted with a coarser fraction of limestone dust (LD), which had a specific gravity of 2.6 and a particle size range between 0.125 mm and 2 mm. Although LD exhibits limited reactivity due to its potential nucleation effects, it was classified as an inert filler in the mix design process and excluded from the cementitious materials category when applying the mix proportioning equations. The particle size distribution curves for both fine and coarse aggregates are presented in Figure 4.5.

4.3.2 Mix design procedures

Various HSSCC mixes were formulated to validate the proposed methodology, with the mix designs based on both target compressive strengths and rheological properties. This experiment included four series of HSSCC mixes, targeting compressive strengths of 70, 80, 90, and 100 MPa, with plastic viscosities ranging from 1.3 to 12 Pa s. Each series comprised four different mixes, each with distinct plastic viscosity values and varying sand to aggregate (S/A) and paste to solid (P/S) ratios. The detailed proportions of the mixes are provided in Table 4.5 and Table 4.6. Mixes labelled A and C were designed with 48% sand by total aggregate weight, while mixes B and D were formulated with higher S/A ratios. Additionally, mixes A and B had lower P/S ratios compared to mixes C and D. The maximum cement replacement, determined through trial and error, was capped at 40% to maintain the desired compressive strength.

The mixing process was conducted using a horizontal pan mixer under ambient laboratory conditions (20 ± 2°C). Initially, all dry components, including cement, GGBS, fly ash, limestone dust, fine aggregate, and coarse aggregate, were added to the mixer and blended for approximately one minute to ensure uniform dispersion. Following this, around 80% of the calculated mixing water was gradually introduced while mixing continued for an additional two minutes. The remaining water, pre-mixed with the designated quantity of superplasticiser, was then added slowly over a period of 30 seconds. The mix was further blended for two minutes to ensure a homogeneous and flowable SCC mix. To stabilise the rheological properties and account for any initial thixotropic recovery, the fresh mixture was allowed to rest for one minute before undergoing a final one-minute mixing. The fresh concrete was immediately subjected to testing and casting to minimise variability in fresh state performance.

Table 4.5 The proportions of produced HSSCC mixes, kg/m^3

Mix code	w/cm	Water	Cementitious materials			SP	Aggregates		
			OPC	GGBS	Fly ash		FA		CA
							Sand	LD	
70A	0.40	188.4	282.5	94.2	94.2	2.8	542.6	237.1	839.7
70B		188.4	282.5	94.2	94.2	2.8	593.6	259.4	763.9
70C		197.2	295.8	98.6	98.6	3.0	527.8	230.6	816.8
70D		197.2	295.8	98.6	98.6	3.0	561.4	245.3	766.9
80A	0.35	174.2	298.6	99.5	99.5	3.5	546.0	238.6	845.1
80B		174.2	298.6	99.5	99.5	3.5	604.0	263.9	750.6
80C		181.9	311.8	103.9	103.9	3.6	532.3	232.6	823.8
80D		181. 9	311.8	103.9	103.9	3.6	574.1	250.9	761.7
90A	0.30	164.4	328.8	109.6	109.6	4.4	538.2	235.2	832.9
90B		164.4	328.8	109.6	109.6	4.4	590.0	257.8	756.0
90C		170.2	340.3	113.5	113.5	4.5	527.0	230.3	815.6
90D		170.2	340.3	113.5	113.5	4.5	566.4	247.5	750.0
100A	0.26	151.7	350.0	116.7	116.7	5.8	537.1	234.7	831.3

100B		151.7	350.0	116.7	116.7	5.8	590.6	258.1	751.1
100C		156.0	360.0	120.0	120.0	6.0	528.0	230.7	817.2
100D		156.0	360.0	120.0	120.0	6.0	563.2	246.1	762.8

Table 4.6 The viscosity and further details of HSSCC mixes

Mix code	Plastic viscosity (Pa s)			Sand/total aggregate by weight (%)	Paste/solid by volume
	Paste	Target	Actual		
70A	0.054	1.6	1.60	48.15	0.61
70B		1.8	1.81	52.76	0.61
70C		1.3	1.30	48.15	0.66
70D		1.4	1.39	51.26	0.66
80A	0.075	2.3	2.34	48.14	0.60
80B		2.7	2.68	53.62	0.60
80C		1.9	1.92	48.15	0.64
80D		2	2.10	51.99	0.64
90A	0.18	5	5.00	48.15	0.62
90B		5.5	5.62	52.86	0.62
90C		4.2	4.28	48.15	0.66
90D		4.6	4.59	52.04	0.66
100A	0.39	10	10.68	48.14	0.63
100B		12	12.02	53.05	0.63
100C		9.5	9.40	48.14	0.66
100D		10	10.06	51.48	0.66

To assess the self-compacting properties, slump flow, J-ring, and L-box tests were conducted following EFNARC guidelines (2005). The procedures and fundamental principles for testing have been outlined in detail in chapter 2. All tests were recorded on video to observe the fresh concrete behaviours, and it was noted that no signs of segregation or bleeding occurred in any of the mixes. From each of the 16 mixes, 15 cubes (100 x 100 x 100 mm) were cast. The cubes were de-moulded after one day and cured in water at (20 ± 1)°C. Compressive strength tests were conducted at 7, 28, and 90 days, according to British standards (BS EN 12390-3 2009; BS EN 12390-6 2009).

This experimental work was conducted in collaboration with my colleague Alshahrani (2024), with whom I shared the experimental results. By working together, we were able to generate a significant amount of experimental data, which allowed us to explore the effects of different variables, such as S/A, on both the mechanical and fresh properties of the concrete. I was responsible for conducting the experiments for mixes C and D, while my colleague handled mixes A and B. This collaborative approach provided a more comprehensive understanding of how various factors influence the behaviours of HSSCC.

4.4 Results and discussion

Following the experimental validation of the proposed HSSCC mix design methodology, the subsequent sections present the results and analysis of the conducted tests. The discussion is divided into three main parts: fresh properties, hardened properties, and sustainability performance. The fresh properties tests focus on the workability and flow characteristics of the HSSCC mixes, while the hardened properties tests assess the mechanical performance, such as compressive strength. Additionally, the sustainability performance is evaluated by examining the environmental impact, specifically carbon dioxide (CO_2) emissions and cement consumption, associated with each mix design. These results provide a comprehensive evaluation of the proposed methodology in terms of both performance and sustainability.

4.4.1 Fresh properties tests

The fresh properties of the HSSCC mixes were assessed through their filling and passing abilities, which were determined using the slump flow, J-ring, and L-box tests. For each mix, three independent measurements were conducted for each test, and the average values were recorded to ensure the reliability of the results. All experimental procedures for the mixes were recorded and saved as video documentation. Figures 4.6-4.8 provide example photographic documentation of the test results for the HSSCC mix labelled 80D.

Figure 4.6 Final spread in slump flow test of the HSSCC 80D mix

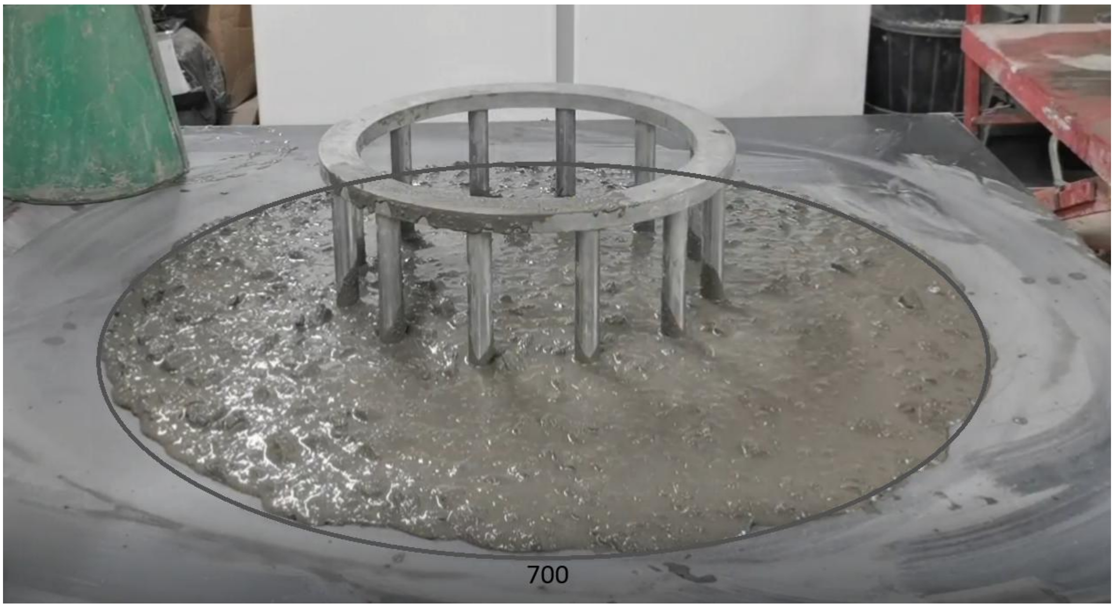

Figure 4.7 Final spread in J-ring test of the HSSCC 80D mix

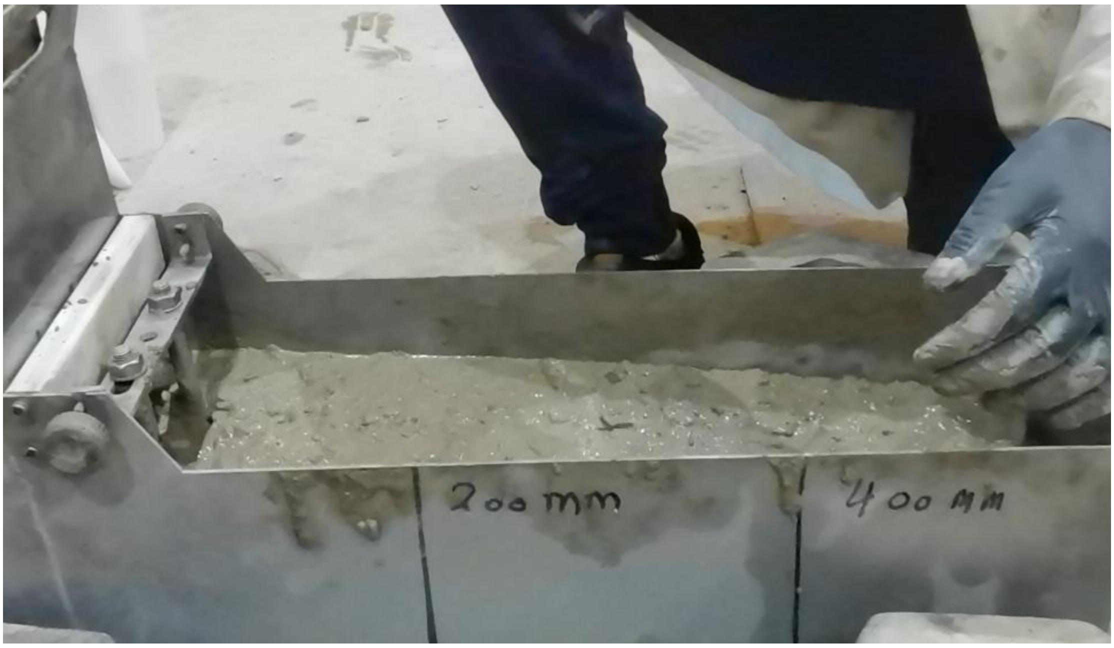

Figure 4.8 Final spread in L-box test of the HSSCC 80D mix

4.4.1.1 Slump flow and T_{500} time

The slump flow test was conducted in strict accordance with BS EN 12350-8 (2009). The SCC mix was poured into the slump cone without vibration or tamping, and the cone was lifted vertically to allow the mix to flow. The time to reach a 500 mm diameter spread (T_{500}) was recorded, and the final slump flow diameter (D_{slump}) was determined by averaging two perpendicular measurements to the nearest 10 mm. The results are shown in Figure 4.9. In this figure, the data points represent the average of the three measurements, while the vertical sticks indicate the recommended specification ranges defined by EFNARC (2005) for slump flow spread. These ranges serve as a reference to evaluate whether the fresh properties of each mix fall within acceptable limits for SCC applications.

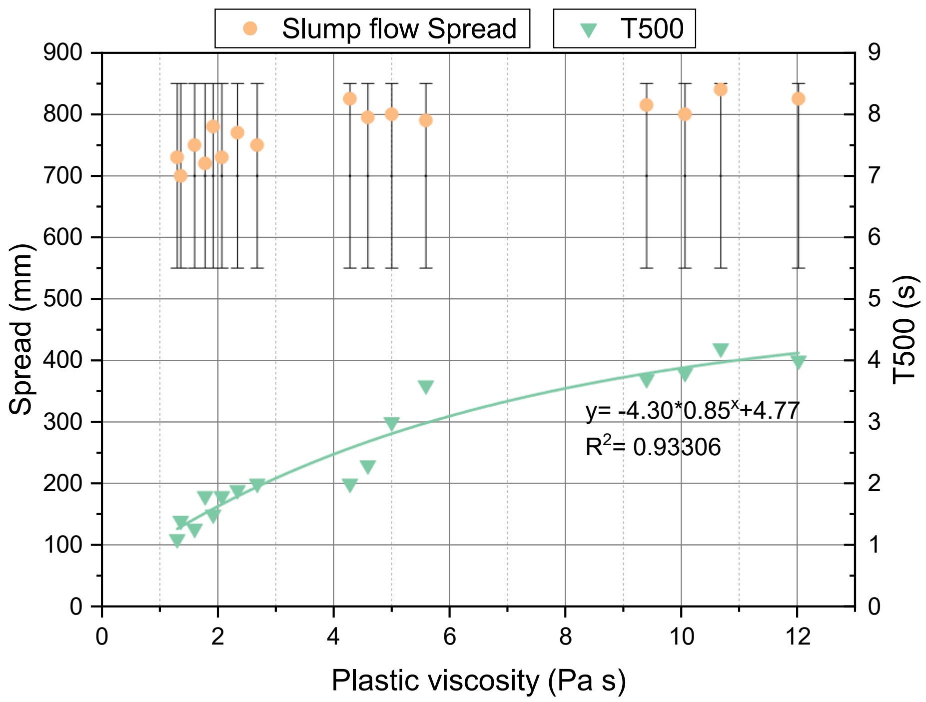

Figure 4.9 Slump flow spread and T_{500} time for HSSCC mix

A consistent trend can be observed where the slump flow spread remains relatively stable across the different mix designs, indicating that the filling ability of the HSSCC mixes was maintained at a satisfactory level according to the EFNARC (2005). The slump flow spread values remain between 700 mm and 800 mm for the majority of mixes, which aligns with the required specifications for SCC in practical applications, ensuring that the mixes can flow and fill formworks without segregation. The trend of increasing T_{500} is consistent with the expected behaviours, as higher paste volumes tend to enhance the cohesion of material, leading to increased resistance to flow. The trade-off between filling ability and viscosity in HSSCC mixes has been clearly represented, which is crucial for mix design optimization.

4.4.1.2 J-ring test

The J-ring test was conducted to evaluate the passing ability of the HSSCC mixes through simulated reinforced bars, mimicking real construction conditions. The test followed the BS EN 12350-12 (2010) using a 300 mm diameter J-ring with 16 steel bars. Similar to the slump flow test, the expansion spread (D_{J-ring}) and T_{500j} time were measured, with results recorded in Figure 4.10. The vertical sticks express the recommended specification ranges defined by EFNARC (2005) for J-ring flow spread. It is evident that the majority of the J-ring flow spread results are relatively consistent, clustering around the higher range of values, suggesting that the HSSCC mixes demonstrate good flowability even in the presence of obstacles. The upward trend of T_{500j} indicates that as the plastic viscosity of the mix increases, the mix takes longer to flow through the J-ring setup, which is expected in highly viscous mixes. The overall results confirm that the HSSCC mixes maintain sufficient passing ability without segregation.

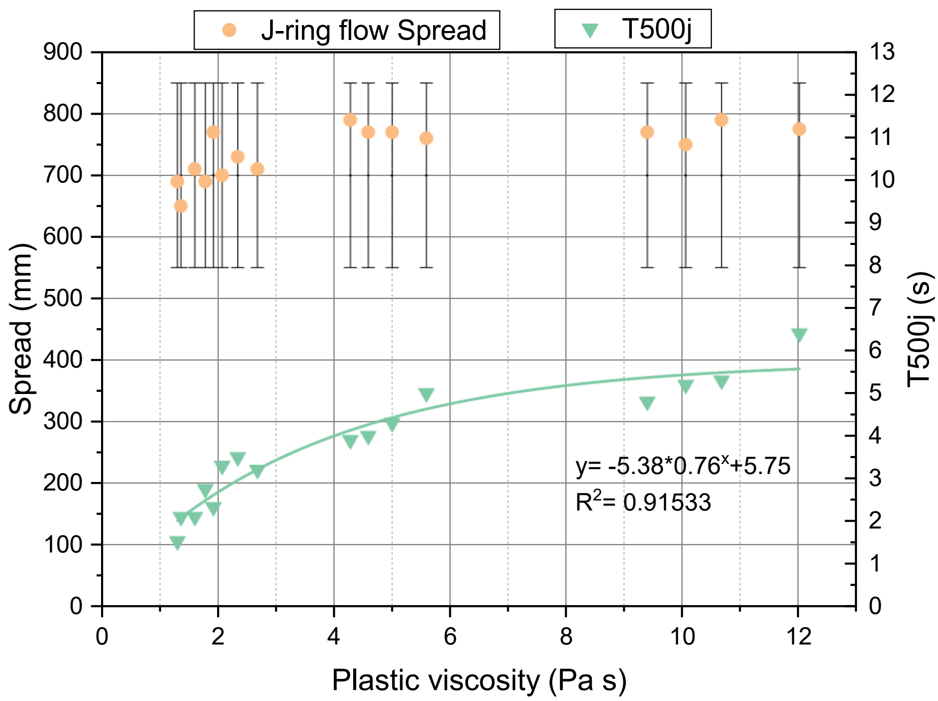

Figure 4.10 J-ring flow spread and T_{500j} time for HSSCC mix

According to ASTM C1621 (2017), the blocking behaviours of the concrete can be assessed by comparing the flow spread diameters obtained from the slump flow and J-ring tests. A difference of less than 25 mm suggests no visible blocking, while a difference between 25 mm and 50 mm indicates minimal to noticeable blocking. If the difference exceeds 50 mm, it is categorised as significant to extreme blocking. As shown in Table 4.7, the observed differences in flow spread were all below 50 mm, confirming that no severe blocking occurred during testing.

Table 4.7 Difference between slump flow and J-ring flow tests

Mix code	D_{slump} (mm)	D_{J-ring} (mm)	$D_{slump} - D_{J-ring}$ (mm)
70A	750	710	40
70B	720	690	30
70C	680	670	10
70D	700	650	50
80A	770	730	40
80B	750	710	40
80C	780	770	10
80D	730	700	30
90A	800	770	30
90B	790	760	30
90C	825	790	35
90D	795	770	25
100A	800	790	10
100B	825	775	50
100C	815	770	45
100D	800	750	50

4.4.1.3 L-box test

L-box tests were employed to evaluate the capacity of HSSCC mixes to flow under their own weight through reinforced bars and into a designated frame.

The two-bar system, with a diameter of 12 mm, was chosen to simulate the gap between the bars similar to that of the J-ring test. The time taken for each mix to flow to distances of 200 mm (T_{200}) and 400 mm (T_{400}) horizontally after the gate was opened was recorded. The passing ability ratio was calculated by comparing the concrete depth at the beginning and end of the horizontal leg of L-box (H_1/H_2). Figure 4.11 demonstrates that all the mixes satisfied the Class PA1 requirement, as outlined in the EFNARC (2005) (vertical sticks), confirming adequate filling and passing abilities. Additionally, an exponential correlation was observed between the flow time and plastic viscosity across all HSSCC mixes, indicating that flow time increased with the increase of plastic viscosity.

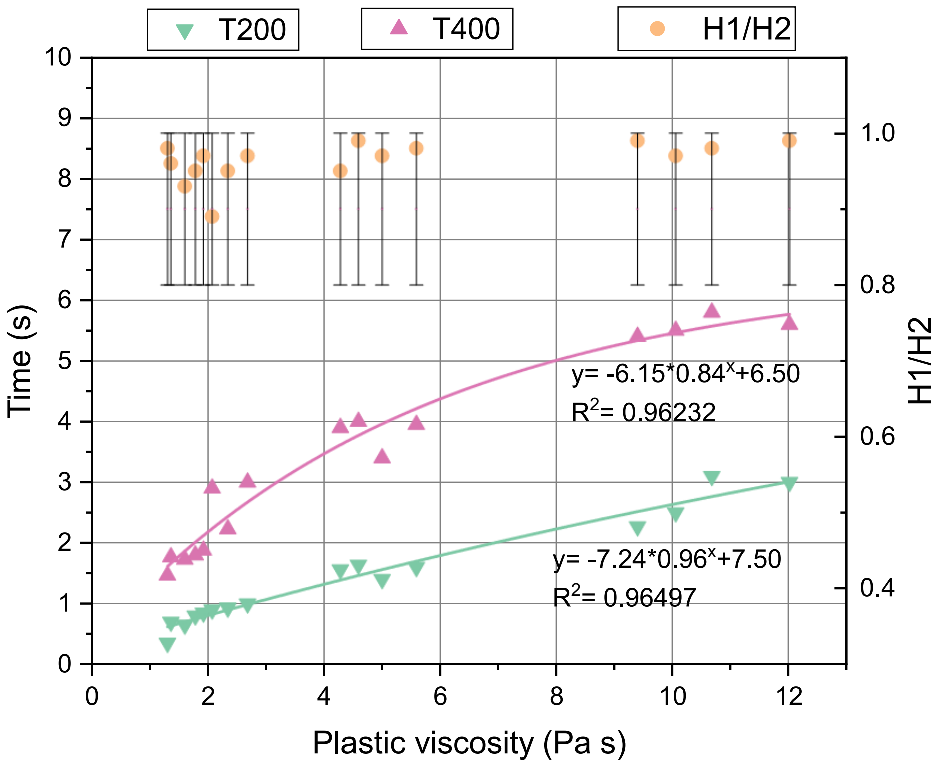

Figure 4.11 L-box flow time and height ratio for HSSCC mix

4.4.2 Hardened properties tests

Table 4.8 presents the compressive strength results of various HSSCC mixes at different curing ages (7, 28, and 90 days) across four target compressive strength classes (70 MPa, 80 MPa, 90 MPa, and 100 MPa). It is observed that compressive strength consistently increased, with a significant gain between 7 and 28 days, followed by a more gradual increase up to 90 days. This demonstrates the effectiveness of the HSSCC mixes in achieving rapid early strength while continuing to gain strength over time.

Table 4.8 Compressive strength of the HSSCC mixes

Mix code	Compressive strength (MPa)		
	7 days	28 days	90 days
70A	48.3	74.9	79.5
70B	45.3	70.4	75.6
70C	47.3	70.1	78.8
70D	48.6	68.6	76.5
80A	63.5	80.3	88.3
80B	62.8	78.4	86.7
80C	60.6	82.2	92.9
80D	60.3	81.1	90.1
90A	72.3	91.1	101.9
90B	69.4	88.4	96.35
90C	71.6	93.2	103.2
90D	70.4	91.3	98.6
100A	80.4	100.2	108.8
100B	74.5	98.1	106.7
100C	77.8	100.4	105.4
100D	76.8	98.3	102.7

Additionally, the variations in mix designs within the same target strength class indicate that fine adjustments in parameters such as the S/A ratio and P/S ratio have a noticeable impact on the final compressive strength. It is also worth noting that replacing natural river sand with a coarser fraction of limestone dust has minimal impact on both the fresh and hardened properties. However, this replacement is economically viable and environmentally sustainable.

4.4.3 Sustainability performance

The sustainability performance of HSSCC is a critical aspect of its overall evaluation, especially in light of the increasing emphasis on reducing the environmental footprint of construction materials. In this section, the environmental impact of various HSSCC mixes is assessed by analysing the CO_2 emissions associated with each mix design. The study explores how ingredient adjustments, such as replacing cement with supplementary materials like GGBS and fly ash, and optimizing the S/A and P/S ratios, can improve both the material efficiency and environmental sustainability of HSSCC. The CO_2 emissions per unit strength and per cubic meter of concrete are compared across different mix designs, offering insights into strategies for minimizing environmental impact while achieving desired mechanical properties.

Figure 4.12 illustrates the quantity of cement required to achieve 1 MPa of compressive strength at 28 days for various HSSCC mixes (A, B, C, and D) across different target compressive strength levels. The data shows a clear trend where cement consumption per MPa generally decreases as the target compressive strength increases from 70 MPa to 100 MPa. This trend aligns with the established principles of high-strength concrete design, where achieving higher compressive strengths often results in more efficient use of cementitious materials per unit of strength.

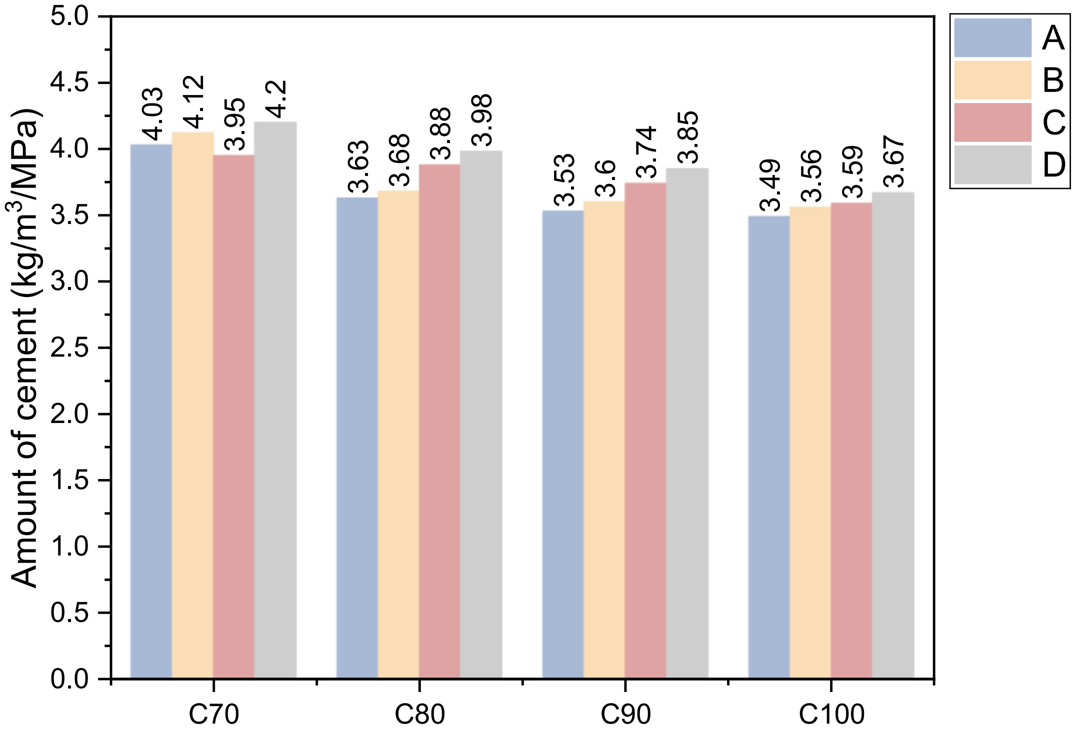

Figure 4.12 Amount of cement required to achieve 1 MPa of compressive strength at 28 days for HSSCC mixes.

Additionally, it is evident from the data in Figure 4.12 that the proposed mix design method requires significantly less cement per MPa compared to the typical value of 5 kg/m^3/MPa reported in previous studies for HSC and HSSCC (Damineli et al. 2010; Deeb and Karihaloo 2013). This finding demonstrates the effectiveness of the proposed method in reducing cement consumption while achieving the desired compressive strength, thus supporting its environmental and economic benefits. Notably, the benchmark proposed by (Habert et al. 2020) suggests that clinker consumption should not exceed 3.5 kg/m^3/MPa for typical concrete classes (30–50 MPa). The proposed HSSCC mixes achieve superior performance, maintaining lower cement consumption and CO_2 emissions per MPa even at higher strength levels, thus showcasing their sustainable advantage.

To evaluate the sustainability of designed HSSCC mixes, CO_2 emission of each material has been collected and summarized in Table 4.9. Recent research further supports these assumptions. According to Habert et al. (2020), the production of OPC contributes approximately 0.90–0.95 kg of CO_2 per kilogram, aligning with the 0.931 value adopted in this study. Additionally, supplementary cementitious materials such as GGBS and fly ash have significantly lower emissions (around 0.0796 kg CO_2/kg and near zero, respectively), making them effective substitutes for reducing the carbon footprint of concrete mixes (MPA 2013).

Figure 4.13 illustrates the CO_2 emissions per 1 m³ of various HSSCC mixes, which can be calculated based on the proportions. It is shown that unit CO_2 emissions increased with the increase in compressive strength, which can be attributed to the higher cement content required for higher strengths. One effective method to reduce the CO_2 emissions of concrete is by replacing part of the cement with industrial by-products that have lower CO_2 emissions. In this experimental design, 40% of the cement was replaced by pozzolanic materials (GGBS and fly ash) by weight, and 30% of the sand was replaced by LD by volume.

Table 4.9 CO_2 emission of HSSCC ingredients reported in the literature

Ingredients	CO_2 emissions (kg CO_2 /kg)	Ref.
OPC	0.931	(Hanif et al. 2017a)
GGBS	0.0796	(MPA 2013)
Fly ash	0.0001	(MPA 2013)
Fine aggregates	0.003	(Hanif et al. 2017b)
Coarse aggregate	0.007	(Hanif et al. 2017b)
LD	0.0016	(Campos et al. 2020b)
SP	0.250	(Hanif et al. 2017b)

It was also observed that the main factor influencing the reduction in CO_2

emissions was the cement replacement, which is consistent with results from previous studies (Celik et al. 2015). However, the replacement of sand had minimal impact on emissions. For instance, in mix 100 A, partially replacing cement reduced CO_2 emissions by 37.80%, while replacing sand reduced emissions by only 0.72%. Nonetheless, as previously mentioned, replacing natural river sand with coarser LD is economically feasible, environmentally friendly, and can enhance the durability of the concrete (Kirthika et al. 2020).

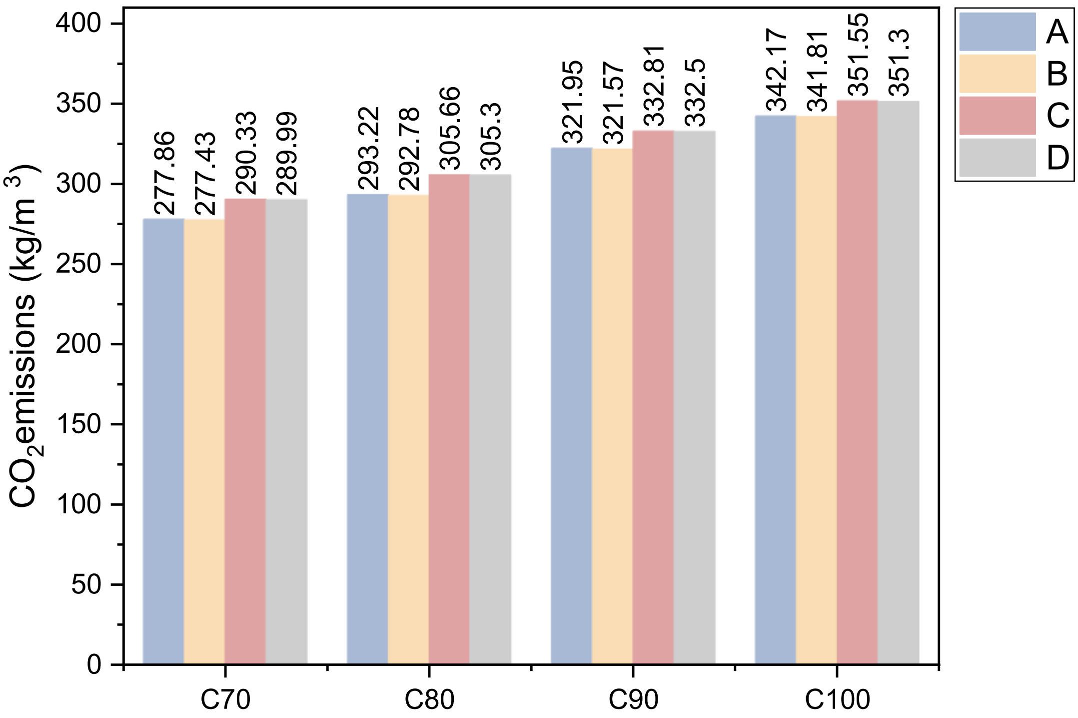

Figure 4.13 CO_2 emission per 1m^3 of HSSCC mixes

To further enhance the sustainability of concrete, developing higher strength mixes is another effective strategy alongside adjusting mix ingredients. HSSCC requires a smaller volume to bear the same load, thereby improving material efficiency. In this context, the environmental impact can be evaluated by examining the CO_2 emissions required to achieve 1 MPa of compressive strength (Campos et al. 2020a).

Figure 4.14 highlights the CO_2 emissions per MPa of compressive strength at 28 days for the four HSSCC mixes. The results indicate a general trend where

CO_2 emissions decrease as the compressive strength increases, reflecting the greater efficiency in material use as strength rises. This aligns with the principle that optimized cementitious material content can deliver higher strength with a smaller environmental footprint. Additionally, slight variations across the different mix designs suggest that the S/A and P/S ratios also play a role in influencing CO_2 emissions. These findings underscore the dual approach of both ingredient optimization and strength enhancement to reduce the environmental impact of concrete.

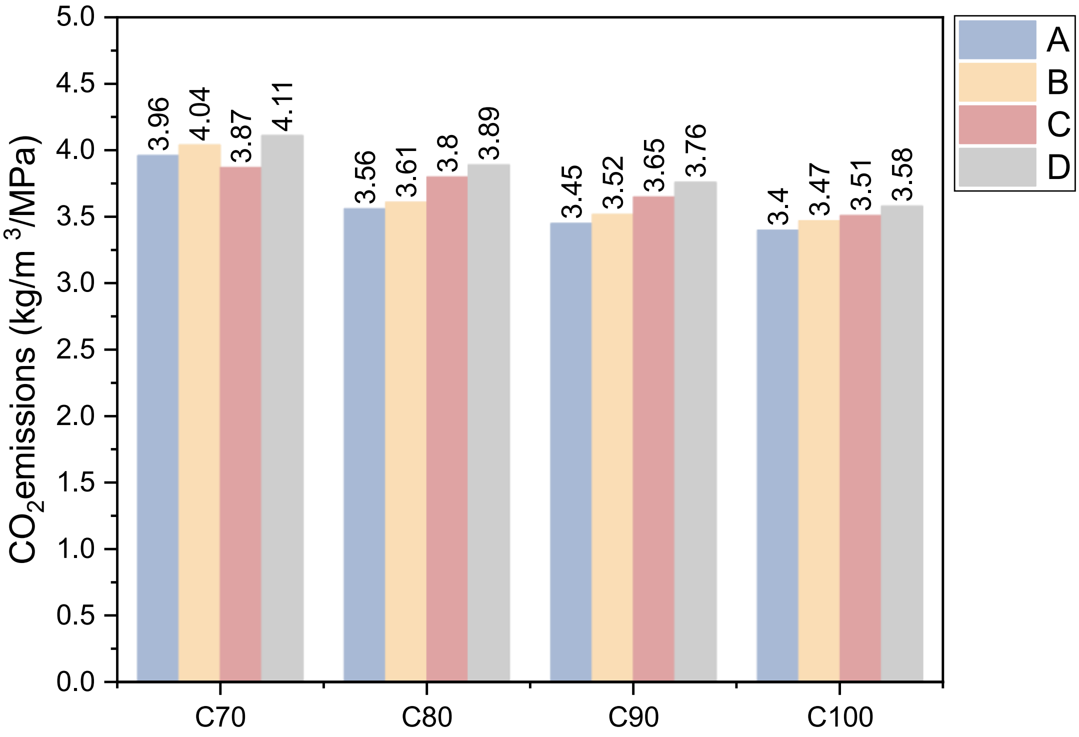

Figure 4.14 CO_2 emissions per MPa of compressive strength at 28 days for HSSCC mixes

4.5 Conclusions

This chapter presented a detailed investigation into the development of sustainable HSSCC through a new mix design methodology. The proposed mix design method was built on optimizing the target compressive strength and plastic viscosity, with a focus on improving workability, mechanical properties, and environmental performance. Design charts were provided for further guidance. Various mix designs were tested with different S/A and P/S ratios to evaluate their influence on both fresh and hardened concrete properties.

Experimental validation demonstrated that the optimized mixes could achieve the desired mechanical properties while maintaining adequate workability. The sustainability performance was enhanced by reducing the cement content and replacing it with supplementary materials like GGBS and fly ash, which led to a significant reduction in CO_2 emissions. The chapter also showed that an increase in compressive strength per MPa could be achieved with less cement and lower environmental impact, validating the efficiency of the proposed design method.

It should be noted, however, that the applicability of the proposed methodology is currently limited to a binder system comprising 60% CEM I 52.5N, 20% GGBS, and 20% fly ash. The plastic viscosity values used in the design charts were obtained from viscometer tests based on this specific composition. Therefore, for other binder systems or cement types, recalibration of the paste viscosity would be necessary to ensure accuracy and consistency of the mix design results.

In conclusion, the findings in this chapter suggest that the optimized design method not only improves the performance of HSSCC but also addresses the growing need for sustainable construction practices by reducing the carbon footprint and improving the resource efficiency of concrete production.

Chapter 5 Machine learning modelling on properties of SCC containing fly ash

5.1 Introduction

The experimental mix design of high-strength SCC forms a critical foundation for achieving the desired balance between workability and strength, particularly in practical applications. However, experimental approaches often require significant resources and are time-consuming. In practice, more efficient methods are needed to predict the performance of SCC, particularly for varying strength levels of SCC commonly used in construction.

To address this issue, this chapter explores the use of machine learning techniques to predict and analyse SCC properties. By employing large datasets and advanced computational algorithms, machine learning provides a robust approach for modelling the complex interactions between SCC mix components and their resulting properties. Integrating machine learning into SCC research holds great potential to optimize the mix design process, reduce material waste, and improve the overall efficiency of construction practices.

Figure 5.1 shows the flowchart of the proposed framework with the main factors considered in this chapter. The primary steps are as follows: (1) Three groups of datasets are established, taking into account the most influential variables on SCC properties from the literature focused on SCC with fly ash. (2) Initial models are developed based on the datasets. (3) Various hyperparameter optimization strategies based on five-fold cross-validation for each model are explored. (4) The predictive models are evaluated using various performance metrics. (5) A comparative study is performed for the optimized models, with results presented via REC curves and Taylor diagrams. The best-performing machine learning models for predicting SCC properties with fly ash are identified based on the comparative study. (6) The impact of mix ingredients on the fresh and hardened properties of SCC is investigated. (7) Potential implementation on the proposed data driven framework is developed.

The content of this chapter has been published in the Journal of Building Engineering (Cui et al. 2024b); details are provided in the List of Publications.

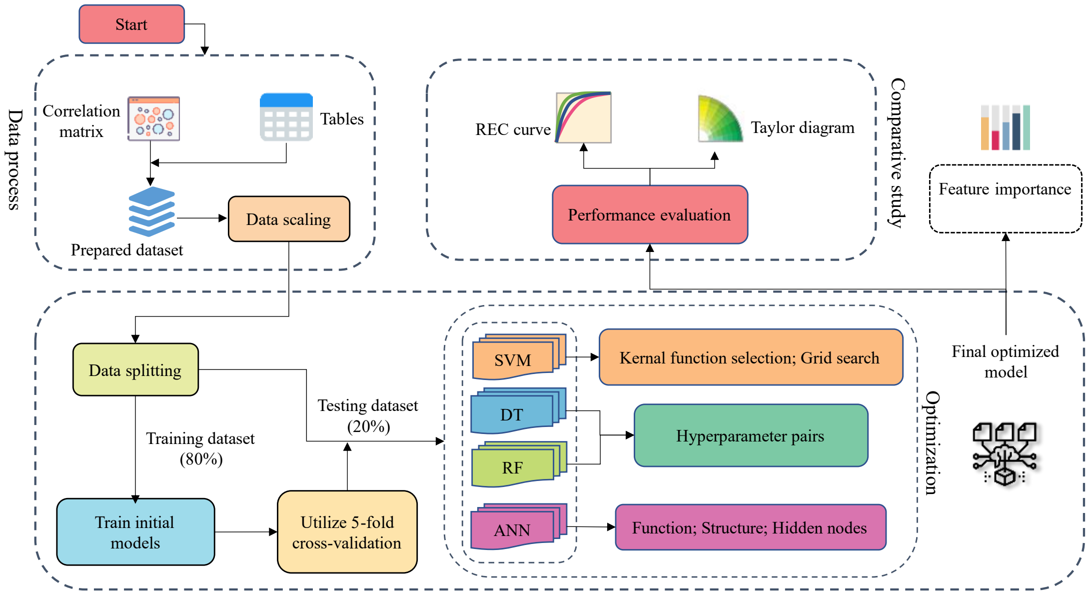

Figure 5.1 Flowchart of the presented data driven framework for the prediction of the SCC properties

5.2 Data process and parameters

This chapter aims to predict both fresh and hardened properties of SCC mixes containing fly ash. Many previous studies had focused mainly on assessing a single output characteristic based on a series of input variables. This chapter considers three output variables to achieve a more comprehensive forecast. Considering the database from the published literature, the properties of SCC mix design, including compressive strength (Fcu) of 501 mixes (Khatib 2008; Sukumar et al. 2008; Sonebi and Cevik 2009; Güneyisi 2010; Liu 2010; Şahmaran et al. 2011; Siddique 2011; Jalal and Mansouri 2012; Uysal et al. 2012; Cuenca et al. 2013; Ramanathan et al. 2013; Siad et al. 2013; Nepomuceno et al. 2014; Ponikiewski and Gołaszewski 2014; Güneyisi et al. 2015; Zhao et al. 2015; Bani Ardalan et al. 2017; Dadsetan and Bai 2017; Esquinas et al. 2018; Matos et al. 2019; Anjos et al. 2020; Choudhary et al. 2020; Guo et al. 2020a; Ting et al. 2020; Sambangi and Arunakanthi 2021;

Kumar et al. 2022; Zhao et al. 2022), slump flow diameter (SD) of 217 mixes (Sukumar et al. 2008; Sonebi and Cevik 2009; Girish et al. 2010; Güneyisi 2010; Liu 2010; Şahmaran et al. 2011; Siddique 2011; Jalal and Mansouri 2012; Uysal et al. 2012; Cuenca et al. 2013; Ramanathan et al. 2013; Siad et al. 2013; Nepomuceno et al. 2014; Ponikiewski and Gołaszewski 2014; Güneyisi et al. 2015; Zhao et al. 2015; Bani Ardalan et al. 2017; Dadsetan and Bai 2017; Guo et al. 2020a; Jain et al. 2020; Ting et al. 2020; Sambangi and Arunakanthi 2021; Kumar and Kumar 2022; Zhao et al. 2022) and V-funnel time (VF) of 144 mixes (Sukumar et al. 2008; Sonebi and Cevik 2009; Güneyisi 2010; Liu 2010; Şahmaran et al. 2011; Siddique 2011; Jalal and Mansouri 2012; Uysal et al. 2012; Cuenca et al. 2013; Ramanathan et al. 2013; Siad et al. 2013; Nepomuceno et al. 2014; Ponikiewski and Gołaszewski 2014; Güneyisi et al. 2015; Bani Ardalan et al. 2017; Dadsetan and Bai 2017; Jain et al. 2020; Sambangi and Arunakanthi 2021; Kumar and Kumar 2022), were collected to evaluate the properties of SCC containing fly ash, by utilizing the machine learning modelling.

To ensure the representativeness of the collected dataset, a comprehensive literature review was conducted across multiple academic databases such as Scopus and Google Scholar. Selection criteria included peer-reviewed journal articles and conference papers that reported detailed mix design parameters and corresponding fresh or hardened properties of SCC incorporating fly ash. Studies with inconsistent reporting, missing values, or unclear measurement procedures were excluded to ensure data reliability. The final dataset incorporated a diverse range of sources across different geographic locations, experimental methods, and material compositions to avoid selection bias and enhance the generalisability of the machine learning models.

The input variables encompass the amount of cement (C), fly ash (F), water to cementitious materials ratio (w/cm), fine aggregates (FA), coarse aggregates

(CA), superplasticizers (SP) and curing age, with the age being employed exclusively for compressive strength prediction. The relationships representing the SCC properties are expressed by Eqs. (5.1) – (5.3).

$$Fcu,(MPa) = f_1(C, F, w/cm, FA, CA, SP, Age) \tag{5.1}$$

$$SD,(mm) = f_2(C, F, w/cm, FA, CA, SP) \tag{5.2}$$

$$VF,(s) = f_3(C, F, w/cm, FA, CA, SP) \tag{5.3}$$

The statistical results which were summarized and calculated from collected datasets are presented in Table 5.1. For the purpose of improving the accuracy of comprehensive predictions in SCC properties, key variables have been confined within a consistent range. For instance, the w/cm is set between 0.26 and 0.7, while the range for SP is established between 0.78 kg/m^3 and 21.84 kg/m^3. The dataset has been cleaned by removing outlier data that was identified from the literature and deemed irrelevant for consideration. In order to reveal more information and to analyse the relationship between all input and output variables, the correlations of variables are provided. For this purpose, the Pearson's correlation coefficient is used as shown in Eq. (3.5). Figure 5.2 displays the heatmaps illustrating the correlations between features within the datasets. There is a significant negative correlation between fly ash content and cement across the three datasets used for compressive strength, slump flow, and V-funnel time predictions, with correlation coefficients of -0.8, -0.78, and -0.82, respectively. On the contrary, the correlation between superplasticizer and components of SCC mixtures is quite weak in Dataset 1 (in Table 5.1), which is consistent with reality.

Table 5.1 Statistical analysis on collected SCC datasets

Variables	Symbol	Unit	Min	Max	Mean	SD	Count
Dataset 1: SCC compressive strength (501 samples)							

Cement	C	kg/m^3	100	670	350	119	501
Water to cementitious material ratio	w/cm	-	0.26	0.70	0.39	0.08	501
Fly ash	F	kg/m^3	0	428	145	95	501
Fine aggregate	FA	kg/m^3	369	1180	828	147	501
Coarse aggregate	CA	kg/m^3	455	1085	790	137	501
Superplasticizer	SP	kg/m^3	0.78	21.84	5.15	4.35	501
Curing age	Age	days	1	720	47	82	501
Compressive strength	Fcu	Mpa	0.36	105.88	42.14	20.38	501
Dataset 2: SCC slump flow (217 samples)							
Cement	C	kg/m^3	0	670	359	114	217
Water to cementitious material ratio	w/cm	-	0.26	0.70	0.37	0.08	217
Fly ash	F	kg/m^3	0	439	170	98	217
Fine aggregate	FA	kg/m^3	369	1180	837	123	217
Coarse aggregate	CA	kg/m^3	455	1085	740	124	217
Superplasticizer	SP	kg/m^3	0.78	21.84	5.52	4.41	217
Slump flow diameter	SD	mm	555	830	712	58	217
Dataset 3: SCC V-funnel (144 samples)							
Cement	C	kg/m^3	0	670	367	126	144
Water to cementitious material ratio	w/cm	-	0.26	0.70	0.38	0.09	144
Fly ash	F	kg/m^3	0	439	146	103	144
Fine aggregate	FA	kg/m^3	369	1180	820	145	144
Coarse aggregate	CA	kg/m^3	533	944	763	103	144
Superplasticizer	SP	kg/m^3	0.78	21.84	6.23	5.17	144
V-funnel time	VF	sec	1.31	22.00	7.29	3.32	144

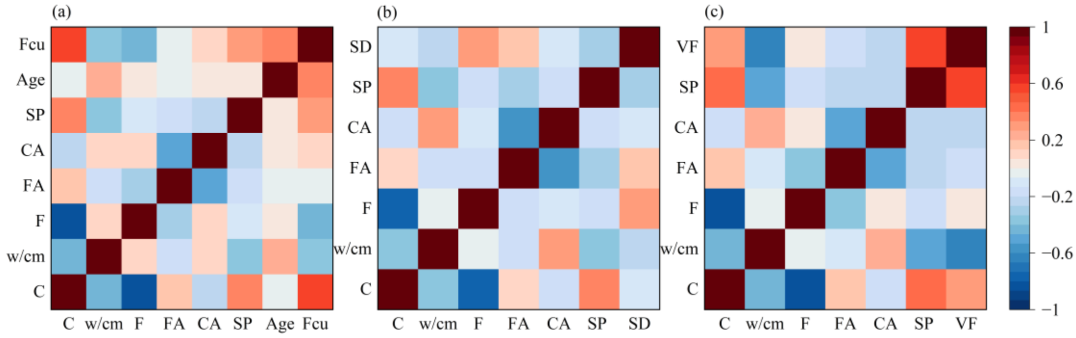

Figure 5.2 Correlation matrix of variables for predicting (a) Compressive strength, (b) Slump flow, (c) V-funnel time

In order to evaluate the generalization error of the predictive models, each dataset was randomly split into two groups. The training sets, which is 80% of all data points, were used for building machine learning models. The remaining 20% were used for testing the trained models. For example, in the case of Dataset 1, 400 groups of measurements were used as training set and 101 measurements were used for the assessment of models. To eliminate the error caused by units and ranges of all variables, it is necessary to process datasets after the data splitting. It has been proven that scaling increases the speed in obtaining the optimal solution in some algorithms and also improves the accuracy of prediction (Ahsan et al. 2021). In this study, the Standard Scaler function in scikit-learn library was employed.

5.3 Determination of optimized machine learning models

The compressive strength and fresh properties of SCC were predicted in this section via four machine learning algorithms which include SVM, decision tree, random forest and ANN. The training of models was implemented in MATLAB and PYTHON 3.6, utilizing essential libraries such as Scikit-learn, NumPy, Pandas, Matplotlib, and Seaborn. In addition to proposing parameter optimization strategies, these strategies were diligently applied within this section. These tactics were intricately executed to fine-tune the performance of models, playing a crucial role in enhancing the quality of prediction outcomes.

5.3.1 Prediction of SVM model

As the SVM algorithm employs the Euclidean distance of the sample data, it is essential to standardize the input and output datasets to prevent data with larger values from dominating the model. Standardization involves transforming all data into a normal distribution with a mean value of 0 and a variance of 1, thereby ensuring a more balanced representation of the data within the algorithm. The selection of kernel function typically relies on domain-specific knowledge, as well as the number of samples and feature variables in the dataset (Sonebi et al. 2016). In this study, four commonly used kernel functions were investigated, encompassing Linear, Polynomial (Poly), Radial basis (RBF), and Sigmoid functions. Table 5.2 shows the performance of each kernel function for the corresponding output variables in different predictive models.

Table 5.2 Statistical results of initial SVM models with various kernel functions

Output variable	Kernel function	Statistical parameters		
		R^2	RMSE	MAE
Fcu	Linear SVM	0.634	12.480	10.002
	Poly SVM	0.636	12.452	9.322
	RBF SVM	0.860	7.721	5.847
	Sigmoid SVM	-24.609	104.447	72.941
SD	Linear SVM	0.578	35.601	28.937
	Poly SVM	0.636	33.078	26.263
	RBF SVM	0.733	28.320	21.918
	Sigmoid SVM	-6.533	150.389	111.121
VF	Linear SVM	0.810	1.352	1.064
	Poly SVM	0.444	2.314	1.908
	RBF SVM	0.860	1.162	0.990
	Sigmoid SVM	-1.149	4.549	3.769

To mitigate the impact of random grouping of training and testing datasets in programming, the random state was set to the optimal fixed value obtained by looping. As can be seen, the RBF kernel function performed the best for all output parameters, exhibiting the highest R^2 values and the lowest errors. Indeed, the R^2 values being less than 0.9, along with relatively high RMSE and MAE values, suggest that while the RBF kernel function outperforms the other kernel functions considered, there is still potential for enhancing the predictive capabilities of models. It should be noticed that the R^2 values for the sigmoid function obtained using Scikit-learn Library are less than zero in some models. This indicates that the prediction error of the fitted function is greater than that of a simple mean-value function (Nakagawa and Schielzeth 2013). In other words, the inferior performance of the sigmoid kernel function, when compared to a model that predicts only the average value of the output, indicates that it is not an appropriate choice for this specific problem domain. In summary, the effective RBF kernel was selected for the subsequent model optimization and performance evaluation.

There are two main factors that need to be set for the RBF kernel function which are parameters C and $gamma$. The selection of optimal parameters significantly affects the accuracy of an SVM model (Hsu et al. 2003; Cherkassky and Ma 2004). The cross-validation based grid search technique was utilized to find the optimal parameter pairs of C and $gamma$. The steps involved in this process are summarised as follows:

Step 1. Set $C \in [2^{-5}, 2^{15}]$ and $gamma \in [2^{-15}, 2^{3}]$. This range of values for C and $gamma$ provides a comprehensive search space to find the optimal parameters (Cherkassky and Ma 2004).

Step 2. Obtain a 20×18 coarse grid within the specific range of values for C and $gamma$.

Step 3. Perform five-fold cross-validation for the parameter pair corresponding to the first point in the grid and calculate five MAE values. Then, compute the average of these MAE values as the representative score for this particular point.

Step 4. Traverse all points in the grid and repeat Step 3 for each point to calculate the corresponding MAE values, identifying the best parameter pair that yields the lowest error.

The graphs of parameter optimization results are shown in Figure 5.3. After setting the optimal values of RBF kernel parameters, models were trained and tested using the same random states for data splitting and cross-validation.

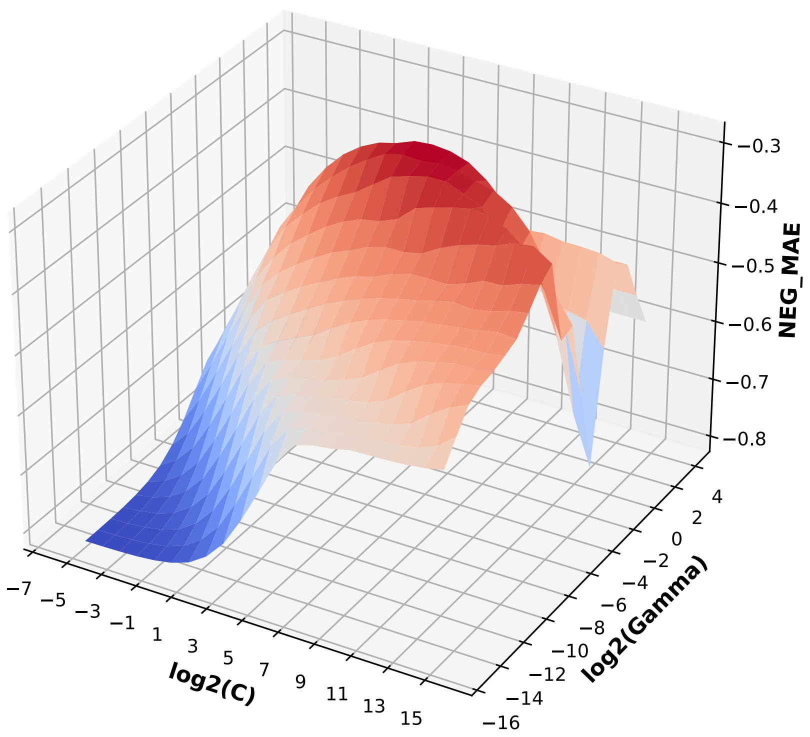

(a) Parameter pairs of Fcu

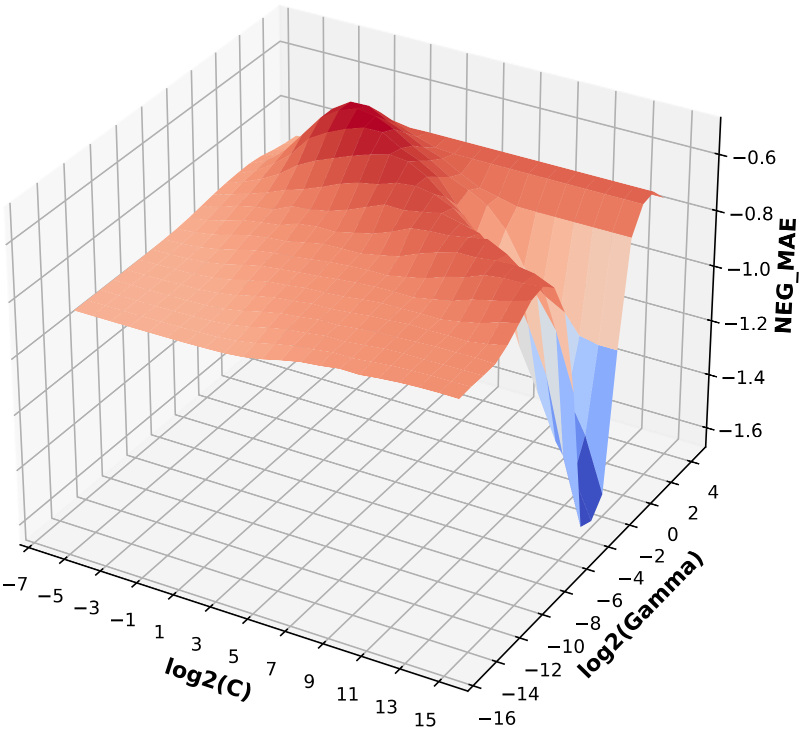

(b) Parameter pairs of SD

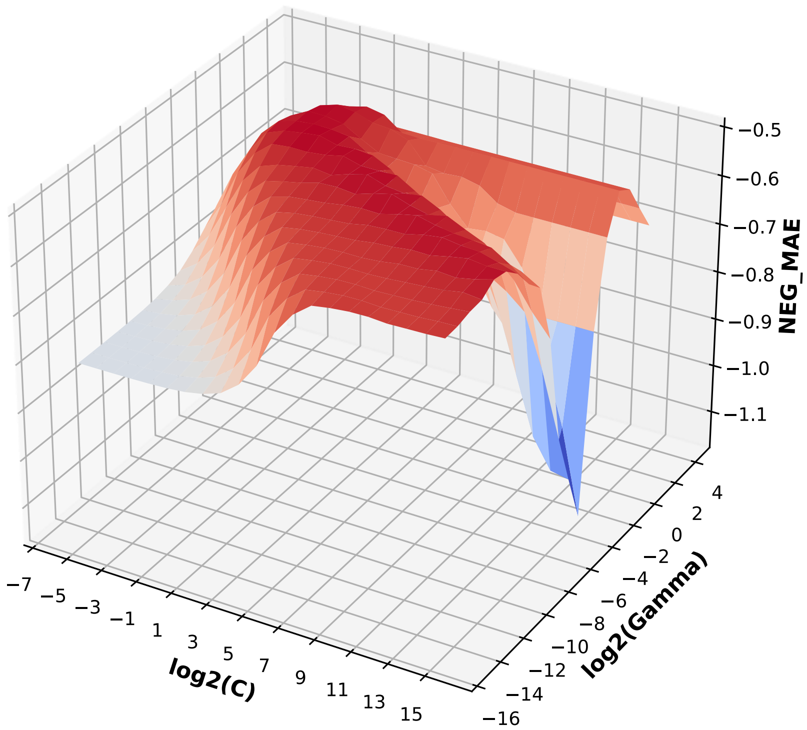

(c) Parameter pairs of VF

Figure 5.3 Negative MAE as a function of $log_2(C)$ and $log_2(gamma)$

Table 5.3 presents the best parameter pairs and performance of the developed SVM models for predicting the compressive strength, slump flow diameter and V-funnel time. It can be observed that the optimized SVM with selected kernel parameters showed highest accuracy in estimating compressive strength of SCC mixes. The average MAE value obtained during the parameter selection process was used to evaluate the performance of the models during the training phase. As determined by five-fold cross-validation, the values were 0.292, 0.495 and 0.476 for the models predicting compressive strength, slump flow diameter and V-funnel time, respectively.

Table 5.3 Kernel parameters and statistical results of developed SVM models

Output variable	RBF parameters selection			Statistical parameters of developed SVM		
	C	$gamma$	MAE	R^2	$RMSE$	MAE
Fcu	32	0.125	0.292	0.936	5.311	4.000
SD	4	0.125	0.495	0.831	25.153	19.498
VF	32	0.031	0.476	0.901	1.000	0.806

Figure 5.4 illustrates the performance of the developed SVM model in the prediction of fresh and hardened properties of SCC mixes (test set). As can be observed, generally the samples from testing datasets aligned well with the 1:1 line, with correlation coefficients of 0.968, 0.911, and 0.949, respectively. In addition, more details on the estimation accuracy of SVM models could be obtained by the statistical parameters given in Table 5.2 and Table 5.3. For instance, the R^2, $RMSE$ and MAE values of developed RBF-SVM models for compressive strength were 0.936, 5.311 and 4.000, respectively, while these parameters for initial RBF-SVM models were 0.860, 7.721 and 5.847, respectively. In this case, the MAE values assessed the performance of the models on the testing datasets. Furthermore, the R^2 values had increased by 8%, 13% and 1% due to the optimization using grid search. Consequently,

optimizing the kernel parameters lead to obtaining a more accurate SVM model for predicting the properties of SCC mixes, with a particular emphasis on the improvement in predicting the slump flow diameter.

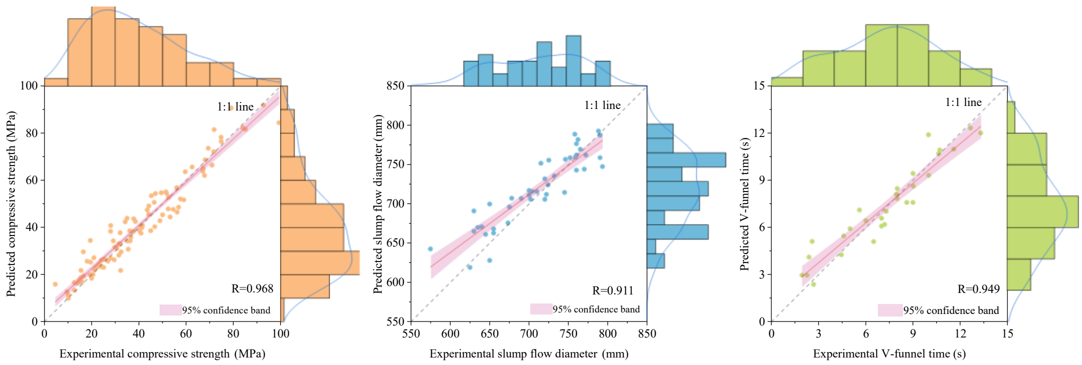

Figure 5.4 Correlation between the experimental and predicted values of SCC properties of SVM

5.3.2 Prediction of ANN model

To conduct an ANN model with good applicability, a MATLAB program was developed (R2021a). The networks with one hidden layer were chosen and Levenberg-Marquardt was defined as the training algorithm. All parameters for training ANN models are summarized in Table 5.4. The maximum training epoch and validation checking epoch were set to be twenty and six iterations, respectively. The calculation stopped when the error is smaller than 10^{-6}. The normalized datasets were split into three groups, with 80% for training and 20% for testing, maintaining the same scale as the testing dataset for previous algorithms.

In order to circumvent the issue of overfitting, this study carefully considered the number of neurons present within the hidden layer. A comprehensive exploration of models was conducted, wherein the number of nodes in the hidden layer was systematically varied from 5 to 15. The model's generalization capability and accuracy were assessed through the R^2 and $RMSE$ metrics, as derived from the testing datasets. The findings, as depicted in Figure 5.5, enabled the identification of optimal models, characterized by the highest R^2 values and the lowest $RMSE$s.

Table 5.4 Parameters selection and performance of ANN models

	Fcu	SD	VF
	Parameters		
Number of input variables	7	6	6
Number of the hidden layer		1	
Number of neurons in the hidden layer	10	10	8
Number of output variables		1	
Training function		Levenberg-Marquardt	
Transfer functions		Sigmoid for hidden layer	
Training epoch		20 iterations	
Training error		10^{-6}	
	Measurements		
R^2	0.927	0.694	0.783
$RMSE$	5.568	35.224	1.675
MAE	4.111	26.633	1.367

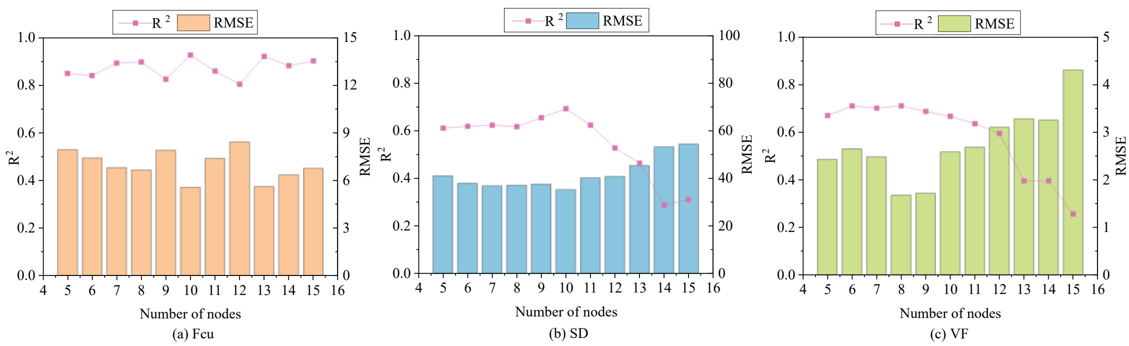

Figure 5.5 Accuracy and generalization of models versus the number of hidden layer nodes

The evaluation metrics for the selected models, featuring optimal hidden node numbers, are presented in Table 5.4. As can be seen, the proposed ANN model for the prediction of compressive strength had the highest accuracy, with R^2 of 0.927, in comparison with the prediction of slump flow and V-funnel time. However, the $RMSE$ and MSE values in the prediction of slump flow were significantly higher than others. As demonstrated in Figure 5.6, there were more scattered data points away from the line of equality between experimental and predicted slump flow results. The correlation coefficients for the output variables were 0.963, 0.833 and 0.885, respectively. In general, the output values predicted by ANN models showed significant correlations with experimental data and the network provided reasonable estimation accuracies.

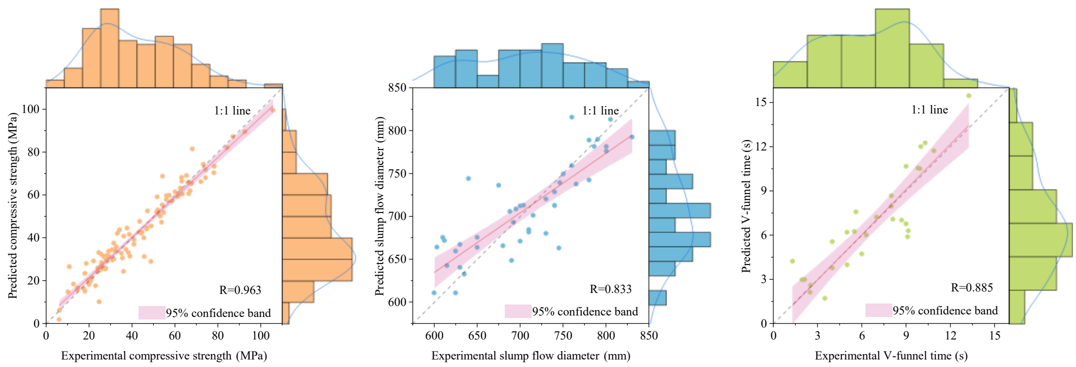

Figure 5.6 Correlation between the experimental and predicted values of SCC properties of ANN

5.3.3 Prediction of decision tree and random forest models

To improve the performance of regression models, it is of paramount importance to identify the optimal hyperparameter combinations for the decision trees and random forests. This chapter employed the Scikit-learn Library in Python to accomplish the parameter tuning. During this process, the training dataset was fed into the model, and grid search combined with five-fold cross-validation was utilized to continuously adjust the parameter combination. The objective is to obtain the maximum R^2 value, ultimately leading to the determination of the optimal parameter combinations.

Decision tree and random forest regressors included 11 and 17 parameters, respectively. This chapter focuses on selecting the primary parameters for each model that have the most significant influence on prediction accuracy. Taking both the processing time and performance of the algorithms into account, this paper provides several suitable values for the selected parameters. The value ranges and optimized values for each parameter of the two models are shown in Table 5.5. Subsequently, best parameter combinations were employed to construct the new models.

The comparison of original models and optimized models are given in Figure 5.7, where scores are represented by R^2 values. The "original score" refers to the R^2 values obtained from the default model settings before applying hyperparameter optimisation via grid search. The optimised scores correspond to the R^2 values achieved on the training and test datasets after tuning. The results indicate that the grid search has benefits on the prediction performance of both decision tree and random forest models.

Table 5.5 Selection of hyperparameters of decision tree and random forest from the grid search

Hyperparameters	Range	Tuned values of RF			Tuned values of DT		
		Fcu	SD	VF	Fcu	SD	VF
n_estimators	(100,150,200, 300,500)	100	100	100	-	-	-
max_depth	[10,20]	17	15	16	17	15	13
min_impurity_decrease	(0,0.001,0.01, 0.1,0.2)	0	0	0	0	0	0
min_samples_leaf	(1,2,5,8,10)	1	1	1	1	1	1
min_samples_split	(2,5,8,10)	2	2	2	2	2	2
random state	[1,1000]	332	83	623	1	6	10

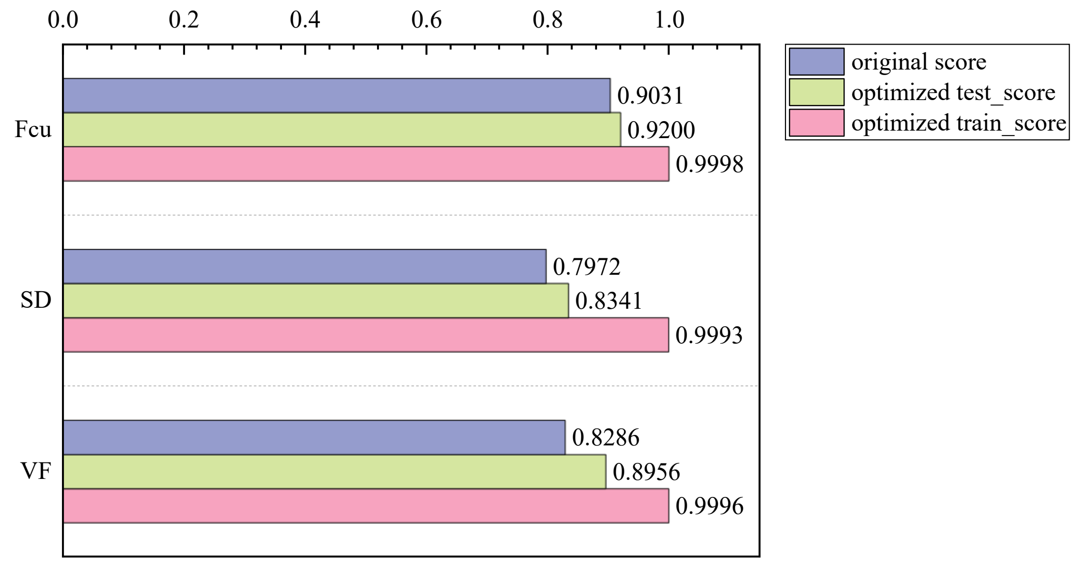

(a) DT

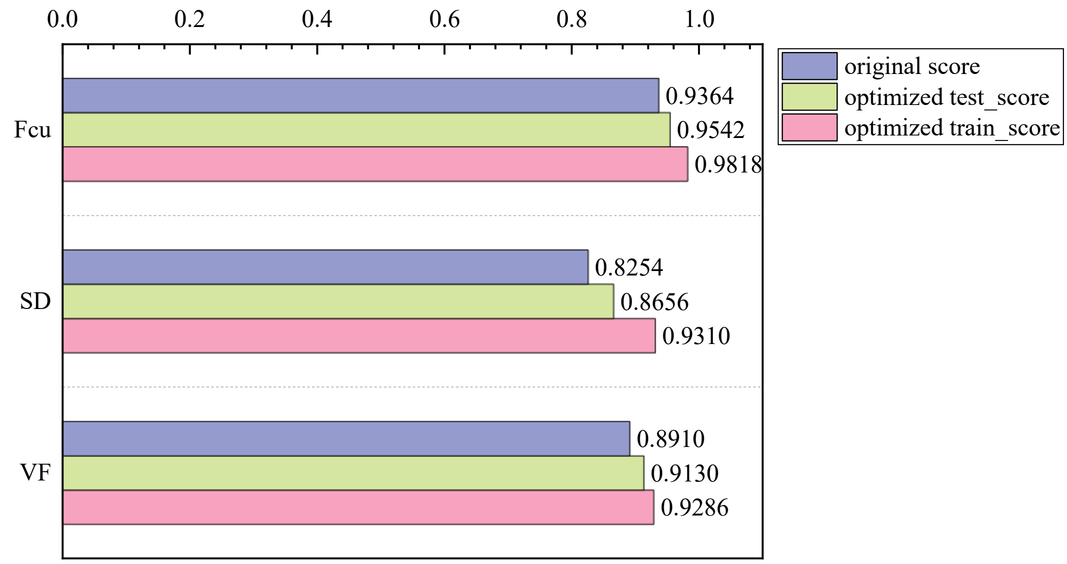

(b) RF

Figure 5.7 Comparison of R^2 scores before and after hyperparameter tuning for decision tree and random forest models

Figure 5.8 demonstrates the performance of the optimised decision tree and random forest models in predicting fresh and hardened properties of SCC mixes, using the correlation coefficient (R) on the test set. These R values correspond to the test set R^2 scores shown in Figure 5.7, providing an alternative measure of model performance. For the decision tree model, the correlation coefficients of experimental and predicted variables were 0.959, 0.913 and 0.946, respectively. The coefficients in the RF model were 0.977, 0.930 and 0.956, respectively. In general, the random forest models gave more accurate predictions for the testing dataset of the three output properties. By developing random forest models, the correlation coefficient of each output variable increased by 1.9%, 1.9% and 1.2%, respectively.

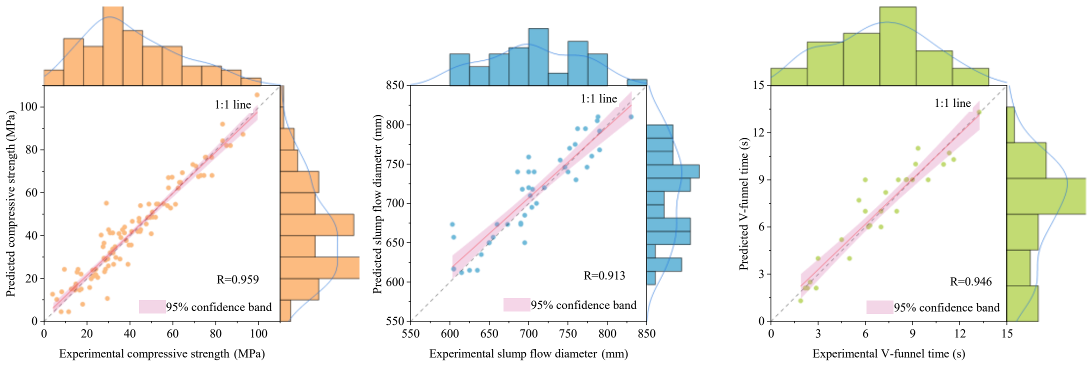

(a) DT

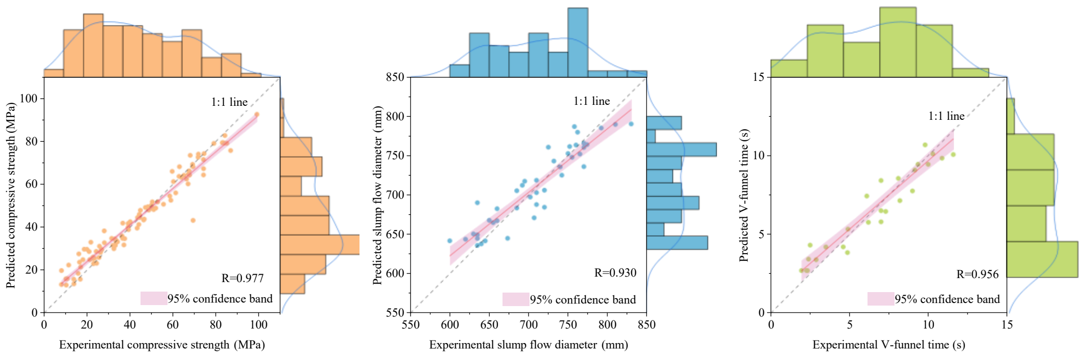

(b) RF

Figure 5.8 Correlation between the experimental and predicted values of SCC properties in decision tree and random forest models

5.4 Comparison of machine learning models

In this section, a comparative assessment of four machine learning algorithms in terms of predicting SCC properties is presented. The values of R^2, $RMSE$ and MAE and the dispersion degrees of the predicted result scatters were considered as the reasonable measures to judge the accuracy of the proposed models. In general, the machine learning models were able to predict all output variables in the test datasets with reasonable accuracy.

Table 5.6 shows a comprehensive comparison between the precision of four machine learning algorithms using the same testing datasets for each property. It can be clearly noticed that the proposed random forest models exhibited superior performance compared to the other algorithms for each SCC performance index, as evidenced by the R^2 values ranging from 0.8656 to 0.9542. In addition to the decision tree models, the proposed models behaved best in terms of predicting compressive strength, where the maximum R^2 was 0.9199. On the other hand, the slump flow spread diameter was more challenging to predict than the other two properties, as the minimum R^2 was 0.6938 achieved by ANN model. In case of all predicted characteristics, the values of $RMSE$ and MAE were relative higher in the prediction of the slump flow spread.

Table 5.6 Performance of tests metrics of various machine learning algorithms

Models	Characteristic	$\boldsymbol{R^2}$	$\boldsymbol{RMSE}$	$\boldsymbol{MAE}$
SVM	Fcu	0.9363	5.3107	3.9999
	SD	0.8306	25.1535	19.4980
	VF	0.9009	0.9997	0.8061
DT	Fcu	0.9199	6.2417	4.6440
	SD	0.8340	25.5630	19.4031
	VF	0.8956	1.0247	0.8014

RF	Fcu	0.9542	5.3037	3.7623
	SD	0.8656	21.1175	16.8765
	VF	0.9130	0.9154	0.7962
ANN	Fcu	0.9269	5.5678	4.1113
	SD	0.6938	35.2245	26.6335
	VF	0.7830	1.6751	1.3670

The REC curves for compressive strength, slump flow diameter, and V-funnel time predictions are shown in Figure 5.9. As described in the section 3.3.3, these curves help assess the cumulative distribution of prediction errors. In this chapter, the REC curves further illustrate the comparative accuracy of different machine learning models across varying error tolerances.

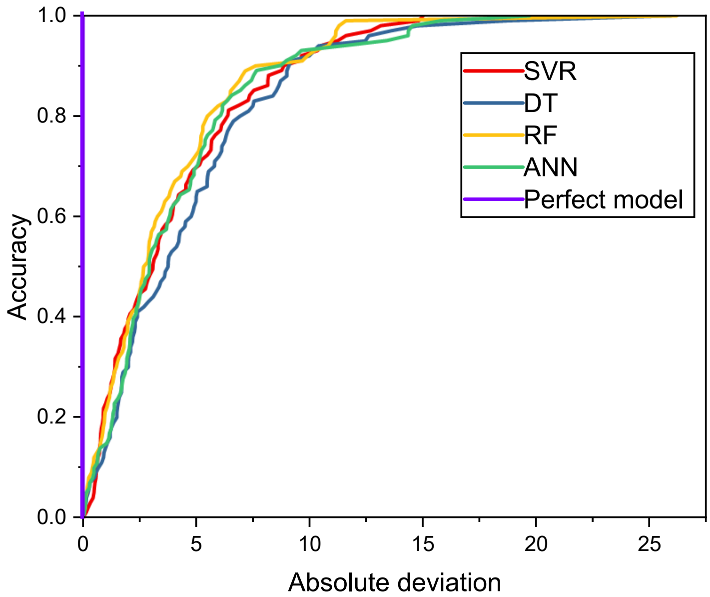

(a) Fcu

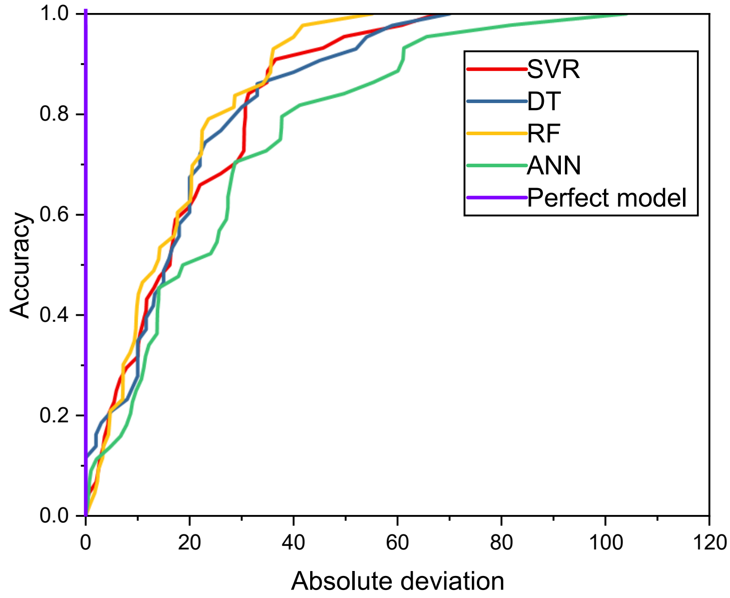

(b) SD

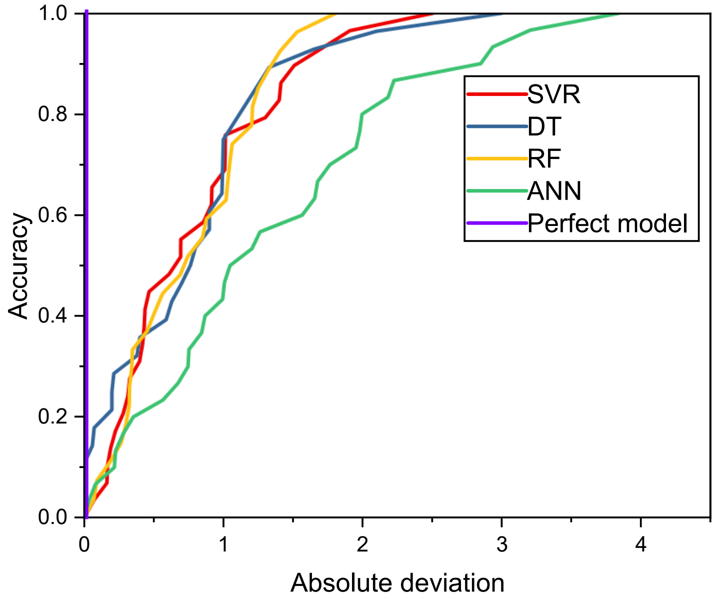

(c) VF

Figure 5.9 REC curves of tests metrics of various machine learning algorithms

The values of area over REC curves and the corresponding area ratios are given in Table 5.7. Overall, the area ratios of the prediction of compressive strength were on the lower side. Besides, the random forest models consistently achieved the lowest area ratios and therefore, appeared to be the best performing models for modelling SCC properties.

Table 5.7 The area over REC curves and area ratios of various machine learning algorithms

Properties	Absolute area				Area ratio (%)			
	SVM	DT	RF	ANN	SVM	DT	RF	ANN
Fcu	3.926	4.514	3.631	4.014	7.851	9.028	7.263	8.027
SD	18.729	18.589	16.236	25.451	20.810	20.655	18.040	28.279
VF	0.763	0.745	0.739	1.303	15.258	14.904	14.772	26.059

In addition to REC curves, the Taylor diagrams were also employed to compare the accuracy of the three parameters as shown in Figure 5.10. The plot measures the respective distance between each model and the reference point labelled as 'Ref'.

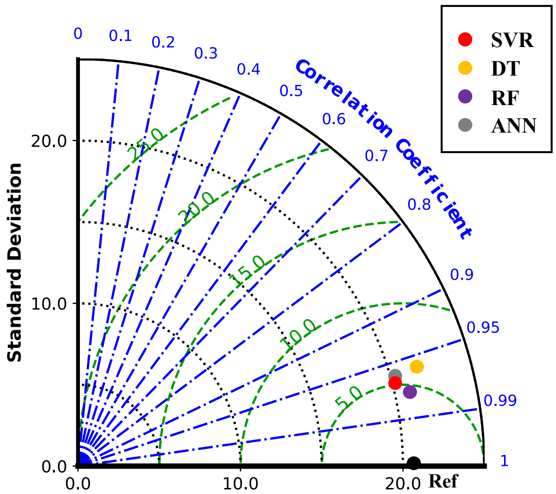

(a) Fcu

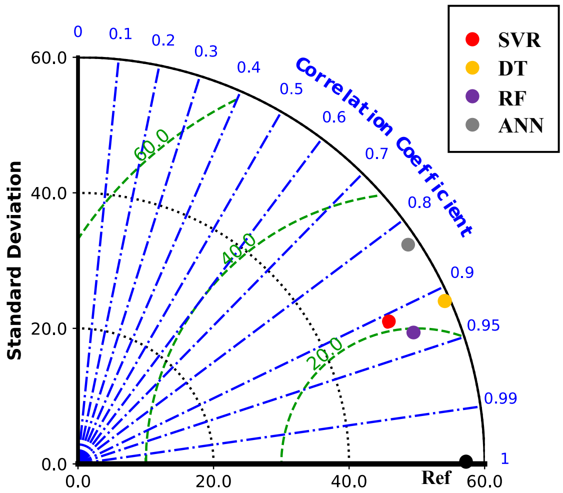

(b) SD

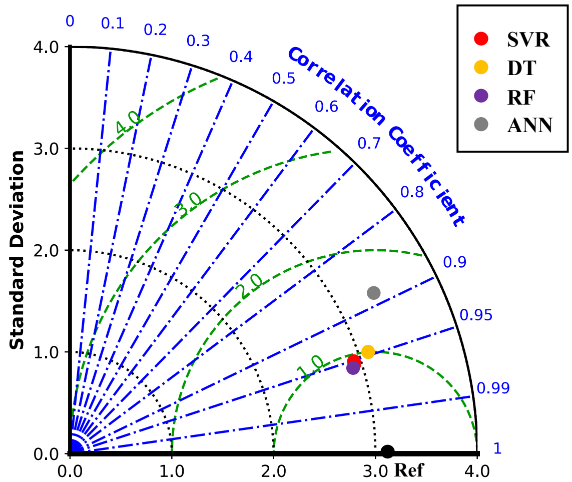

(c) VF

Figure 5.10 Taylor diagrams of different machine learning models for SCC prediction

Decision tree models showed the highest standard deviation in all predictions, indicating that the predicted values were more spread out from the mean value compared to the other models. The random forest models, which exhibited lower $RMSE$ values and higher correlation coefficient values, were found to be located closer to the true data points. This indicated that the random forest models appeared to be the best performing models for modelling SCC properties, which is fairly consistent with the previous discussion.

In summary, from the statistical analysis and the visual interpretation of predictive performance of four machine learning algorithms, the random forest models were proven to demonstrate the highest accuracy among all. This superior performance can be attributed to the ensemble learning characteristic of the random forest. This ensemble approach could enhance performance compared to individual models like the decision tree, helping reduce variance and the risk of overfitting (Kang et al. 2021). For instance, the training scores of decision tree for predicting all SCC properties are high, often exceeding 0.999, as shown in Figure 5.7. However, despite these high training scores, the accuracy of the decision tree models on the test datasets tends to be nearly 0.03 lower than that of the random forest models. Furthermore, random forest is less sensitive to outliers in the dataset than SVM and ANN, due to the method of aggregating the prediction from multiple trees (Dev et al. 2024). Moreover, random forest can effectively capture the nonlinear relationship between the compositions and properties of SCC (Zhang et al. 2019), while SVR and DT may struggle with the complex patterns. Additionally, when compared with SVM and ANN models, random forest models showed great potential due to the visual tree structure, which can be easily understood even by non-experts. Although the ANN models exhibited comparatively inferior performance relative to the other models, they still demonstrated a satisfactory level of accuracy.

The models proposed in this chapter were compared with others highlighted in the current literature, as illustrated in Figure 5.11. For the purposes of this comparison, the correlation coefficient (testing set only) was employed as the benchmark criterion. It is evident that all the models under investigation predict the compressive strength of SCC more accurately than its fresh properties. Notably, the algorithms formulated in this chapter outperformed the majority of the examined models, excelling particularly in predicting both compressive strength and flowability properties of SCC.

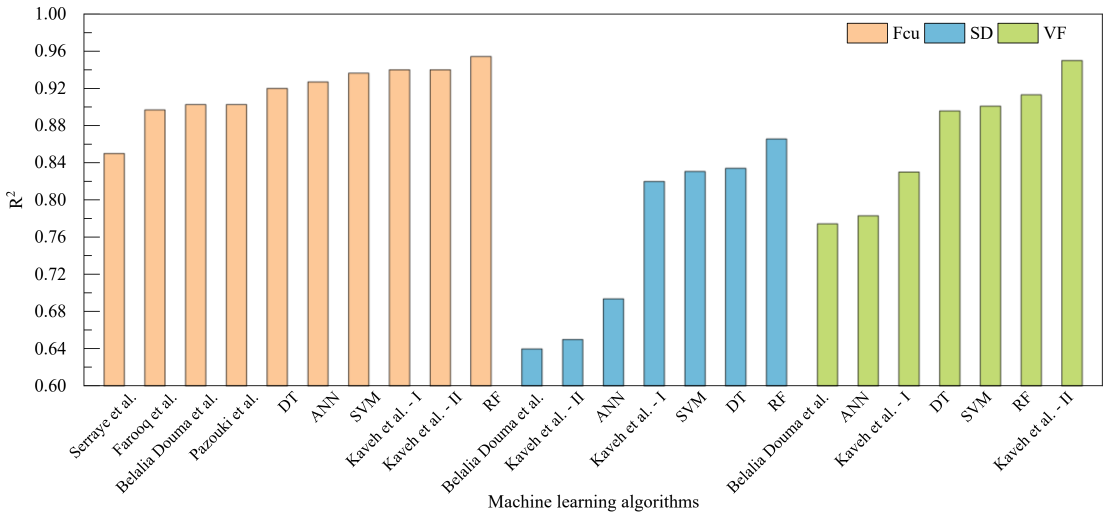

Figure 5.11 Comparative analysis of proposed models with existing literature

Comparing discussions on the V-funnel time prediction with those presented in the study of Kaveh et al. (2018), despite the comparatively lower R^2 value observed on the test set, the smaller RMSE (0.915<1.11) suggests a heightened precision in predictions. Conversely, on the overall dataset, a higher R^2 value (0.926>0.87) exhibited in the proposed RF model, indicating a superior capacity for explicating variance in the entirety of the data and adeptly accommodating diverse subsets of data. Nonetheless, considering that no model can flawlessly predict SCC properties, there remains potential for further enhancement on the dataset collection and algorithmic approaches.

It should be noted that the dataset used in this study is different from those adopted in the referenced machine learning studies (Belalia Douma et al. 2017; Kaveh et al. 2018; Farooq et al. 2021; Pazouki et al. 2021; Serraye et al. 2021). Therefore, the comparison is not based on identical dataset but rather on performance indicators (e.g., R^2 values) reported in the respective studies. While such comparisons offer a general sense of model capability, they must be interpreted with caution due to differences in dataset characteristics, such as the number of mixes, data diversity, and feature ranges. Furthermore, in this chapter, a data preprocessing step involving outlier removal and variable selection was employed to enhance model robustness. This may also contribute to the improved predictive performance of the proposed models. This issue is further addressed in Section 5.7 as part of the model limitations and assumptions.

5.5 Feature importance of influencing variables

After conducting a comparison of the predictive performance of all algorithms, the random forest models with optimal hyperparameters were obtained. In conjunction with the SCC characteristics, six features were used for predicting fresh properties, and seven features were employed for predicting compressive strength in the random forest models. Figure 5.12 and Figure 5.13 display the importance of each input variable for the regression models based on the method of SHAP analysis. As a game theory-based approach, in SHAP, the output model is structured as a linear combination of the input variables, determining the contributions of each input variable to every prediction (Wu and Zhou 2022).

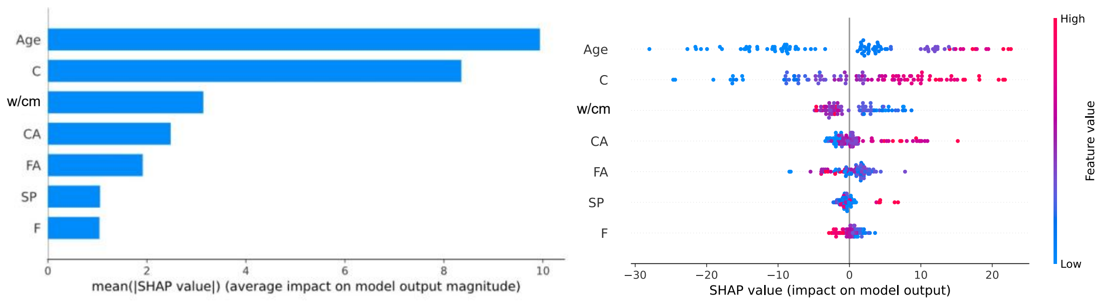

Figure 5.12 Feature importance and SHAP summary plot using RF models for predicting Fcu

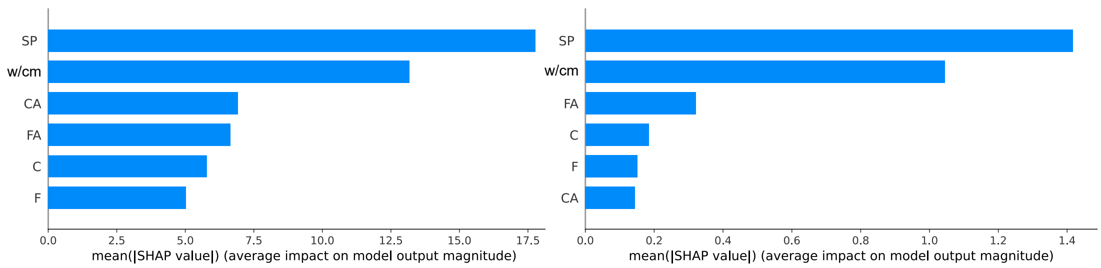

Figure 5.13 Feature importance plot using RF models for predicting SD and VF

In Figure 5.12, it is revealed that curing age, the content of cement and w/cm ratio are the most sensitive factors dominating the compressive strength of SCC mixes, with the mean absolute SHAP value of 9.94, 8.35 and 3.14, respectively. This result is in agreement with the findings of previous studies (Nikbin et al. 2014; Farooq et al. 2021; Huang et al. 2023b). In contrast, the SHAP value of fly ash is 1.04, indicating that the influence of fly ash is relatively less significant. This is because, relatively low chemical activity and hydration rate of fly ash make it less effective than cement in enhancing the early strength of concrete (Bulut and Şahin 2022). Similarly, the dosage of SP contributes less to SCC strength, with the SHAP value of 1.05. Conversely, it has the highest influence on predicting the fresh properties of SCC, as shown in Figure 5.13. This suggests that the impact of SP on enhancing the workability of concrete is greater than its direct contribution to strength (Zeyad and Almalki 2020).

The SHAP summary plot is also shown in Figure 5.12, with the x-axis representing the weight of influence, and the colour of scatter points indicating the impact degree of input variables on the predicted properties (Huang et al. 2023b). Therefore, a wider regional distribution signifies a greater influence of this variable. It can be observed that the compressive strength of SCC significantly increases with the progression of curing age, higher cement content, and more aggregates. However, a higher water to binder ratio results in a negative SHAP value, indicating a lower compressive strength of SCC. This finding is consistent with published literatures (Kannan 2018; Benaicha et al. 2019b; Devi et al. 2020). Additionally, the impact of fly ash is opposite to that of cement; an increase in fly ash content decreases SCC compressive strength, as observed in existing experimental investigations (Khodair and Bommareddy 2017; Concha and Baccay 2020; Guo et al. 2020b). Besides, the influence of SP dosage is not as pronounced.

Figure 5.13 illustrates the feature importance of six input parameters in predicting SCC fresh properties, as evaluated by mean absolute SHAP values.

Following the most influential parameter, SP, w/cm ratio exhibits a strong impact on both slump flow diameter and V-funnel time. The significant effect can be observed in existing studies (Türkel and Kandemir 2010; Mardani-Aghabaglou et al. 2013; Al-Jaberi 2019; Xie et al. 2021). As a main ingredient in SCC, the aggregate content is demonstrated to have considerable effect on the slump flow diameter, as evident in published studies (Sahraoui and Bouziani 2019). Compared to other main factors, the content of cement and fly ash has less impact on fresh properties. The flow behaviour of SCC is the result of SP-cement interaction and can be modified by adding cementitious materials such as fly ash. Fly ash promotes the adsorption of SP on cement particles, which depends on the concentration of C_3A cement phase and the amount of gypsum in the system (Almuwbber et al. 2018). Although both cement and fly ash contribute to the enhancement of microstructure and workability of SCC, their effects in the fresh state are not as pronounced as those of water and chemical additives. It is worth noting that the feature importance analysed in this chapter are based on the specific dataset used. Thus, the results could be more representative with the expansion of dataset and the inclusion of more variables.

5.6 Potential applications of the proposed framework

The design codes of SCC mixes typically rely on the conventional strength-based mix design methodologies used for normal vibrated concrete (Ashish and Verma 2019). Studies in the past have also suggested reliable SCC mix design tactics that consider both strength and plastic viscosity (Abo Dhaheer et al. 2016). However, the designed characteristics of SCC mixes might be subjected to several constraints because of the additional restrictions on the mixture contents, such as maximum value of w/cm ratio and the aggregate contents. Furthermore, the synergistic effect of fly ash and other supplementary materials significantly impacts the properties of SCC, posing a great challenge to the conventional proportioning approach. In response to evolving design prerequisites, there has been a growing demand for a precise and sustainable SCC design and validation framework in the construction industry. Consequently, this section proposes the development of a data driven machine learning framework.

It has been proven in the previous discussion that the optimized machine learning models can accurately predict both fresh and hardened properties of SCC containing fly ash. These models could serve as a pre-experimental validation tool to ensure workload optimization, thus providing robust experimental support. Moreover, the efficacy of this framework can be further enhanced with other SCC proportioning methods by dynamically modulating the dosage of each ingredient in line with predictive outcomes.

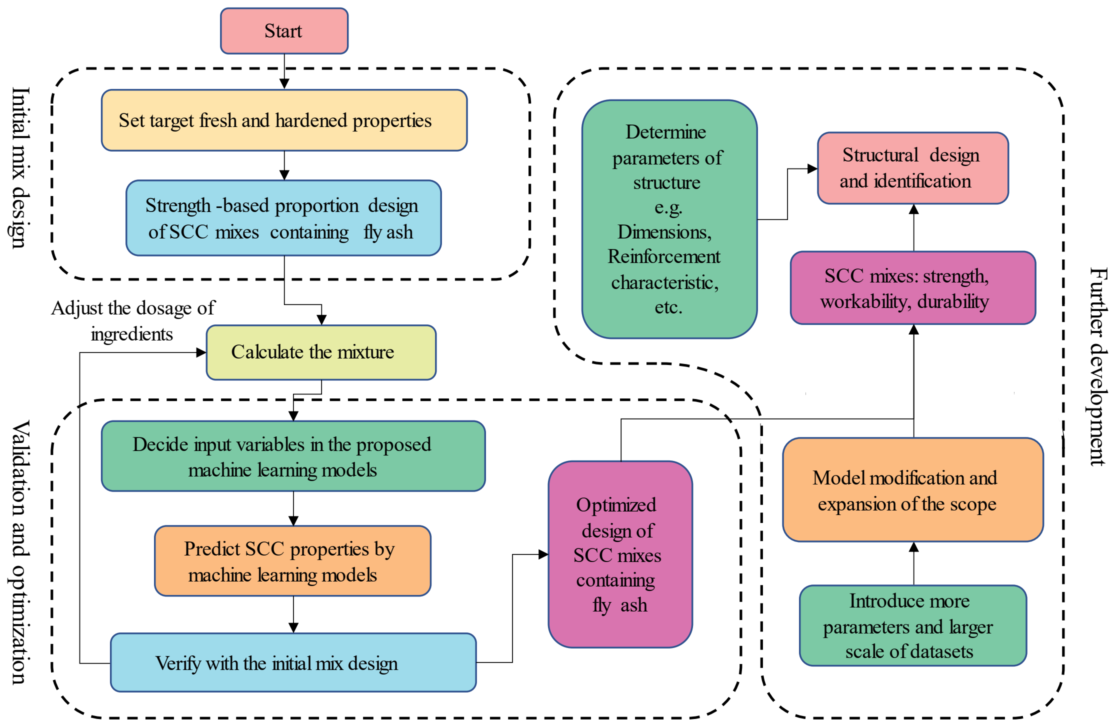

Figure 5.14 The application framework of the proposed data driven models and further development

The execution of this framework, along with its further development, is depicted in Figure 5.14. Initially, the target properties of SCC with fly ash are determined, followed by the calculation of the preliminary proportions based on strength-based mix design methods. These mix proportions are then input into the finely tuned machine learning models to predict SCC properties. By verifying and contrasting with the initial mix design, the dosage of each ingredient is adjusted to a suitable range, resulting in an optimized mix design. To further develop the data driven framework, it is recommended to incorporate larger datasets and more specific variables for model modification and broadening the applicability. Moreover, by considering the structure related parameters and the output from the proposed machine learning models, a more complex framework for structural design and identification could be developed.

5.7 Limitations of this research

The discussion on the development and comparative analysis of various predictive models has been carried out, demonstrating the effectiveness of the RF model in predicting the properties of SCC. While these findings are significant, it is important to acknowledge certain limitations present within this chapter. All machine learning models were developed and optimized based on comprehensive datasets derived from a significant portion of existing literature about SCC with fly ash. However, the overall size of datasets remains relatively limited. This constraint may affect the generalizability of the models across different SCC mixes.

Additionally, while this chapter considers several critical factors affecting SCC properties, there remains room to include additional variables that might further influence the behaviour of SCC. A more detailed categorization of input variables, based on the characteristics of materials, was not fully explored in current analysis. For instance, factors such as the strength grade of cement, the size of aggregates, and the specific chemical composition of supplementary materials were not thoroughly classified. This limitation could potentially impact the accuracy of developed models. To achieve a balance between the breadth of datasets and the practical constraints, further research involving more experiments could be taken, ultimately enhancing the robustness of the findings.

Furthermore, this chapter employed a limited selection of four machine learning algorithms. Although these models were proven effectiveness in similar applications, the exclusion of other algorithms may limit the scope of the finding.

It should be noted that the performance comparison with literature was based on independently developed datasets, rather than a unified dataset across all models. Therefore, differences in data sources, preprocessing approaches, and variable definitions may have influenced the results. While the comparison provides a general indication on the competitiveness of the proposed models, the inconsistency in datasets limits the direct comparability of performance.

5.8 Conclusion

In this chapter, four machine learning algorithms, including SVM, decision tree, random forest and ANN were employed to predict both fresh and hardened properties of SCC mixes with fly ash. All models demonstrated the potential to predict these properties with reasonable accuracy. The specific findings of this chapter are outlined below:

- Various hyperparameter optimization strategies are examined in detail, with the efficacy of various algorithms subjected to comparative evaluation. These include the choice of kernel functions and grid search techniques in SVM modelling, the determination of key parameters in decision tree and random forest modelling, and the selection process for hidden nodes in ANN modelling.
- The random forest models exhibited the highest accuracy in predicting all SCC properties, as indicated by the high R^2 values of 0.9542, 0.8656 and 0.9130 for compressive strength, slump flow diameter and V-funnel time, respectively. Meanwhile, decision tree, SVM and ANN models also showed

promising results.

- The content of cement, curing age, and w/cm ratio were found to be the main factors influencing the compressive strength of SCC mixes, which is consistent with previous findings.
- The feature importance analysis indicated that the content of superplasticizers, w/cm ratio, and aggregate were the most influential factors on the fresh properties of SCC mixes.
- The REC curves and Taylor diagrams were utilized to compare the performance of all machine learning algorithms used. The random forest models consistently showed the lowest area ratios and smallest distance to the observation point in Taylor diagrams, indicating the highest level of accuracy among the four models.
- The models proposed in this chapter were compared with others highlighted in the current literature. The algorithms formulated in this chapter outperformed the majority of the examined models.
- The proposed machine learning models, particularly the random forest models, can provide valuable insights for designing and optimizing SCC mixes containing fly ash, which can ultimately lead to more sustainable construction practices.
- A framework of the proposed data driven approach has been constructed, showcasing significant promise in its practical application. The accuracy of this newly-established structure has been evaluated, focusing on its ability and accuracy in predicting the fresh and hardened properties of SCC.

While the use of three extensive and reliable datasets contributed to accurate predictions of SCC properties containing fly ash, there is potential for further model improvement through the inclusion of additional variables and larger datasets. More efficient ensemble machine learning algorithms can be developed to accelerate the process of parameter tuning and selection. In addition, by leveraging the inherent adaptive learning capabilities of reinforcement learning techniques, the accuracy and efficiency of models are expected to be further enhanced in the application of SCC properties. Meanwhile, the development of models to predict other properties of SCC and soundness of produced structures are recommended for future research.

Chapter 6 Ensembled machine learning modelling on mechanical properties of steel fibre reinforced SCC

6.1 Introduction

The inclusion of steel fibres in SCC has become increasingly important in modern construction. Steel fibres provide crucial benefits, such as enhancing the tensile strength, toughness, and crack resistance of concrete, making steel fibre reinforced self-compacting concrete (SFRSCC) a valuable material for applications requiring high durability and structural performance (Akcay and Tasdemir 2012; Alrawashdeh and Eren 2022; Liu et al. 2023). However, the addition of fibres introduces significant complexity to the mix design, as the fibre content, aspect ratio, and distribution within the matrix influence the mechanical properties in complex and nonlinear ways.

Traditional machine learning models have demonstrated effectiveness in predicting SCC properties by learning complex patterns and capturing nonlinear relationships from large datasets. In the previous chapter, these models have been successfully applied to SCC due to their ability to handle multifactorial relationships among numerous mix components (Cui et al. 2024b). However, the unique properties and interactions introduced by steel fibres require more advanced modelling techniques to accurately capture their influence on the mechanical behaviour of SFRSCC. To address these complexities, ensemble methods combine the strengths of multiple models to improve prediction accuracy and generalization capabilities. By aggregating the results of individual models, ensemble techniques reduce overfitting and enhance the model’s robustness in handling the complex relationship between SFRSCC components and properties. Unlike chapter 5, which explored the general optimization of SCC properties and fresh and hardened behaviours using large datasets, this chapter employs ensemble machine learning techniques to address the nonlinear and multifactorial interactions introduced by steel fibres.

Figure 6.1 illustrates the framework for developing models to predict the properties of SFRSCC. (1) The process begins with data scaling to standardize the input features, followed by data splitting to create training and testing sets. The selected input variables are chosen to encompass a comprehensive range of information relevant to the prediction of SFRSCC properties. (2) Traditional machine learning models are trained and optimized using support vector machine (SVM), decision tree (DT), and artificial neural network (ANN). (3) For improved accuracy, ensemble models, including random forest (RF), gradient boosted decision trees (GBDT), XGBoost, and LightGBM, are developed and fine-tuned to enhance model robustness. (4) Performance of all models are evaluated and compared by employing radar charts and error analysis. (5) The best performed models are selected for feature importance analysis, allowing for an in-depth investigation of the influence of individual SFRSCC components.

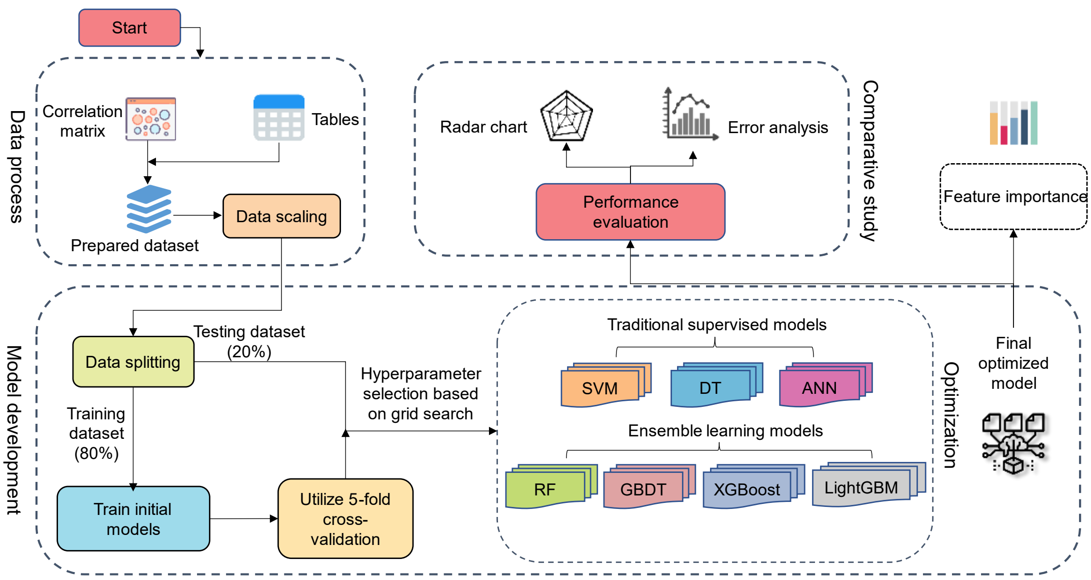

Figure 6.1 Flowchart of the presented data driven framework for the prediction of the SFRSCC properties

6.2 Data process and methodology

6.2.1 Dataset description

This chapter develops separate predictive models for the mechanical properties of SFRSCC, specifically targeting compressive strength, tensile strength, and flexural strength. The dataset, compiled from previous literature (AL-Ameeri 2013; Pająk and Ponikiewski 2013; Yardimci et al. 2014; Madandoust et al. 2015; Mashhadban et al. 2016; Siddique et al. 2016; Zeyad et al. 2018; Alabduljabbar et al. 2019; Ghasemi et al. 2019; Sulthan and Saloma 2019; Ganta et al. 2020; Sanjeev and Sai Nitesh 2020; Ouedraogo et al. 2021; Öz et al. 2021; Turk et al. 2022), includes 233 samples for compressive strength (Fcu), 193 samples for tensile strength (Fts), and 137 samples for flexural strength (Ff). Each sample represents a distinct SFRSCC mix with corresponding mechanical property measurements. To ensure consistency and minimize variability due to fibre type, the dataset is restricted to mixes reinforced solely with 2D hooked-end steel fibres.

The input variables for the model were selected based on their demonstrated impact on SFRSCC mechanical properties. As a result, the dataset incorporates nine input variables, covering both material composition and fibre properties. These variables include cement content, water to cementitious material ratio, limestone powder, fly ash, sand to aggregate ratio, maximum size of coarse aggregate, superplasticizer content, as well as steel fibre volume fraction and aspect ratio. Curing age is also included as an input variable to account for the influence of hydration on mechanical performance. The relationships representing the SFRSCC properties are formulated through the following equations:

$$Fcu, (MPa) = f_1\left(C, w/cm, LP, F, \frac{S}{A}, maxCA, SP, VF, AR, Age\right) \quad (6.1)$$

$$Fts, (MPa) = f_2\left(C, w/cm, LP, F, \frac{S}{A}, maxCA, SP, VF, AR, Age\right) \quad (6.2)$$

$$Ff, (MPa) = f_3\left(C, w/cm, LP, F, \frac{S}{A}, maxCA, SP, VF, AR, Age\right) \quad (6.3)$$

Table 6.1 Statistical analysis of SFRSCC datasets

Variables	Symbol	Unit	Min	Max	Mean	SD	Count
Cement	C	kg/m^3	290	600	437	64	233
Water to cementitious material ratio	w/cm	-	0.23	0.51	0.36	0.04	233
Limestone powder	LP	kg/m^3	0	289	75	71	233
Fly ash	F	kg/m^3	0	250	47	74	233
Sand to aggregate ratio	S/A	-	0.29	0.42	0.37	0.02	233
Maximum size of CA	maxCA	mm	8	20	14	4	233
Superplasticizer	SP	kg/m^3	2.60	17.00	5.72	3.18	233
Volume fraction	VF	%	0.00	2.00	0.61	0.49	233
Aspect ratio	AR	-	26.00	100.00	63.89	14.41	233
Curing age	Age	days	7	90	37	27	233
Compressive strength	Fcu	MPa	20.04	98.20	42.17	18.06	233
Tensile strength	Fts	MPa	1.25	10.85	4.31	1.56	193
Flexural strength	Ff	MPa	1.96	13.90	6.42	2.70	137

A statistical summary of these variables, including mean values, standard deviations, and ranges, is provided in Table 6.1. In terms of mechanical properties, compressive strength shows a wide range from 20.04 to 98.20 MPa, with a mean of 42.17 MPa, highlighting the dataset's diversity in strength performance. Tensile strength and flexural strength also exhibit substantial variability, with mean values of 4.31 MPa and 6.42 MPa, respectively, indicating the distinct mechanical behaviour captured for different SFRSCC mixes. The datasets for compressive strength (Fcu), tensile strength (Fts), and flexural strength (Ff) are partially overlapping. Among the total data collected, compressive strength represents the largest subset (233 mixes), followed by tensile strength (193 mixes) and flexural strength (137 mixes). However, not every mix includes all three mechanical properties, as different studies reported varying sets of results.

To further understand the relationships among variables, a correlation matrix (presented as a heatmap in Figure 6.2) was generated. Limestone Powder shows a negative correlation with compressive strength (-0.544), suggesting that an increase in limestone powder may reduce compressive strength. This could be due to dilution effects or a reduction in binder content. Additionally, the aspect ratio and volume fraction of steel fibres exhibit strong positive correlations with both tensile strength and flexural strength, indicating the crucial role of fibre characteristics in enhancing these strengths.

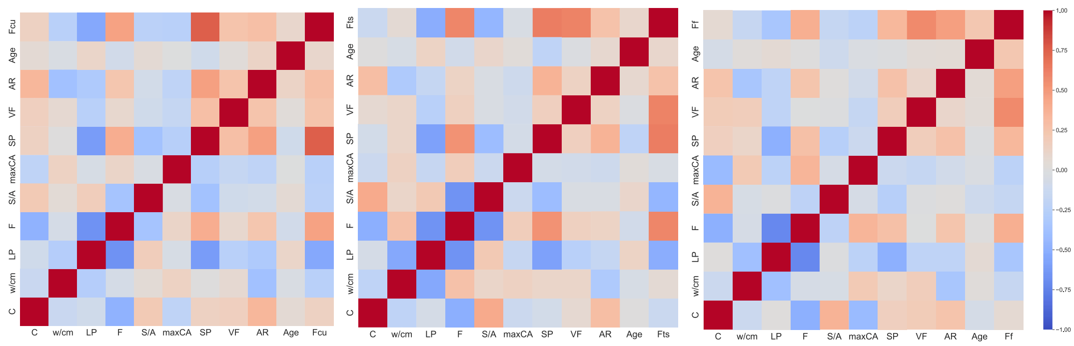

Figure 6.2 Correlation matrix of datasets (a) Compressive strength, (b) Tensile strength, (c) Flexural strength

Before building the machine learning models, the dataset was randomly split into two groups, with 80% of the data used for training and the remaining 20% reserved for testing. Given the varying units and ranges of the variables, the data were standardized to follow a standard normal distribution. This transformation was performed using the Standard Scaler function from scikit-learn to ensure consistency across features.

6.2.2 Models and hyperparameter settings

This chapter develops a range of machine learning models to predict the mechanical properties of SCC. The models include traditional supervised learning approaches, such as SVM, ANN, and DT, as well as advanced ensemble methods like RF, GBDT, XGBoost, and LightGBM. The underlying principles of these models were covered in chapter 3. They have been chosen to capture the complex relationships within the SFRSCC dataset, with a particular emphasis on enhancing prediction robustness and generalization.

Table 6.2 Selection of hyperparameters for machine learning models

Model	Search space of hyperparameters	Selected value		
		Fcu	Fts	Ff
SVM	$C \in [2^{-5}, 2^{15}]$	32	8	256
	$gamma \in [2^{-15}, 2^{3}]$	0.0625	0.0625	0.125
	kernel function = [Linear, RBF, Poly, Sigmoid]	RBF		
ANN	neurons in the hidden layer $\in$ [5,15]	5	8	6
	training algorithm = [Bayesian regularization, Scaled conjugate gradients, Levenberg-Marquardt]	Levenberg-Marquardt		
	transfer function = [ReLU, Sigmoid, Tanh]	Sigmoid		
DT	max_depth $\in$ [5,20]	10	10	8
	min_impurity_decrease = [0,0.001,0.01,0.1,0.2]	0		
	min_samples_leaf = [1,2,3,5,8,10]	3	3	1
	min_samples_split = [2,5,8,10]	2	2	5
RF	n_estimators = [100,150,200,300,500]	150		
	max_depth $\in$ [5,20]	10		
	min_impurity_decrease = [0,0.001,0.01,0.1,0.2]	0		
	min_samples_leaf = [1,2,3,5,8,10]	1		
	min_samples_split = [2,5,8,10]	2		

GBDT	learning_rate = [0.01, 0.05, 0.1, 0.2]	0.2	0.05	0.2
	max_depth = [3, 5, 7, 10]	5	3	5
	min_samples_leaf = [1, 2, 5, 10]	5	1	10
	min_samples_split = [2, 5, 10]	5	2	5
	n_estimators = [50, 100, 200, 300]	100	300	50
XGBoost	colsample_bytree = [0.6, 0.8, 1.0]		0.8	
	learning_rate = [0.01, 0.05, 0.1, 0.2]		0.1	
	max_depth = [3, 5, 7, 10]		3	
	n_estimators = [100, 200, 300]		150	
	subsample = [0.6, 0.8, 1.0]		0.8	
LightGBM	learning_rate = [0.01, 0.05, 0.1, 0.2]		0.2	
	max_depth = [3, 5, 7, 10]		5	
	n_estimators = [100, 200, 300]		300	
	num_leaves = [20, 30, 40]	20	20	40
	subsample = [0.6, 0.8, 1.0]	0.6	0.6	0.8
	feature_fraction = [0.6, 0.8, 1.0]		1	

To optimize the performance of the machine learning models, careful selection of hyperparameters is essential. Hyperparameters directly influence the model's ability to learn patterns within the data and can significantly impact prediction accuracy, particularly when dealing with complex relationships as seen in the mechanical properties of SFRSCC. Table 6.2 provides an overview of the search space for each model's hyperparameters, as well as the final selected values determined by grid search and five-fold cross validation. For each model, key hyperparameters were adjusted, such as the C and gamma values for SVM, the number of neurons and training algorithm for the ANN, and the maximum depth and minimum samples for DT. For ensemble methods like RF, GBDT, XGBoost, and LightGBM, parameters such as the number of estimators, learning rate, and depth were fine-tuned to maximize performance across target properties.

6.3 Performance of traditional supervised learning models

This section examines the performance of the traditional supervised machine learning models developed to predict the compressive strength, tensile strength and flexural strengths of SFRSCC, using optimized SVM, ANN and DT models. The predictive accuracy of each model was evaluated by comparing their results with experimental data, allowing for an effectiveness assessment of each algorithm.

The performance of the SVM model for predicting SFRSCC properties was optimized by selecting the best combination of hyperparameters C and gamma through a grid search. As shown in Figure 6.3, contour plots illustrate the negative MAE values across a range of C and gamma values (both expressed in log scale). The optimal regions, highlighted in yellow, indicate parameter combinations yielding minimal prediction errors for strength.

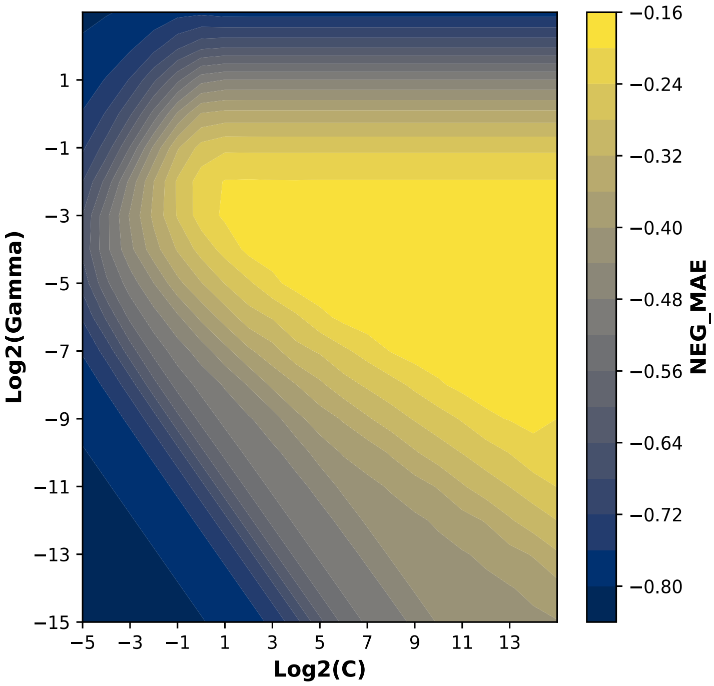

(a)

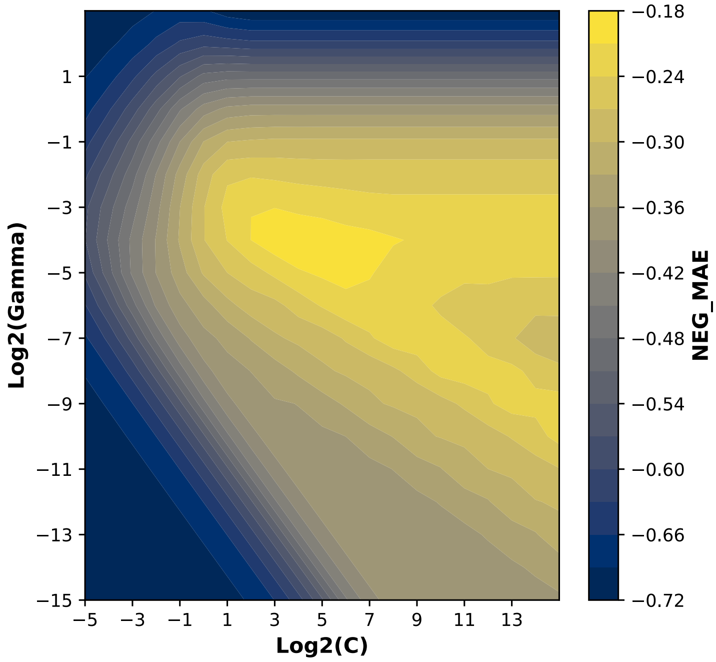

(b)

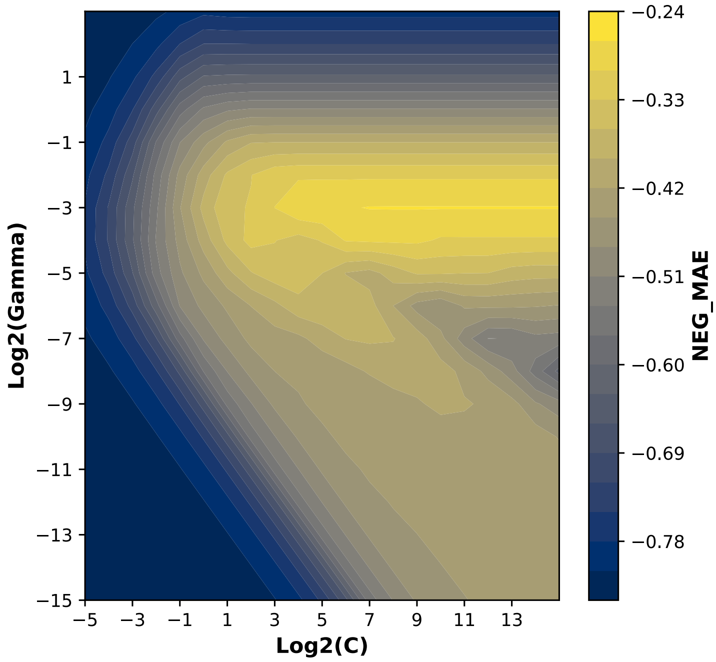

(c)

Figure 6.3 Selection of C and gamma based on grid search (a) Compressive strength, (b) Tensile strength, (c) Flexural strength

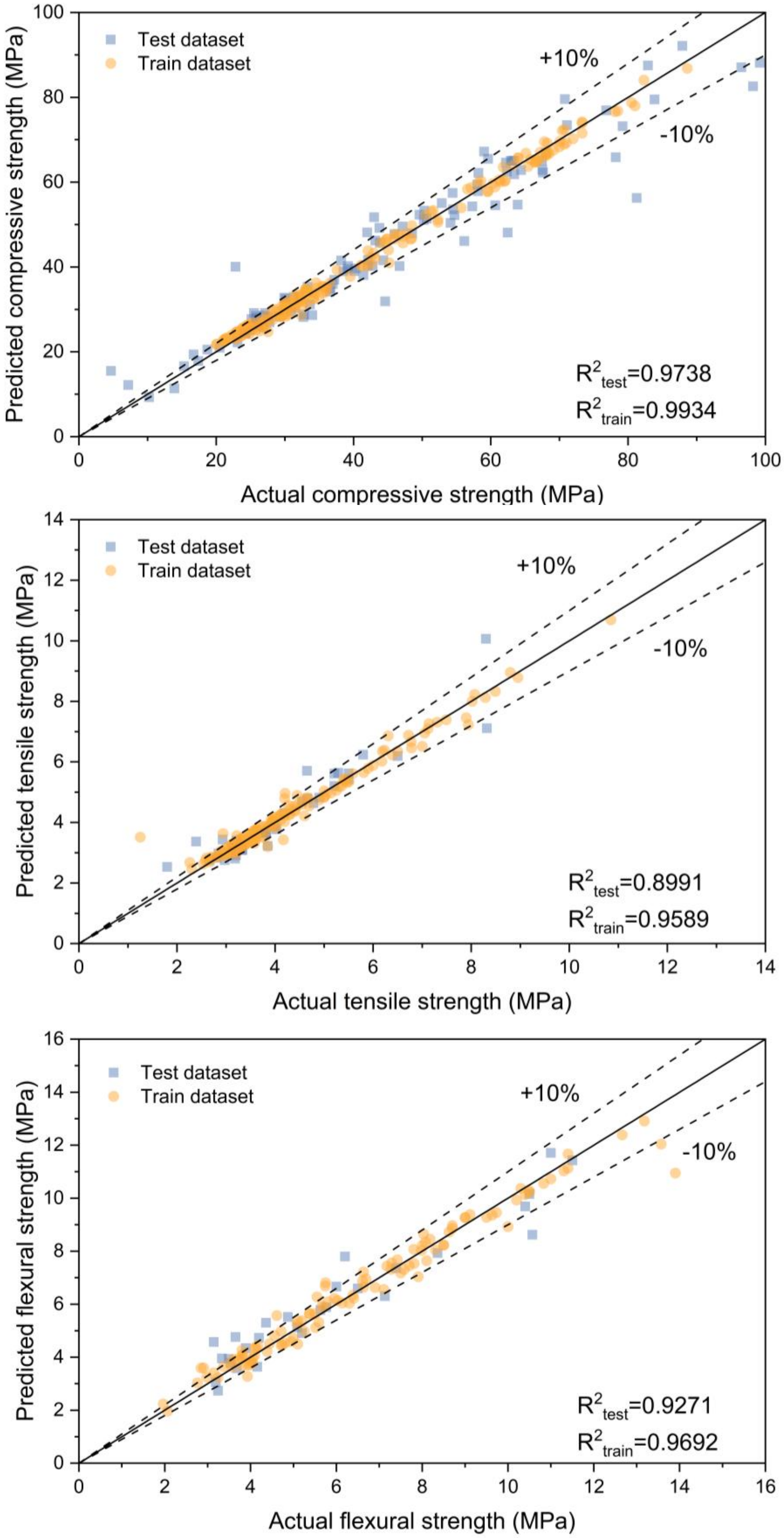

Figure 6.4 Correlation between the actual and predicted SFRSCC properties of SVM

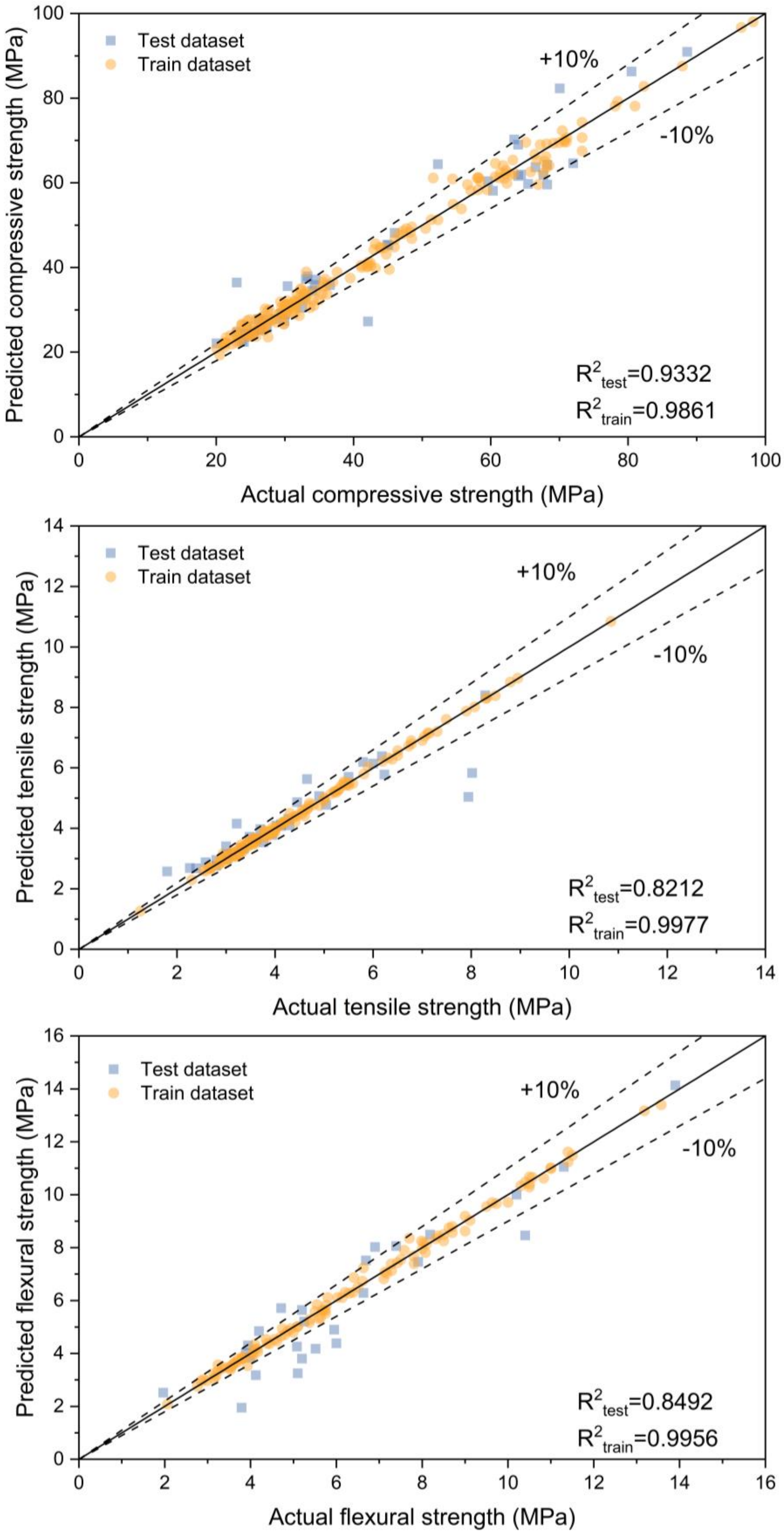

Figure 6.5 Correlation between the actual and predicted SFRSCC properties of ANN

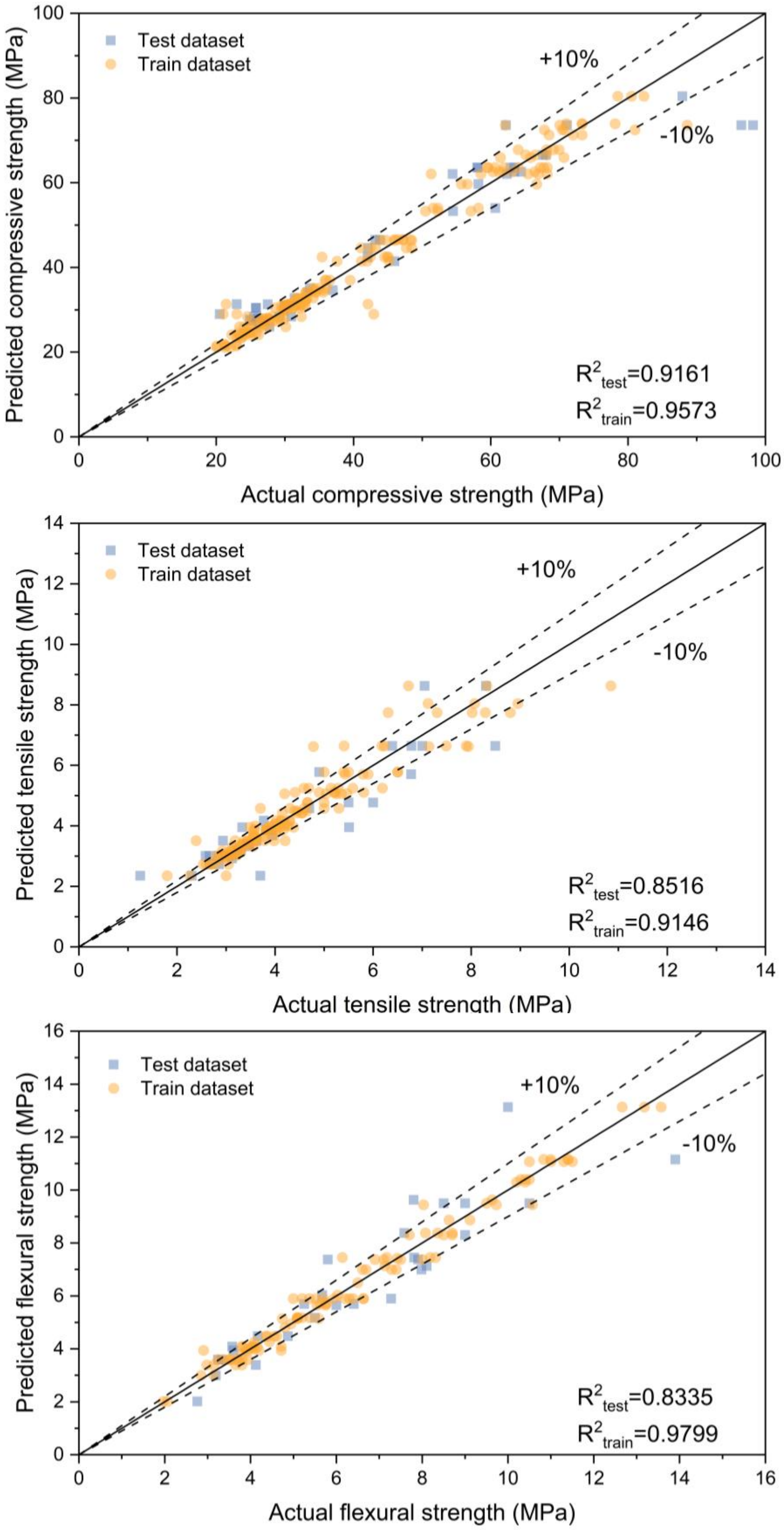

Figure 6.6 Correlation between the actual and predicted SFRSCC properties of DT

Figures 6.4-6.6 present the correlation between actual and predicted values for SFRSCC mechanical properties in both the training and testing datasets. The SVM model demonstrated the highest predictive accuracy, as indicated by the R^2 values close to 1 across all properties: $R^2_{test} = 0.9738$ for compressive strength, $R^2_{test} = 0.8991$ for tensile strength, and $R^2_{test} = 0.9271$ for flexural strength. This strong alignment along the diagonal line suggested that the SVM model captured the underlying relationships effectively, with most predictions falling within a ±10% error range of the actual values.

The ANN and DT models achieved solid predictive accuracy, though slightly lower than SVM. Both models demonstrated reasonable alignment with the actual values and showed good generalization capability in predicting SFRSCC properties, making them valuable for proposed modelling approach.

6.4 Performance of ensemble learning models

Figures 6.7-6.9 illustrate the correlation between actual and predicted values for each strength property, providing insights into the generalization ability of ensemble models across different mechanical properties. All models showed strong predictive accuracy, with data points closely aligned along the diagonal line, indicating a high level of agreement between predicted and actual values.

For compressive strength, the R^2 values are consistently high for both training and testing datasets, reaching up to 0.9801 on the test set and consistently exceeding 0.98 on the training set. This suggests that the models achieve excellent fit and generalization, performing well on both known and unseen data. In predicting tensile strength, there is a slight drop in R^2 compared to compressive strength, with the highest R^2 reaching 0.9583. Although slightly lower, this still indicates strong predictive capability. For flexural strength, the R^2 values are above 0.92 on the test set and over 0.94 on the training set. While slightly lower than the values for compressive strength, these results still demonstrate high reliability, especially on the test data. The slight decrease in R^2 for tensile and flexural strengths may reflect the more complex relationships between mix variables and these properties. Flexural and tensile strengths are strongly influenced by fibre characteristics, which introduce additional non-linear interactions that can impact generalization of models.

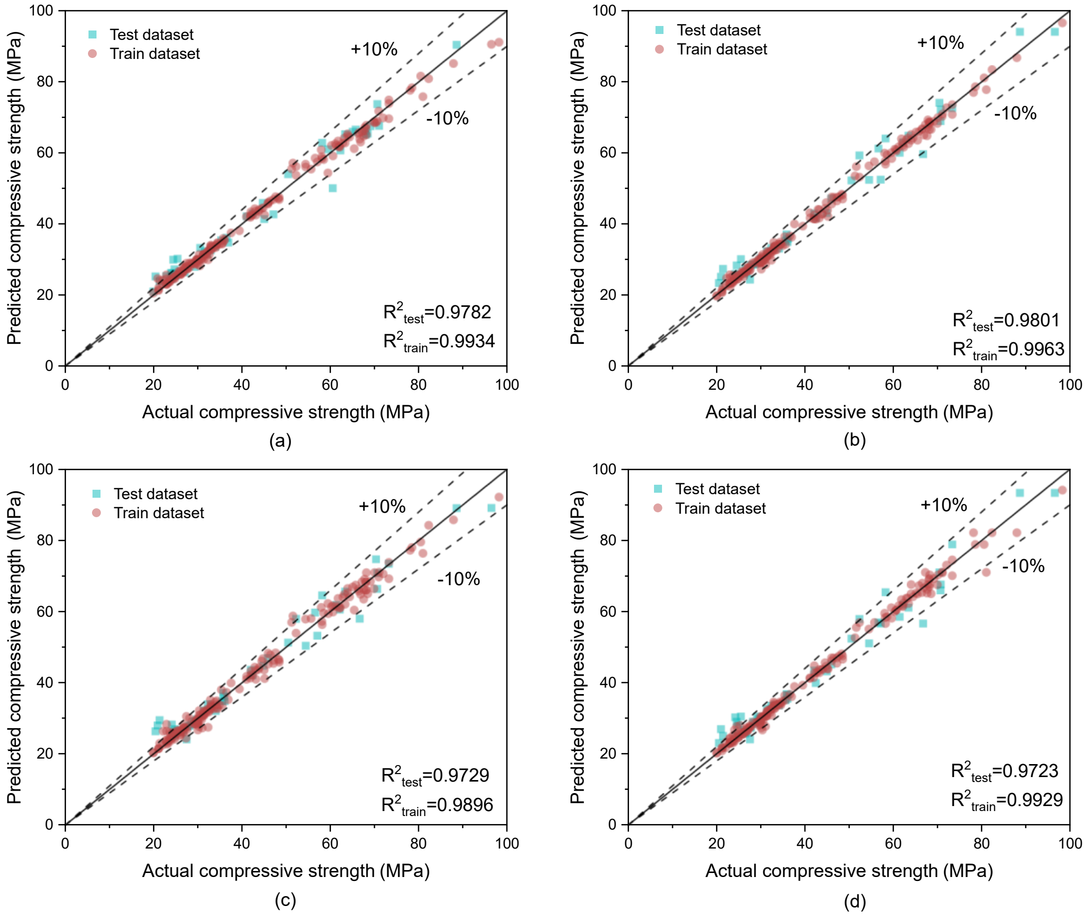

Figure 6.7 Ensemble model performance on SFRSCC compressive strength prediction (a) RF, (b) GBDT, (c) XGBoost and (d) LightGBM

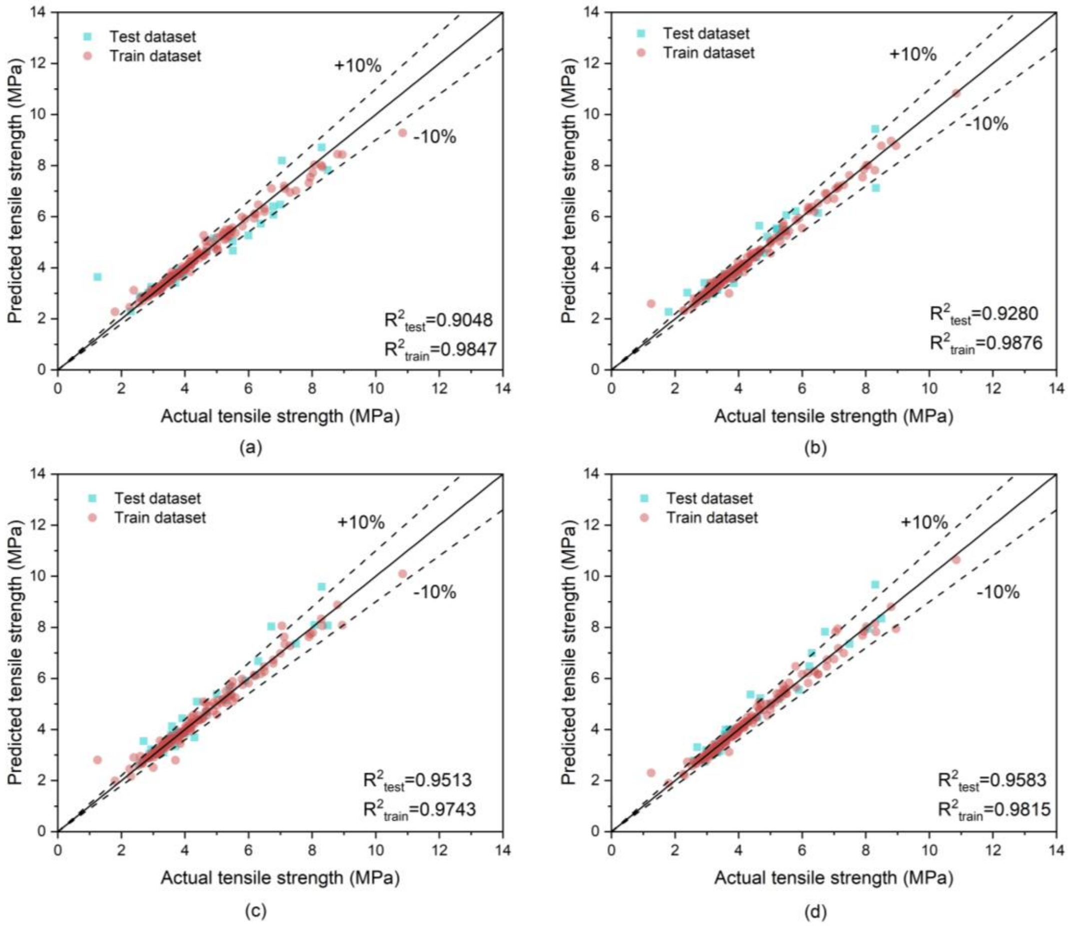

Figure 6.8 Ensemble model performance on SFRSCC tensile strength prediction (a) RF, (b) GBDT, (c) XGBoost and (d) LightGBM

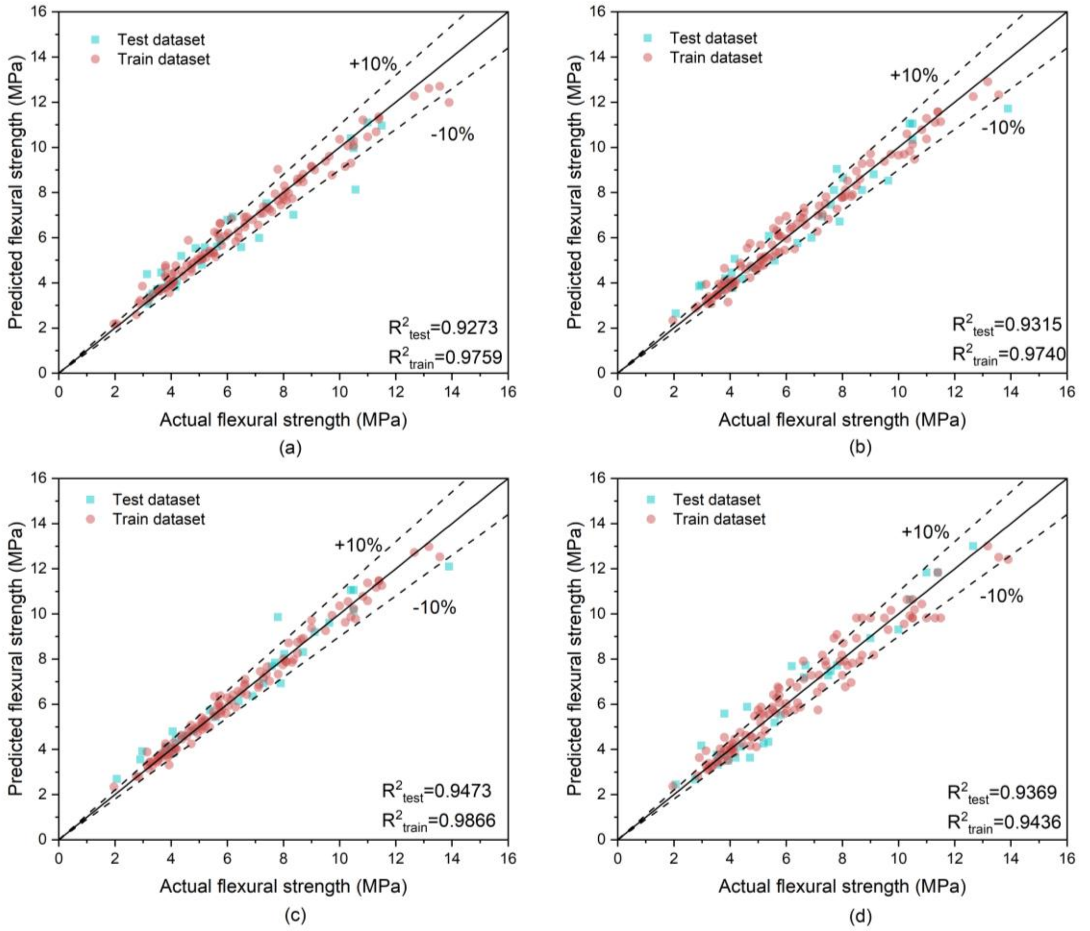

Figure 6.9 Ensemble model performance on SFRSCC flexural strength prediction (a) RF, (b) GBDT, (c) XGBoost and (d) LightGBM

6.5 Comparison of machine learning models

To facilitate a comprehensive comparison, various types of visualizations were created to explore the predictive capabilities of both traditional and ensemble models on SFRSCC mechanical properties. These figures provide detailed insights into the strengths and limitations of each model in the prediction.

Figure 6.10 displays radar charts summarizing the evaluation metrics for ensemble models across compressive, tensile, and flexural strengths of SFRSCC. For compressive strength, GBDT achieves the highest predictive accuracy on the test set with $R^2 = 0.9801$. RMSE and MAE values for GBDT and RF are relatively low at 2.76 and 2.0, respectively, demonstrating their effectiveness in minimizing prediction errors.

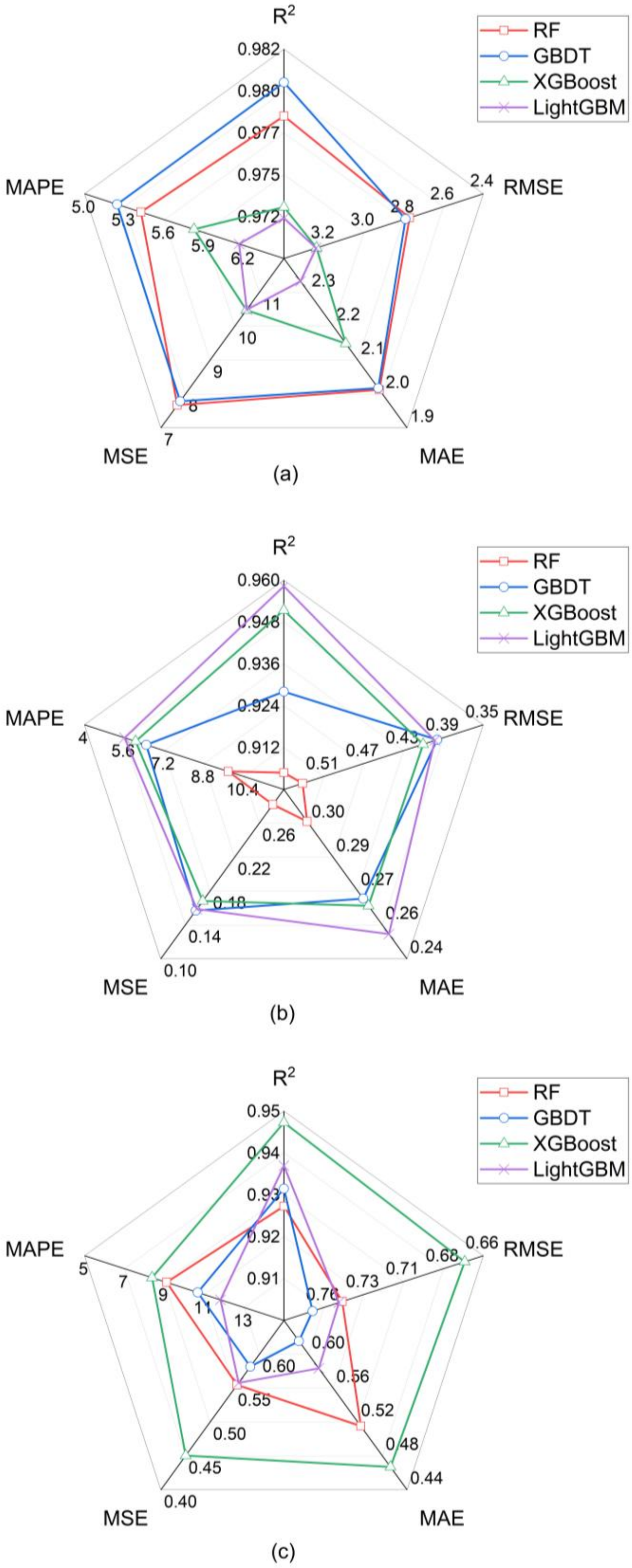

Figure 6.10 Radar chart of the performance evaluation of ensemble models (a) compressive strength, (b) tensile strength and (c) flexural strength

For tensile strength, the R^2 values are slightly lower than those for compressive strength, with LightGBM achieving the highest at 0.9583, closely followed by XGBoost at 0.9513. Both models maintain RMSE and MAE values below 0.43 and 0.27, indicating consistent performance across metrics. RF shows higher error values (RMSE of 0.51 and MAE of 0.35), indicating a slight decline in accuracy for tensile strength. In predicting flexural strength, XGBoost reaches the highest R^2 value at 0.9473. GBDT exhibits relatively higher RMSE and MAE values, suggesting that XGBoost provides the most accurate predictions, while GBDT has more difficulty in reducing error for this property.

Figure 6.11 presents box plots of prediction errors for traditional and ensemble models across the three strength properties (test set). For compressive strength, GBDT demonstrates narrow error distributions with median errors near zero and minimal outliers, indicating stable predictions. In contrast, ANN and DT have broader error distributions and more outliers, with maximum errors of 13.44 MPa and 11.40 MPa, respectively, reflecting less consistent predictions. For tensile strength, XGBoost and LightGBM show smaller error spreads, indicating higher reliability in predictions. In flexural strength predictions, DT exhibits a wider error distribution, while XGBoost maintains a tighter range, supporting the observation that XGBoost handles flexural strength predictions with more consistency.

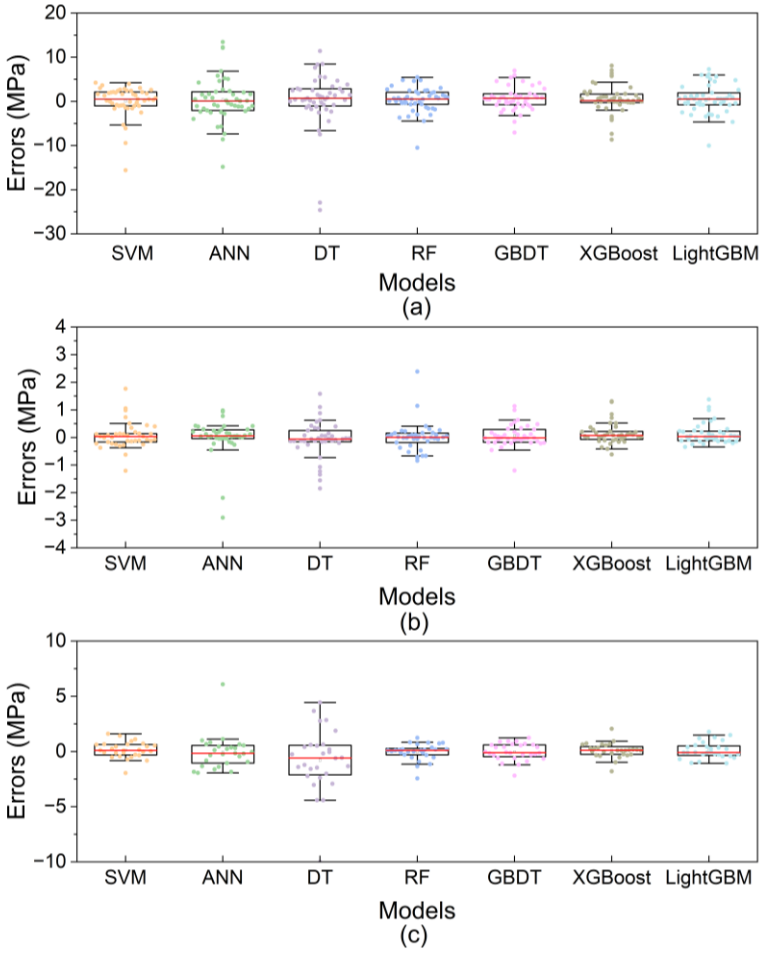

Figure 6.11 Errors between actual values and predicted values (a) compressive strength, (b) tensile strength and (c) flexural strength

Figure 6.12 provides a direct comparison of all models in terms of R^2, RMSE, and MAE values for predicting SFRSCC mechanical properties (test set). For compressive strength, GBDT achieves the highest R^2 (0.9801) with relatively low RMSE and MAE, closely followed by RF. In contrast, ANN and DT show lower R^2 values (0.9332 and 0.9161) and higher RMSE/MAE, highlighting the superiority of ensemble methods in capturing the complexity of compressive strength. In tensile strength predictions, LightGBM and XGBoost perform well, with R^2 values of 0.9583 and 0.9513, respectively, and lower RMSE/MAE values. Other models, such as DT and ANN, show higher error values, with ANN displaying the lowest R^2 at 0.8212, indicating limited effectiveness for tensile strength.

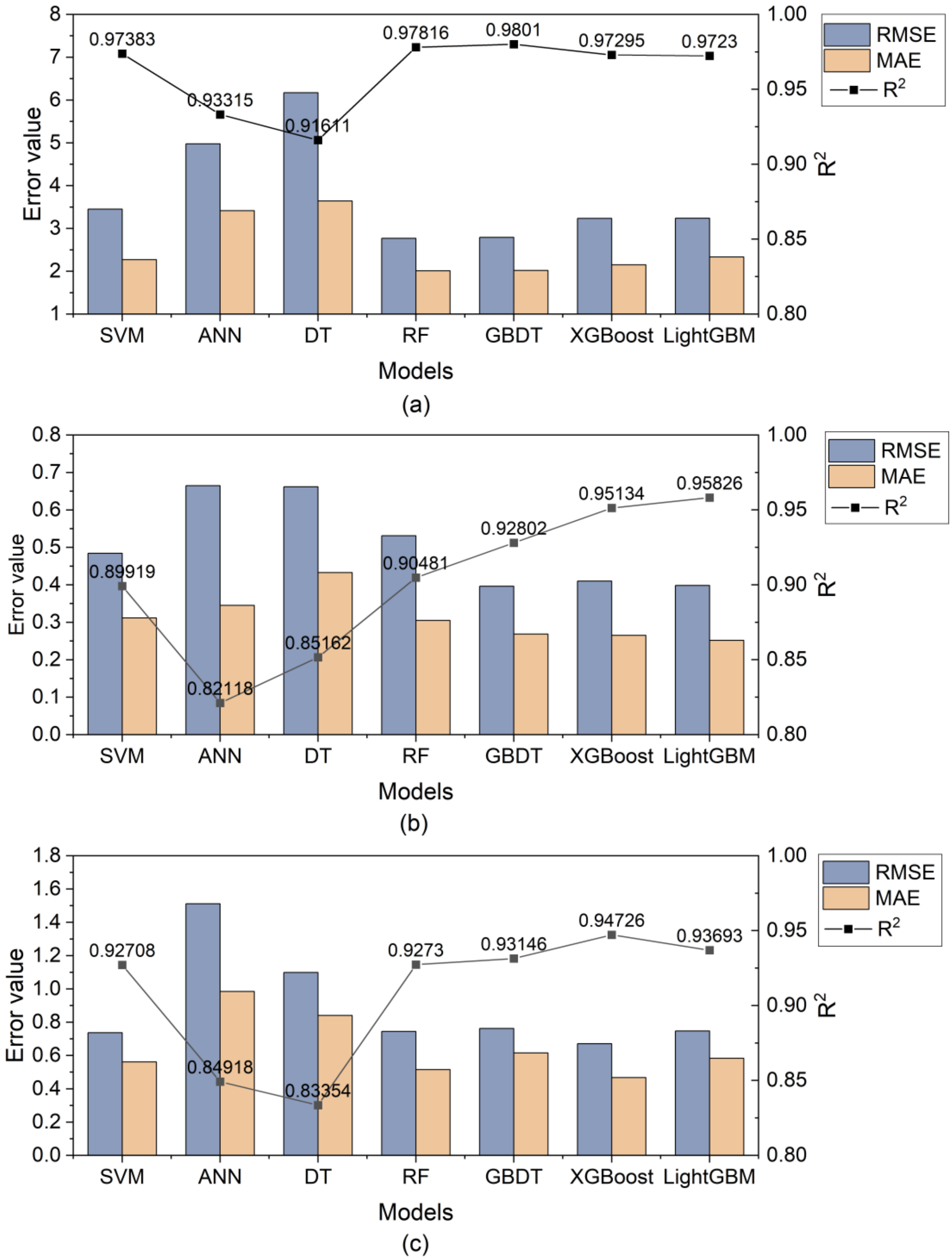

Figure 6.12 Comparison of the performance of all models: (a) compressive strength, (b) tensile strength and (c) flexural strength.

For flexural strength predictions, XGBoost achieves the highest R^2 at 0.9473, followed by LightGBM at 0.9369, with both models showing lower error values compared to others. ANN and DT show reduced predictive reliability with R^2

values of 0.8492 and 0.8335, respectively, indicating they may be less suited for flexural strength prediction.

It is evident that ensemble models, particularly GBDT, XGBoost, and LightGBM, consistently demonstrate superior performance across all strength properties, with higher R^2 values and lower error metrics compared to traditional models, underscoring their robustness in predicting SFRSCC mechanical properties.

6.6 Feature importance analysis using SHAP

6.6.1 SHAP analysis for compressive strength

The interpretative analysis of SFRSCC compressive strength prediction based on the GBDT model is summarized in Figure 6.13. The mean SHAP values illustrate the average impact of each feature on the model's predictions, highlighting the significant influence of limestone powder, curing age, superplasticizer content, maximum coarse aggregate size, and w/cm.

Limestone powder has the largest impact, with an increase in powder content substantially reducing compressive strength. This finding is consistent with previous studies (Celik et al. 2015; Benaicha et al. 2019a; Skender et al. 2021) and is primarily attributed to the dilution effect resulting from the partial replacement of cement with limestone powder. As an inert filler, limestone powder does not participate in hydration, so substituting cement with it reduces the amount of reactive material in the mix. Consequently, fewer hydration products are formed, which are critical to strength development. Superplasticizer content also plays a crucial role, positively affecting compressive strength, with a mean SHAP value of 3.39. The contribution of SP is greater than that of aggregates, underscoring its importance in enhancing strength. Superplasticizers could improve workability, allowing for a denser packing of particles and a more cohesive mix, which contributes to increased compressive strength in SFRSCC. In contrast, an increase in the maximum size of coarse aggregate has a strong negative effect on compressive strength. Larger aggregate sizes may lead to weaker interfacial zones between aggregates and paste, reducing the load-bearing capacity (Nepomuceno et al. 2016). This effect highlights the need for careful selection of aggregate sizes to optimize compressive strength. Among all features, steel fibre-related variables exhibit relatively little impact on compressive strength. This minimal influence indicates that, while fibres are essential for enhancing tensile strength and toughness, they contribute only marginally to compressive strength.

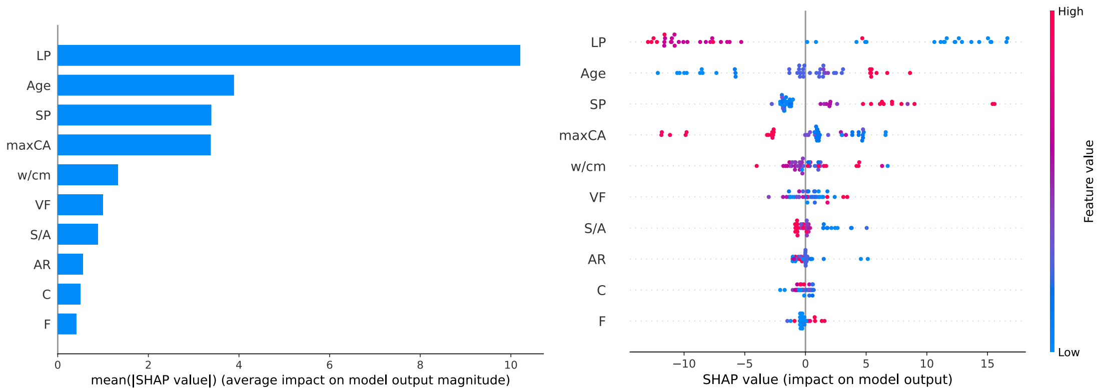

Figure 6.13 Feature importance and SHAP summary plot for SFRSCC compressive strength prediction

The feature contribution analysis for three samples was conducted to evaluate the impact of key factors, as shown in Figure 6.14. With a baseline value of 42.1, the predicted compressive strengths for samples a, b, and c are 35.47, 50.79, and 47.04, respectively. Single feature's contribution to the final prediction is represented by an arrow, with the length and colour of the arrow indicating the strength and direction of the effect. This single-sample contribution analysis shows how each feature affects the model's prediction for the specific samples.

Limestone powder has a marked effect on compressive strength, with higher content generally lowering the predicted value. For example, in samples b and c, where limestone powder is set to zero, no negative impact on compressive strength is observed. In contrast, with limestone powder set to 120 in sample a, experiences a significant reduction in predicted strength, pulling the value well below the baseline. In the contrast, increasing SP from 3.7 in sample a to 12 in sample b notably boosts the predicted strength, underscoring the positive contribution of superplasticizers to compressive strength. Furthermore, the increase of maximum size of coarse aggregate results in a substantial downward adjustment in the predicted strength. Comparing samples b and c, it is evident that a lower w/cm ratio increases the predicted compressive strength by enhancing mix density.

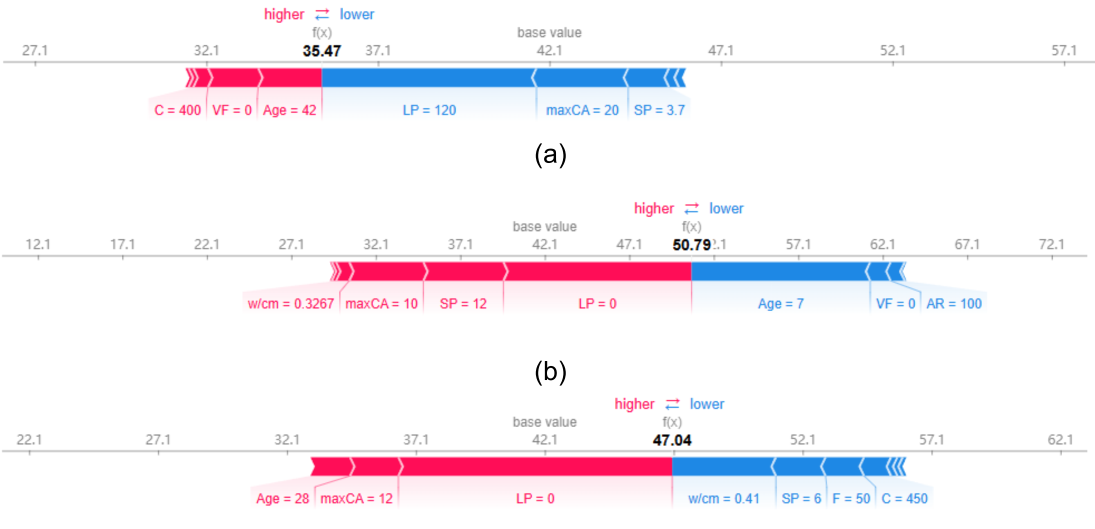

(c)

Figure 6.14 Single sample contribution plot for SFRSCC compressive strength prediction

6.6.2 SHAP analysis for tensile strength

Figure 6.15 presents the feature analysis of SFRSCC tensile strength prediction based on the LightGBM model. The results indicate that increasing limestone powder, maximum size of coarse aggregate negatively impact tensile strength of SFRSCC, while higher volume fraction of steel fibre and superplasticizers can significantly enhance it.

The mechanism by which limestone powder reduces tensile strength is similar to its effect on compressive strength, as discussed in the previous section.

Limestone powder acts as an inert filler, diluting the cementitious content and reducing the formation of hydration products essential for strength. However, unlike compressive strength, the impact of the fibre volume fraction on tensile strength is notably more pronounced. This is attributed to the crack-bridging behaviour of hooked-end steel fibres, which effectively increase the material’s resistance to tensile stress. The dense distribution of fibres helps to bridge microcracks within the concrete, transferring tensile stress from the concrete matrix to the fibres. As these fibres are randomly and uniformly distributed, they effectively inhibit the propagation of larger macrocracks, thereby significantly enhancing the tensile strength of SFRSCC (Alrawashdeh and Eren 2022).

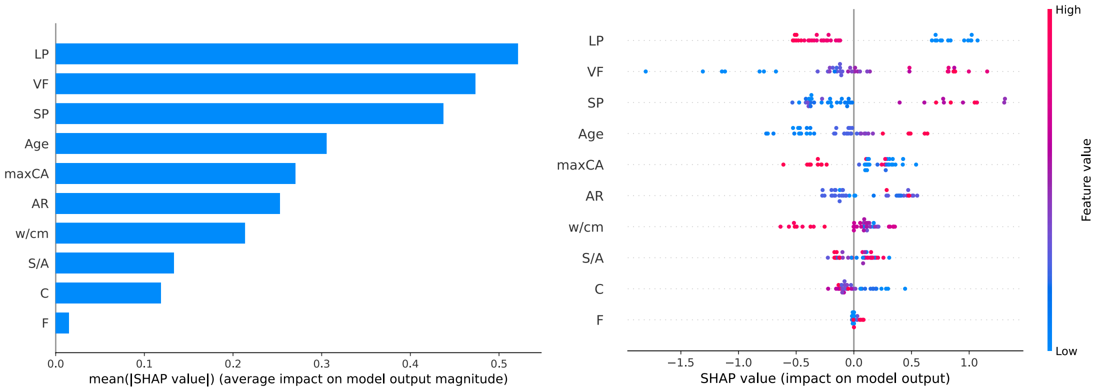

Figure 6.15 Feature importance and SHAP summary plot for SFRSCC tensile strength prediction

The individual impact of these features on tensile strength predictions is further analysed in Figure 6.16. The baseline tensile strength value is set at 4.2295, with predicted values for the three samples being 3.09, 4.47, and 4.99, respectively. By comparing these samples, it can be observed that increasing the volume fraction of steel fibres from 0.38 to 0.75 and then to 1.5 results in a corresponding increase in the predicted tensile strength. This trend illustrates the substantial role of fibre content in enhancing tensile strength.

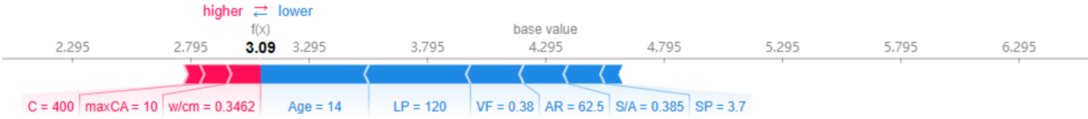

(a)

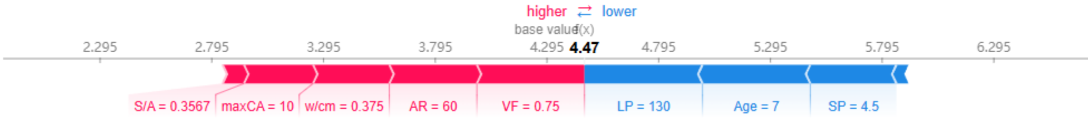

(b)

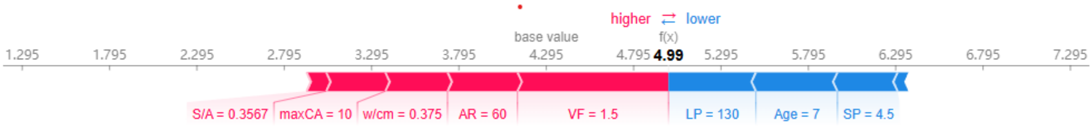

(c)

Figure 6.16 Single sample contribution plot for SFRSCC tensile strength prediction

6.6.3 SHAP analysis for flexural strength

Figure 6.17 presents the feature importance ranking and distribution for SFRSCC flexural strength prediction based on the developed XGBoost models. It is evident that properties related to steel fibres, including the volume fraction and aspect ratio of steel fibres, play a dominant role in enhancing flexural strength. As the values of these two variables increase, flexural strength shows a marked improvement. A higher volume of steel fibres strengthens the internal structure by closely linking microcracks within the concrete, while longer fibres enhance this effect by bridging more cracks. This crack-bridging mechanism contributes to increased concrete toughness and improved resistance to crack propagation, which collectively enhances flexural strength.

The inclusion of fly ash also has a positive effect on flexural strength, may attributed to its role in improving the particle packing density, which enhances the microstructure of the concrete (Cao et al. 2000). Additionally, an increase in the w/cm negatively impacts flexural strength. Higher w/cm ratios lead to larger gaps between aggregates and increase voids left by evaporated water, thereby reducing flexural strength. This finding aligns with results reported in several studies, where excessive w/cm was found to weaken the structural integrity of concrete.

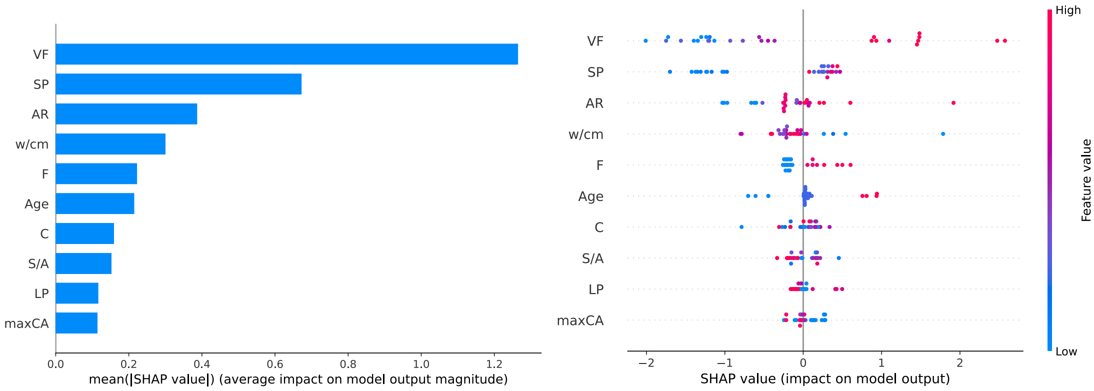

Figure 6.17 Feature importance and SHAP summary plot for SFRSCC flexural strength prediction

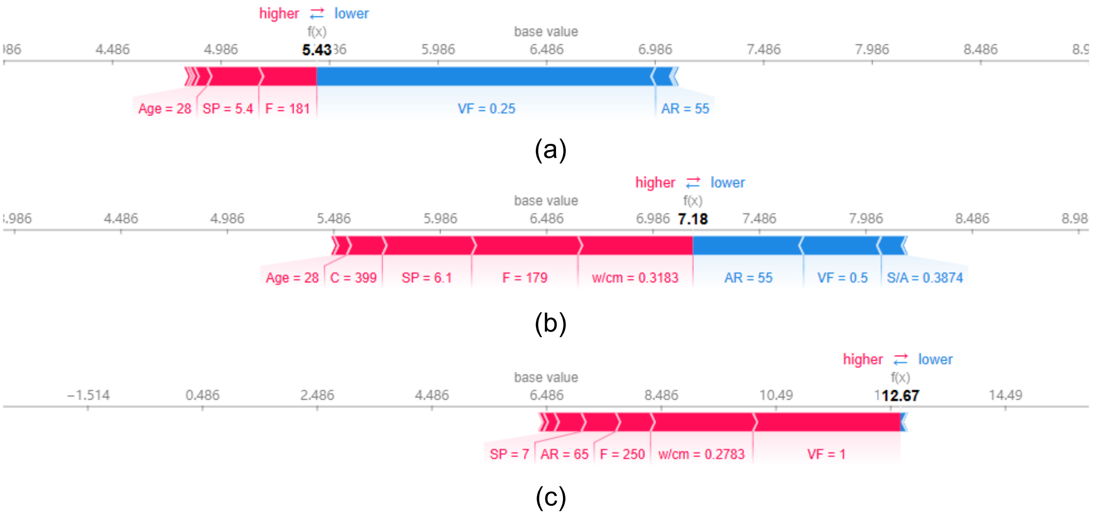

Figure 6.18 Single sample contribution plot for SFRSCC flexural strength prediction

Further analysis of individual variable effects on SFRSCC flexural strength predictions is shown in Figure 6.18. The baseline flexural strength value is set at 6.486, with predicted values for three samples being 5.43, 7.18, and 12.67, respectively. Comparing these samples reveals that increasing both the volume fraction and aspect ratio of steel fibres boosts the predicted flexural strength above the baseline. This reinforces the importance of optimizing fibre characteristics to achieve higher flexural strength. Additionally, increasing the superplasticizer content from 5.4 to 7 results in an increase in flexural strength, as superplasticizers enhance the mix workability and allow for better particle packing. Conversely, reducing the w/cm ratio also increases flexural strength by minimizing voids, leading to a denser and more cohesive concrete structure.

6.6.4 Summary

The feature importance analysis using SHAP for SFRSCC compressive, tensile, and flexural strength reveals key variables that influence each strength type differently. Limestone powder consistently shows a negative impact across compressive and tensile strengths, due to its dilution effect on hydration products. Superplasticizer content positively affects all strength types by improving workability and particle packing, enhancing the concrete matrix. For tensile and flexural strengths, steel fibre properties, such as volume fraction and aspect ratio, emerge as dominant factors due to their crack-bridging capabilities, which enhance toughness and resistance to crack propagation. Additionally, the w/cm ratio negatively impacts all strength types as higher ratios lead to increased voids, weakening structural integrity.

This comprehensive SHAP-based analysis provides crucial insights into optimizing SFRSCC mix design for specific strength requirements. By identifying the most impactful variables and understanding their effects, engineers can better tailor SFRSCC compositions for targeted mechanical properties, enhancing the material’s performance in various structural applications.

6.7 Limitation of this research

Despite incorporating a range of detailed input variables, such as the maximum size of aggregate, this study's predictive capacity remains limited by several factors. Although more variables can potentially provide greater insight into the mechanisms within SFRSCC, the limitations of the dataset impact the overall robustness and generalizability of the models. Firstly, the dataset was compiled from literature sources, which limits the availability and diversity of data. Smaller sample sizes in this chapter are less representative and may not capture the full variability of SFRSCC compositions. For instance, in the dataset used, samples containing limestone powder were sparse, potentially leading to an exaggerated effect of limestone powder in predictions, as the models might overestimate its influence due to limited examples. Moreover, this study primarily used data from different studies and experimental conditions, which introduces inconsistencies. Variations in testing procedures, environmental conditions, and sample preparation methods across sources can introduce noise and potential biases in the dataset, which may compromise model performance.

6.8 Conclusion

In this chapter, a comprehensive approach to predicting the mechanical properties of SFRSCC was presented using both traditional supervised learning models and advanced ensemble learning models. The models were developed and fine-tuned using optimization strategies, including SVM, decision tree, ANN, and ensemble methods such as RF, GBDT, XGBoost, and LightGBM. The performance of these models was evaluated and compared to identify the most effective algorithms for accurately predicting compressive, tensile, and flexural strengths. Following this, SHAP analysis was applied to the best-performing models to assess feature importance, providing insights into the influence of specific components in SFRSCC. Through this study, the following conclusions had been reached:

- Traditional supervised learning models demonstrated satisfactory predictive accuracy, with SVM models performing the best among them. The SVM models achieved R^2 values of 0.9738, 0.8992, and 0.9271 for compressive, tensile, and flexural strengths, respectively.

- Ensemble models generally demonstrated superior predictive accuracy and robustness, as evidenced by radar charts and error analysis. For compressive strength, GBDT achieved the highest predictive accuracy with $R^2 = 0.9801$. For tensile strength, the R^2 values of LightGBM were the highest at 0.9583. In predicting flexural strength, XGBoost reached the highest R^2 value at 0.9473.
- The SHAP-based feature importance analysis revealed that limestone powder negatively impacts compressive and tensile strengths, while superplasticizer content, steel fibre properties, and a lower w/cm ratio positively influence SFRSCC's mechanical properties. This analysis highlights the key factors for optimizing SFRSCC mix design, enabling engineers to tailor compositions for enhanced performance in structural applications.

Chapter 7 Conclusions and recommendations for further research

7.1 Conclusion

This research has addressed critical challenges in the design, optimisation, and prediction of sustainable self-compacting concrete (SCC) performance through a combination of experimental studies and machine learning methodologies. The findings significantly contribute to the understanding of high strength SCC (HSSCC) and steel fibre reinforced SCC (SFRSCC) in both academic and practical contexts. The key research findings can be summarized as follows:

- A pragmatic mix design methodology was proposed for HSSCC, integrating supplementary cementitious materials (SCMs) to achieve specific targets for compressive strength and plastic viscosity while reducing cement consumption. This approach not only optimises fresh and hardened properties but also contributes to environmental sustainability by minimising CO_2 emissions. The development of comprehensive design charts (70-100 MPa) further enhances the practical applicability of the methodology, offering a straightforward tool for practitioners in the research area and construction industry.
- Experimental validation confirmed that the proposed HSSCC mixes met the desired performance requirements, with environmental analysis demonstrating a significant reduction in CO_2 emissions. Various mix designs were tested with different sand to aggregate (S/A) and paste to solid ratios (P/S) to evaluate their influence on both fresh and hardened concrete properties.
- Machine learning models, including support vector machines (SVM), artificial neural networks (ANN), decision trees (DT), and random forests (RF), were employed to predict the performance of SCC containing fly ash, focusing on both fresh and hardened properties. Among the models developed, RF demonstrated the highest predictive accuracy, with high R^2 values of 0.9542, 0.8656 and 0.9130 for compressive strength, slump flow

diameter and V-funnel time, respectively. These results underline the potential of data-driven approaches in capturing the complex interactions between SCC components and performance outcomes, providing a more efficient alternative to traditional trial-and-error methods. A feature importance analysis was performed to demonstrate the influence of SCC components on its properties, offering valuable insights for the design and optimisation of SCC mixes containing fly ash.

- A comprehensive approach was developed to predict the mechanical properties of SFRSCC using both traditional supervised learning models and advanced ensemble learning models. The models, including SVM, ANN, DT, and ensemble methods such as RF, GBDT, XGBoost, and LightGBM, were developed and fine-tuned using optimisation strategies. Their performance was evaluated and compared to identify the most effective algorithms for accurately predicting compressive, tensile, and flexural strengths. Among these, ensemble models generally demonstrated superior predictive accuracy and robustness. SHAP analysis was applied to the best-performing models to assess feature importance, providing valuable insights into the influence of specific components in SFRSCC.

While the outcomes of this research offer significant advancements, certain limitations must be acknowledged. Firstly, the experimental validation was conducted under specific conditions and material parameters, which may limit the generalisability of the results to other contexts. Key mix parameters, such as cement strength class and admixture type, were not included as model inputs due to inconsistent reporting across datasets. Secondly, the datasets and variables utilised for machine learning were constrained because of the limitation of literature source, which could affect the flexibility of the predictive models in diverse applications. Long-term performance aspects, such as durability under varied environmental conditions, were also beyond the scope of this study.

Additionally, chapter 4 primarily focuses on the design of HSSCC, but the data availability in the literature for HSSCC properties was limited. As a result, the models developed in chapters 5 and 6 were based on datasets for normal range of SCC rather than HSSCC. While these models provide valuable insights into SCC performance, they may not fully capture the complex interactions and behaviours unique to high-strength formulations.

7.2 Recommendations for further research

Based on the findings and limitations of this study, several avenues for future research are suggested to further advance the understanding and application of SCC, particularly in the domains of HSSCC and SFRSCC:

- The proposed mix design methodology could be expanded to accommodate a broader range of SCMs beyond ground granulated blast furnace slag (GGBS) and fly ash. By including materials such as rice husk ash or silica fume, the methodology could become a more versatile and universal design tool. Future studies can explore the feasibility of incorporating these materials without only compromising fresh and hardened properties, while also evaluating their environmental benefits in terms of CO_2 reduction and waste utilisation.
- Conducting large-scale experimental studies is essential to provide extensive datasets that capture a wider range of HSSCC compositions and performance metrics. These datasets would significantly improve the predictive accuracy and reliability of machine learning models tailored for HSSCC formulations. Furthermore, incorporating sustainability indicators into the mix design process could enhance the applicability of HSSCC in green construction projects, aligning with global carbon reduction targets.
- Future research could focus on evaluating the long-term durability of

HSSCC and SFRSCC under varying environmental conditions, including freeze-thaw cycles, carbonation, and chloride attack. Given the superior capability of machine learning in handling complex problems, more advanced predictive models could be developed to simplify the evaluation process. These models would enable efficient assessments of how changes in mix design parameters affect lifecycle performance and degradation mechanisms.

- Translating research outcomes into practical, user-friendly design tools would greatly benefit practitioners. Tools such as mix design software, interactive design charts, and performance prediction interfaces could assist engineers in creating HSSCC and SFRSCC mixes without requiring extensive computational expertise. Such tools could simplify and accelerate the design process, reducing the reliance on manual calculations or complex code operations.
- Beyond predicting SCC performance, real-time monitoring systems could be developed to dynamically adjust mix proportions during production and placement. Tools like digital twins could be employed to establish feedback loops, enabling the real time optimisation of SCC properties during construction. Such systems could improve the consistency of SCC performance on site and reduce material wastage, contributing to more sustainable and efficient construction practices.

References

Aaron, W.S., Hamlin, M.J. and Surendra, P.S. 2001. New Methodology for Designing Self-Compacting Concrete. *ACI Materials Journal* 98(6), pp. 429–439. doi: 10.14359/10841.

Abo Dhaheer, M.S., Al-Rubaye, M.M., Alyhya, W.S., Karihaloo, B.L. and Kulasegaram, S. 2016. Proportioning of self–compacting concrete mixes based on target plastic viscosity and compressive strength: Part I - mix design procedure. *Journal of Sustainable Cement-Based Materials* 5(4), pp. 199–216. Available at: http://dx.doi.org/10.1080/21650373.2015.1039625.

Abunassar, N., Alas, M. and Ali, S.I.A. 2022. Prediction of Compressive Strength in Self-compacting Concrete Containing Fly Ash and Silica Fume Using ANN and SVM. *Arabian Journal for Science and Engineering*. doi: 10.1007/s13369-022-07359-3.

ACI Committee 238. 2008. *238.1R-08: Report on Measurements of Workability and Rheology of Fresh Concrete*.

Adler, J. and Parmryd, I. 2010. Quantifying colocalization by correlation: The pearson correlation coefficient is superior to the Mander's overlap coefficient. *Cytometry Part A* 77(8), pp. 733–742. doi: 10.1002/cyto.a.20896.

Afshoon, I., Miri, M. and Mousavi, S.R. 2023. Comprehensive experimental and numerical modeling of strength parameters of eco-friendly steel fiber reinforced SCC containing coarse copper slag aggregates. *Construction and Building Materials* 367, p. 130304. doi: 10.1016/J.CONBUILDMAT.2023.130304.

Aggarwal, Y. and Aggarwal, P. 2011. Prediction of compressive strength of self-compacting concrete containing bottom ash using artificial neural networks. *International Journal of Mathematical and Computational Sciences* 5(5), pp. 762–767. doi: 10.1016/j.advengsoft.2011.05.016.

Ahari, R.S., Erdem, T.K. and Ramyar, K. 2015. Thixotropy and structural breakdown properties of self consolidating concrete containing various supplementary cementitious materials. *Cement and Concrete Composites* 59, pp. 26–37. Available at: http://dx.doi.org/10.1016/j.cemconcomp.2015.03.009.

Ahsan, M., Mahmud, M., Saha, P., Gupta, K. and Siddique, Z. 2021. Effect of Data Scaling Methods on Machine Learning Algorithms and Model Performance. *Technologies* 9(3), p. 52. doi: 10.3390/technologies9030052.

Ben aicha, M., Al Asri, Y., Zaher, M., Alaoui, A.H. and Burtschell, Y. 2022. Prediction of rheological behavior of self-compacting concrete by multi-variable regression and artificial neural networks. *Powder Technology* 401, p. 117345. doi: 10.1016/j.powtec.2022.117345.

Aïtcin, P.C. 2016. The importance of the water–cement and water–binder ratios. *Science and Technology of Concrete Admixtures*, pp. 3–13. doi: 10.1016/B978-0-08-100693-1.00001-1.

Akcay, B. and Tasdemir, M.A. 2012. Mechanical behaviour and fibre dispersion of hybrid steel fibre reinforced self-compacting concrete. *Construction and Building Materials* 28(1), pp. 287–293. doi: 10.1016/J.CONBUILDMAT.2011.08.044.

Alabduljabbar, H., Alyousef, R., Alrshoudi, F., Alaskar, A., Fathi, A. and Mohamed, A.M. 2019. Mechanical effect of steel fiber on the cement replacement materials of self-compacting concrete. *Fibers* 7(4). doi: 10.3390/fib7040036.

AL-Ameeri, A. 2013. The Effect of Steel Fiber on Some Mechanical Properties of Self Compacting Concrete. *American Journal of Civil Engineering* 1(3), p. 102. doi: 10.11648/j.ajce.20130103.14.

Alani, N.Y., Al-Jumaily, I.A. and Hilal, N. 2021. Effect of nanoclay and burnt limestone powder on fresh and hardened properties of self-compacting concrete. *Nanotechnology for Environmental Engineering* 6(1), pp. 1–26. Available at: https://doi.org/10.1007/s41204-021-00114-3.

Alipour, P., Behforouz, B., Mohseni, E. and Zehtab, B. 2019. Investigation of SCC characterizations incorporating supplementary cementitious materials. *Emerging Materials Research* 8(3), pp. 492–507. doi: 10.1680/jemmr.18.00024.

Al-Jaberi, L.A. 2019. Effects of Chemical Admixtures on the Rheological, Fresh and Hardened Properties of Self-Compacting Concrete. *Academic J. for Engineering and Science* 1(1), pp. 19–25. Available at: https://www.researchgate.net/publication/340298064_Effects_of_Chemical_Admixtures_on_the_Rheological_Fresh_and_Hardened_Properties_of_Self-Compacting_Concrete.

Almuwbber, O., Haldenwang, R., Mbasha, W. and Masalova, I. 2018. The influence of variation in cement characteristics on workability and strength of SCC with fly ash and slag additions. *Construction and Building Materials* 160, pp. 258–267. doi: 10.1016/J.CONBUILDMAT.2017.11.039.

Al-Oran, A.A.A., Safiee, N.A. and Nasir, N.A.M. 2019. Fresh and hardened properties of self-compacting concrete using metakaolin and GGBS as cement replacement. *European Journal of Environmental and Civil Engineering,*. Available at: https://www.tandfonline.com/action/journalInformation?journalCode=tece20.

Alrawashdeh, A. and Eren, O. 2022. Mechanical and physical characterisation of steel fibre reinforced self-compacting concrete: Different aspect ratios and volume fractions of fibres. *Results in Engineering* 13. doi: 10.1016/j.rineng.2022.100335.

Alshahrani, A. 2024. *Towards Sustainable Construction: Experimental Approach and Multi-Scale Simulation in High-Strength Self-Compacting*

Concrete Design.

Alshahrani, A., Cui, T., Almutlaqah, A. and Kulasegaram, S. 2024. Designing sustainable high-strength self-compacting concrete with high content of supplementary cementitious materials. *European Journal of Environmental and Civil Engineering* 28(8), pp. 1830–1849. doi: 10.1080/19648189.2023.2279563.

Anjos, M.A.S., Camões, A., Campos, P., Azeredo, G.A. and Ferreira, R.L.S. 2020. Effect of high volume fly ash and metakaolin with and without hydrated lime on the properties of self-compacting concrete. *Journal of Building Engineering* 27, p. 100985. doi: 10.1016/J.JOBE.2019.100985.

Ashish, D.K. and Verma, S.K. 2019. Determination of optimum mixture design method for self-compacting concrete: Validation of method with experimental results. *Construction and Building Materials* 217, pp. 664–678. doi: 10.1016/j.conbuildmat.2019.05.034.

Asteris, P.G. and Kolovos, K.G. 2019. Self-compacting concrete strength prediction using surrogate models. *Neural Computing and Applications* 31, pp. 409–424. doi: 10.1007/s00521-017-3007-7.

Asteris, P.G., Kolovos, K.G., Douvika, M.G. and Roinos, K. 2016. Prediction of self-compacting concrete strength using artificial neural networks. *European Journal of Environmental and Civil Engineering* 20, pp. s102–s122. Available at: http://dx.doi.org/10.1080/19648189.2016.1246693.

Asteris, P.G., Skentou, A.D., Bardhan, A., Samui, P. and Pilakoutas, K. 2021. Predicting concrete compressive strength using hybrid ensembling of surrogate machine learning models. *Cement and Concrete Research* 145, p. 106449. doi: 10.1016/J.CEMCONRES.2021.106449.

ASTM C1621. 2017. Standard Test Method for Passing Ability of Self-Consolidating Concrete by J-Ring.

Atiş, C.D. 2002. Heat evolution of high-volume fly ash concrete. *Cement and Concrete Research* 32(5), pp. 751–756. doi: 10.1016/S0008-8846(01)00755-4.

Ayaz, Y., Kocamaz, A.F. and Karakoç, M.B. 2015. Modeling of compressive strength and UPV of high-volume mineral-admixtured concrete using rule-based M5 rule and tree model M5P classifiers. *Construction and Building Materials* 94, pp. 235–240. doi: 10.1016/J.CONBUILDMAT.2015.06.029.

Azimi-Pour, M., Eskandari-Naddaf, H. and Pakzad, A. 2020. Linear and non-linear SVM prediction for fresh properties and compressive strength of high volume fly ash self-compacting concrete. *Construction and Building Materials* 230. doi: 10.1016/j.conbuildmat.2019.117021.

Bani Ardalan, R., Joshaghani, A. and Hooton, R.D. 2017. Workability retention and compressive strength of self-compacting concrete incorporating pumice powder and silica fume. *Construction and Building Materials* 134, pp. 116–122. doi: 10.1016/J.CONBUILDMAT.2016.12.090.

Bao, C., Bi, J.H., Xu, D., Guan, J. and Cheng, W.X. 2020. Numerical simulation of the distribution and orientation of steel fibres in SCC. *Magazine of Concrete Research* 72(21), pp. 1102–1111. doi: 10.1680/jmacr.18.00432.

Bartos, P.J.M., Sonebi, M. and Tamimi, A.K. 2002. *Report 24: Workability and Rheology of Fresh Concrete: Compendium of Tests*. Bartos, P. J. M., Sonebi, M., and Tamimi, A. K. eds. RILEM publications.

Beale, M.H., Hagan, M.T. and Demuth, H.B. 2010. *Neural Network Toolbox™ 7 User's Guide*. doi: 10.1016/j.fuel.2020.118589.

Behnood, A., Verian, K.P. and Modiri Gharehveran, M. 2015. Evaluation of the splitting tensile strength in plain and steel fiber-reinforced concrete based on the compressive strength. *Construction and Building Materials* 98, pp. 519–529. doi: 10.1016/j.conbuildmat.2015.08.124.

Belalia Douma, O., Boukhatem, B., Ghrici, M. and Tagnit-Hamou, A. 2017. Prediction of properties of self-compacting concrete containing fly ash using artificial neural network. *Neural Computing and Applications* 28(s1), pp. 707–718. doi: 10.1007/s00521-016-2368-7.

Benaicha, M., Belcaid, A., Alaoui, A.H., Jalbaud, O. and Burtschell, Y. 2019a. Effects of limestone filler and silica fume on rheology and strength of self-compacting concrete. *Structural Concrete* 20(5), pp. 1702–1709. doi: 10.1002/suco.201900150.

Benaicha, M., Hafidi Alaoui, A., Jalbaud, O. and Burtschell, Y. 2019b. Dosage effect of superplasticizer on self-compacting concrete: Correlation between rheology and strength. *Journal of Materials Research and Technology* 8(2), pp. 2063–2069. Available at: https://doi.org/10.1016/j.jmrt.2019.01.015 [Accessed: 21 July 2021].

Bentz, D.P., Ferraris, C.F. and Snyder, K.A. 2013. *Best Practices Guide for High-Volume Fly Ash Concretes : Assuring Properties and Performance*. Gaithersburg, MD. Available at: https://nvlpubs.nist.gov/nistpubs/TechnicalNotes/NIST.TN.1812.pdf.

Berry, E.E., Hemmings, R.T. and Cornelius, B.J. 1990. Mechanisms of hydration reactions in high volume fly ash pastes and mortars. *Cement and Concrete Composites* 12(4), pp. 253–261. doi: 10.1016/0958-9465(90)90004-H.

Bocciarelli, M., Cattaneo, S., Ferrari, R., Ostinelli, A. and Terminio, A. 2018. Long-term behavior of self-compacting and normal vibrated concrete: Experiments and code predictions. *Construction and Building Materials* 168, pp. 650–659. doi: 10.1016/J.CONBUILDMAT.2018.02.139.

Boukendakdji, O., Kadri, E.H. and Kenai, S. 2012. Effects of granulated blast furnace slag and superplasticizer type on the fresh properties and compressive strength of self-compacting concrete. *Cement and Concrete Composites* 34(4), pp. 583–590. doi: 10.1016/J.CEMCONCOMP.2011.08.013.

Brady, J.F. 1983. The Einstein viscosity correction in n dimensions. *International Journal of Multiphase Flow* 10(1), pp. 113–114. doi: 10.1016/0301-9322(83)90064-2.

Brameshuber, W. and Stephan Uebachs. 2001. Practical experience with the application of self-compacting concrete in Germany. In: *Proceedings of the 2nd International Symposium on Self-Compacting Concrete*. pp. 687–696.

Breiman, L. 1996a. *Bagging Predictors*.

Breiman, L. 1996b. *Stacked Regressions*.

Breiman, L. 2001. Random Forests. *Machine Learning* 45, pp. 5–32. doi: https://doi.org/10.1023/A:1010933404324.

Bro, R., Kjeldahl, K., Smilde, A.K. and Kiers, H.A.L. 2008. Cross-validation of component models: A critical look at current methods. *Analytical and Bioanalytical Chemistry* 390(5), pp. 1241–1251. doi: 10.1007/s00216-007-1790-1.

BS EN 206-9. 2010. *Concrete. Additional rules for self-compacting concrete (SCC)*.

BS EN 12350-8. 2009. *Testing fresh concrete Part 8: Self-compacting concrete - Slump-flow test*.

BS EN 12350-9. 2010. *Testing fresh concrete Part 9: Self-compacting concrete — V-funnel test*.

BS EN 12350-10. 2010. *Testing fresh concrete Part 10 : Self-compacting concrete — L box test*.

BS EN 12350-11. 2010. Testing fresh concrete Part 11: Self-compacting concrete — Sieve segregation test.

BS EN 12350-12. 2010. *Testing fresh concrete Part 12 :Self-compacting concrete — J-ring test*.

BS EN 12390-3. 2009. *Testing hardened concrete. Compressive strength of test specimens*.

BS EN 12390-6. 2009. *Testing hardened concrete. Tensile splitting strength of test specimens*.

Bui, V.K., Montgomery, D., Hinczak, I. and Turner, K. 2002. Rapid testing method for segregation resistance of self-compacting concrete. *Cement and Concrete Research* 32(9), pp. 1489–1496. doi: 10.1016/S0008-8846(02)00811-6.

Bulut, H.A. and Şahin, R. 2022. Radiological characteristics of Self-Compacting Concretes incorporating fly ash, silica fume, and slag. *Journal of Building Engineering* 58, p. 104987. doi: 10.1016/J.JOBE.2022.104987.

Busari, A.A., Akinmusuru, J.O. and Dahunsi, B.I. 2018. Review of sustainability in self-compacting concrete: The use of waste and mineral additives as supplementary cementitious materials and aggregates. *Portugaliae Electrochimica Acta* 36(3), pp. 147–162. doi: 10.4152/pea.201803147.

Campos, H.F., Klein, N.S. and Marques Filho, J. 2020a. Proposed mix design method for sustainable high-strength concrete using particle packing optimization. *Journal of Cleaner Production* 265, p. 121907. doi: 10.1016/J.JCLEPRO.2020.121907.

Campos, H.F., Klein, N.S. and Marques Filho, J. 2020b. Proposed mix design method for sustainable high-strength concrete using particle packing optimization. *Journal of Cleaner Production* 265, p. 121907. Available at:

https://doi.org/10.1016/j.jclepro.2020.121907.

Cao, C., Sun, W. and Qin, H. 2000. The analysis on strength and fly ash effect of roller-compacted concrete with high volume fly ash. *Cement and Concrete Research* 30(1), pp. 71–75. doi: 10.1016/S0008-8846(99)00203-3.

Caruana, R. and Niculescu-Mizil, A. 2006. An empirical comparison of supervised learning algorithms. In: *Proceedings of the 23rd International Conference on Machine Learning*. ICML ’06. New York, NY, USA: Association for Computing Machinery, pp. 161–168. Available at: https://doi.org/10.1145/1143844.1143865.

Celik, K., Meral, C., Petek Gursel, A., Mehta, P.K., Horvath, A. and Monteiro, P.J.M. 2015. Mechanical properties, durability, and life-cycle assessment of self-consolidating concrete mixtures made with blended portland cements containing fly ash and limestone powder. *Cement and Concrete Composites* 56, pp. 59–72. doi: 10.1016/J.CEMCONCOMP.2014.11.003.

Centing, M., Jönsson, U., Nilsson, H., Tuutti, K. and Widenbrant, M. 2002. Site applications of self compacting and pigmented concrete. In: *Innovations and Developments In Concrete Materials And Construction*. Thomas Telford Publishing, pp. 465–472. Available at: https://www.icevirtuallibrary.com/doi/abs/10.1680/iadicmac.31791.0045.

Chandru, P., Natarajan, C. and Karthikeyan, J. 2018. Influence of sustainable materials in strength and durability of self-compacting concrete: a review. *Journal of Building Pathology and Rehabilitation* 3(1). doi: 10.1007/s41024-018-0037-1.

Chen, T. and Guestrin, C. 2016. XGBoost: A scalable tree boosting system. In: *Proceedings of the ACM SIGKDD International Conference on Knowledge Discovery and Data Mining*. Association for Computing Machinery, pp. 785–794.

doi: 10.1145/2939672.2939785.

Chen, T. and He, T. 2015. *XGBoost: Extreme Gradient Boosting*.

Chen, Z., Iftikhar, B., Ahmad, A., Dodo, Y., Abuhussain, M.A., Althoey, F. and Sufian, M. 2023. Strength evaluation of eco-friendly waste-derived self-compacting concrete via interpretable genetic-based machine learning models. *Materials Today Communications* 37. doi: 10.1016/j.mtcomm.2023.107356.

Cheng, M.Y., Chou, J.S., Roy, A.F.V. and Wu, Y.W. 2012. High-performance Concrete Compressive Strength Prediction using Time-Weighted Evolutionary Fuzzy Support Vector Machines Inference Model. *Automation in Construction* 28, pp. 106–115. doi: 10.1016/j.autcon.2012.07.004.

Cherkassky, V. and Ma, Y. 2004. Practical selection of SVM parameters and noise estimation for SVM regression. *Neural Networks* 17(1), pp. 113–126. doi: 10.1016/S0893-6080(03)00169-2.

Choudhary, R., Gupta, R. and Nagar, R. 2020. Impact on fresh, mechanical, and microstructural properties of high strength self-compacting concrete by marble cutting slurry waste, fly ash, and silica fume. *Construction and Building Materials* 239, p. 117888. Available at: https://doi.org/10.1016/j.conbuildmat.2019.117888 [Accessed: 8 November 2021].

Collepardi, M., Collepardi, S., Olagot, J.J.O., Troli, R. and Collepardi, M. 2003. Laboratory-tests and field-experiences of high-performance SCCs. In: *3rd Int. RILEM Symp. on Self-Compacting Concrete*. Cachan Cedex: RILEM Publication, pp. 904–912.

Concha, N.C. and Baccay, M.A. 2020. Effects of mineral and chemical admixtures on the rheological properties of self compacting concrete. *International Journal of GEOMATE* 18(66), pp. 24–29. doi:

10.21660/2020.66.9138.

Corinaldesi, V. and Moriconi, G. 2011. The role of industrial by-products in self-compacting concrete. *Construction and Building Materials* 25(8), pp. 3181–3186. doi: 10.1016/J.CONBUILDMAT.2011.03.001.

Cortes, C., Vapnik, V. and Saitta, L. 1995. *Support-Vector Networks Editor*. Kluwer Academic Publishers.

Cuenca, J., Rodríguez, J., Martín-Morales, M., Sánchez-Roldán, Z. and Zamorano, M. 2013. Effects of olive residue biomass fly ash as filler in self-compacting concrete. *Construction and Building Materials* 40, pp. 702–709. doi: 10.1016/J.CONBUILDMAT.2012.09.101.

Cui, T., Alshahrani, A. and Kulasegaram, S. 2024a. Effects of mineral additions on the rheological properties of self-compacting concrete: a review. *Proceedings of Institution of Civil Engineers: Construction Materials*. doi: 10.1680/jcoma.22.00105.

Cui, T., Kulasegaram, S. and Li, H. 2024b. Design automation of sustainable self-compacting concrete containing fly ash via data driven performance prediction. *Journal of Building Engineering* 87, p. 108960. doi: 10.1016/J.JOBE.2024.108960.

Dadsetan, S. and Bai, J. 2017. Mechanical and microstructural properties of self-compacting concrete blended with metakaolin, ground granulated blast-furnace slag and fly ash. *Construction and Building Materials* 146, pp. 658–667. doi: 10.1016/J.CONBUILDMAT.2017.04.158.

Damineli, B.L., Kemeid, F.M., Aguiar, P.S. and John, V.M. 2010. Measuring the eco-efficiency of cement use. *Cement and Concrete Composites* 32(8), pp. 555–562. doi: 10.1016/J.CEMCONCOMP.2010.07.009.

Deeb, R. and Karihaloo, B.L. 2013. Mix proportioning of self-compacting normal and high-strength concretes. *Magazine of Concrete Research* 65(9), pp. 546–556. doi: 10.1680/macr.12.00164.

de-Prado-Gil, J., Palencia, C., Silva-Monteiro, N. and Martínez-García, R. 2022. To predict the compressive strength of self compacting concrete with recycled aggregates utilizing ensemble machine learning models. *Case Studies in Construction Materials* 16, p. e01046. Available at: https://linkinghub.elsevier.com/retrieve/pii/S2214509522001784.

DeRousseau, M.A., Kasprzyk, J.R. and Srubar, W. V. 2018. Computational design optimization of concrete mixtures: A review. *Cement and Concrete Research* 109, pp. 42–53. doi: 10.1016/j.cemconres.2018.04.007.

Dev, B., Rahman, M.A., Islam, M.J., Rahman, M.Z. and Zhu, D. 2024. Properties prediction of composites based on machine learning models: A focus on statistical index approaches. *Materials Today Communications* 38, p. 107659. doi: 10.1016/J.MTCOMM.2023.107659.

Devi, K., Aggarwal, P. and Saini, B. 2020. Admixtures Used in Self-Compacting Concrete: A Review. *Iranian Journal of Science and Technology - Transactions of Civil Engineering* 44(2), pp. 377–403. Available at: https://doi.org/10.1007/s40996-019-00244-4.

Dey, S., Kumar, V.V.P., Goud, K.R. and Basha, S.K.J. 2021. State of art review on self compacting concrete using mineral admixtures. *Journal of Building Pathology and Rehabilitation* 6(1). doi: 10.1007/s41024-021-00110-9.

Dinakar, P., Sethy, K.P. and Sahoo, U.C. 2013. Design of self-compacting concrete with ground granulated blast furnace slag. *Materials and Design* 43, pp. 161–169. doi: 10.1016/j.matdes.2012.06.049.

Dransfield, J. 2003. Admixtures for concrete, mortar and grout. *Advanced concrete technology* 3, pp. 3–36.

Drucker·, H., Burges, C.J.C., Kaufman, L., Smola, A. and Vapnik, V. 1996. Support Vector Regression Machines. In: *Advances in Neural Information Processing Systems 9 (NIPS 1996)*. pp. 155–161.

EFNARC. 2005. *The European Guidelines for Self-Compacting Concrete*. Available at: http://www.efnarc.org/pdf/SCCGuidelinesMay2005.pdf.

Einstein, A. 1956. *Investigations on the Theory of the Brownian Movement*. Courier Corporation.

Elyamany, H.E., Abd Elmoaty, A.E.M. and Mohamed, B. 2014. Effect of filler types on physical, mechanical and microstructure of self compacting concrete and Flow-able concrete. *Alexandria Engineering Journal* 53(2), pp. 295–307. doi: 10.1016/J.AEJ.2014.03.010.

Esquinas, A.R., Ledesma, E.F., Otero, R., Jiménez, J.R. and Fernández, J.M. 2018. Mechanical behaviour of self-compacting concrete made with non-conforming fly ash from coal-fired power plants. *Construction and Building Materials* 182, pp. 385–398. doi: 10.1016/J.CONBUILDMAT.2018.06.094.

Faraj, R.H., Mohammed, A.A., Omer, K.M. and Ahmed, H.U. 2022. Soft computing techniques to predict the compressive strength of green self-compacting concrete incorporating recycled plastic aggregates and industrial waste ashes. *Clean Technologies and Environmental Policy* 24(7), pp. 2253–2281. doi: 10.1007/s10098-022-02318-w.

Farooq, F. et al. 2021. A Comparative Study for the Prediction of the Compressive Strength of Self-Compacting Concrete Modified with Fly Ash. *Materials*. Available at: https://doi.org/10.3390/ma14174934.

Feldman, R.F., Carette, G.G. and Malhotra, V.M. 1990. Studies on mechanics of development of physical and mechanical properties of high-volume fly ash-cement pastes. *Cement and Concrete Composites* 12(4), pp. 245–251. doi:

10.1016/0958-9465(90)90003-G.

Felekoğlu, B., Türkel, S. and Baradan, B. 2007. Effect of water/cement ratio on the fresh and hardened properties of self-compacting concrete. *Building and Environment* 42(4), pp. 1795–1802. doi: 10.1016/j.buildenv.2006.01.012.

Ferdosian, I. and Camões, A. 2021. Mechanical performance and post-cracking behavior of self-compacting steel-fiber reinforced eco-efficient ultra-high performance concrete. *Cement and Concrete Composites* 121, p. 104050. doi: 10.1016/J.CEMCONCOMP.2021.104050.

Ferrara, L., Bamonte, P., Caverzan, A., Musa, A. and Sanal, I. 2012. A comprehensive methodology to test the performance of Steel Fibre Reinforced Self-Compacting Concrete (SFR-SCC). *Construction and Building Materials* 37, pp. 406–424. doi: 10.1016/j.conbuildmat.2012.07.057.

Feys, D. 2006. The rheology of self-compacting concrete made with Belgian materials. (September). doi: 10.1617/2351580028.060.

Feys, D., Cepuritis, R., Jacobsen, S., Lesage, K., Secrieru, E. and Yahia, A. 2017. Measuring Rheological Properties of Cement Pastes: Most common Techniques, Procedures and Challenges. *RILEM Technical Letters* 2, pp. 129–135. doi: 10.21809/rilemtechlett.2017.43.

Feys, D., Verhoeven, R. and De Schutter, G. 2008. Fresh self compacting concrete, a shear thickening material. *Cement and Concrete Research* 38(7), pp. 920–929. doi: 10.1016/j.cemconres.2008.02.008.

Frazão, C., Camões, A., Barros, J. and Gonçalves, D. 2015. Durability of steel fiber reinforced self-compacting concrete. *Construction and Building Materials* 80, pp. 155–166. doi: 10.1016/J.CONBUILDMAT.2015.01.061.

Freund, Y. and Schapire, R.E. 1997. *Journal of Computer and System Sciences s SS1504 journal of computer and system sciences*.

Friedman, J.H. 2001. *Greedy Function Approximation: A Gradient Boosting Machine*.

Ganta, J.K., Seshagiri Rao, M. V., Mousavi, S.S., Srinivasa Reddy, V. and Bhojaraju, C. 2020. Hybrid steel/glass fiber-reinforced self-consolidating concrete considering packing factor: Mechanical and durability characteristics. *Structures* 28, pp. 956–972. doi: 10.1016/J.ISTRUC.2020.09.042.

Gesoĝlu, M., Güneyisi, E., Mahmood, S.F., öz, H. öznur and Mermerdaş, K. 2012. Recycling ground granulated blast furnace slag as cold bonded artificial aggregate partially used in self-compacting concrete. *Journal of Hazardous Materials* 235–236, pp. 352–358. doi: 10.1016/J.JHAZMAT.2012.08.013.

Ghanbari, A. and Karihaloo, B.L. 2009. Prediction of the plastic viscosity of self-compacting steel fibre reinforced concrete. *Cement and Concrete Research* 39(12), pp. 1209–1216. Available at: http://dx.doi.org/10.1016/j.cemconres.2009.08.018 [Accessed: 21 October 2021].

Ghasemi, M., Ghasemi, M.R. and Mousavi, S.R. 2019. Studying the fracture parameters and size effect of steel fiber-reinforced self-compacting concrete. *Construction and Building Materials* 201, pp. 447–460. Available at: https://doi.org/10.1016/j.conbuildmat.2018.12.172.

Ghazi, K. and Al Jadiri, R.S. 2010. New method for proportioning self-consolidating concrete based on compressive strength requirements. *ACI Materials Journal* 107(5), pp. 490–497.

Girish, S., Ranganath, R. V. and Vengala, J. 2010. Influence of powder and paste on flow properties of SCC. *Construction and Building Materials* 24(12), pp. 2481–2488. doi: 10.1016/j.conbuildmat.2010.06.008.

Golafshani, E.M. and Ashour, A. 2016. Prediction of self-compacting concrete elastic modulus using two symbolic regression techniques. *Automation in Construction* 64, pp. 7–19. doi: 10.1016/J.AUTCON.2015.12.026.

Gudivada, V.N., Apon, A. and Ding, J. 2017. Data Quality Considerations for Big Data and Machine Learning: Going Beyond Data Cleaning and Transformations. *International Journal on Advances in Software* 10(1), pp. 1–20. Available at: www.iaria.org.

Gueciouer, D., Youcef, G. and Tarek, N. 2022. Rheological and mechanical optimization of a steel fiber reinforced self-compacting concrete using the design of experiments method. *European Journal of Environmental and Civil Engineering* 26(3), pp. 1097–1117. doi: 10.1080/19648189.2019.1697758.

Güneyisi, E. 2010. Fresh properties of self-compacting rubberized concrete incorporated with fly ash. *Materials and Structures/Materiaux et Constructions* 43(8), pp. 1037–1048. doi: 10.1617/s11527-009-9564-1.

Güneyisi, E., Gesoglu, M., Al-Goody, A. and Ipek, S. 2015. Fresh and rheological behavior of nano-silica and fly ash blended self-compacting concrete. *Construction and Building Materials* 95, pp. 29–44. doi: 10.1016/j.conbuildmat.2015.07.142.

Guo, Z., Jiang, T., Zhang, J., Kong, X., Chen, C. and Lehman, D.E. 2020a. Mechanical and durability properties of sustainable self-compacting concrete with recycled concrete aggregate and fly ash , slag and silica fume. *Construction and Building Materials* 231, p. 117115. doi: 10.1016/j.conbuildmat.2019.117115.

Guo, Z., Zhang, J., Jiang, T., Jiang, T., Chen, C., Bo, R. and Sun, Y. 2020b. Development of sustainable self-compacting concrete using recycled concrete aggregate and fly ash, slag, silica fume. *European Journal of Environmental and Civil Engineering*. Available at:

https://www.tandfonline.com/action/journalInformation?journalCode=tece20.

Gupta, N., Siddique, R. and Belarbi, R. 2021. Sustainable and Greener Self-Compacting Concrete incorporating Industrial By-Products: A Review. *Journal of Cleaner Production* 284, p. 124803. doi: 10.1016/J.JCLEPRO.2020.124803.

Habert, G., Miller, S.A., John, V.M., Provis, J.L., Favier, A., Horvath, A. and Scrivener, K.L. 2020. Environmental impacts and decarbonization strategies in the cement and concrete industries. *Nature Reviews Earth and Environment* 1(11), pp. 559–573. doi: 10.1038/s43017-020-0093-3.

Habert, G. and Roussel, N. 2009. Study of two concrete mix-design strategies to reach carbon mitigation objectives. *Cement and Concrete Composites* 31(6), pp. 397–402. doi: 10.1016/J.CEMCONCOMP.2009.04.001.

Han, T., Jiang, D., Zhao, Q., Wang, L. and Yin, K. 2017. Comparison of random forest, artificial neural networks and support vector machine for intelligent diagnosis of rotating machinery. *Transactions of the Institute of Measurement and Control* 40(8), pp. 2681–2693. Available at: https://doi.org/10.1177/0142331217708242.

Hanif, A., Kim, Y., Lu, Z. and Park, C. 2017a. Early-age behavior of recycled aggregate concrete under steam curing regime. *Journal of Cleaner Production* 152, pp. 103–114. doi: 10.1016/J.JCLEPRO.2017.03.107.

Hanif, A., Kim, Y., Lu, Z. and Park, C. 2017b. Early-age behavior of recycled aggregate concrete under steam curing regime. *Journal of Cleaner Production* 152, pp. 103–114. doi: 10.1016/j.jclepro.2017.03.107.

Hayakawa, M., Matsuoka, Y. and Yokota, K. 1995. Application of superworkable concrete in the construction of 70-story building in Japan. *Special Publication* 154, pp. 381–398.

Heirman, G., Vandewalle, L., Van Gemert, D. and Wallevik, Ó. 2008. Integration approach of the Couette inverse problem of powder type self-compacting concrete in a wide-gap concentric cylinder rheometer. *Journal of Non-Newtonian Fluid Mechanics* 150(2–3), pp. 93–103. doi: 10.1016/j.jnnfm.2007.10.003.

Hooton, R.D. and Emery, J.C. 1983. Glass Content Determination and Strength Development Predictions for Vitrified Blast Furnace Slag. *Publication SP - American Concrete Institute* 2, pp. 943–962.

Hsu, C.-W., Chang, C.-C. and Lin, C.-J. 2003. A Practical Guide to Support Vector Classification. pp. 1–16.

Huang, P., Dai, K. and Yu, X. 2023a. Machine learning approach for investigating compressive strength of self-compacting concrete containing supplementary cementitious materials and recycled aggregate. *Journal of Building Engineering* 79. doi: 10.1016/j.jobe.2023.107904.

Huang, P., Dai, K. and Yu, X. 2023b. Machine learning approach for investigating compressive strength of self-compacting concrete containing supplementary cementitious materials and recycled aggregate. *Journal of Building Engineering* 79. doi: 10.1016/j.jobe.2023.107904.

Hubel, D.H. and Wiesel, A.T.N. 1962. Receptive fields, binocular interaction and functional architecture in the cat's visual cortex. *J. Phyiiol* 160(1), pp. 106–154.

Jagadesh, P., de Prado-Gil, J., Silva-Monteiro, N. and Martínez-García, R. 2023. Assessing the compressive strength of self-compacting concrete with recycled aggregates from mix ratio using machine learning approach. *Journal of Materials Research and Technology* 24, pp. 1483–1498. doi: 10.1016/j.jmrt.2023.03.037.

Jain, A., Gupta, R. and Chaudhary, S. 2020. Sustainable development of self-compacting concrete by using granite waste and fly ash. *Construction and*

Building Materials 262, p. 120516. doi: 10.1016/J.CONBUILDMAT.2020.120516.

Jalal, M. and Mansouri, E. 2012. Effects of fly ash and cement content on rheological, mechanical, and transport properties of high-performance self-compacting concrete. *Science and Engineering of Composite Materials* 19(4), pp. 393–405. doi: 10.1515/secm-2012-0052.

Kamilaris, A. and Prenafeta-Boldú, F.X. 2018. Deep learning in agriculture: A survey. *Computers and Electronics in Agriculture* 147, pp. 70–90. doi: 10.1016/J.COMPAG.2018.02.016.

Kanellopoulos, A., Petrou, M.F. and Ioannou, I. 2012. Durability performance of self-compacting concrete. *Construction and Building Materials* 37, pp. 320–325. doi: 10.1016/j.conbuildmat.2012.07.049.

Kanellopoulos, A., Savva, P., Petrou, M.F., Ioannou, I. and Pantazopoulou, S. 2020. Assessing the quality of concrete – reinforcement interface in Self Compacting Concrete. *Construction and Building Materials* 240. doi: 10.1016/j.conbuildmat.2019.117933.

Kang, M.C., Yoo, D.Y. and Gupta, R. 2021. Machine learning-based prediction for compressive and flexural strengths of steel fiber-reinforced concrete. *Construction and Building Materials* 266. doi: 10.1016/j.conbuildmat.2020.121117.

Kannan, V. 2018. Strength and durability performance of self compacting concrete containing self-combusted rice husk ash and metakaolin. *Construction and Building Materials* 160, pp. 169–179. doi: 10.1016/J.CONBUILDMAT.2017.11.043.

Kaveh, A., Bakhshpoori, T. and Hamze-Ziabari, S.M. 2018. M5' and mars based prediction models for properties of selfcompacting concrete containing fly ash.

Periodica Polytechnica Civil Engineering 62(2), pp. 281–294. doi: 10.3311/PPci.10799.

Ke, G. et al. 2017. LightGBM: A Highly Efficient Gradient Boosting Decision Tree. In: Guyon, I., Luxburg, U. Von, Bengio, S., Wallach, H., Fergus, R., Vishwanathan, S., and Garnett, R. eds. *Advances in Neural Information Processing Systems*. Curran Associates, Inc. Available at: https://proceedings.neurips.cc/paper_files/paper/2017/file/6449f44a102fde848669bdd9eb6b76fa-Paper.pdf.

Khaleel, O.R., Al-Mishhadani, S.A. and Abdul Razak, H. 2011. The Effect of Coarse Aggregate on Fresh and Hardened Properties of Self-Compacting Concrete (SCC). *Procedia Engineering* 14, pp. 805–813. doi: 10.1016/J.PROENG.2011.07.102.

Khaloo, A., Raisi, E.M., Hosseini, P. and Tahsiri, H. 2014. Mechanical performance of self-compacting concrete reinforced with steel fibers. *Construction and Building Materials* 51, pp. 179–186. doi: 10.1016/J.CONBUILDMAT.2013.10.054.

Khan, S.U. and Ayub, T. 2022. Mechanical Properties of Hybrid Self-Compacting Fibre-Reinforced Concrete (SCC-FRC) Containing PVA and PP Fibres. *Iranian Journal of Science and Technology - Transactions of Civil Engineering* 46(3), pp. 2677–2695. doi: 10.1007/s40996-021-00652-5.

Khatib, J.M. 2008. Performance of self-compacting concrete containing fly ash. *Construction and Building Materials* 22(9), pp. 1963–1971. doi: 10.1016/J.CONBUILDMAT.2007.07.011.

Khayat, K.H. 1999. Workability, testing, and performance of self-consolidating concrete. *ACI Materials Journal* 3(96), p. 346.

Khayat, K.H., Ghezal, A. and Hadriche, M.S. 1999. *Factorial design models for* *proportioning self-consolidating concrete*.

Khayat, K.H., Ghezal, A. and Hadriche, M.S. 2000. *Utility of statistical models in proportioning self-consolidating concrete*.

Khodair, Y. and Bommareddy, B. 2017. Self-consolidating concrete using recycled concrete aggregate and high volume of fly ash, and slag. *Construction and Building Materials* 153, pp. 307–316. doi: 10.1016/J.CONBUILDMAT.2017.07.063.

Kirthika, S.K., Singh, S.K. and Chourasia, A. 2020. Alternative fine aggregates in production of sustainable concrete- A review. *Journal of Cleaner Production* 268, p. 122089. doi: 10.1016/J.JCLEPRO.2020.122089.

Koehler, E.P. and Fowler, D.W. 2007. *Aggregates in Self-Consolidating Concrete*. Austin.

Kohavi, R. 1995. *A Study of Cross-Validation and Bootstrap for Accuracy Estimation and Model Selection*. Available at: http://robotics.stanford.edu/~ronnyk.

Krieger, I.M. and Dougherty, T.J. 1959. A Mechanism for Non-Newtonian Flow in Suspensions of Rigid Spheres. *Transactions of the Society of Rheology* 3(1), pp. 137–152. doi: 10.1122/1.548848.

De Kruif, C.G., Van Iersel, E.M.F., Vrij, A. and Russel, W.B. 1985. Hard sphere colloidal dispersions: Viscosity as a function of shear rate and volume fraction. *The Journal of Chemical Physics* 83(9), pp. 4717–4725. doi: 10.1063/1.448997.

Kumar, B.N. and Kumar, P.P. 2022. Prediction on Flexural strength of High Strength Hybrid Fiber Self Compacting Concrete by using Artificial Intelligence. *Journal of Artificial Intelligence and Capsule Networks* 4(1), pp. 1–16. doi: 10.36548/jaicn.2022.1.001.

Kumar, S., Murthi, P., Awoyera, P., Gobinath, R. and Kumar, S. 2022. Impact Resistance and Strength Development of Fly Ash Based Self-compacting Concrete. *Silicon* 14, pp. 481–492. Available at: https://doi.org/10.1007/s12633-020-00842-2.

Kumar, S., Rai, B., Biswas, R., Samui, P. and Kim, D. 2020. Prediction of rapid chloride permeability of self-compacting concrete using Multivariate Adaptive Regression Spline and Minimax Probability Machine Regression. *Journal of Building Engineering* 32. doi: 10.1016/j.jobe.2020.101490.

Kurad, R., Silvestre, J.D., de Brito, J. and Ahmed, H. 2017. Effect of incorporation of high volume of recycled concrete aggregates and fly ash on the strength and global warming potential of concrete. *Journal of Cleaner Production* 166, pp. 485–502. doi: 10.1016/J.JCLEPRO.2017.07.236.

Kurda, R., Salih, A., Shakor, P., Saleh, P., Alyousef, R., Ahmed, H. and Aslanif, F. 2022. Mix design of concrete: Advanced particle packing model by developing and combining multiple frameworks. *Construction and Building Materials* 320, p. 126218. doi: 10.1016/J.CONBUILDMAT.2021.126218.

Lecun, Y., Bengio, Y. and Hinton, G. 2015. Deep learning. *Nature* 521(7553), pp. 436–444. Available at: http://colah.github.io/.

Leemann, A., Münch, B., Gasser, P. and Holzer, L. 2006. Influence of compaction on the interfacial transition zone and the permeability of concrete. *Cement and Concrete Research* 36(8), pp. 1425–1433. doi: 10.1016/j.cemconres.2006.02.010.

Lessard, M., Brian Salazar and Caroline Talbot. 2003. Self-consolidating concrete solves challenging placement problems. *Concrete international* 25(12), pp. 80–81.

Li, Q.F. and Song, Z.M. 2022. High-performance concrete strength prediction based on ensemble learning. *Construction and Building Materials* 324, p. 126694. doi: 10.1016/J.CONBUILDMAT.2022.126694.

Li, W., Huang, Z., Cao, F., Sun, Z. and Shah, S.P. 2015. Effects of nano-silica and nano-limestone on flowability and mechanical properties of ultra-high-performance concrete matrix. *Construction and Building Materials* 95, pp. 366–374. doi: 10.1016/J.CONBUILDMAT.2015.05.137.

Liu, J., Li, C., Ye, M. and Liu, Z. 2019. On the shear viscosity of dilute suspension containing elliptical porous particles at low Reynolds number. *Powder Technology* 354, pp. 108–114. doi: 10.1016/J.POWTEC.2019.05.068.

Liu, J., Zang, S., Yang, F., Hai, R. and Yan, Y. 2023. Fracture properties of steel fibre reinforced high-volume fly ash self-compacting concrete. *Case Studies in Construction Materials* 18, p. e02110. doi: 10.1016/J.CSCM.2023.E02110.

Liu, M. 2010. Self-compacting concrete with different levels of pulverized fuel ash. *Construction and Building Materials* 24(7), pp. 1245–1252. doi: 10.1016/J.CONBUILDMAT.2009.12.012.

Liu, Z. et al. 2020. Carbon Monitor, a near-real-time daily dataset of global CO2 emission from fossil fuel and cement production. *Scientific Data* 7(1). doi: 10.1038/s41597-020-00708-7.

Long, G., Gao, Y. and Xie, Y. 2015. Designing more sustainable and greener self-compacting concrete. *Construction and Building Materials* 84, pp. 301–306. doi: 10.1016/j.conbuildmat.2015.02.072.

Long, W., Cheng, B., Luo, S., Li, L. and Mei, L. 2023. Interpretable auto-tune machine learning prediction of strength and flow properties for self-compacting concrete. *Construction and Building Materials* 393. doi: 10.1016/j.conbuildmat.2023.132101.

Lundberg, S. and Lee, S.-I. 2017. A Unified Approach to Interpreting Model

Predictions. *Advances in neural information processing systems* 30. Available at: http://arxiv.org/abs/1705.07874.

Madandoust, R., Ranjbar, M.M., Ghavidel, R. and Fatemeh Shahabi, S. 2015. Assessment of factors influencing mechanical properties of steel fiber reinforced self-compacting concrete. *Materials and Design* 83, pp. 284–294. doi: 10.1016/j.matdes.2015.06.024.

Mahmood, M.S. et al. 2023. Enhancing compressive strength prediction in self-compacting concrete using machine learning and deep learning techniques with incorporation of rice husk ash and marble powder. *Case Studies in Construction Materials* 19. doi: 10.1016/j.cscm.2023.e02557.

Mardani-Aghabaglou, A., Tuyan, M., Yilmaz, G., Ariöz, Ö. and Ramyar, K. 2013. Effect of different types of superplasticizer on fresh, rheological and strength properties of self-consolidating concrete. *Construction and Building Materials* 47, pp. 1020–1025. doi: 10.1016/J.CONBUILDMAT.2013.05.105.

Mashhadban, H., Kutanaei, S.S. and Sayarinejad, M.A. 2016. Prediction and modeling of mechanical properties in fiber reinforced self-compacting concrete using particle swarm optimization algorithm and artificial neural network. *Construction and Building Materials* 119, pp. 277–287. doi: 10.1016/j.conbuildmat.2016.05.034.

Matos, P.R. de, Foiato, M. and Prudêncio, L.R. 2019. Ecological, fresh state and long-term mechanical properties of high-volume fly ash high-performance self-compacting concrete. *Construction and Building Materials* 203, pp. 282–293. Available at: https://doi.org/10.1016/j.conbuildmat.2019.01.074.

Miarka, P., Seitl, S., Bílek, V. and Cifuentes, H. 2022. Assessment of fatigue resistance of concrete: S-N curves to the Paris' law curves. *Construction and Building Materials* 341, p. 127811. doi: 10.1016/J.CONBUILDMAT.2022.127811.

Miura, T., Takeda, N. and Chikamatsu, R. 1993. Application of super workable concrete to reinforced concreted structures with difficult construction conditions. *Special Publication* 140, pp. 163–186. doi: 10.14359/3787.

Mohammed, A.M., Asaad, D.S. and Al-Hadithi, A.I. 2022. Experimental and statistical evaluation of rheological properties of self-compacting concrete containing fly ash and ground granulated blast furnace slag. *Journal of King Saud University - Engineering Sciences* 34(6), pp. 388–397. doi: 10.1016/J.JKSUES.2020.12.005.

Moro, C., El Fil, H., Francioso, V. and Velay-Lizancos, M. 2021. Influence of water-to-binder ratio on the optimum percentage of nano-TiO2 addition in terms of compressive strength of mortars: A laboratory and virtual experimental study based on ANN model. *Construction and Building Materials* 267, p. 120960. doi: 10.1016/J.CONBUILDMAT.2020.120960.

Mostofinejad, D., Bahmani, H., Eshaghi-Milasi, S. and Nozhati, M. 2023. Empirical Relationships for Prediction of Mechanical Properties of High-Strength Concrete. *Iranian Journal of Science and Technology - Transactions of Civil Engineering* 47(1), pp. 315–332. doi: 10.1007/s40996-022-01023-4.

MPA. 2013. *Fact Sheet 18 Embodied CO 2 e of UK cement , additions and cementitious material*. Available at: https://cement.mineralproducts.org/documents/Factsheet_18.pdf.

Mukharjee, B.B. and Patra, R.K. 2022. Effect of Coarse Recycled Aggregate and Rice Husk Ash on Concrete: A Factorial Design Approach. *Iranian Journal of Science and Technology - Transactions of Civil Engineering* 46(6), pp. 4169–4185. doi: 10.1007/s40996-022-00856-3.

Nafees, A. et al. 2022. Modeling of Mechanical Properties of Silica Fume-Based Green Concrete Using Machine Learning Techniques. *Polymers* 14(1).

Available at: https://www.mdpi.com/2073-4360/14/1/30.

Nakagawa, S. and Schielzeth, H. 2013. A general and simple method for obtaining R2 from generalized linear mixed-effects models. *Methods in Ecology and Evolution* 4(2), pp. 133–142. doi: 10.1111/j.2041-210x.2012.00261.x.

Nepomuceno, M.C.S., Pereira-De-Oliveira, L.A. and Lopes, S.M.R. 2014. Methodology for the mix design of self-compacting concrete using different mineral additions in binary blends of powders. *Construction and Building Materials* 64, pp. 82–94. Available at: http://dx.doi.org/10.1016/j.conbuildmat.2014.04.021.

Nepomuceno, M.C.S., Pereira-De-Oliveira, L.A., Lopes, S.M.R. and Franco, R.M.C. 2016. Maximum coarse aggregate's volume fraction in self-compacting concrete for different flow restrictions. *Construction and Building Materials* 113, pp. 851–856. Available at: http://dx.doi.org/10.1016/j.conbuildmat.2016.03.143.

Ngueilbaye, A., Wang, H., Mahamat, D.A. and Junaidu, S.B. 2021. Modulo 9 model-based learning for missing data imputation. *Applied Soft Computing* 103, p. 107167. doi: 10.1016/J.ASOC.2021.107167.

Nikbin, I.M., Beygi, M.H.A., Kazemi, M.T., Vaseghi Amiri, J., Rabbanifar, S., Rahmani, E. and Rahimi, S. 2014. A comprehensive investigation into the effect of water to cement ratio and powder content on mechanical properties of self-compacting concrete. *Construction and Building Materials* 57, pp. 69–80. doi: 10.1016/j.conbuildmat.2014.01.098.

Okamura, H. and Masahiro, O. 2003. Self-compacting concrete. *Journal of advanced concrete technology* 1(1), pp. 5–15.

Okamura, H. and Ouchi, M. 2003. Self-compacting concrete. *Journal of Advanced Concrete Technology* 1(1), pp. 5–15. doi: 10.3151/jact.1.5.

Okamura, H., Ozawa, K. and Ouchi, M. 2000. Self-compacting concrete.

Structural Concrete 1(1), pp. 3–17. Available at: https://www.icevirtuallibrary.com/doi/abs/10.1680/stco.2000.1.1.3.

Oreta, A.W.C. and Kawashima, K. 2003. Neural Network Modeling of Confined Compressive Strength and Strain of Circular Concrete Columns. *Journal of Structural Engineering* 129(4), pp. 554–561. doi: 10.1061/(asce)0733-9445(2003)129:4(554).

Ouchi, M., Osterberg, T. and Hallberg, S.-E. 2003. *Applications of self-compacting concrete in Japan, Europe and the United States*.

Ouedraogo, H.A., Özen, S., Kobya, V., Sagiroglu, S. and Mardani-Aghabaglou, A. 2021. Comparison of fresh and hardened properties of self-compacting concrete mixture from different aspect ratio of steel fiber view point. *Journal of Green Building* 16(1), pp. 115–138. Available at: http://meridian.allenpress.com/jgb/article-pdf/16/1/115/3017539/i1943-4618-16-1-115.pdf.

Öz, A., Bayrak, B. and Aydın, A.C. 2021. The effect of trio-fiber reinforcement on the properties of self-compacting fly ash concrete. *Construction and Building Materials* 274. doi: 10.1016/j.conbuildmat.2020.121825.

Ozawa, K. 1989. High performance concrete based on the durability design of concrete structures. In: *The Second East Asia-Pasific Conference on Structural Engineering & Construction*.

Ozawa, K. 1992. Role of powder materials on the filling capacity of fresh concrete. In: *Proceeding of the first international symposium of fly ash, silica fume, slag and natural pozzolans in concrete*. Istanbul.

Pająk, M. and Ponikiewski, T. 2013. Flexural behavior of self-compacting concrete reinforced with different types of steel fibers. *Construction and Building Materials* 47, pp. 397–408. doi: 10.1016/j.conbuildmat.2013.05.072.

Pal, S.C., Mukherjee, A. and Pathak, S.R. 2003. Investigation of hydraulic activity of ground granulated blast furnace slag in concrete. *Cement and Concrete Research* 33(9), pp. 1481–1486. doi: 10.1016/S0008-8846(03)00062-0.

Pang, L., Liu, Z., Wang, D. and An, M. 2022. Review on the Application of Supplementary Cementitious Materials in Self-Compacting Concrete. *Crystals* 12(2). doi: 10.3390/cryst12020180.

Paris M, Tavano S and Albiero E. 2003. Self-compacting concrete (SCC): the construction of the base for the mill of the unimed cement plant of Barletta (Italy). In: *International RILEM Symposium on Self-Compacting Concrete*. RILEM Publications SARL, pp. 1017–1025.

Pazouki, G., Golafshani, E.M. and Behnood, A. 2021. Predicting the compressive strength of self-compacting concrete containing Class F fly ash using metaheuristic radial basis function neural network. *Structural Concrete*. doi: 10.1002/suco.202000047.

Péra, J., Husson, S. and Guilhot, B. 1999. Influence of finely ground limestone on cement hydration. *Cement and Concrete Composites* 21(2), pp. 99–105. doi: 10.1016/S0958-9465(98)00020-1.

Persson, B. 2001. A comparison between mechanical properties of self-compacting concrete and the corresponding properties of normal concrete. (31), pp. 193–198.

Pigott, T.D. 2001. A review of methods for missing data. *International Journal of Phytoremediation* 21(1), pp. 353–383. doi: 10.1076/edre.7.4.353.8937.

Ponikiewski, T. and Gołaszewski, J. 2014. The effect of high-calcium fly ash on selected properties of self-compacting concrete. *Archives of Civil and Mechanical Engineering* 14(3), pp. 455–465. doi: 10.1016/j.acme.2013.10.014.

Ponikiewski, T. and Katzer, J. 2014. Properties of fresh SCC mix reinforced by different types of steel and polymer fibre. *Construction and Building Materials* 62, pp. 96–101. doi: 10.1016/J.CONBUILDMAT.2014.03.037.

Ramanathan, P., Baskar, I., Muthupriya, P. and Venkatasubramani, R. 2013. Performance of self-compacting concrete containing different mineral admixtures. *KSCE Journal of Civil Engineering* 17(2), pp. 465–472. Available at: www.springer.com/12205.

Rasekh, H., Joshaghani, A., Jahandari, S., Aslani, F. and Ghodrat, M. 2020. Rheology and workability of SCC. In: *Self-Compacting Concrete: Materials, Properties and Applications*. Woodhead Publishing, pp. 31–63. doi: 10.1016/B978-0-12-817369-5.00002-7.

Revilla-Cuesta, V., Ortega-López, V., Skaf, M. and Manso, J.M. 2020. Effect of fine recycled concrete aggregate on the mechanical behavior of self-compacting concrete. *Construction and Building Materials* 263. doi: 10.1016/j.conbuildmat.2020.120671.

Robalo, K., Soldado, E., Costa, H., do Carmo, R., Alves, H. and Júlio, E. 2021. Efficiency of cement content and of compactness on mechanical performance of low cement concrete designed with packing optimization. *Construction and Building Materials* 266, p. 121077. doi: 10.1016/J.CONBUILDMAT.2020.121077.

Roh, Y., Heo, G. and Whang, S.E. 2021. A Survey on Data Collection for Machine Learning: A Big Data-AI Integration Perspective. *IEEE Transactions on Knowledge and Data Engineering* 33(4), pp. 1328–1347. doi: 10.1109/TKDE.2019.2946162.

Rosenblatt, F. 1958. The perceptron: A probabilistic model for information storage and organization in the brain. *Psychological Review* 65(6), pp. 386–

408.

Rumelhart, D.E., Hinton, G.E. and Williams, R.J. 1986. Learning representations by back-propagating errors. *Nature* 323(6088), pp. 533–536. Available at: https://doi.org/10.1038/323533a0.

Saha, P., Debnath, P. and Thomas, P. 2020. Prediction of fresh and hardened properties of self-compacting concrete using support vector regression approach. *Neural Computing and Applications* 32(12), pp. 7995–8010. doi: 10.1007/s00521-019-04267-w.

Şahmaran, M., Lachemi, M., Erdem, T.K. and Yücel, H.E. 2011. Use of spent foundry sand and fly ash for the development of green self-consolidating concrete. *Materials and Structures/Materiaux et Constructions* 44(7), pp. 1193–1204. doi: 10.1617/s11527-010-9692-7.

Sahraoui, M. and Bouziani, T. 2019. Effects of fine aggregates types and contents on rheological and fresh properties of SCC. *Journal of Building Engineering* 26, p. 100890. doi: 10.1016/J.JOBE.2019.100890.

Sai Neeraja, V. and Sharma, V. 2023. An overview of fresh and mechanical properties of recycled coarse aggregate self- compacting concrete. In: *Materials Today: Proceedings*. Elsevier Ltd, pp. 211–216. doi: 10.1016/j.matpr.2023.07.120.

Saleh Ahari, R., Kemal Erdem, T. and Ramyar, K. 2015. Effect of various supplementary cementitious materials on rheological properties of self-consolidating concrete. *Construction and Building Materials* 75, pp. 89–98. doi: 10.1016/J.CONBUILDMAT.2014.11.014.

Sambangi, A. and Arunakanthi, E. 2021. Fresh and mechanical properties of SCC with fly ash and copper slag as mineral admixtures. *Materials Today: Proceedings* 45, pp. 6687–6693. Available at:

https://doi.org/10.1016/j.matpr.2020.12.144 [Accessed: 4 February 2022].

Sánchez, V.D.A. 2003. Advanced support vector machines and kernel methods. *Neurocomputing* 55(1–2), pp. 5–20. doi: 10.1016/S0925-2312(03)00373-4.

Sanjeev, J. and Sai Nitesh, K.J.N. 2020. Study on the effect of steel and glass fibers on fresh and hardened properties of vibrated concrete and self-compacting concrete. In: *Materials Today: Proceedings*. Elsevier Ltd, pp. 1559–1568. doi: 10.1016/j.matpr.2020.03.208.

Serraye, M., Kenai, S. and Boukhatem, B. 2021. Prediction of compressive strength of self-compacting concrete (SCC) with silica fume using neural networks models. *Civil Engineering Journal (Iran)* 7(1), pp. 118–139. doi: 10.28991/cej-2021-03091642.

Sharifani, K. and Amini, M. 2023. Machine Learning and Deep Learning: A Review of Methods and Applications. *World Information Technology and Engineering Journal* 10(7), pp. 3897–3904. Available at: https://ssrn.com/abstract=4458723.

Shi, C., Wu, Z., Lv, K. and Wu, L. 2015. A review on mixture design methods for self-compacting concrete. *Construction and Building Materials* 84, pp. 387–398. Available at: http://dx.doi.org/10.1016/j.conbuildmat.2015.03.079.

Siad, H., Kamali-Bernard, S., Mesbah, H.A., Escadeillas, G., Mouli, M. and Khelafi, H. 2013. Characterization of the degradation of self-compacting concretes in sodium sulfate environment: Influence of different mineral admixtures. *Construction and Building Materials* 47, pp. 1188–1200. doi: 10.1016/J.CONBUILDMAT.2013.05.086.

Siddique, R. 2011. Properties of self-compacting concrete containing class F fly ash. *Materials & Design* 32(3), pp. 1501–1507. doi: 10.1016/J.MATDES.2010.08.043.

Siddique, R., Kaur, G. and Kunal. 2016. Strength and permeation properties of self-compacting concrete containing fly ash and hooked steel fibres. *Construction and Building Materials* 103, pp. 15–22. doi: 10.1016/j.conbuildmat.2015.11.044.

Simalti, A. and Singh, A.P. 2021. Comparative study on performance of manufactured steel fiber and shredded tire recycled steel fiber reinforced self-consolidating concrete. *Construction and Building Materials* 266, p. 121102. doi: 10.1016/J.CONBUILDMAT.2020.121102.

Skender, Z., Bali, A. and Kettab, R. 2021. Self-compacting concrete (SCC) behaviour incorporating limestone fines as cement and sand replacement. *European Journal of Environmental and Civil Engineering* 25(10), pp. 1852–1873. Available at: https://doi.org/10.1080/19648189.2019.1607564.

Sonebi, M. 2001. Factorial design modelling of mix proportion parameters of underwater composite cement grouts. *Cement and Concrete Research* 31(11), pp. 1553–1560. doi: 10.1016/S0008-8846(01)00583-X.

Sonebi, M. 2004. Medium strength self-compacting concrete containing fly ash: Modelling using factorial experimental plans. *Cement and Concrete Research* 34(7), pp. 1199–1208. doi: 10.1016/J.CEMCONRES.2003.12.022.

Sonebi, M. and Bartos, P.J.M. 1999. Hardened SCC and its bond with concrete. In: *Proceeding of First International RILEM Symposium on Self-Compacting Concrete (PRO 7)*. Stockholm, pp. 275–289.

Sonebi, M. and Cevik, A. 2009. Prediction of Fresh and Hardened Properties of Self-Consolidating Concrete Using Neurofuzzy Approach. *Journal of Materials in Civil Engineering* 21(11), pp. 672–679. doi: 10.1061/(asce)0899-1561(2009)21:11(672).

Sonebi, M., Cevik, A., Grünewald, S. and Walraven, J. 2016. Modelling the fresh properties of self-compacting concrete using support vector machine approach. *Construction and Building Materials* 106, pp. 55–64. Available at: http://dx.doi.org/10.1016/j.conbuildmat.2015.12.035.

Sonebi, M. and Yahia, A. 2020. Mix design procedure, tests, and standards. *Self-Compacting Concrete: Materials, Properties and Applications*, pp. 1–30. doi: 10.1016/B978-0-12-817369-5.00001-5.

Struble, L. and Sun, G.K. 1995. Viscosity of Portland cement paste as a function of concentration. *Advanced Cement Based Materials* 2(2), pp. 62–69. doi: 10.1016/1065-7355(95)90026-8.

Su, N., Hsu, K.-C. and Chai, H.-W. 2001. A simple mix design method for self-compacting concrete. *Cement and Concrete Research* (31), pp. 1799–1807.

Sukumar, B., Nagamani, K. and Srinivasa Raghavan, R. 2008. Evaluation of strength at early ages of self-compacting concrete with high volume fly ash. *Construction and Building Materials* 22(7), pp. 1394–1401. doi: 10.1016/J.CONBUILDMAT.2007.04.005.

Sulthan, F. and Saloma. 2019. Influence of Hooked-EndSteel Fibers on Fresh and Hardened Properties of Steel Fiber Reinforcement Self-Compacting Concrete (SFRSCC). In: *Journal of Physics: Conference Series*. Institute of Physics Publishing. doi: 10.1088/1742-6596/1198/3/032005.

Sun, J. and Xia, Y. 2024. Pretreating and normalizing metabolomics data for statistical analysis. *Genes & Diseases* 11(3), p. 100979. doi: 10.1016/J.GENDIS.2023.04.018.

Sun, J., Zhang, J., Gu, Y., Huang, Y., Sun, Y. and Ma, G. 2019. Prediction of permeability and unconfined compressive strength of pervious concrete using evolved support vector regression. *Construction and Building Materials* 207, pp. 440–449. doi: 10.1016/j.conbuildmat.2019.02.117.

Tadi, C. and Rao, T.C. 2022. Investigating the performance of self-compacting concrete pavement containing GGBS. *Materials Today: Proceedings* 49, pp. 2013–2018. doi: 10.1016/J.MATPR.2021.08.160.

Tanaka, K., Sato, K., Watanabe, S., Arima, I. and Suenaga, K. 1993. Development and utilization of high performance concrete employed in the Akashi Kaikyo bridge. *Special Publication* 140, pp. 25–52.

Taylor, K.E. 2001. Summarizing multiple aspects of model performance in a single diagram. *Journal of Geophysical Research Atmospheres* 106(D7), pp. 7183–7192. doi: 10.1029/2000JD900719.

Ting, T.Z.H., Rahman, M.E. and Lau, H.H. 2020. Sustainable lightweight self-compacting concrete using oil palm shell and fly ash. *Construction and Building Materials* 264, p. 120590. doi: 10.1016/J.CONBUILDMAT.2020.120590.

Tso, G.K.F. and Yau, K.K.W. 2007. Predicting electricity energy consumption: A comparison of regression analysis, decision tree and neural networks. *Energy* 32(9), pp. 1761–1768. doi: 10.1016/j.energy.2006.11.010.

Turk, K., Bassurucu, M. and Bitkin, R.E. 2021. Workability, strength and flexural toughness properties of hybrid steel fiber reinforced SCC with high-volume fiber. *Construction and Building Materials* 266, p. 120944. doi: 10.1016/J.CONBUILDMAT.2020.120944.

Turk, K., Oztekin, E. and Kina, C. 2022. Self-compacting concrete with blended short and long fibres: experimental investigation on the role of fibre blend proportion. *European Journal of Environmental and Civil Engineering* 26(3), pp. 905–918. doi: 10.1080/19648189.2019.1686069.

Türkel, S. and Kandemir, A. 2010. Fresh and Hardened Properties of SCC Made with Different Aggregate and Mineral Admixtures. *Journal of Materials in Civil Engineering* 22(10), pp. 1025–1032. doi: 10.1061/(asce)mt.1943-

5533.0000107.

Uysal, M. and Yilmaz, K. 2011. Effect of mineral admixtures on properties of self-compacting concrete. *Cement and Concrete Composites* 33(7), pp. 771–776. doi: 10.1016/J.CEMCONCOMP.2011.04.005.

Uysal, M., Yilmaz, K. and Ipek, M. 2012. The effect of mineral admixtures on mechanical properties, chloride ion permeability and impermeability of self-compacting concrete. *Construction and Building Materials* 27(1), pp. 263–270. doi: 10.1016/J.CONBUILDMAT.2011.07.049.

Vapnik, V. 1999. *The nature of statistical learning theory*. Springer science \& business media.

Vasilić, K. 2015. *A Numerical Model for Self-Compacting Concrete Flow through Reinforced Sections : a Porous Medium Analogy*.

Vejmelková, E., Keppert, M., Grzeszczyk, S., Skaliński, B. and Černý, R. 2011. Properties of self-compacting concrete mixtures containing metakaolin and blast furnace slag. *Construction and Building Materials* 25(3), pp. 1325–1331. doi: 10.1016/J.CONBUILDMAT.2010.09.012.

Van Der Vurst, F., Grünewald, S., Feys, D., Lesage, K., Vandewalle, L., Vantomme, J. and De Schutter, G. 2017. Effect of the mix design on the robustness of fresh self-compacting concrete. *Cement and Concrete Composites* 82, pp. 190–201. doi: 10.1016/J.CEMCONCOMP.2017.06.005.

Wallevik, O.H. 2003. Rheology—a scientific approach to develop self-compacting concrete. In: *3rd International RILEM Symposium on Self-Compacting Concrete*. Reykjavik, pp. 23–31.

Wallevik, O.H. and Wallevik, J.E. 2011a. Rheology as a tool in concrete science: The use of rheographs and workability boxes. *Cement and Concrete Research* 41(12), pp. 1279–1288. Available at:

http://dx.doi.org/10.1016/j.cemconres.2011.01.009 [Accessed: 1 August 2021].

Wallevik, O.H. and Wallevik, J.E. 2011b. Rheology as a tool in concrete science: The use of rheographs and workability boxes. *Cement and Concrete Research* 41(12), pp. 1279–1288. doi: 10.1016/J.CEMCONRES.2011.01.009.

Wang, D., Shi, C., Farzadnia, N., Shi, Z., Jia, H. and Ou, Z. 2018. A review on use of limestone powder in cement-based materials: Mechanism, hydration and microstructures. *Construction and Building Materials* 181, pp. 659–672. doi: 10.1016/J.CONBUILDMAT.2018.06.075.

Wang, X., Wang, K., Taylor, P. and Morcous, G. 2014. Assessing particle packing based self-consolidating concrete mix design method. *Construction and Building Materials* 70, pp. 439–452. doi: 10.1016/J.CONBUILDMAT.2014.08.002.

Wang, X.Y. and Park, K.B. 2015. Analysis of compressive strength development of concrete containing high volume fly ash. *Construction and Building Materials* 98, pp. 810–819. doi: 10.1016/J.CONBUILDMAT.2015.08.099.

Wesche, K. 1991. *Fly ash in concrete: properties and performance*.

Wu, M. et al. 2021. Material design and engineering application of Fair-faced self-compacting concrete. *Construction and Building Materials* 300, p. 123992. doi: 10.1016/J.CONBUILDMAT.2021.123992.

Wu, Y. and Zhou, Y. 2022. Hybrid machine learning model and Shapley additive explanations for compressive strength of sustainable concrete. *Construction and Building Materials* 330, p. 127298. doi: 10.1016/J.CONBUILDMAT.2022.127298.

Xie, T., Mohamad Ali, M.S., Elchalakani, M. and Visintin, P. 2021. Modelling fresh and hardened properties of self-compacting concrete containing supplementary cementitious materials using reactive moduli. *Construction and*

Building Materials 272, p. 121954. Available at: https://doi.org/10.1016/j.conbuildmat.2020.121954.

Xing, H., Zou, B., Liu, X., Wang, X., Chen, Q., Fu, X. and Li, Y. 2020. Effect of particle size distribution on the preparation of ZTA ceramic paste applying for stereolithography 3D printing. *Powder Technology* 359, pp. 314–322. doi: 10.1016/J.POWTEC.2019.09.066.

Yahia, A. and Aïtcin, P.C. 2016. Self-consolidating concrete. In: *Science and Technology of Concrete Admixtures*. Woodhead Publishing, pp. 491–502. doi: 10.1016/B978-0-08-100693-1.00026-6.

Yahia, A. and Khayat, K.H. 2001. Analytical models for estimating yield stress of high-performance pseudoplastic grout. *Cement and Concrete Research* 31(5), pp. 731–738. doi: 10.1016/S0008-8846(01)00476-8.

Yahia, A., Tanimura, M. and Shimoyama, Y. 2005. Rheological properties of highly flowable mortar containing limestone filler-effect of powder content and W/C ratio. *Cement and Concrete Research* 35(3), pp. 532–539. doi: 10.1016/J.CEMCONRES.2004.05.008.

Yang, S., Zhang, J., An, X., Qi, B., Shen, D. and Lv, M. 2021. Effects of fly ash and limestone powder on the paste rheological thresholds of self-compacting concrete. *Construction and Building Materials* 281, p. 122560. Available at: https://doi.org/10.1016/j.conbuildmat.2021.122560 [Accessed: 19 July 2021].

Yardimci, M.Y., Baradan, B. and Taşdemir, M.A. 2014. Effect of fine to coarse aggregate ratio on the rheology and fracture energy of steel fibre reinforced self-compacting concretes. *234Sadhana - Academy Proceedings in Engineering Sciences* 39(6), pp. 1447–1469. doi: 10.1007/s12046-014-0257-2.

Young, B.A., Hall, A., Pilon, L., Gupta, P. and Sant, G. 2019. Can the compressive strength of concrete be estimated from knowledge of the mixture proportions?: New insights from statistical analysis and machine learning methods. *Cement and Concrete Research* 115, pp. 379–388. doi: 10.1016/J.CEMCONRES.2018.09.006.

Yousef, E.A., Mouhcine, B.A., Mounir, Z. and Adil, H.A. 2022. Prediction of compressive strength of self-compacting concrete using four machine learning technics. *Materials Today: Proceedings*. doi: 10.1016/j.matpr.2022.02.487.

Zeyad, A.M. and Almalki, A. 2020. Influence of mixing time and superplasticizer dosage on self-consolidating concrete properties. *Journal of Materials Research and Technology* 9(3), pp. 6101–6115. doi: 10.1016/J.JMRT.2020.04.013.

Zeyad, A.M., Saba, A.M., Shathly, A.B. and Alfaufy, T.H. 2018. Influence of steel fiber content on fresh and hardened properties of self-compacting concrete. In: *AIP Conference Proceedings*. American Institute of Physics Inc. doi: 10.1063/1.5062659.

Zhang, J., Ma, G., Huang, Y., sun, J., Aslani, F. and Nener, B. 2019. Modelling uniaxial compressive strength of lightweight self-compacting concrete using random forest regression. *Construction and Building Materials* 210, pp. 713–719. doi: 10.1016/J.CONBUILDMAT.2019.03.189.

Zhang, J., Xu, P. and Gao, X. 2021. Multi-scale particles optimization for some rheological properties of Eco-SCC: Modelling and experimental study. *Construction and Building Materials* 308, p. 125151. doi: 10.1016/J.CONBUILDMAT.2021.125151.

Zhao, H., Sun, W., Wu, X. and Gao, B. 2015. The properties of the self-compacting concrete with fly ash and ground granulated blast furnace slag mineral admixtures. *Journal of Cleaner Production* 95, pp. 66–74. Available at: http://dx.doi.org/10.1016/j.jclepro.2015.02.050 [Accessed: 9 July 2021].

Zhao, H., Sun, W., Wu, X. and Gao, B. 2022. Sustainable self-compacting concrete containing high-amount industrial by-product fly ash as supplementary cementitious materials. *Environmental Science and Pollution Research* 29, pp. 3616–3628. Available at: https://doi.org/10.1007/s11356-021-15883-2.

Zhao, Z.Q., Zheng, P., Xu, S.T. and Wu, X. 2019. Object Detection with Deep Learning: A Review. *IEEE Transactions on Neural Networks and Learning Systems* 30(11), pp. 3212–3232. doi: 10.1109/TNNLS.2018.2876865.

Zhuang, J., Xu, R., Pan, C. and Li, H. 2022. Dynamic stress–strain relationship of steel fiber-reinforced rubber self-compacting concrete. *Construction and Building Materials* 344, p. 128197. doi: 10.1016/J.CONBUILDMAT.2022.128197.

Zuo, W., Liu, J., Tian, Q., Xu, W., She, W., Feng, P. and Miao, C. 2018. Optimum design of low-binder Self-Compacting Concrete based on particle packing theories. *Construction and Building Materials* 163, pp. 938–948. doi: 10.1016/J.CONBUILDMAT.2017.12.167.

Appendices

Appendix A – Effect of cementitious materials SCC rheology

Table A.7.1 Effect of fly ash on rheological properties of SCC

Reference	w/cm ratio	Replacement ratio (%)	Evaluation of Rheology	Rheological Properties
(Matos et al. 2019)	0.38	40, 50, and 60	Slump flow, V-funnel and L-box tests.	Substituting cement with fly ash enhances the flowability of SCC, leading to decreased requirements for superplasticizer content.
(Yang et al. 2021)	0.33, 0.36 and 0.4	20 and 30	The rheological properties were calculated using Equations based on mini-slump test results.	In the original model, the paste plastic viscosity threshold slightly increases with 30% compared to 20% fly ash, whereas, in the modified model, it significantly decreases for 30% relative to 20% fly ash.
(Mohammed et al. 2022)	0.25	10, 20, 30, 40, 50 and 60	V-funnel and slump flow tests.	The spherical particles of Fly Ash significantly contributed to faster speeds and shorter flow times.
(Concha and	-	15 and 25	V-funnel, slump flow, L-	The ball-bearing effect of spherical fly ash

Baccay 2020)			box, U-box, and screen stability tests.	particles enhances the fluidity of SCC by improving lubrication and reducing cohesion among aggregated particles.
(Ponikiewski and Gołaszewski 2014)	0.41 and 0.38	10, 20 and 30	V-funnel, slump flow, L-box tests.	Self-compacting properties and overall workability of the mix decline with the addition of more ash, while also accelerating the rate at which workability is lost over time.
(Saleh Ahari et al. 2015)	0.44, 0.50, 0.56	18 and 36	Coaxial cylinder concrete rheometer (ConTec 4SCC). The protocol gradually increased the impeller speed to 0.7 rps over 36 seconds and then decreased it stepwise to measure torque,	The partial replacement of PC by fly ash have increased plastic viscosity and yield stress of control mixes. Higher plastic viscosity values in type C fly ash mixtures compared to class F fly ash are attributed to the grain shape, thus improving workability and decreasing plastic viscosity.

generating torque-

rotational velocity data

that linearly corresponded

to a Bingham fluid model.

Table A.7.2 Effect of GGBS on rheological properties of SCC

Reference	w/cm ratio	Replacement ratio (%)	Evaluation of Rheology	Rheological Properties
(Al-Oran et al. 2019)	0.38	15, 20, 25 and 30	Slump flow, V-funnel and L-box tests.	Increasing GGBS up to 25% improves viscosity and reduces flow time due to its larger particle size and lower yield stress compared to cement, facilitating quicker initiation of flow and enhancing overall workability.
(Boukendakdji et al. 2012)	0.4	10, 15, 20 and 25	Slump flow, V-funnel and J-ring tests.	Optimal flowability and reduced T_{500} flow time are achieved at 15% GGBS content, beyond which both segregation and viscosity increase, compromising workability.
(Zhao et al. 2015)	0.35	20, 30 and 40	Slump flow, L-box tests and GTM screen stability test.	The incorporation of GGBS enhances mix flowability by increasing paste volume and reducing friction between aggregates and cementitious materials, owing to the spherical

				nature of GGBS.
(Tadi and Rao 2022)	0.32	10, 20, 30, 40, 50 and 60	Slump flow, V-funnel and L-Box tests.	Increasing slag content decreases plastic viscosity and improves flowability, as evidenced by reduced T50cm slump test times, with mixtures containing 40%, 50%, and 60% GGBS showing notably better results.
(Vejmelková et al. 2011)	0.26	56	Slump flow, J-ring test. Rotary rheometer Con Tec Viscometer with coaxial cylinders was applied, with yield stress and plastic viscosity determined from the rotational moment measurements at speeds ranging from 0.4 to 0.08 rps, aligning with controlled	SCC mix containing GGBS exhibited characteristics of Newtonian fluids, with zero yield stress and increased viscosity

			rates, stresses, and a standard adjustment model.	
(Gesoĝlu et al. 2012)	0.32	Replacement of the Coarse aggregate at level of 20, 40, 60, 80, and 100.	Slump flow, V-funnel, and L-box tests.	SCC mixtures with GGBS demonstrated improved workability, evidenced by reduced times in slump and V-funnel tests and lower viscosity.

Table A.7.3 Effect of LP on rheological properties of SCC

Reference	w/cm ratio	Replacement ratio (%)	Evaluation of Rheology	Rheological Properties
(Uysal and Yilmaz 2011)	0.33	10, 20 and 30	Slump flow and L-box tests.	The addition of LP improved workability, with higher slump flow values and reduced T_{500}.
(Yahia et al. 2005)	0.35, 0.40 and 0.45	20, 30 and40	Slump flow and V-funnel tests.	Within certain limits, LP addition did not alter the fluidity of a mixture with a fixed w/cm and HRWR dosage, but beyond a critical dosage, it significantly increased viscosity.
(Li et al. 2015)	0.16 to 0.22	Nano LP: 1, 2, 3 and 4	Flowability test.	Increasing the content of nano-limestone powder led to lower flowability due to its fine particle sizes, which have higher surface areas that absorb water
(Skender et al. 2021)	0.4	Replacement of cement at level of 0, 5, 10, 15, 20 and 25;	Slump flow, V-funnel, and L-box tests.	Adding LP up to 20% as partial replacement for sand and cement improved SCC properties at the fresh state. The addition of LP lengthens V-

		Replacement of sand at level of 0, 5, 10, 15, 20 and 25		funnel flow times, more noticeably in mixes with sand substituted by LP
(Alani et al. 2021)	0.35	16, 23 and 29	Slump flow, V-funnel, L-box tests.	Incorporating LP into SCC resulted in reduced slump flow spread and increased V-funnel time, indicating a decrease in flowability and an increase in the viscosity.

Appendix B - A MATLAB program for designing HSSCC (C90)

```
%************************************************************************************
% A MATLAB Code for designing Self-Compacting Concrete mixes 2022 Tianyi
% Based on the target compressive strength and plastic viscosity
%************************************************************************************
% List of variables
%************************************************************************************
% WCM Water to cementitious materials ratio
% PV Paste viscosity (values based on w/cm and SP dosage)
% TMV Target mix viscosity
% Z, U and X Random names are used to solve equations
% t1 and t2 Arbitrarily factors are chosen such that t1*t2 =1
% H Unity factor (H=t1*t2)
% CM Cementitious materials (kg)
% WTR Water content (kg)
% CEM Cement content (kg)
% GG Cement replacement materials (kg) e.g. GGBS
% FLA Fly ash(kg)
% SP Superplasticiser dosage (kg)
% VPS Volume of paste per cubic meter
% FS Volume fraction of fine aggregate
```

% FG Volume fraction of coarse aggregate

% WS Mass of fine aggregate

% WG Mass of coarse aggregate

% VLP Volume of filler per cubic meter

% VS Volume of fine aggregate per cubic meter

% VG Volume of coarse aggregate per cubic meter

% TV Total volume of the mix (m3)

% PSRATIO Paste to solid ratio

% FFS A factor larger than unity that predicts the increase in the plastic viscosity induced by addition of fine aggregate

% FFG A factor larger than unity that predicts the increase in the plastic viscosity induced by addition of coarse aggregate

% AMV Actual mix plastic viscosity calculated by micromechanical procedure

% ERR Percentage difference between target (TMV) and actual mix viscosity (AMV)

% PWDR Powder content (Any materials<=125μm)

% WTPR Water to powder ratio

% FIRSTLINE Normalized cementitious materials content

% SECONDLINE Normalized cementitious materials and fine aggregate

% THIRDLINE Normalized cementitious materials, fine aggregate contents and coarse aggregate contents

%***

```
%********************************************************************************
clear
clc
% Input water to cementitious materials ratio from Eq. (4.1)
WCM=0.30;       %HSSCC_C90
% Input the paste viscosity from *Material of particle size smaller than 0.125 mm
```

Table 4.2

```
PV=0.177;
%********************************************************************************
s=0;
p=0;
for TMV=5:0.05:15
Z=0.63^ (-1.9)*0.74^ (-1.9);
U= (TMV/PV*Z) ^ (-1/1.9);
X=U^ (1/2);
t1=0.63/X ;
t2=0.74/X ;
a=linspace (0, t1, 500) ;
b=linspace (0, t2, 500) ;
```

```
for i= 1:500

for j= 1:500


H=a (i)*b (j);

if (H<=1.0001 && H>=0.9999)

s=s+1;

% Input the cementitious materials contents limits

for CM=380:5:600

WTR(s) =CM*WCM;

CEM(s) =0.6*CM;

GG(s) =0.2*CM;

FLA(s)=0.2*CM;

SP(s) =0.008*CM; %change the dosage of SP

VPS(s)
=CEM(s)/3150+GG(s)/2400+FLA(s)/2400+WTR(s)/1000+SP(s)/1070+0.02;


FS(s) =0.63-a (i)*X;

FG(s) =0.74-b (j)*X;


WS(s) =2550*FS(s)*VPS(s)/(1-FS(s));

WG(s) =2650*FG(s)*(VPS(s) + (WS(s)/2550))/ (1-FG(s));
```

```
VS(s) =WS(s)/2550;

VG(s) =WG(s)/2650;

TV(s) =VS(s) +VG(s) +VPS(s)-0.02;


WCEMnew(s) =CEM(s)*0.98/TV(s);

WGGnew(s) =GG(s)*0.98/TV(s);

WFLAnew(s) =FLA(s)*0.98/TV(s);

WWTRnew(s) =WTR(s)*0.98/TV(s);

WSPnew(s) =SP(s)*0.98/TV(s);

WSnew(s) =WS(s)*0.98/TV(s);

WGnew(s) =WG(s)*0.98/TV(s);


VCEMnew(s) =WCEMnew(s)/3150;

VGGnew(s) =WGGnew(s)/2400;

VFLAnew(s) =WFLAnew(s)/2400;

VWTRnew(s) =WWTRnew(s)/1000;

VSPnew(s) =WSPnew(s)/1070;

VSnew(s) =WSnew(s)/2550;

VGnew(s) =WGnew(s)/2650;


TVnew(s) =VCEMnew(s) +VGGnew(s)+VFLAnew(s) +VWTRnew(s) +VSPnew(s) +VSnew(s) +VGnew(s) +0.02;
```

```
WCMnew(s) =WCEMnew(s) +WGGnew(s)+WFLAnew(s);

STAG(s) =VSnew(s)/ (VSnew(s) +VGnew(s))*100;

GTAG(s) =VGnew(s)/ (VSnew(s) +VGnew(s))*100;

VPSnew(s)     =VCEMnew(s)     +VGGnew(s)     +VFLAnew(s)+VWTRnew(s)
+VSPnew(s) +0.02;

PSRATIO(s) = VPSnew(s)/ (VSnew(s) +VGnew(s));

FSnew(s) =VSnew(s)/ (VSnew(s)    +VPSnew(s));

FGnew(s) =VGnew(s)/ (VGnew(s) +VSnew(s)    +VPSnew(s));


FFS(s) = (1-FSnew(s)/0.63) ^ (-1.9);

FFG(s) = (1-FGnew(s)/0.74) ^ (-1.9);

AMV(s) =PV*FFS(s)*FFG(s);


ERR(s) = (AMV(s)-TMV)/TMV*100;

PWDR=WCMnew(s);

WTPR(s) =VWTRnew(s)/ (VCEMnew(s) +VGGnew(s)+VFLAnew(s))*100;

 A=TVnew(s);

 C=WSnew(s);

 D=WGnew(s);

 E=STAG(s);

 F=GTAG(s);

 G=PSRATIO(s);
```

```
 I=AMV(s);
 L=ERR(s);
 J=WTPR(s);
 K=WCMnew(s);
 R=WSPnew(s);
 WCMRnew(s) =WWTRnew(s)/WCMnew(s);
 EEE=WCMRnew(s);
 WWTR=WWTRnew(s);

% Check the typical range of SCC mix compositions according to EFNARC

 if (WWTR>=150 && WWTR<=210)
 if (D>=750 && D<=1000)

 if (E>=48 && E<=55)
% Check the percentage difference between (TMV) and (AMV)
 if (L>=-5 && L<=5)

 p=p+1;
AA (p) =K/I;
CC (p) =(K+C)/I;
```

```
DD (p) =(K+C+D)/I;

EE (p) =C/I;

FF (p) =D/I;

TT (p) =(C+D)/I;

StoTOTAL (p) =E/I;

CMplusSAND (p) = (K+C)/I;


AAA=AA (p);

CCC=CC (p);

DDD=DD (p);

GGG=EE (p);

FFF=FF (p);

TTT=TT (p);

STST=StoTOTAL (p);

CMSAND=CMplusSAND (p);


TotalVolume (p) =A;

Sand (p) =C;

CoarseAGG (p) =D;

StoTAG (p) =E;

GtoTAG (p) =F;
```

```
PtoSRATIO (p) =G;

Viscosity (p) =I;

ERROR (p) =L;

SUPER (p) =R;

WATER (p) =WWTR;

CMmaterials (p) =K;

WtoPRatio (p) =J;

FIRSTLINE (p) =AAA;

SECONDLINE (p) =CCC;

THIRDLINE (p) =DDD;

WATERtoCM (p) =EEE;

SANDtoVISCOSITY (p) =GGG;

GRAVELtoVISCOSITY (p) =FFF;

CAplusFA (p) =TTT;

StoTOTALAGG (p) =STST;

CMandSAND (p) =CMSAND;


 end

 end

 end

 end
```

```
  end
  end
end
end
end

%********************************************************************************

% print the results in order to plot the graphs
GtoTAG = round (GtoTAG);
Sand = round (Sand);
CoarseAGG = round (CoarseAGG);
StoTAG = round (StoTAG);
TotalVolume = round (TotalVolume*1000)/1000;
ERR = round (ERR);
PSRATIO = round (PSRATIO);
%********************************************************************************
% Desired parameters to be printed in the output sheet
myMatrix =
[CMmaterials;Sand;CoarseAGG;WATER;SUPER;TotalVolume;WATERtoCM;
WtoPRatio;StoTAG;GtoTAG;PtoSRATIO;ERROR;Viscosity;FIRSTLINE;SECO
NDLINE;THIRDLINE]';
```

```
HeaderNames='CMmaterials,Sand,CoarseAGG,WATER,SUPER,TotalVolume,WATERtoCM,WtoPRatio,StoTAG,GtoTAG,PtoSRATIO,ERROR,Viscosity,FIRSTLINE,SECONDLINE,THIRDLINE';

%********************************************************************************

fileName ='Proportions for C90.csv';

outid = fopen (fileName, 'w+');

fprintf (outid, '%s', HeaderNames);

fclose (outid);

dlmwrite(fileName,myMatrix,'roffset',1,'-append', 'precision', 4);

% you may need to increase precision to allow all digits to be saved

disp (strcat ('Generated report ''', fileName,''''))

%********************************************************************************

%********************************************************************************
```